THE UNIVERSITY OF QUEENSLAND

AUSTRALIA

Processing and Imaging Techniques for Microwave-Based Head Imaging

Lei Guo

B. Sc., M. Eng.

A thesis submitted for the degree of Doctor of Philosophy at

The University of Queensland in 2016

The School of Information Technology and Electrical Engineering

Abstract

Microwave imaging systems for medical applications have been widely investigated in recent years due to their potential to provide portable diagnostic tools that are safe, low cost, and nonionizing. Among many medical applications, brain stroke detection and classification using microwave techniques has been attracting an increasing interest due to the need for a portable onsite, real-time stroke diagnosis that can be used by paramedics. A complete microwave imaging system includes hardware components and software algorithms. The processing and imaging techniques, which are the topic of this thesis, use the collected microwave signals via the antenna array to generate the images of the brain. Numerous microwave imaging techniques applied on bio-medical applications have been researched during recent years. Those proposed techniques exhibited great potential, however, they suffer from several serious drawbacks that need to be solved. This thesis aims to solve four main problems (including a large number of antenna elements, a large number of frequency samples, sensitivity to initial guess of the effective dielectric properties of the image domain and sparsity of the imaged domain), in current microwave imaging techniques and in doing so makes four main research contributions.

The first contribution is the development of a novel algorithm based on compressive sensing (CS). The main target is to develop CS-based imaging algorithm to reduce the number of antennas used in the array. A CS model is constructed based on confocal imaging algorithm, and a convex optimization problem is solved in order to reconstruct the reflection coefficients of the imaging domain. The proposed algorithm is successfully tested on a head model. Followed by that, another CS-based algorithm is proposed to reduce the number of stepped frequencies used in the microwave transceiver system. A CS model is constructed based on the sparse time domain signal received by the antenna array. The algorithm is tested using a developed microwave head imaging system. The results indicate that by using 25% of the original stepped frequencies, the image can be ideally recovered by using the proposed algorithm.

The second contribution is the development of an optimization based confocal imaging algorithm. In all of the traditional confocal imaging algorithms, the effective dielectric constant of the imaging area has to be initially estimated. Since the generated image is sensitive to the effective dielectric constant, a small error in the estimation will cause large distortion in the image. The proposed algorithm proposes a novel concept in which the effective dielectric constant is considered a variable that depends on the signal's entry point in the imaged object (the head). Based on this concept, multiple

effective dielectric constants are optimized with the aim to achieve the most focused (best) image. This optimization is implemented by using particle swarm optimization method. The proposed method is compared with traditional confocal imaging algorithms. The results indicate that the proposed algorithm can achieve much better images with lower cluster effects and insensitive to the initial values of the effective dielectric constants.

The third contribution is the development of a CS based tomography method. A critical problem, which is the sparsity of the imaging domain, is firstly investigated. Since the electrical properties of human head is non-sparse, the wavelet transform is used to transform the non-sparse profile into a sparse wavelet domain. After that, a CS based algorithm named block sparse Bayesian learning (BSBL) is used to recover the electrical properties of the head by using less number of antennas. The proposed algorithm is compared with other traditional tomography methods, and the results indicate that since less number of antennas is used in the system, the images generated by using traditional methods are largely distorted because less information is obtained from the received signal. However, by using the proposed algorithm, the electrical properties of the target area can be ideally recovered by using only 4 antennas with satisfactory results whereas traditional methods require at least 32 antennas.

The last contribution is the development of a framework for brain stroke classification. Two databases are firstly constructed by using two numerical head phantoms. The first database is used to train the classifier whereas the second database is used to evaluate the performance of the built classifier. The databases are composed with brain images generated by using Born iterative method. The validity of the framework is verified with various strokes (haemorrhagic or ischaemic) with different sizes and positions. Two machine learning based techniques named K-means clustering and support vector machine are used to build the classifier. The constructed classifier is tested by using the second database, and the results indicate that when different noise levels are considered, the proposed framework can achieve 88% accuracy rate. The receiver operator characteristic curve is also used to test the framework and the results indicate that the framework can successfully localize the stroke and achieve 91% sensitivity and 87% specificity.

Declaration by author

This thesis *is composed of my original work, and contains* no material previously published or written by another person except where due reference has been made in the text. I have clearly stated the contribution by others to jointly-authored works that I have included in my thesis.

I have clearly stated the contribution of others to my thesis as a whole, including statistical assistance, survey design, data analysis, significant technical procedures, professional editorial advice, and any other original research work used or reported in my thesis. The content of my thesis is the result of work I have carried out since the commencement of my research higher degree candidature and does not include a substantial part of work that has been submitted *to qualify for the award of any* other degree or diploma in any university or other tertiary institution. I have clearly stated which parts of my thesis, if any, have been submitted to qualify for another award.

I acknowledge that an electronic copy of my thesis must be lodged with the University Library and, subject to the policy and procedures of The University of Queensland, the thesis be made available for research and study in accordance with the Copyright Act 1968 unless a period of embargo has been approved by the Dean of the Graduate School.

I acknowledge that copyright of all material contained in my thesis resides with the copyright holder(s) of that material. Where appropriate I have obtained copyright permission from the copyright holder to reproduce material in this thesis.

Publications during candidature

Peer-reviewed Journal Papers

1. **L. Guo** and A. Abbosh, "Optimization-based confocal microwave imaging in medical applications," *IEEE Trans. Antennas and Propag*., vol. 63, no. 8, pp. 3531-3539, Aug. 2015. **(R. W. P. King Paper Award from IEEE AP-S in 2016)**

2. **L. Guo** and A. Abbosh, "Microwave imaging of nonsparse domain using Born iterative method with wavelet transform and block sparse Bayesian learning," *IEEE Trans. Antennas and Propag*., vol. 63, no. 11, pp. 4877-4888, Nov. 2015.

3. **L. Guo** and A. Abbosh, "Microwave stepped frequency head imaging using compressive sensing with limited number of frequency steps," *IEEE Antennas Wireless Propag. Lett*., vol. 14, pp. 1133-1136, 2015

4. **L. Guo** and A. Abbosh, "Phase shifters with wide range of phase and ultra-wideband performance using stub-loaded coupled structure," *IEEE Microw. Wireless Compon. Lett*., vol. 23, no. 3, pp. 167-169, Nov. 2014.

5. **L. Guo**, H. Zhu, and A. Abbosh, "Wideband tunable in-phase power divider using three-line coupled structure," *IEEE Microw. Wireless Compon. Lett*., vol. 26, no. 5, May. 2016.

6. **L. Guo**, H. Zhu, and A. Abbosh, "Wideband phase shifter with wide phase range using parallel coupled lines and L-shaped networks," *IEEE Microw. Wireless Compon. Lett*., vol. 26, no. 5, Jun. 2016.

7. **L. Guo**, A. Abbosh, and H. Zhu, "Ultra-wideband in-phase power divider using stepped-impedance three-line coupled structure and microstrip-to-slotline transitions," *Electron. Lett*., vol. 50, no. 5, pp. 383-384, Feb. 2014.

8. H. Zhu, A. Abbosh, and **L. Guo**, "Ultra-wideband unequal in-phase power divider using three-line coupled structure," *Electron. Lett*., vol. 50, no. 15, pp. 1081-1082, Jul. 2014.

9. H. Zhu, A. Abbosh, and **L. Guo**, "Wideband four-way filtering power divider with sharp selectivity and wide stopband using looped coupled-line structure," *IEEE Microw. Wireless Compon. Lett*., vol. 26, no. 5, May. 2016.

10. **L. Guo**, H. Zhu, and A. Abbosh, "Phase reconfigurable power divider," *IEEE Trans. Microw. Theory Tech*. (Submitted)

11. H. Zhu, **L. Guo**, and A. Abbosh, "Planar in-phase power divider with tunable power division and controllable wideband filtering response," *IEEE Trans. Microw. Theory Tech.* (Subimtted)

Peer-reviewed Conference Papers

1. **L. Guo** and A. Abbosh, "Wavelet-based compressive sensing for head imaging," in *International Symposium on Antennas and Propagation (ISAP)*, Hobart, Australia, pp. 1-3, 2015. **(Best Student Paper Award)**

2. **L. Guo** and A. Abbosh, "Compressive sensing for stroke detection in microwave-based head imaging," in *Proceedings 2014 IEEE International Symposium on Antennas and Propagation*, Memphis, USA, pp. 1911-1912, 2014.

3. **L. Guo** and A. Abbosh, "Ultra-wideband phase shifter using broadside-coupled microstrip coplanar waveguide," *Asia Pacific Microwave Conference 2013*, Seoul, Korea, pp. 951-953, Nov, 2013.

4. **L. Guo** and A. Abbosh, "Multilayer phase shifter with wide range of phase and ultra-wideband performance," *Asia Pacific Microwave Conference 2013*, Seoul, Korea, pp. 16-18, Nov, 2013.

5. **L. Guo**, H. Zhu, and A. Abbosh, "Planar UWB phase shifter using parallel coupled lines combined with short-ended stubs and impedance transformer," in *Asia-Pacific Microwave Conference (APMC)*, Nanjing, China, pp. 1-3, 2015.

6. **L. Guo** and A. Abbosh, "Microwave technique for brain stroke localization and classification using block sparse Bayesian learning with wavelet transform," in *Asia-Pacific Microwave Conference (APMC)*, Nanjing, China, pp. 1-3, 2015.

7. **L. Guo** and A. Abbosh, "Microwave head imaging using multi-frequency tomography," in *International Conference on Electromagnetic in Advanced Applications*, Cairns, Australia, 2016.

Publications included in this thesis

Peer-reviewed Journal Papers

1. **L. Guo** and A. Abbosh, "Optimization-based confocal microwave imaging in medical applications," *IEEE Trans. Antennas and Propag*., vol. 63, no. 8, pp. 3531-3539, Aug. 2015. **(R. W. P. King Paper Award from IEEE AP-S in 2016)** – Partly incorporated as paragraph in Chapter 5.

Contributor	Statement of contribution
Lei Guo (Candidate)	Designed algorithms (85%) Wrote the paper (75%)
A. Abbosh	Designed algorithms (15%) Wrote and edited paper (25%)

2. **L. Guo** and A. Abbosh, "Microwave imaging of nonsparse domain using Born iterative method with wavelet transform and block sparse Bayesian learning," *IEEE Trans. Antennas and Propag*., vol. 63, no. 11, pp. 4877-4888, Nov. 2015. – Partly incorporated as paragraph in Chapter 4.

Contributor	Statement of contribution
Lei Guo (Candidate)	Designed algorithms (85%) Wrote the paper (75%)
A. Abbosh	Designed algorithms (15%) Wrote and edited paper (25%)

3. **L. Guo** and A. Abbosh, "Microwave stepped frequency head imaging using compressive sensing with limited number of frequency steps," *IEEE Antennas Wireless Propag. Lett*., vol. 14, pp. 1133-1136, 2015. – Partly incorporated as paragraph in Chapter 3.

Contributor	Statement of contribution
Lei Guo (Candidate)	Designed algorithms (85%) Wrote the paper (75%)
A. Abbosh	Designed algorithms (15%) Wrote and edited paper (25%)

Peer-reviewed Conference Papers

1. **L. Guo** and A. Abbosh, "Wavelet-based compressive sensing for head imaging," in *International Symposium on Antennas and Propagation (ISAP)*, Hobart, Australia, pp. 1-3, 2015. **(Best Student Paper Award)** – Partly incorporated as paragraph in Chapter 4.

Contributor	Statement of contribution
Lei Guo (Candidate)	Designed algorithms (85%) Wrote the paper (75%)
A. Abbosh	Designed algorithms (15%) Wrote and edited paper (25%)

2. **L. Guo** and A. Abbosh, "Compressive sensing for stroke detection in microwave-based head imaging," in *Proceedings 2014 IEEE International Symposium on Antennas and Propagation*, Memphis, USA, pp. 1911-1912, 2014. – Partly incorporated as paragraph in Chapter 3.

Contributor	Statement of contribution
Lei Guo (Candidate)	Designed algorithms (85%) Wrote the paper (75%)
A. Abbosh	Designed algorithms (15%) Wrote and edited paper (25%)

Contributions by others to the thesis

Assoc. Prof. Amin Abbosh contributed closely in defining research problem, overall conception and direction of the thesis.

Statement of parts of the thesis submitted to qualify for the award of another degree

None

Acknowledgements

I would like to express my sincerest gratitude to my principle supervisor, Associate Professor Dr. Amin Abbosh, for guidance, encouragement, and feedback during my PhD study.

I thank my colleagues at Microwave group, in particular Dr. Konstanty Bialkowski for his kind suggestions on signal processing. I also thank the colleagues at Engineering & Technical Support Group, especially Denis Bill, Richard Newport and John Kohlbach for their kind help on manufacturing the components and devices.

I would like to thank the School of Information Technology and Electrical Engineering (ITEE), The University of Queensland for the scholarship support.

Last but not least, I would like to thank my family for their continuous encouragement and the moral support throughout my PhD study.

Keywords

microwave head imaging technique, confocal imaging algorithm, microwave tomography, compressive sensing, wavelet transform, brain stroke classification, optimization, machine learning.

Australian and New Zealand Standard Research Classifications (ANZSRC)

ANZSRC code: 090699, Electrical and Electronic Engineering not elsewhere classified, 100%

Fields of Research (FoR) Classification

FoR code: 0906, Electrical and Electronic Engineering, 100%

Table of Contents

Processing and Imaging Techniques for Microwave-Based Head Imaging I
Lei Guo I
B. Sc., M. Eng. I
Abstract II
Publications during candidature V
Publications included in this thesis VII
Acknowledgements X
List of Figures XIV
List of Tables XVII
List of Abbreviations XVIII
Chapter 1: Introduction 1
1.1 Background and Motivation 1
1.2 Microwave Systems Applied for Brain Stroke Diagnosis 2
1.3 Drawbacks of the Current Algorithms 5
1.4 Original Contributions 7
1.5 Thesis Organization 8
Chapter 2: Literature Review of Microwave Imaging Techniques 10
2.1 Introduction 10
2.2 Development of Radar-Based Technique for Bio-Medical Application 10
2.2.1 Beamforming Imaging Algorithm 10
2.2.2 Confocal Imaging Algorithm 12
2.2.3 Radar-based Microwave Head Imaging System 16
2.3 Development of Tomography-Based Technique for Bio-Medical Application 19
2.3.1 Inverse Scattering Problem 19
2.3.2 Born Iterative Method and Distorted Born Iterative Method 19
2.3.3 Tomography-based Microwave Head Imaging System 24
2.4 Discussions and Conclusions 25
2.4.1 Challenges and Problems in Radar-based Microwave Imaging Techniques 25
2.4.2 Challenges and Problems in Tomography-based Microwave Imaging Techniques 29
Chapter 3: Compressive Sensing in Radar-based Imaging Techniques 33
3.1 Theory of Compressive Sensing 33
3.2 Compressive Sensing to Reduce the Number of Antennas 36
3.2.1 Theory 36
3.2.2 Simulation Results and Discussions 40
3.3 Compressive Sensing to Reduce the Number of Stepped Frequencies 42
3.3.1 Theory 43
3.3.2 Imaging Results and Discussions 47
3.4 Discussions and Conclusions 52
Chapter 4: Compressive Sensing with Tomography -based Imaging Techniques 54
4.1 Compressive Sensing on Non-Sparse Imaging Domain 54
4.1.1 Born Iterative Method Framework 56
4.1.2 Wavelet Transform 58
4.1.3 Block-Sparse Bayesian Learning 63
4.2 Evaluation on Simple Non-Sparse Model 69
4.3 Evaluation on Numerical Head Phantom 75
4.4 Discussions and Conclusions 78
Chapter 5: Optimization Techniques for Radar-based Imaging 80
5.1 Optimization-based Confocal Algorithm in Microwave Head Imaging 80

5.2 Particle Swarm Optimization 86
5.3 Evaluation in Full-Wave Simulation Environment 88
5.4 Evaluation on Realistic Measurement Data 95
5.5 Discussions and Conclusions 100
Chapter 6: Brain Stroke Classification in Microwave Imaging 101
6.1 Classification Using Machine Learning Techniques 101
6.1.1 K-Means Clustering 101
6.1.2 Support Vector Machine 107
6.2 Classifier Training Procedure 112
6.3 Classification Results 113
6.4 Discussions and Conclusions 116
Chapter 7: Conclusions and Future Work 117
7.1 Conclusions 117
7.2 Future Work 119

List of Figures

Fig 2. 1: The generated images using delay-and-sum beamforming algorithm. (a) a 2 mm diameter tumor was placed at (5.0 cm, 1.1 cm), (b) a 2 mm diameter tumor was placed at (8.0 cm, 2.1 cm) [26]..... 11
Fig 2. 2: (a) The breast model from MRI scan, (b) the generated image using confocal imaging algorithm [29] 13
Fig 2. 3: The wave propagation mode for (a) incident wave and (b) scattered wave [72]..... 13
Fig 2. 4: The configuration of the microwave head imaging scenario in [69]. The imaging domain was denoted as $\mathbb{Z}$ with gray color, the boundary points B_i was used to represent the entry point of the signal and the point inside the brain was denoted as p 15
Fig 2. 5: The numerical head phantom used to test the confocal imaging algorithm in [69]. (a) the dielectric constant profile of the head phantom, (b) the conductivity profile of the head phantom 15
Fig 2. 6: The generated images using confocal imaging algorithm when the haemorrhagic stroke was placed at four different positions. The position of the stroke was marked with cross-hairs [69]..... 15
Fig 2. 7: (a)-(b) the configuration and platform of microwave head imaging system developed in [36] and (c)-(d) the configuration and platform of microwave head imaging system developed in [40]. 17
Fig 2. 8 (a) Distribution of the isosceles triangle patch antenna; (b) prototype of the microwave head stroke detection system [43] 18
Fig 2. 9: Comparison between the dielectric constant profile of the head phantom and the reconstructed profile at (i) 0.6 GHz, (ii) 0.85 GHz and (iii) 1 GHz. (a) were the original dielectric constant profiles of the head phantoms, (b) were the reconstructed profiles with noiseless data, (c) were the reconstructed profiles with SNR=20 dB and (d) were the reconstructed profiles with SNR=10 dB [50]. 20
Fig 2. 10: Comparison between the conductivity profile of the head phantom and the reconstructed profile at (i) 0.6 GHz, (ii) 0.85 GHz and (iii) 1 GHz. (a) were the original conductivity profiles of the head phantoms, (b) were the reconstructed profiles with noiseless data, (c) were the reconstructed profiles with SNR=20 dB and (d) were the reconstructed profiles with SNR=10 dB [50]..... 21
Fig 2. 11: $NRMS2$ values varied with the iteration numbers under different SNR levels when the incident frequencies are (a) 0.6 GHz, (b) 0.85 GHz and (c) 1 GHz [50]. 22
Fig 2. 12: (a), (c) (e), and (g) are the breast phantoms with different distributions of breast tissues, (b), (d), (f), and (h) are the reconstructed dielectric profiles using DBIM corresponding to the phantoms in (a), (c), (e), and (g), respectively [47]. 24
Fig 2. 13 (a) Configuration of the tomography-based head imaging system, (b) system prototype of the tomography-based imaging system [41]-[42] 24
Fig 2. 14: Dielectric constant of different head tissues across the band 0.1-3 GHz used in head imaging [139] 26
Fig 3. 1: The entire process of compressive sensing reconstruction [90]. 34
Fig 3. 2: Configuration of the imaging cells 39
Fig 3. 3: The block diagram of the entire CS reconstruction process 40
Fig 3. 4: Antenna array setup. The elliptical area represents the head model and the discrete red points denote M antenna array elements. 41
Fig 3. 5: Head imaging results with high contrast of target area. (a) The used head model with a bleeding stroke indicated by a bright square; (b) Image from using 16 antennas and confocal imaging algorithm; (c) Image from using 4 antennas and confocal algorithm; (d) Image from using 4 antennas and CS-based imaging algorithm. 41
Fig 3. 6: CS-based imaging result with low contrast of target area. (a) Image from using original CS algorithm; (b) Image from using improved CS algorithm (with approximated TV transformation)..... 42
Fig 3. 7: A general domain of microwave imaging system using antenna array of P antenna elements..... 44
Fig 3. 8: Examples of time domain correlation signals received at each of the 16 antennas from 401 frequency steps using the head imaging system in [36]..... 45
Fig 3. 9: System platform used to obtain the measured data [36]..... 45
Fig 3. 10: The fabricated realistic head phantom used to obtain the measurement data [36]..... 47
Fig 3. 11: Comparison between the average correlation coefficients (ACC) of the original and recovered TDC signals for different antennas using three different l_1 norm optimization solvers. 48

Fig 3. 12: Constructed head images from using (a) full number (M=401) of available frequency steps in the traditional method, and (b), (c), and (d) under-sampled frequency steps (M=300, M=200, and M=100, respectively) using traditional and three CS methods. 49
Fig 3. 13: Average NER using traditional and CS methods under different number of frequency steps 50
Fig 3. 14: Number of successful reconstructions and values of quality metric β using non-CS and CS methods for different number of frequency steps. 50
Fig 4. 1: Diagram of a general imaging problem 54
Fig 4. 2: Block diagram of the proposed imaging scheme 55
Fig 4. 3: The non-sparse model used to test the wavelet transformation 59
Fig 4. 4: The Haar wavelet coefficients (one-dimensional representation) for the non-sparse model used to assess the proposed imaging shceme 59
Fig 4. 5: The Haar wavelet coefficients (two-dimensional representation) for the non-sparse model used to assess the proposed imaging scheme. 60
Fig 4. 6: The realistic head model used to test the wavelet transformation 61
Fig 4. 7: Normalized dielectric profile (NDP) of the realistic head phantom with a hemorrhagic stroke located at different positions. 61
Fig 4. 8: The Haar wavelet coefficients (one-dimensional representation) for the head model with a hemorrhagic stroke placed at three different positions. 62
Fig 4. 9: The Haar wavelet coefficients (two-dimensional representation) for the head model with a hemorrhagic stroke placed at three different positions. 62
Fig 4. 10: Reconstructed normalized dielectric profile (NDP) using proposed technique at (a)-(d) 1 GHz, (e)-(h) 1.5 GHz, and (i)-(l) 2 GHz with different SNR levels. 69
Fig 4. 11: NER performance of the proposed technique versus SNR at different frequencies. 71
Fig 4. 12: The convergence rate of the expectation-maximization (EM) method used in the internal iteration at different incident frequencies and noise levels. 71
Fig 4. 13: The convergence rate for NER of the estimated NDP in the external iteration at different incident frequencies and noise levels. 72
Fig 4. 14: Reconstructed NDP at 1.5 GHz using (a)-(d) proposed, (e)-(h) BIM-LS [50], (i)-(l) CoSaMP [110], and [m]-[p] CGLS methods [135]. 72
Fig 4. 15: Performance of different imaging techniques at (a) 1 GHz, (b) 1.5 GHz, and (c) 2 GHz. 73
Fig 4. 16: The reconstructed dielectric profiles of a realistic head phantom with a haemorrhagic stroke located at different positions using the proposed imaging technique. The performance is evaluated under different SNR levels and the incident frequency f=0.6 GHz. 76
Fig 4. 17: The reconstructed dielectric profiles of a realistic head phantom with a haemorrhagic stroke located at different positions using the proposed imaging technique. The performance is evaluated under different SNR levels and the incident frequency f=0.8 GHz. 76
Fig 4. 18: The reconstructed dielectric profiles of a realistic head phantom with a haemorrhagic stroke located at different position using the proposed imaging technique. The performance is evaluated under different SNR levels and the incident frequency f=1 GHz. 77
Fig 4. 19: NER as the function of iteration time under different noise levels. 77
Fig 4. 20: NER of the proposed techniques when used in head imaging with different SNR 78
Fig 5. 1: The imaging domain 80
Fig 5. 2: Expansion and sub-gridding of the imaged area V 83
Fig 5. 3: Flowchart of the proposed algorithm 85
Fig 5. 4: Two-dimensional section of the numerical head model used in simulations. (a) Shallow, (b) deep stroke, and (c) healthy brain. 89
Fig 5. 5: Simulation results using the traditional and proposed methods for head with shallow stroke indicated by the black square. 89
Fig 5. 6: Simulation results using traditional and proposed method for head with deep stroke 90
Fig 5. 7: Simulation results using traditional and proposed methods for healthy head. 90
Fig 5. 8: Variation of the convergence index μ with number of iterations for (a) shallow stroke, (b) deep stroke, and (c) healthy head 92
Fig 5. 9: The value of (a) γ and (b) σ from using the traditional and proposed method on two cases (shallow and deep stroke) and different initial values of dielectric constants, and (c) γ for a healthy case. 94

Fig 5. 10: The experimental system used to test the proposed algorithm. (a) System described in [40], and (b) system described in [141]. 96
Fig 5. 11: Experimental results using the system in [141]. 97
Fig 5. 12: Experimental results using the system in [40]. 97
Fig 5. 13: The convergence index μ with iteration time for (a) 1st experiment and (b) 2nd experiment. 98
Fig 5. 14: Quality metrics (a) γ and (b) σ of images produced using the traditional and proposed method in two experiments. 99
Fig 6. 1: (a)-(b) The phantom A with ICH stroke and (c)-(d) phantom A with IS stroke, (e)-(h) the calculated NDP using BIM corresponding to each of the cases shown in (a)-(d). 102
Fig 6. 2: (a)-(b) The phantom B with ICH stroke and (c)-(d) the phantom B with IS stroke, (e)-(h) the calculated NDP using BIM corresponding to each of the cases shown in (a)-(d). 102
Fig 6. 3: The calculated $\mathcal{C}_X$ for (a) phantom A with ICH; (b) phantom A with IS; (c) phantom B with ICH and (d) phantom B with IS. 103
Fig 6. 4: The clustered $\mathcal{C}_X$ profile for phantom A using k-means method when two types of stroke (ICH and IS) are placed inside the brain. 103
Fig 6. 5: The clustered $\mathcal{C}_X$ profile for phantom B using k-means method when two types of strokes (ICH and IS) are placed inside the brain. 104
Fig 6. 6: The third clusters of the ICH cases for phantom A and B indicate that the inner part of the head boundary is not a null space. 105
Fig 6. 7: The number of non-zero pixels within the inner part of the third cluster for both ICH and IS cases when the SNRs are 40, 25, and 10 dB for (a)-(c) phantom A and (d)-(f) phantom B. 106
Fig 6. 8: SVM classifier: the decision boundary $f(\boldsymbol{x}) = \boldsymbol{w}^T\boldsymbol{x} + b$ (the thick line) which is defined by a normal vector of the hyperplane and an offset. The margin is the minimal distance of any training points in the two classes (blank circle represents the IS case and solid circle represents the ICH case) to the hyperplane. The support vectors are the training samples lying on the boundary hyperplanes of the two classes. 108
Fig 6. 9: Flowchart of the proposed algorithm framework 110
Fig 6. 10: Database structure used in the SVM training and testing 112
Fig 6. 11: The ROC curves for (a) SNR=40 dB, (b) SNR=25 dB, (c) SNR=10 dB, (d) all the three SNR cases combined. The AUC value is indicated in the legend of each graph 114
Fig 6. 12: Variation of the sensitivity and specificity with the threshold values in SVM for (a) SNR=40 dB, (b) SNR=25 dB, (c) SNR=10 dB, (d) all the three SNR cases combined. 115

List of Tables

Table 4. 1: Computation time of different methods 74
Table 6. 1: Support vector machine (SVM) classification accuracy under four scenarios 113

List of Abbreviations

CT	Computed Tomography
MRI	Magnetic Resonant Imaging
SAR	Synthetic Aperture Radar
ISAR	Inverse Synthetic Aperture Radar
GPR	Ground Penetration Radar
VNA	Vector Network Analyser
EM	Electromagnetic
SFCW	Step Frequency Continuous Wave
SDR	Software Defined Radar
ADC	Analog to Digital Converter
SVM	Support Vector Machine
BIM	Born Iterative Method
DBIM	Distorted Born Iterative Method
CS	Compressive Sensing
PSO	Particle Swarm Optimization
FIR	Finite Impulse Response
FDTD	Finite Difference Time Domain
UWB	Ultra-Wideband
NDP	Normalized Dielectric Profile
SNR	Signal to Noise Ratio
RIP	Restricted Isometry Property
LP	Linear Programming
3D	Three Dimensional
TV	Total Variation
TDC	Time Domain Correlation
CSF	Cerebral Spinal Fluid
ACC	Average Correlation Coefficient
NER	Normalized Error Rate
BCS	Bayesian Compressive Sensing
BSBL	Block Sparse Bayesian Learning
EM	Expectation-Maximization
LS	Least Square

CGLS	Conjugate Gradient Least Square
ICH	Intra Cerebral Haemorrhagic
IS	Ischaemic
SVD	Singular Value Decomposition
KKT	Karush-Kuhn-Tucker
ROC	Receiver Operator Characteristic
AUC	Area Under the Curve

Chapter 1: Introduction

1.1 Background and Motivation

Brain stroke is a fatal disease which is challenging to detect and classify especially at early stages. In Australia, nearly 60,000 stroke patients are diagnosed per year, and the number of new stroke cases are increasing. This huge number of stroke cases costs the Australian government $2.14 billion per annum. The impact of stroke makes on patients is substantial. For example, 20% of the stroke patients will die within a month and more than 30% of them will die within 12 months. Approximately 88% survivors suffer several types of disabilities [1].

Brain stroke can be generally divided into two types: the haemorrhagic stroke and ischaemic stroke. The investigation indicates that around 15% of all the strokes are haemorrhagic stroke and nearly 85% strokes account for ischaemic stroke [2]. Haemorrhagic stroke is caused by either the rupture of saccular aneurysms in the subarachnoid area or the rupture of the blood vessel. Blood leaks from the vessel, spreads into the brain and results in high pressure, thus damaging the tissues in the brain. Ischaemic stroke is caused by a blood clot. The blood vessel is blocked by the blood clot and thus the blood cannot reach the brain [3]. Different types of the brain strokes correspond to different therapy treatment, and incorrect treatment imposed on the patient will cause fatal results. Therefore, it is vital to classify the type of the stroke before any therapy treatment is applied.

The diagnosis (includes detection and classification) mainly rely on the brain images. Several brain stroke detection and imaging techniques have been researched and developed during the past few decades such as computed tomography (CT) scans, magnetic resonant imaging (MRI) and ultrasound [4]-[6]. The quality of image generated from ultrasound technique is largely influenced by the operator who manipulates the scanner thus it is ‘operator-dependent’. Moreover, the image quality is also degraded when the patient has thick skull as the penetration depth of ultrasound is decreased when bone or air is present. The brain imaging techniques based on CT and MRI provide accurate and high resolution images which can be used to detect and classify the stroke, however, some drawbacks still exist in these techniques, such as high cost, non-portable and radiative (for CT). Most of the brain stroke cases happened under unexpected scenarios and emergent treatment need to be performed on the patient. The most important time for a patient to be rehabilitated from brain stroke is the first two hours from the onset of the stroke. Therefore, it is important to detect and classify the stroke in a short time once the stroke symptom is observed. Due to the high cost and non-portable

features of MRI and CT systems, these two systems are not suitable to be used onsite by paramedics or utilized in rural areas.

Motivated by this situation, it is desirable to develop low-cost and portable diagnosis system which can be used to overcome the drawbacks of conventional instruments such as MRI and CT. The new system is required to possess compact size, low-cost, and the ability to detect and classify the brain stroke within a short period of time. Driven by these requirements, bio-medical imaging systems using microwave technology have been researched and developed during the past few decades. Microwave imaging systems were firstly researched as far-field imaging technique such as synthetic aperture radar (SAR), inverse synthetic aperture radar (ISAR) or ground penetration radar (GPR). In early of 1970s, the nonionizing electromagnetic wave effects in biological materials was investigated [7] and in 1982, it was proposed that microwave technique may be used to detect cerebral edema [8]. Breast tumour detection using microwave technology was widely researched since 1998 [9]-[10]. The proposed concept is based on two properties of breast tissues at microwave frequency range. Firstly, the dielectric properties between malignant tumors and normal tissues exhibit significant difference, and secondly, the signal attenuation on normal breast tissue is weak for microwave frequencies, thus it is possible to distinguish the malignant tumors from the normal tissues using microwave system. Based on this concept, various hardware (such as antenna designs for microwave breast imaging) [11]-[17] and algorithms [18]-[29] have been proposed and developed for microwave breast imaging application.

Inspired by the successful application of using microwave technique on breast cancer detection, it is straightforward to rise up a question: if microwave technique can be applied on other bio-medical applications? Followed with this question, numerous researchers proposed diverse bio-medical applications using microwave technique. Among all of those proposals, brain stroke detection and classification using microwave system is drawing more interests during the past few years. Due to the features of microwave imaging system (low-cost, safety and portability), it is becoming a potential instrument which can be used to solve the problems from MRI and CT system as mentioned before.

1.2 Microwave Systems Applied for Brain Stroke Diagnosis

In 1982, J. Lin and M. Clarke proposed the idea that use microwave system to detect the cerebral edema [8]. This was the first time that microwave imaging system was applied on diagnosing brain disease. D. Ireland and M. Bialkowski proposed the idea that apply microwave technique on brain

stroke detection in 2010 [30]. The fundamental reason that microwave system can be used on brain stroke detection is because the significant contrast among different brain tissues can be observed with regard to the dielectric constant at microwave frequency range. This property implies that it is possible to distinguish different brain tissues based on the received signals. Some initial investigations have been made in [31]-[35] with regard to the antenna's design and signal processing. A complete microwave head imaging system was presented in [36]. The system utilized a circular antenna array which was composed with corrugated tapered slot antennas to transmit and receive the signals. The signals received from the antenna array were further processed using vector network analyser (VNA) which was used to transfer the electromagnetic (EM) wave into S-parameters. The collected S-parameters were used to generate the head images by using the algorithm proposed in [37]. The system was evaluated using a realistic head phantom which was manufactured based on the data reported in [38]-[39] and the results indicated that the system can localize the position of the haemorrhagic stroke when the stroke was placed at shallow position inside the brain. Similar system with enhanced hardware and head phantom was presented in [40]. A new unidirectional antenna design was used in the antenna array and more accurate head phantom was manufactured using 3-D printing technology. A novel portable transceiver from Agilent Tech (N7081A) was used to collected the S-parameters. The results shown in [40] indicated that the position of haemorrhagic stroke can be accurately localized even when the stroke was placed at deep position inside the head. Some other head stroke imaging or classification systems based on microwave technique were proposed in [41]-[43]. In [41]-[42], complete microwave head imaging systems were constructed based on tomography method. Totally 160 antennas were used in the system and operated at the frequency of 1 GHz. Matching medium was used in the system to reduce the strong reflection from the brain skin. In [43], a microwave system was built for brain stroke classification purpose. Totally 10-12 patch antennas were used in a helmet shaped array to transmit and receive the signals. An integrated network analyser was used to collect the reflection coefficients of the antennas. Based on the collected reflection coefficients, a machine learning technique was used to classify the types of the strokes (haemorrhagic stroke or ischaemic stroke). The system was evaluated in clinic trails, and the results indicated that when 90% patients with haemorrhagic stroke can be diagnosed, 65% patients with ischaemic stroke can also be correctly diagnosed. These promising results implied that brain stroke classification can also be implemented using microwave system.

A complete microwave imaging system is composed with two parts: the hardware and software. The hardware part includes the antenna array, transceiver and switching system. The software part includes the imaging and stroke classification algorithm. Apart from the hardware design, software design is also an important part in microwave imaging system. Microwave imaging algorithm can be

generally divided into two categories: the radar-based algorithms and tomography based algorithms. Radar-based algorithms localize the position of the target (brain stroke) based on the time delay between the transmitted signals and received signals. To achieve acceptable resolution for the images, wideband frequency need to be used in this technique. Under this requirement, the hardware (antennas and transceivers) is usually designed with wideband performance. In most of the bio-medical applications, such as breast cancer and brain stroke detection, the reflected signals from the skin are much stronger than those reflected from the true target (tumor or stroke) thus the reflected signals from the targets are buried by those from the skin. This phenomenon largely affects the signals' time delay calculation and further influences the generated images. Some additional methods need to be used to eliminate the reflected signals from the skin, such as using matching medium to surround the imaging area or using some specific algorithms to pre-process the received signals.

The radar-based imaging algorithms, which are used to pre-process the signals and generate the final images, are widely researched during the past few years. These algorithms can be generally divided into two categories, the imaging algorithms and the signals pre-processing algorithms. The imaging algorithms include beamforming [26] and confocal techniques [29] and the signals pre-processing algorithms include signal subtraction [37] and entropy-based techniques [25]. Tomography-based algorithms reconstruct the contrast dielectric properties (permittivity and conductivity) of the imaging area using the scattered signals. Multi-static antenna array is used to transmit and receive the scattered signals. Tomography-based algorithms operate at single frequency thus the selection of appropriate frequency is important for the reconstruction performance. Since the reconstruction process is based on solving an ill-posed inverse problem thus signal subtraction method is not applicable to eliminate the strong reflection from the skin. Instead of using some signal pre-processing techniques, matching medium can also be used to reduce the strong reflection from the skin. The ill-posed inverse problem in tomography-based methods is a non-linear problem hence some approximations need to be used firstly. Born approximation and Rytov approximation [44] are two main methods which are used to linearize the inverse problem. Several tomography methods applied on bio-medical applications have been reported in [45]-[50]. The results indicated that the contrast dielectric profiles of the breast or the head can be reconstructed based on the received scattered signals. These results implied that tomography-based methods could be a suitable choice for brain stroke classification since the types of the strokes (haemorrhagic and ischaemic) can be classified from their contrast dielectric properties (the contrast dielectric property of haemorrhagic stroke is different from the ischaemic stroke).

1.3 Drawbacks of the Current Algorithms

Despite of the successful usage of those imaging algorithms mentioned above on bio-medical applications, numerous drawbacks still exist in the current algorithms. In this research project, those problems and drawbacks are investigated as summarized below.

1. In the current microwave head imaging systems, large number of antennas are required to be used in the antenna array. For radar-based imaging algorithms, large number of antennas represent more illumination views, thus it will decrease the possibility that the algorithms focuse on false targets (especially for confocal algorithms). For tomography-based methods, large number of antennas are used to collect more scattered data thus the ill-posedness of the inverse problem can be somehow alleviated. However, increasing the number of antennas in the array brings about several problems. Firstly, the mutual coupling between adjacent antennas will largely affect the received signals since it will change the radiation properties of the antennas and distort the generated images [51]. Secondly, the usage of large number of antennas in the array largely increase the size of the entire system. This limitation impedes researchers from building portable microwave brain imaging system.
2. For the systems using radar-based technique, wideband frequency range is required to achieve satisfied resolution. To generate the required incident signals with wideband frequency, step-frequency-continuous-wave (SFCW) is usually used since it is difficult to generate single pulse with wideband spectrum. The generation of SFCW signals can be easily achieved by using VNA, however, under the requirement of constructing portable and low-cost microwave imaging system, the usage of VNA is replaced by portable transceiver [16], [56] or software-defined-radar (SDR) technique [52]-[55]. Either portable transceiver or SDR system needs to use wide frequency band which implies large number of pulses with stepped frequencies has to be generated. In portable transceiver design, dense stepped frequencies increase the difficulties for designing the sampling circuit or analog-to-digital converter (ADC). Also, in SDR system design, dense stepped frequencies imply large amount of time is required for the calibration procedure since for each frequency step the system needs to calibrate the signal one time [52]-[55]. These drawbacks prohibit designing efficient and high-speed portable transceiver or SDR systems.

3. Confocal imaging algorithm [29] is widely used in bio-medical microwave imaging systems. To focus the received signals on the target correctly, effective dielectric constant of the imaged area is needed. All the current microwave imaging algorithms based on confocal method use one certain dielectric constant without considering the position of the target to be imaged, the position of the transmitters, or the entry point of the signal in the imaging area. This assumption might be valid when the imaging area contains small number of bio-tissues with relatively similar electrical properties, such as the imaging scenario in breast cancer detection, however, it is not suitable for the scenario where the imaging area contains highly heterogeneous targets, such as brain stroke detection. In such scenario, the effective dielectric constant depends on the signals' entry points in that imaging area, the tissues through which the signals propagate before being reflected and the locations of the transmitting or receiving antennas. The usage of single effective dielectric constant with inappropriate choice leads to serious distortion in the generate images for microwave brain imaging application.
4. Radar-based microwave imaging technique can only localize the position of the targets (tumor and brain stroke), however, it cannot distinguish the electrical properties (permittivity and conductivity) of different targets. This drawback might not affect the practical value of microwave breast imaging system since for that application, localizing the position of tumor is considered as the most important purpose. Conversely, for microwave brain imaging system, a stroke can be either haemorrhagic stroke or ischaemic stroke and different types of stroke correspond to different treatment therapies (incorrect treatment on brain stroke patient might lead to fatal results). Thus, the ability of distinguishing the electrical properties of different target is considered as another important purpose. For most of current microwave head imaging systems, localizing the position of stroke is the only purpose considered in their systems and the classification of stroke is rarely considered. Although one system was proposed in [43] with stroke classification ability, the imaging ability was dropped and the classification accuracy still need to be improved.

In this research project, these problems and challenges will be described and analysed in details. The solutions for each of the four problems will be proposed and evaluated. The proposed methods to solve these problems are helpful to build more efficient and accurate microwave head imaging systems.

1.4 Original Contributions

Four major drawbacks in current microwave head imaging algorithms were illustrated in the previous section. The works undertaken in this thesis aim to solve these four independent problems one by one. Due to the limitations of experimental conditions, some of the algorithms are tested in a realistic simulation environment. High resolution head phantom from MRI scan is used in the simulation and related interpretations are given in the corresponding chapters.

To solve these four drawbacks in current microwave head imaging algorithms, this thesis possesses four original contributions which were listed below:

1. Novel algorithms using compressive sensing technique are proposed in radar-based microwave imaging techniques which can be used to reduce the number of antennas in the antenna array or decrease the number of stepped frequencies used in the portable transceiver and SDR system. The proposed algorithms are firstly implemented and evaluated on simple numerical head model, then measurement data collected from developed microwave head imaging system is used to evaluate the proposed algorithms. The detailed illustrations of the verification for this algorithm using measurement data collected from developed microwave head imaging system are exhibited in Chapter 3.
2. Novel algorithm using wavelet transform and block sparse Bayesian learning is proposed on tomography-based microwave imaging technique which can be used to reduce the number of antennas used in the antenna array. The proposed algorithm is evaluated using numerical head phantom from MRI scan, and the method is also compared with several other algorithms to indicate the advantage of the proposed algorithm. The detailed illustrations of the verification for this algorithm using MRI scanned phantom are exhibited in Chapter 4.
3. Novel algorithm based on particle swarm optimization is proposed for confocal microwave imaging techniques. The proposed algorithm solves the problem in traditional confocal-based methods that single effective dielectric constant has to be guessed at beginning. The proposed algorithm is firstly implemented and evaluated using simulation data from CST microwave studio. Accurate head phantom is used in the simulation and follow with the simulation results, measurement data from up-to-data microwave head imaging system are used to test the proposed algorithm. Realistic head phantom manufactured with 3-D printing technology is used in the measurement. Both the simulation and measurement results are compared with those from traditional confocal-based algorithms and the comparison results indicate obvious advantage and improvement of the proposed method. The detailed illustrations of the

verification for this algorithm using measurement data collected from developed microwave imaging system are exhibited in Chapter 5.

4. A novel framework based on k-means clustering and support vector machine (SVM) is proposed for brain stroke detection. The framework is based on several machine learning techniques, such as K-mean clustering and SVM technique. A database includes sets of images with different types, size, and positions of strokes is constructed. Two different numerical head phantoms from MRI scans are used to build the database then the database is used to construct the SVM model. The constructed SVM model is used to classify the types of strokes (haemorrhagic or ischaemic) when the new case is under tested. The classification results indicate the proposed framework can classify the types of strokes with desirable accuracy. The detailed illustrations of the verification for this algorithm using MRI scanned phantom are exhibited in Chapter 6.

1.5 Thesis Organization

1. Chapter 2 presents a brief overview on the current microwave imaging techniques. Two main techniques used in bio-medical applications, which are radar-based technique and tomography-based technique, are separately introduced. For radar-based technique, three main aspects are reviewed in details; the surface reflection suppression, beamforming algorithms and confocal algorithms. For tomography-based technique, two main algorithms are reviewed in details which are Born iterative method (BIM) and distorted Born iterative method (DBIM). The challenges and problems existed in these two techniques are also presented and discussed.
2. Chapter 3 presents two novel algorithms which apply compressive sensing (CS) technique on radar-based imaging technique. The usage of CS technique aims to reduce the number of antennas used in the array or decrease the number of stepped frequencies required in the transceiver system. The theories of these two algorithms are explained in this chapter. The first algorithm is tested using a simple head model and the second algorithm is evaluated using measurement data from developed microwave head imaging system. The results for both of the two algorithms are exhibited to indicate the feasibility of these two algorithms on microwave head imaging system.
3. Chapter 4 presents a novel algorithm that applies CS technique on tomography-based imaging technique. The main problem in current CS technique for tomography-based technique is

illustrated, and a method to solve this problem is also proposed in this chapter. Simple model is firstly used to test the proposed algorithm, followed with the evaluation on realistic model. A comparison among the proposed algorithm and several other methods is presented to indicate the superiority of the proposed algorithm.

4. Chapter 5 presents a novel algorithm that applies optimization method on current confocal-based algorithm to significantly improve the performance. The main problem in current radar-based techniques for bio-medical imaging is firstly illustrated. A novel method based on particle swarm optimization (PSO) is proposed to solve that problem. The proposed algorithm is firstly tested in full-wave simulation environment, followed with the evaluation on realistic measurement data from developed microwave head imaging system. The results are compared with those achieved using conventional methods to exhibit the superiority of the proposed algorithm.
5. Chapter 6 presents a brain stroke classification framework using microwave technique. The current development and problems for brain stroke classification using microwave technique are firstly illustrated in details. The method of constructing the database which is used to build the classifier model is explained in this chapter, then the method of building the classifier model is proposed, followed with the evaluation on realistic head phantom from MRI scan. The classification results are presented at the end of this chapter to illustrate the advantage of the proposed framework.

Chapter 2: Literature Review of Microwave Imaging Techniques

2.1 Introduction

Microwave imaging techniques are widely investigated in traditional applications such as synthesis aperture radar (SAR), inverse synthesis aperture radar (ISAR) or ground penetration radar (GPR). Microwave imaging techniques for bio-medical application were firstly proposed in 1970s by C. Johnson *et al.*, which was utilized to investigate the electromagnetic effects in biological materials [7]. This concept was then developed and utilized on breast cancer detection in 1998 [9]. Further researches were conducted based on [9] and two clinical microwave breast imaging systems were built at Dartmouth College by Meaney *et al.* [57] in 2000, and by Klemm *et al.* at the University of Bristol [58] in 2009. A complete microwave imaging system is composed of antenna array, signal transceiver and processing and imaging algorithms. This thesis focusses on the processing and imaging algorithm part, which can be categorized into two types, the radar-based imaging algorithm and tomography-based algorithm. Radar-based methods utilize wideband signals to localize the position of the target (such as tumor or brain stroke), whereas tomography-based methods reconstruct the electrical properties of the imaging area (permittivity and conductivity) through solving an ill-posed inverse problem. The following sections introduce some recent developments on both radar-based and tomography-based algorithms. Some challenges and problems existed in those methods are also discussed.

2.2 Development of Radar-Based Technique for Bio-Medical Application

2.2.1 Beamforming Imaging Algorithm

Delay-and-sum beamforming algorithm is widely used in microwave bio-medical imaging applications. The algorithm is based on special filtering concept illustrated in [66] and was firstly applied on microwave breast cancer detection in [26]. The concept of the algorithm is based on the time delay of the received signals from all the used antennas and sum the signals to generate a synthetically focused signal.

The essential theory of this algorithm is based on a penalized least square problem shown as:

$$\min_{\boldsymbol{w}} \|\boldsymbol{w}^T \boldsymbol{A} - \boldsymbol{f}_d\|_2^2 + \lambda \|\boldsymbol{w}\|_2^2 \tag{2.1}$$

where $\boldsymbol{w}$ is the filtering coefficient vector expressed as $\boldsymbol{w} = [\boldsymbol{w}_1^T, \dots, \boldsymbol{w}_N^T]^T$, N is the number of antennas, matrix $\boldsymbol{A}$ is defined as $\boldsymbol{A} = [\boldsymbol{d}(r_o, \omega_l), \dots, \boldsymbol{d}(r_o, \omega_u)]$, $\boldsymbol{f}_d$ is a vector defined as $\boldsymbol{f}_d = \left[e^{-j\omega_l \frac{L-1}{2f_s}}, \dots, e^{-j\omega_u \frac{L-1}{2f_s}}\right]$, ω is the angular frequency of the transmit signal, f_s is the sampling frequency of the time domain signal and λ is a parameter used to trade the balance between the system error and the solution norm. The element in matrix $\boldsymbol{A}$ can be defined as:

$$\boldsymbol{d}(r_o, \omega) = \begin{bmatrix} \tilde{S}_{11}(r_o,\omega)\boldsymbol{d}(\omega) \\ \tilde{S}_{22}(r_o,\omega)\boldsymbol{d}(\omega) \\ \vdots \\ \tilde{S}_{NN}(r_o,\omega)\boldsymbol{d}(\omega) \end{bmatrix} \tag{2.2}$$

where $\tilde{S}_{kk}(r_o, \omega)$ is an effective transfer function which represents the propagation from the kth antenna to the tumor located at r_o and reflected back and $\boldsymbol{d}(\omega) = \left[1, e^{-\frac{j\omega}{f_s}}, \dots, e^{-\frac{j\omega(L-1)}{f_s}}\right]$.

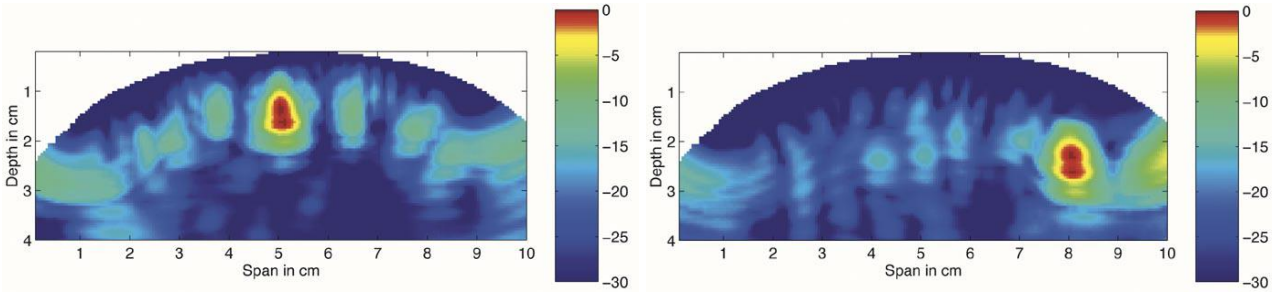

(a) (b)

Fig 2. 1: The generated images using delay-and-sum beamforming algorithm. (a) a 2 mm diameter tumor was placed at (5.0 cm, 1.1 cm), (b) a 2 mm diameter tumor was placed at (8.0 cm, 2.1 cm) [26].

The solution of (2.2) can be achieved as:

$$\boldsymbol{w} = (\boldsymbol{A}\boldsymbol{A}^H + \lambda \boldsymbol{I})^{-1} \boldsymbol{A} \boldsymbol{f}_{\boldsymbol{d}}^H \tag{2.3}$$

After the filtering coefficients $\boldsymbol{w}$ were calculated, the time-delayed and filtered signals at all the N antennas are summed up and the summed signal was denoted as $z[n]$. Before $z[n]$ was used to generate the final image, it was windowed through a window function to eliminate the clutter effect outside the portion of tumor reflection signal. The window function was designed as:

$$h[r_o, n] = \begin{cases} 1, & n_h \le n \le n_h + l_h \\ 0, & otherwise \end{cases} \tag{2.4}$$

where the time area $(n_h, n_h + l_h)$ contain the scattered signal from the tumor. The final image was generated by using the energy function which is dependent on the location r_o

$$p(r_o) = \sum_n z[n]\, h[r_o, n]^2 \tag{2.5}$$

The delay-and-sum beamforming algorithm illustrated above was evaluated by using a numerical breast model in [26]. The model was built based on MRI scan, the thickness of the skin is 2 mm and the diameter of the tumor is 2 mm. Totally 17 electric-current sources were placed on the surface of the breast and the incident signal was selected as a 100 ps differentiated Gaussian pulse. The backscatter signals were computed using the finite-difference time-domain (FDTD) method. The dispersive properties along with the inhomogeneous properties of the breast were also included in the FDTD simulation. The obtained results in [26] are shown in Fig 2.1. It can be seen from Fig 2.1 that the position of the tumor can be clearly localized by using the delay-and-sum beamforming algorithm presented in [26].

2.2.2 Confocal Imaging Algorithm

Microwave confocal imaging algorithm was evolved from the delay-and-sum beamforming method and it is widely used in current microwave head imaging systems [36], [40]. It was firstly proposed by X. Li, in 2001 [29], for breast cancer detection. In [29], the calibrated signals after integrating over time was denoted as vectors: B_1, B_2, …, B_M, where M is the number of antennas. The reconstructed images was generated by time shifting the signals B_m based on the round-trip time from the mth antenna to a certain point in the breast and summing the signals from all the M antennas as:

$$I(\boldsymbol{r}) = \left[\sum_{m=1}^{M} w_m B_m\big(\tau_m(\boldsymbol{r})\big)\right]^2 \tag{2.6}$$

where $I(\boldsymbol{r})$ is the image intensity for a certain point located at position $\boldsymbol{r}$ inside the breast, w_m is the coefficient for the mth antenna aim to compensate the radial spreading of the propagating wave, and $\tau_m(\boldsymbol{r})$ is the time shift from the mth antenna to the point $\boldsymbol{r}$. The time shift value was based on the length of the round-trip path and the velocity of the propagating wave. It can be calculated as:

$$\tau_m(\boldsymbol{r}) = \frac{2d_m(\boldsymbol{r})}{v\Delta t} \tag{2.7}$$

where $d_m(\boldsymbol{r}) = \boldsymbol{r} - \boldsymbol{r_m}$, $\boldsymbol{r_m}$ is the position of the mth antenna located outside the breast, v is the speed of the propagating wave and Δt is the interval of the sampling time. The proposed confocal algorithm was evaluated using a breast model from MRI scan shown in Fig 2.2 (a) and the imaging result is shown in Fig 2.2 (b). The simulation was implemented using FDTD method and totally 17 monopoles were placed along the surface of the breast with a distance of 8 cm between any two of

them. Fig 2.2 indicates that the position of the tumor could be localized using the confocal imaging algorithm proposed in [29]. Followed with the successful application of confocal imaging algorithm on microwave breast cancer detection, the algorithm was widely applied on microwave head imaging system such as the system built by B. Mohammad [36] and A. Mobashsher [40] in 2014. The confocal imaging algorithm used in microwave imaging system was modified from its original version and the

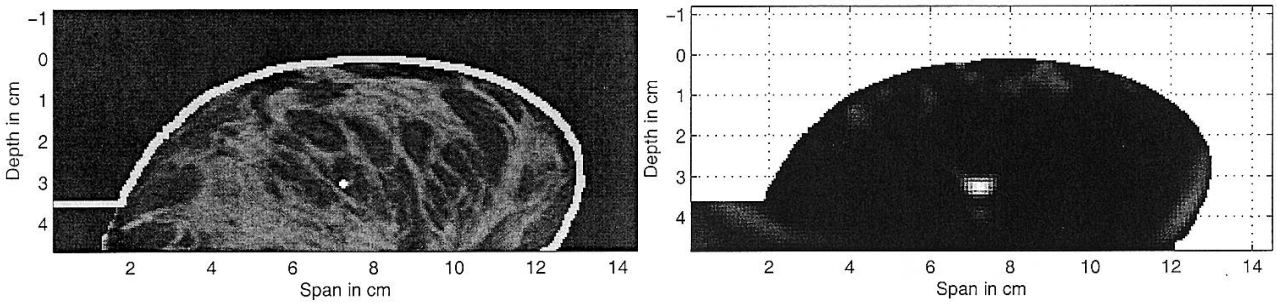

(a) (b)

Fig 2. 2: (a) The breast model from MRI scan, (b) the generated image using confocal imaging algorithm [29]

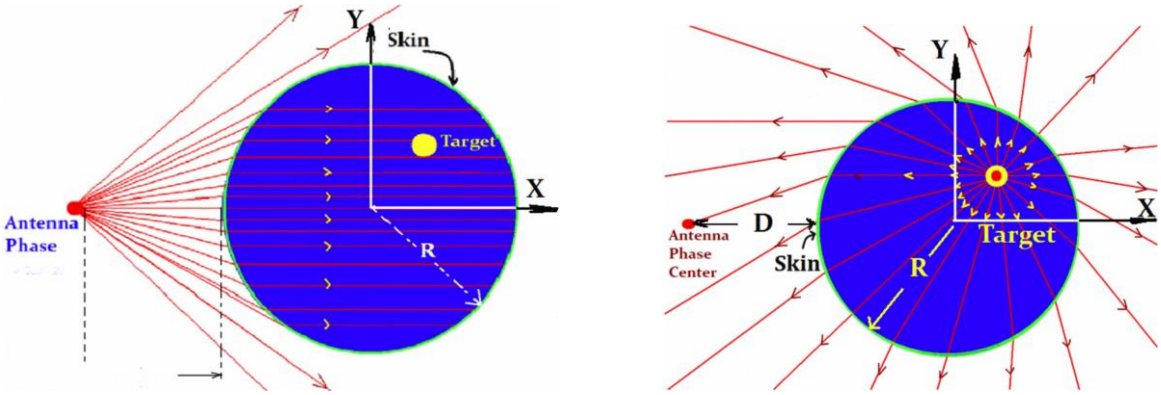

(a) (b)

Fig 2. 3: The wave propagation mode for (a) incident wave and (b) scattered wave [72].

details of applying this method on head stroke detection was illustrated by D. Ireland and M. Bialkowski in [69]. The method described in [69] was based on the confocal imaging algorithm developed for breast imaging by the same research group in [70]-[72]. The algorithm can be generally concluded as nine steps [72]:

1. The time domain signals were obtained from 24 antennas denoted as $\{x_k(t)\}$, $k = 1,2, \ldots,24$.
2. The strong reflection from the background (skin) was removed by subtracting the signals between two adjacent antennas, which was expressed as: $C_1(t) = x_2(t) - x_1(t)$, $C_2(t) = x_3(t) - x_2(t)$, …, $D_{24}(t) = x_1(t) - x_{24}(t)$, where $C_k(t)$ represented the calibrated signal.
3. The positive values of the calibrated signals were kept and the negative values were eliminated to avoid the "ghost image". The final signals were denoted as $F_k(t)$.
4. The signals obtained from step 3 were normalized as $N_k(t) = F_k(t)/\max(F_k(t))$.

5. The relative dielectric constant ε_{er} of the imaging area was estimated for further calculating the length of the propagation path.
6. The length of the wave propagation path was calculated using the estimated relative dielectric constant and the radiation mode shown in Fig 2.3. The incident wave propagated as planar wave as shown in Fig 2.3 (a) and the scattered wave propagated as radial wave. The round-trip time taken from one antenna to a certain position in the imaging area was calculated as $\tau = 2\left[D + \sqrt{\varepsilon_{er}}(R + X)\right]/c$ where c is the velocity of light in the free space.
7. Map the signal $N_k(t)$ onto all the points in the imaging area using the round-trip time obtained from step 6.
8. Repeat step 7 for all the 24 antennas.
9. Superimpose the results obtained from step 7 and 8 and achieve the final image. The location of the target can be identified by the maximum image intensity.

This process illustrated in [72] was further applied on microwave head imaging scenario and the pseudocode of the algorithm was presented as [69]

Monostatic Confocal Imaging Algorithm

begin
  for $n \leftarrow 1$ to N **do**
    for $\forall p \in \mathbb{Z}$ **do**
      for $d \leftarrow 1$ to N_b **do**
        $D_d \leftarrow \|S_n - B_d\| + \sqrt{\varepsilon_{er}}\|p - B_d\|$
      $d \leftarrow min\{D_1, D_2, \dots, D_{N_b}\}$
      $\tau \leftarrow 2 \times d/c$
      $I(p) \leftarrow I(p) + |F_n(\tau)|$
return $I(p)$

The parameters used in the pseudocode were indicated in Fig 2.4 and $F_n(\tau)$ was the compensate value which was used to compensate the signal losses result from the wave propagation. The value of $F_n(\tau)$ was calculated by $F_n(t) = D_n(t)y(t)$ where $n = 1, 2, \dots, N$. $y(t)$ is the compensation factor and it was defined as $y(t) = 1/e^{-\alpha t}$ in [69] where α is another factor used to adjust the slope of the compensation factor. It is notable that in the algorithm elaborated above, the length of the wave propagation path was selected as the minimum length among all the distance between each boundary points to the imaging point inside the brain. This criterial was proposed by Y. Wang in [73]. In [73],

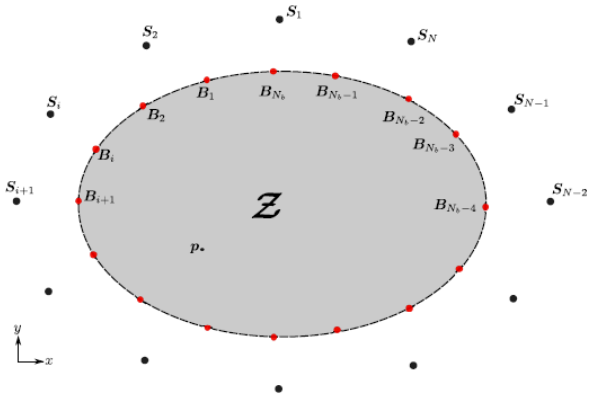

Fig 2. 4: The configuration of the microwave head imaging scenario in [69]. The imaging domain was denoted as $\mathcal{Z}$ with gray color, the boundary points $\boldsymbol{B_i}$ was used to represent the entry point of the signal and the point inside the brain was denoted as $\boldsymbol{p}$

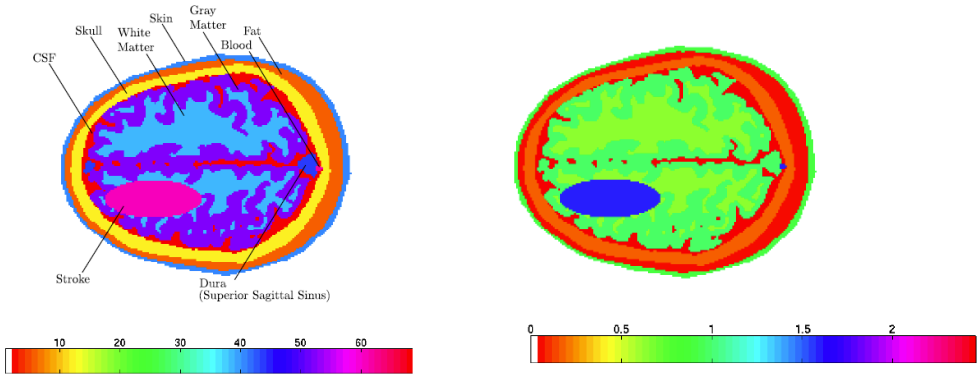

(a) (b)

Fig 2. 5: The numerical head phantom used to test the confocal imaging algorithm in [69]. (a) the dielectric constant profile of the head phantom, (b) the conductivity profile of the head phantom

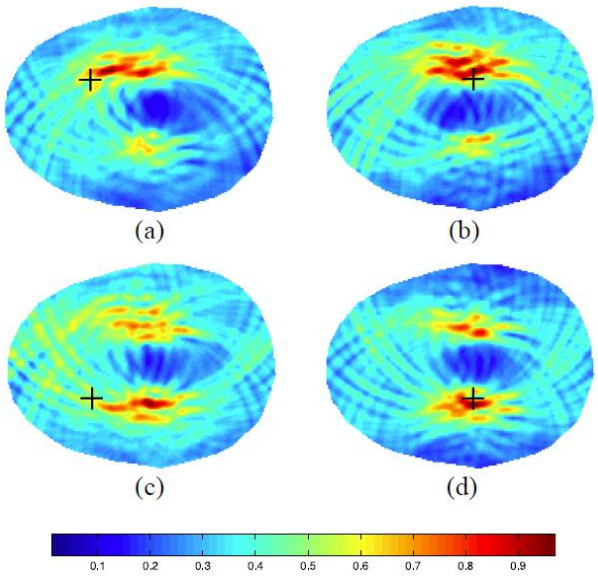

Fig 2. 6: The generated images using confocal imaging algorithm when the haemorrhagic stroke was placed at four different positions. The position of the stroke was marked with cross-hairs [69].

the authors proposed that the length of the wave propagation path should follow the Fermat's principle, which indicates that the wave propagation path should be the path with least travelling time. Under this principle, the path was selected as the minimum one among all of the possible pathes. The confocal imaging algorithm illustrated in [69] was evaluated using numerical head phantom derived from MRI scan as shown in Fig 2.5.The simulation was implemented using FDTD method, and totally 72 antennas were used to transmit and receive the signals. A Gausssian pulse with 0.5-2 GHz bandwidth was used as the incident signal and a white noise with 20 dB signal to noise ratio was added to the received signals. A haemorrhagic stroke composed with bleeding was placed inside the brain and the imaging results were shown in Fig 2.6. Fig 2.6 indicates that the position of the haemorrhagic stroke can be generally localized using the confocal imaging algorithm in [69].

2.2.3 Radar-based Microwave Head Imaging System

The microwave imaging algorithms proposed in [26], [29], [69], [72] were evaluated using numerical breast or head phantoms due to the fact that these algorithms built the fundamental of microwave bio-medical imaging technique and they were developed on initial step. Several microwave imaging systems were constructed based on these algorithms during the following years. Microwave head imaging system is an up-to-date application for these algorithms and the development of this system is drawing increasing interests during recent years. Three microwave head imaging systems developed by A. Abbosh, etc., [36], [40] and M. Persson, etc., [43] are typical systems and can be used to represent the mainstream of the development in microwave head imaging community. Figure 2.7 illustrates the configurations and detailed platforms of two microwave head imaging systems developed by A. Abbosh, etc. The system exhibited in Figure 2.7 (a)-(b) was constructed by using stationary antenna array. The antenna array was composed with 16 exponentially corrugated tapered slot antennas with the operation band of 1-4 GHz and directional radiation pattern. The directional radiation pattern guaranteed that the radiated power was confined in the target area. The details of the antenna design can be found in [34]. The platform was fabricated by using polyvinyl-chloride and separated with two levels. The first level had an inner radius of 17 cm and outer radius of 47 cm. This level was adjustable so the antenna array can be longitudinally adjusted to fit different size of head phantom. The antennas were inserted into 16 slits in the first level thus they were all fixed. The second level was used to hold the head phantom with the radius of 34 cm. The signals were transmitted and received by using R&S ZVA24 vector network analyser (VNA) and the antennas were selected by using two single-pole eight-throw (SP8T) microwave, coaxial switches. The antennas numbered with 1-8 were selected using the first switch and the antennas numbered with 9-16 were selected using the second switch. The head phantom used in the system shown in Fig 2.7 (a)-(b) included the major

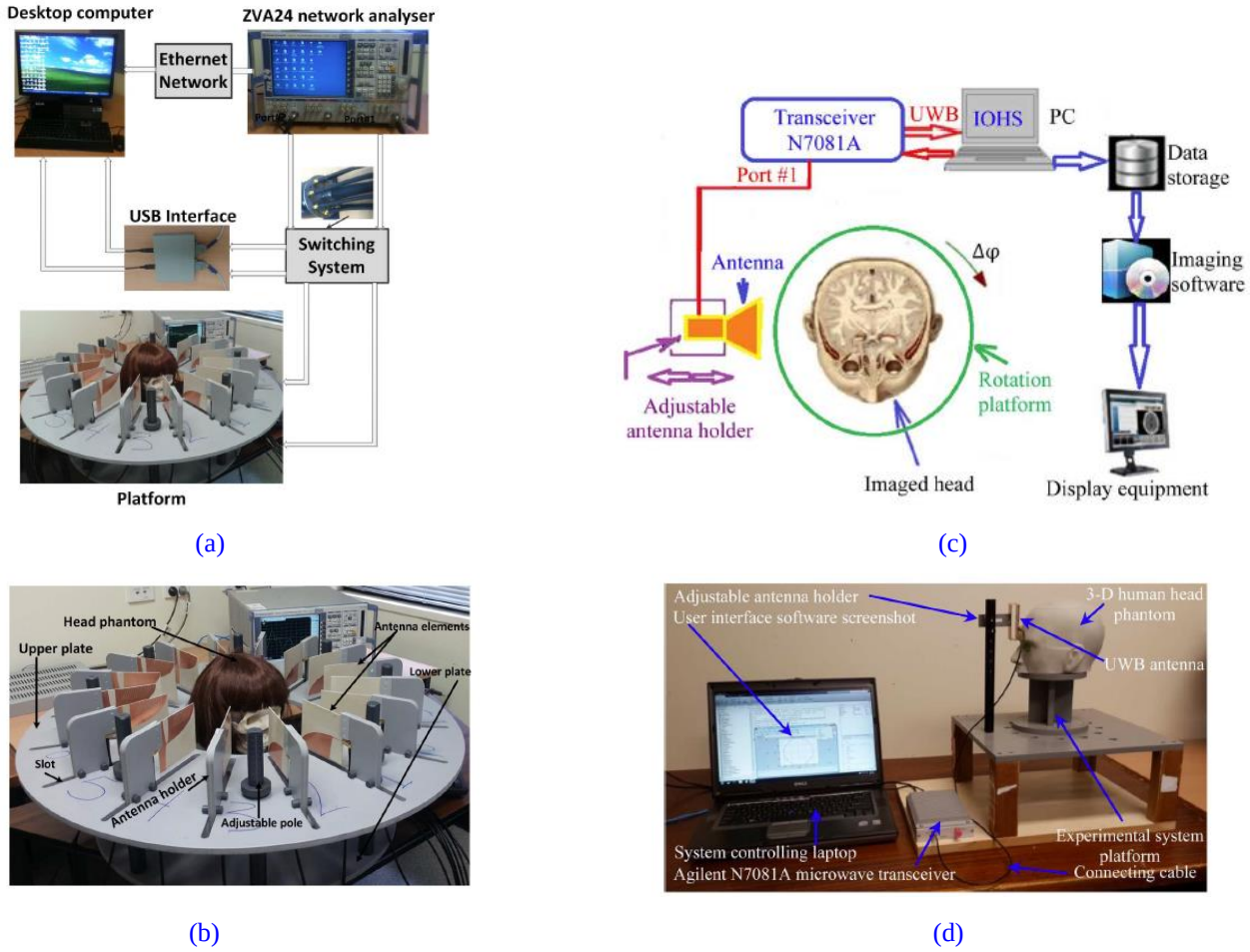

Fig 2. 7: (a)-(b) the configuration and platform of microwave head imaging system developed in [36] and (c)-(d) the configuration and platform of microwave head imaging system developed in [40].

tissues in human brain, which are skull, white matter, cerebral spinal fluid (CSF) and gray matter. Mixture materials were used to fabricate the phantom and the details of the fabrication procedure can be found in [144].

The system exhibited in Fig 2.7 (c)-(d) was constructed by using rotational antenna array. An adjustable holder was used to fix the position of the antenna thus through adjusting the holder, the position of the antenna can be changed. A horizontal rotation platform was used to place the head phantom and through varying the orientations of the platform, different scanning angles can be achieved thus a virtual antenna array was built by using a single antenna. The antenna used in this system is composed with a slotted dipole element and a folded parasitic structure [40]. The operating band for the antenna is from 1.1-3.4 GHz with unidirectional radiation pattern. The detailed design procedures can be found in [40]. Compared with the previous system as shown in Fig 2.7 (a)-(b), one critical and important improvement was the usage of a low-cost and portable transceiver system. As shown in Fig 2.7 (d), a portable custom-made transceiver system from Agilent Tech (N7081A) was used to transmit and receive the signal thus largely reduce the size and cost of the entire imaging

system. Another important improvement in this system was the usage of a more accurate head phantom. The head phantom used in this system was built by a 3D printer facility (Sinterstation 2500plus) with a resolution of 2 mm. The major tissues inside human brain were contained in the phantom which included skin, skull, fat, some muscular part, Dura, CSF, white matter and gray matter. Same mixture materials as reported in [144] were used in the fabrication and the fabricated phantom was tested using dielectric probe HP85070. The accuracy with regard to the electrical properties was less than $\pm 5\%$ differences between the actual values [80] and the measured values over the entire operating band.

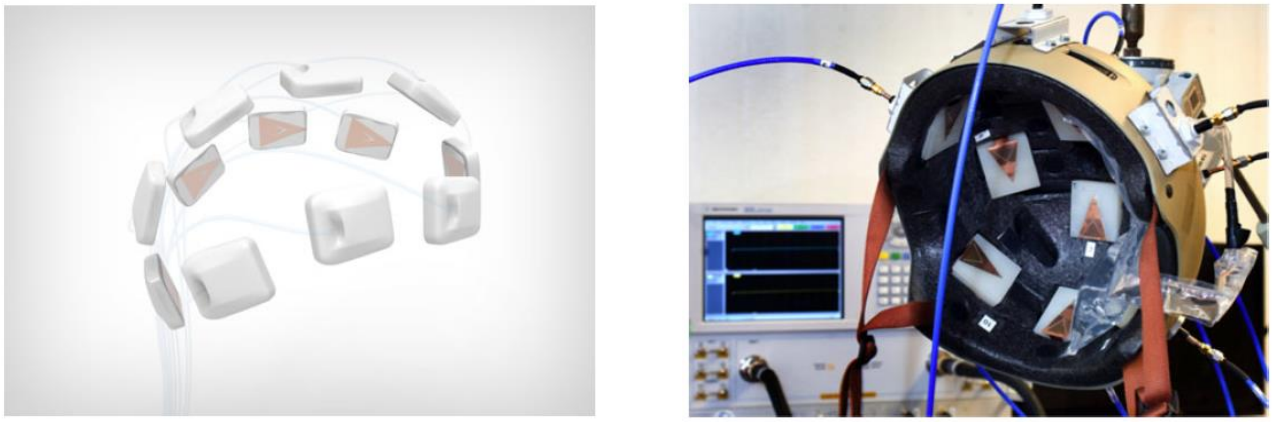

(a) (b)

Fig 2. 8 (a) Distribution of the isosceles triangle patch antenna; (b) prototype of the microwave head stroke detection system [43]

Figure 2.8 exhibited a brain stroke detection system built by M. Persson, etc. [43]. The system contained 12 triangle antennas operating from the band from 0.3-3 GHz. The antennas were mounted on a bicycle helmet. The main difference between the system in [43] and the systems reported in [36], [40] is that in [36], [40], the systems were built for brain imaging task and only haemorrhagic stroke was considered in the imaging task whereas in the system reported in [43], the design purpose of the system was merely for brain stroke detection and classification (distinct the types of stroke between haemorrhagic and ischaemic stroke). Briefly speaking, the systems in [36], [40] can localize the position of the stroke but without the knowledge of the types of stroke and the system in [43] can classify the types of stroke but with the disability to localize the position of stroke. A two-port network analyser (Agilent E8362 B PNA) was used to transmit and receive the signal in [43] and a classification algorithm based on singular value decomposition (SVD) was used to classify the types of stroke depend on the received signal.

2.3 Development of Tomography-Based Technique for Bio-Medical Application

2.3.1 Inverse Scattering Problem

Different from radar-based imaging techniques in which only the position of the target can be localized, tomography-based techniques can reconstruct the electrical properties (dielectric constant and conductivity) of the targets by using the scattered signals. Microwave tomography was originated by solving an integral equation [74]. In [74], the procedure of deriving the integral equation was thoroughly explained and it was summarized below.

The integral equation is generated from solving an inhomogeneous wave equation and the core equation after implementing some algebra implementations is

$$E_{inc}(\vec{r}) = E(\vec{r}) - \int_V G(\vec{r},\vec{r}')\,\mathcal{O}(\vec{r}')E(\vec{r}')d\vec{r}' \tag{2.8}$$

where $\mathcal{O}(\vec{r}') = \omega^2\mu_b[\epsilon(\vec{r}') - \epsilon_b] = k^2(\vec{r}') - k_b^2$. The integral equation (2.8) is also known as Fredholm integral equation of the second kind since the unknown values are both inside and outside the integral operator. In the integral equation (2.8), the incident field $E_{inc}(\vec{r})$ usually can be calculate since the pattern of the current source is known. However, the total electric field $E(\vec{r})$ is unknown thus the integral equation can only be solved by using numerical method. In the following section, two commonly used numerical methods, Born iterative method [75] and distorted Born iterative method [76] are introduced in details.

2.3.2 Born Iterative Method and Distorted Born Iterative Method

The details of Born iterative method (BIM) was elaborated in [50] which was applied on head stroke detection. To utilize BIM on electrical properties reconstruction, the normalized dielectric profile (NDP) was firstly defined as:

$$\chi(x,y) = \frac{\left[\varepsilon_r(x,y) + \frac{\sigma(x,y)}{j\omega}\right]}{\tilde{\varepsilon}_s} \tag{2.9}$$

where $\tilde{\varepsilon}_s$ is the effective dielectric constant of the surrounding medium expressed as $\tilde{\varepsilon}_s = \varepsilon_s + j\sigma_s/\omega$. The Green's function in (2.8) can be expressed using the zero order Hankel function as $G(\vec{r},\vec{r}') = H_o^{(2)}(k_s\rho)$ where $\rho = \sqrt{(x'-x)^2 + (y'-y)^2}$ is the distance between the antenna and a

certain point in the imaging area, $k_s = \sqrt{\omega^2 \mu_o \varepsilon_o \varepsilon_s - \frac{j\omega\mu_o\sigma_s}{\varepsilon_o}}$ is the wave number in inhomogeneous environment, ε_o and μ_o are the permittivity and permeability of free space. Under this substitution of $G(\vec{r}, \vec{r}')$, the integral equation in (2.8) can be re-expressed as:

$$E_{inc}^{q}(r) = E_{tot}^{q}(r) + \frac{jk_s^2}{4} \iint_V [\chi(r') - 1] E_{tot}^{q}(r') H_0^{(2)}(k_s \rho) dr', r \in S;\ r' \in V; q = 1, \dots, Q \quad (2.10)$$

where $r = (x, y)$ is the coordinate of a point on the measurement contour S, $r' = (x', y')$ is the coordinate of a point in the imaging domain V, q is the index of antenna and Q is the total number of antennas used in the array. Based on the fact that $E_{scat}^{q}(r) = E_{tot}^{q}(r) - E_{inc}^{q}(r)$, the scattered filed received by the antenna q can be calculated as:

$$E_{scat,q}(r) = -\frac{jk_s^2}{4} \iint_V \left[\chi^i(r') - 1\right] E_{tot,q}^{i-1}(r') H_0^{(2)}(k_s \rho) dr',\ r \in S;\ r' \in V; q = 1, \dots, Q \quad (2.11)$$

where i is the iteration index, $E_{tot,q}^{i-1}(r')$ is the total filed of the imaging domain calculated in the last iteration step, and $\chi^i(r')$ is the unknown NDP need to be reconstructed in the current iteration. The integral equation (2.11) can be rearranged to a matrix form as:

$$\mathcal{B}_q^{i-1} \vec{\chi}^i = \vec{m}_q \quad (2.12)$$

where $\vec{m}_q = [E_q(r_1), \dots, E_q(r_M)]^T$, $\vec{\chi}^i = [\chi^i(r_1), \dots, \chi^i(r_N)]$; $r_m \in S, m = 1, \dots, M$, $r_n \in V, n = 1, \dots, N$, ($M$ is the number of receiving antennas $M = Q - 1$, and N is the number of imaging cells),

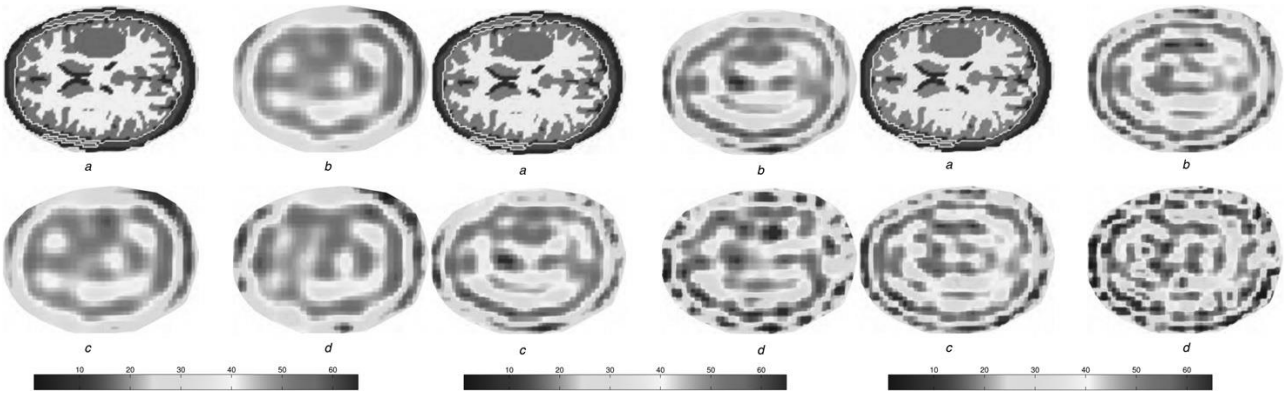

(i) (ii) (iii)

Fig 2. 9: Comparison between the dielectric constant profile of the head phantom and the reconstructed profile at (i) 0.6 GHz, (ii) 0.85 GHz and (iii) 1 GHz. (a) were the original dielectric constant profiles of the head phantoms, (b) were the reconstructed profiles with noiseless data, (c) were the reconstructed profiles with SNR=20 dB and (d) were the reconstructed profiles with SNR=10 dB [50].

and $\mathcal{B}_q^{i-1}$ is the Born iterative integral matrix which was calculated in the last iteration under the qth incident wave. The element in the integral matrix $\mathcal{B}_q^{i-1}$ can be calculated as:

$$b_{mn} = -\frac{jk_s^2}{4}\iint_{V_n} E_{tot,q}^{i-1}(r_n')H_0^{(2)}(k_s\rho)dr' \tag{2.13}$$

The surface integral in (2.13) can be numerically calculated using Richmond's method in [77]. To alleviate the ill-poseness of the under-determined system (2.12), Tikhonov's regularization scheme [78] was used and (2.12) can be re-wrote as:

$$\begin{bmatrix} \mathcal{B}_q^{i-1} \\ \lambda I \end{bmatrix} \vec{\chi}^i = \begin{bmatrix} \vec{m}_q \\ 0 \end{bmatrix} \tag{2.14}$$

where I is an identity matrix with the size of $N \times M$, 0 is a null vector with the length of M and λ is the scalar regularization factor which is chosen as 0.1 in [50]. The reconstructed NDP $\vec{\chi}^i$ for the current iteration i was determined by solving the least squares optimization problem:

$$\vec{\chi}^i = arg\min_{\vec{\chi}^i} \left\| \begin{bmatrix} \mathcal{B}_q^{i-1} \\ \lambda I \end{bmatrix} \vec{\chi}^i - \begin{bmatrix} \vec{m}_q \\ 0 \end{bmatrix} \right\|^2 \tag{2.15}$$

In [50], the Born iterative method described above was evaluated using a numerical head phantom derived from MRI scan [79] and the dielectric properties of the brain tissues were derived from [80]. The method was tested under three different signal to noise ratio (SNR) which was defined as [81] $SNR = 10log(\|\vec{m}\|^2/2QM\sigma^2)$ and three different incident frequencies were used to reconstruct the NDP of the brain. Figure 2.9 shows the original dielectric constant profile of the head phantom along

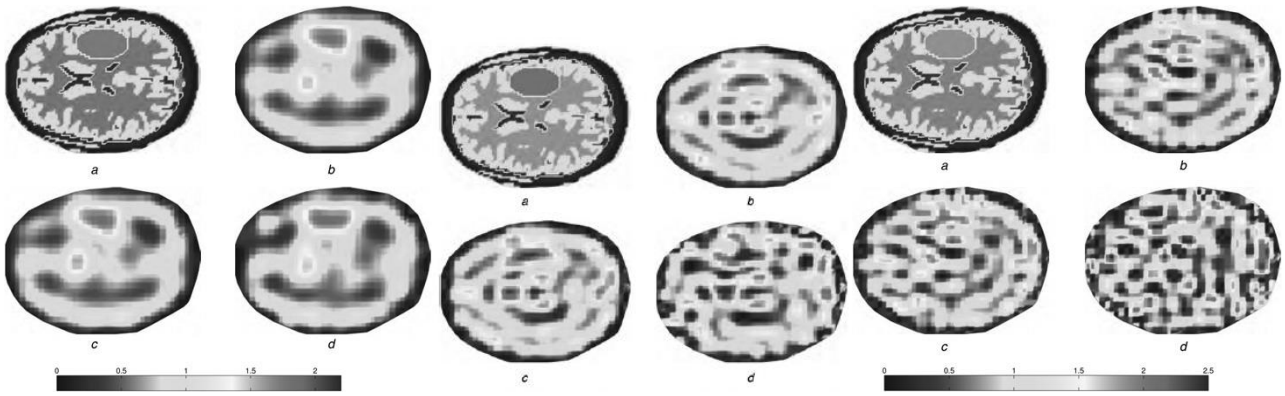

(i) (ii) (iii)

Fig 2. 10: Comparison between the conductivity profile of the head phantom and the reconstructed profile at (i) 0.6 GHz, (ii) 0.85 GHz and (iii) 1 GHz. (a) were the original conductivity profiles of the head phantoms, (b) were the reconstructed profiles with noiseless data, (c) were the reconstructed profiles with SNR=20 dB and (d) were the reconstructed profiles with SNR=10 dB [50].

with the reconstructed profiles under different SNR level and incident frequencies. Figure 2.10 shows the original conductivity profile of the head phantom along with the reconstructed profiles under different SNR level and incident frequencies. It can be seen from Figure 2.9 and 2.10 that the NDP of the numerical head phantom can be generally reconstructed by using Born iterative method. The position of the haemorrhagic stroke can be localized especially when the incident frequency was 0.85 GHz. It is also notable that the conductivity profile can be recovered better than the dielectric constant profile for all the three different incident frequencies. The reconstruction results were also quantitatively assessed using the $NRMS_2$ metric defined as:

$$NRMS_2 = \sqrt{\frac{1}{N}\sum_{n=1}^{N}\left|\frac{\chi_G(x_n, y_n) - \vec{\chi}(x_n, y_n)}{\chi_G(x_n, y_n)}\right|^2} \tag{2.46}$$

where $\chi_G(x_n, y_n)$ is the NDP of the ground truth, i.e., the real profile. The value of $NRMS_2$ represent the reconstruction error with regard to the difference between the reconstructed and real NDP and the value of $NRMS_2$ close to 0 implies perfect reconstruction. Figure 2.11 shows the change of $NRMS_2$ values varied with the iteration numbers. It can be seen from Figure 2.11 that the Born iterative method achieved convergent results after 30 iteration times and the best $NRMS_2$ value (around 1.5) can be achieved when the incident frequency was 0.6 GHz.

Distorted Born iterative method (DBIM) is an alternative method which can be used to reconstruct the NDP of the imaging domain from the received scattered data. The main difference between BIM and DBIM is that DBIM can achieve faster convergence rate but with the cost of additional computational complexity. BIM requires more iterations times to achieve convergent result but it is

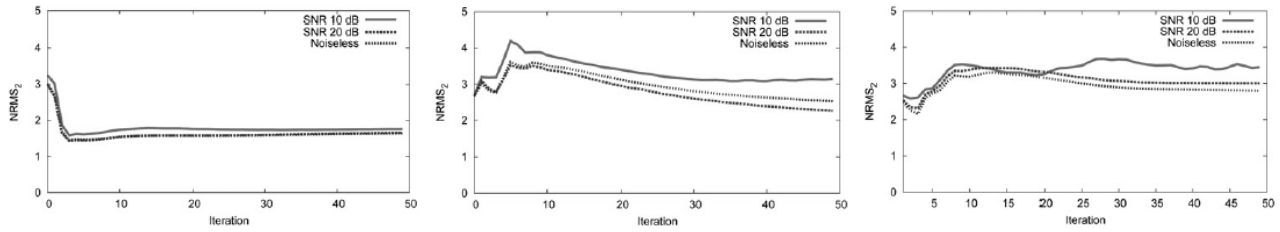

(a) (b) (c)

Fig 2. 11: $\boldsymbol{NRMS_2}$ values varied with the iteration numbers under different SNR levels when the incident frequencies are (a) 0.6 GHz, (b) 0.85 GHz and (c) 1 GHz [50].

more robust to the noise. From the numerical implementation point of view, the difference between BIM and DBIM is that BIM uses homogeneous Green's function in each iteration steps and DBIM updates the Green's function during each iteration steps using the NDP reconstructed from the last iteration. The general steps of implementing DBIM can be summarized as follows [76]:

1. In the first step, solve of inverse problem (2.12) by using the Born approximation to calculate the integral matrix $\mathcal{B}$ (Born approximation assumes the total field in the imaging domain can be approximated as the incident field) and the homogenous Green's function is used to calculate the surface integral (2.13).
2. The total field in the imaging domain and at the receiving antenna points are calculated by solving a forward problem as shown below by using the method of moments [77], [82]:

$$\sum_{n=1}^{N} C_{mn} E_{tot,n} = E_{inc,m}, m = 1, \dots, N \tag{2.17}$$

   where C_{mn} are calculated as:

$$C_{mn} = 1 + \frac{j}{2}(\chi_m - 1)\left[\pi k_s a_m H_1^{(2)}(k_s a_m) - 2j\right], when\ n = m \tag{2.18}$$

$$C_{mn} = \frac{j\pi k_s a_n}{2}(\chi_m - 1) J_1(k_s a_n) H_0^{(2)}(k_s \rho_{mn}), when\ n \neq m \tag{2.19}$$

   In (2.18) and (2.19), a_m is the radius of each imaging cells, and $\rho_{mn} = \sqrt{(x_m - x_n)^2 + (y_m - y_n)^2}$. To update the Green's function, the incident field in the imaging domain for each of the receiving antennas are calculated and substitute in the right-hand side of (2.17) to calculate the new Green's function with the updated χ as the background NDP.

3. The calculated filed and new Green's function are substituted in the inverse problem (2.12) and subtract the scattered field at the receiving antennas from the right-hand side of (2.12). Then solve the new generated inverse problem and obtain the corrections for the last reconstructed NDP. The new NDP is calculated by adding the corrections to the previous NDP.
4. Repeat step 2 and 3 until the entire process is convergent.

The distorted Born iterative method was applied on breast imaging in [47]. Numerical breast phantom derived from MRI scans [83]-[84] were used in [47] to assess the method. The dielectric properties of the breast tissues were derived from [85]-[86], and three different breast phantoms with varied constitution of breast tissues were used in the evaluation. Figure 2.12 shows the three original breast phantoms along with the reconstructed dielectric constant profiles using frequency of 1 GHz. The results shown in Figure 2.12 indicate that the dielectric constant profile of the three breast phantoms can be generally recovered using distorted Born iterative method.

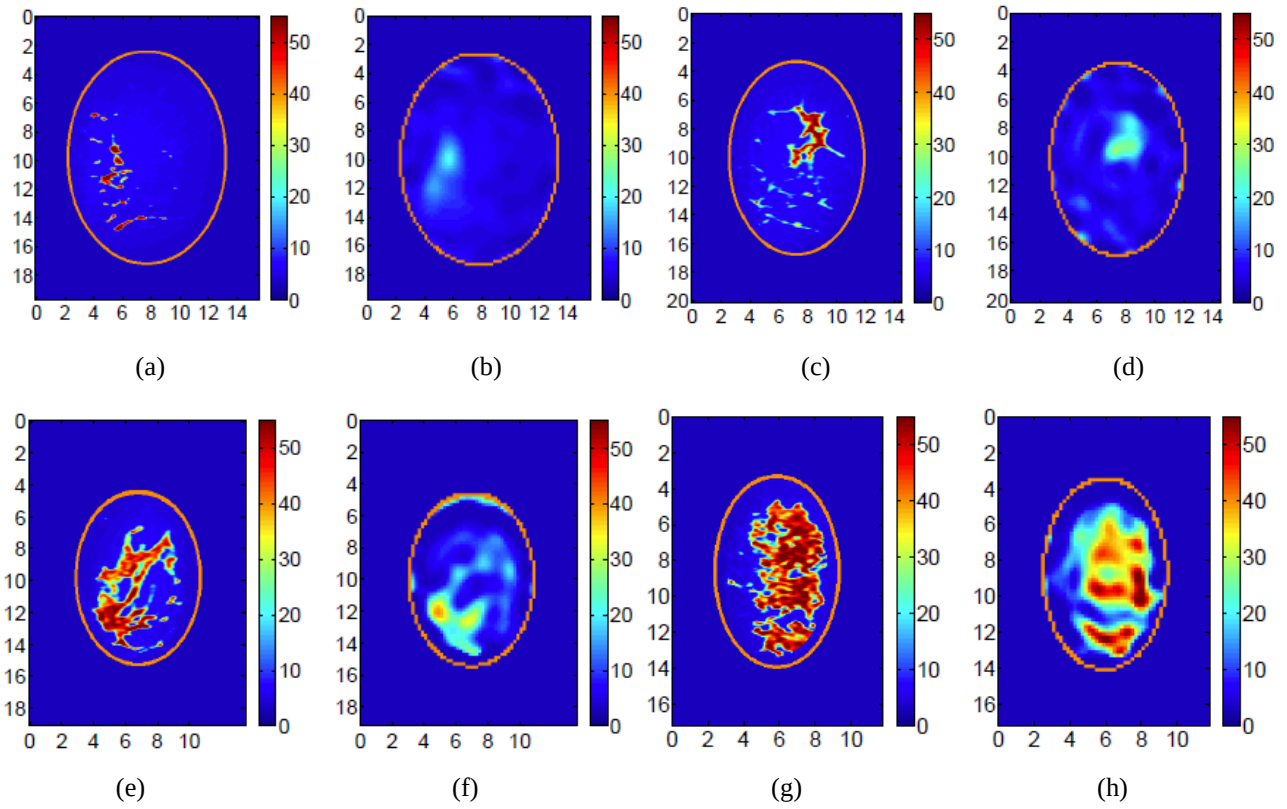

(a) (b) (c) (d)

(e) (f) (g) (h)

Fig 2. 12: (a), (c) (e), and (g) are the breast phantoms with different distributions of breast tissues, (b), (d), (f), and (h) are the reconstructed dielectric profiles using DBIM corresponding to the phantoms in (a), (c), (e), and (g), respectively [47].

2.3.3 Tomography-based Microwave Head Imaging System

Compared with traditional radar-based microwave imaging system, tomography-based imaging system is drawing more attentions during recent years particularly on medical imaging application.

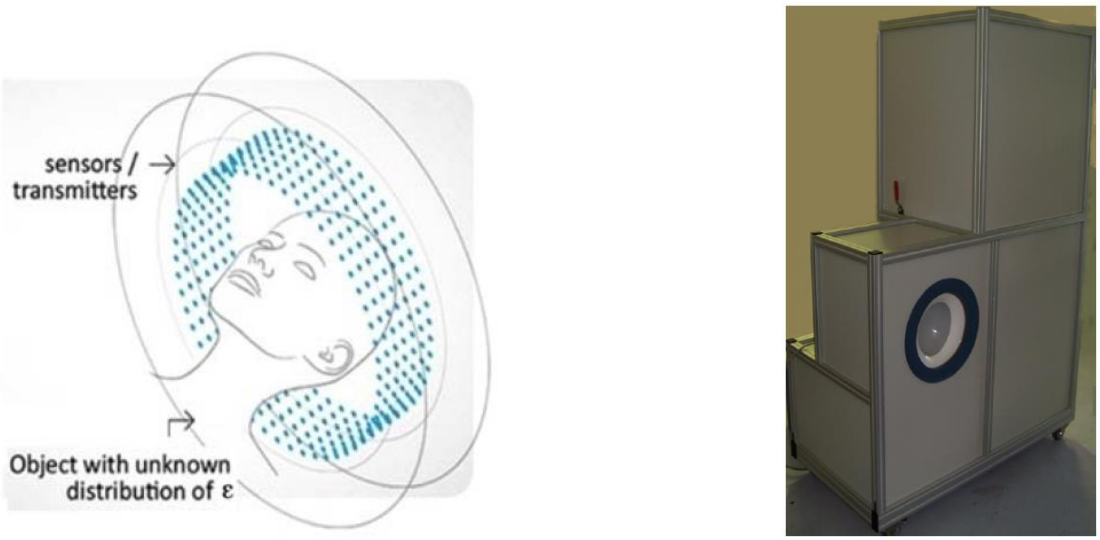

(a) (b)

Fig 2. 13 (a) Configuration of the tomography-based head imaging system, (b) system prototype of the tomography-based imaging system [41]-[42]

However, only a few tomography-based microwave head imaging systems were built over the past few years and the system reported in [41]-[42] is a typical one. Fig 2.13 (a)-(b) illustrate the configuration and prototype of the tomography-based head imaging system. The basic structure of the system was a cylinder with radius of 14.25 cm. Five circular rings were mounted on the cylinder and each ring was composed with 32 antennas. Each antenna was built with ceramic loaded waveguide and the operation bandwidth of the antenna was between 0.9 GHz and 1.1 GHz. The data acquisition process was electronically controlled thus short data acquisition time was needed in the system. An imaging chamber was designed to fit the human head and the chamber was filled with matching liquid. The matching liquid was made with a mixture of glycerol and saline. Specific membrane was used to isolate the human head from the matching medium and the membrane was manufactured in a special way so the shape was fit to the human head. 160 antennas were contained in the system and all of them can work as receivers whereas only 32 antennas were working as transmitters and receivers. Different from the radar-based microwave head imaging systems introduced in the previous section in which monostatic configuration was used in the array, multistatic configuration was used in the tomography-based system which means the transmitting antennas consequentially radiated signals and all the other antennas received the scattered signals. This process was repeated for all the remaining transmitting antennas until all of them performed the transmitting function.

The system was tested on volunteers in the hospital and promising results can be seen in [42]. However, some drawbacks still exist in this system and will be illustrated in the later section.

2.4 Discussions and Conclusions

2.4.1 Challenges and Problems in Radar-based Microwave Imaging Techniques

The radar-based imaging algorithms described above can achieve satisfactory results, the position of the target can be localized using received signals. The computation complexity is low thus the results can be generated within a short time. Those algorithms constructed the fundamentals of microwave bio-medical imaging using radar-based techniques. However, several drawbacks still existed in those algorithms and they are summarized below:

1. In the radar-based bio-medical microwave imaging algorithms, large number of antennas should be used in the array. For instance, totally 17 antennas were used in [26], [29] for achieving two dimensional breast image, 45 antennas were used in [27] for achieving three

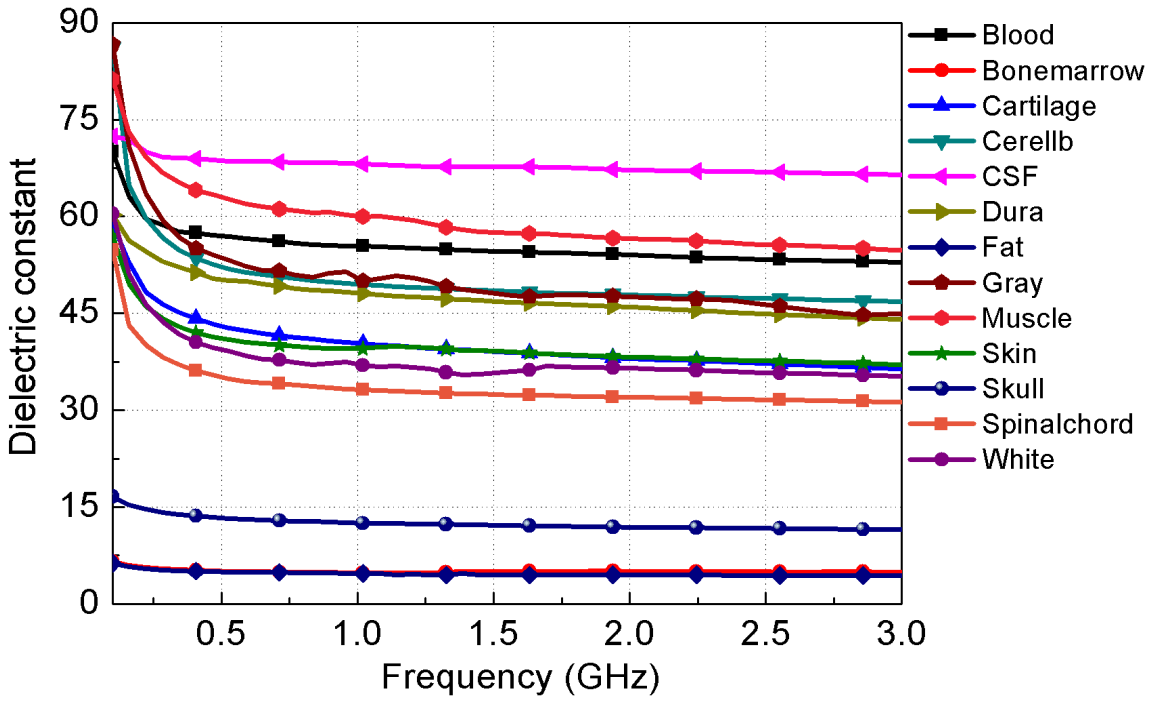

Fig 2. 14: Dielectric constant of different head tissues across the band 0.1-3 GHz used in head imaging [139]

dimensional image, and 32 antennas were used in [36], [40] for achieving two dimensional brain image. The large number of antennas used in the array lead to several problems. Firstly, the mutual coupling between two adjacent antennas will be increased and this undesirable mutual coupling results in image distortion [51]. Secondly, the usage of large number of antennas will increase the size of the entire system. This limitation is opposite to the object that build a portable microwave imaging system for bio-medical application. Although for monostatic imaging systems, virtual antenna array can be used (only one antenna was used in the system and the antenna was rotated to cover all the positions required in the array), a mechanical rotation motor was required in the system and it also increased the complexity of the entire system [40].

2. To achieve high resolution images, wideband signals were used in the aforementioned radar-based algorithms. For example, ultra-wideband (UWB) signals were used in [26], [29] to generate high resolution breast images, the microwave head imaging system in [36] used the signal cover the band from 1 to 4 GHz (120% fractional bandwidth), and the head imaging system presented in [40] used the signal cover the band from 1.1 to 3.4 GHz (102% fractional bandwidth). Since it is difficult to generate a single pulse with more than 100% fractional

bandwidth, stepped frequency continuous wave (SFCW) are usually used in the signal generator's design. The usage of wideband signal might be suitable for the systems using vector network analyser (VNA) as the signal generator [36], [40], however, to design portable and low-cost microwave imaging systems, the bulky and expensive VNA need to be replaced by portable transceivers [16], [56] or software defined radio (SDR) [52]-[55]. In the portable transceiver or SDR designs, wideband signal implies more stepped frequencies, and the large number of stepped frequencies implies high performance sampling circuit or analog-to-digital converter (ADC) have to be designed [16], [56]; and longer calibration time was required in the system [52] since for each stepped frequency, the system need to implement the calibration procedure one time.

In Chapter 3, two algorithms based on compressive sensing (CS) technique are proposed to reduce the number of antennas and reduce the number of stepped frequencies, respectively. The CS reconstruction model is built based on the confocal imaging algorithms. Through solving the l_1 norm optimization problem, high quality images can be achieved by using less number of antennas or less number of stepped frequencies. The proposed algorithms are firstly evaluated by using simple head model, then the measurement data from developed microwave head imaging system is used to further assess the performance of the proposed algorithms. A quantitative analysis is also implemented to indicate the minimum number of stepped frequencies which can be used to ideally recover the image

3. Confocal imaging algorithm has been proved to be a simple and efficient algorithm which are used in current microwave head imaging systems [36], [40]. However, to map scatterers within the imaged object, confocal algorithm requires the effective dielectric constant of the area within that object extending from the signal entry point to the assumed location of each scatterer. All the published papers that are based on confocal algorithms use one certain dielectric constant irrespective of the position of the scatterer to be mapped, position of the antennas, or the entry point of the signal in the imaged object. While such an assumption might be acceptable when imaging an object that has small number of tissues with relative close electrical properties, a fatty breast for example [137]-[138], it cannot be used when imaging other highly heterogeneous objects. In such objects, the effective dielectric constant depends on the location of the antennas transmitting or receiving the signals, signal's entry point in that object and tissues through which the signal penetrates before being reflected. One of the notable examples of such objects is the head, which includes many tissues with wide range of values for their dielectric constants as depicted in Figure 5.1 [139]. Therefore,

assuming one certain average value for the dielectric constant when using confocal algorithms in microwave head imaging might result in an incorrect detection, such as false positives or wrong stroke location. While a trial-and-error approach to find a proper effective dielectric constant might be possible in experimental works involving artificial phantoms, this is not possible when imaging subjects with no *a priori* knowledge of the exact electrical properties of their heads and their health conditions. Obviously, a trial-and-error cannot be used in that real-life scenario. Instead, an automated technique is needed to guide the confocal algorithm to the correct value(s) of the dielectric constant when mapping the subject's head in search for any notable scatterer that can be a stroke or tumour, for example.

In Chapter 5, an optimization-based confocal algorithm is proposed and verified in haemorrhagic brain stroke detection. The algorithm divides the boundary of the head into certain number of uniformly distributed signal's entry points. Each of those points is assigned a certain initial effective dielectric constant. A confocal imaging algorithm is then used to generate an initial image of the head. The quality of that image is quantified using a certain metric. The values of the initial assumed dielectric constants are then optimized based on the calculated metric using particle swarm optimization (PSO) [140]. The final image is obtained when the metric value converges to its maximum value indicating a high quality image. The proposed method is assessed in simulations using an accurate numerical head model [139] and experiments using realistic head phantoms [40], [141]. The simulated and experimental results indicate that the image quality and thus accuracy of detection are dramatically improved compared with using the traditional confocal algorithm without introducing false positive targets.

4. The radar-based imaging techniques mentioned above can localize the position of the target, however, they cannot differentiate the type of the target with respect to its dielectric constant or conductivity. This disadvantage largely affects the practical value of those techniques applied in microwave head imaging systems since classify the type of brain stroke (haemorrhagic or ischaemic) is another important object in head imaging scenario. It might be possible to derive different head images with haemorrhagic and ischaemic strokes and distinguish the type of stroke based on the image intensity of the stroke. However, it is still difficult to define a hard threshold between these two strokes because the obtained images are diverse with different measurement environment and conditions of the head.

In Chapter 6, the stroke classification problem is investigated and a solution based on support vector machine is proposed. The detailed statements with regard to the brain stroke classification using microwave technique will be discussed in the following section.

2.4.2 Challenges and Problems in Tomography-based Microwave Imaging Techniques

The tomography-based imaging algorithms described above can achieve satisfied results. The electrical properties of the imaging area can be reconstructed from the received scattered data and the described algorithms were evaluated using numerical phantoms (head phantom or breast phantom) from MRI scans. Although this technique exhibited promising results when it was applied on bio-medical applications, some problems still exist in the current algorithms and they are summarized below:

1. Tomography-based methods reconstruct the electrical properties of the imaging area by solving an ill-posed inverse problem. A wide range of techniques were applied to solve this problem, such as Born/distorted Born iterative methods [50], [76] and the optimization-based techniques like the conjugate-gradient method, genetic algorithm, differential evolution algorithm, and ant colony optimizer [111]-[115]. To mitigate the intrinsic ill-posedness of the inverse problem or avoid local optimum results, the aforementioned techniques require a large number of antennas with huge computational time. Compressive sensing (CS) technique is an alternative class of methods which has drawn a huge attention due to its potential to solve the ill-posed inverse problem efficiently, while using small number of antennas. In recent developments, CS techniques combined with microwave tomography methods have been proposed for biomedical applications [116]-[119]. In [116], a CS-based method based on l_1 norm minimization was used to find the sparse solution in a sparse domain. In [117]-[119], a method based on the Bayesian compressive sensing (BCS) [120] was utilized to solve an inverse scattering problem. Compared with the traditional l_1 norm minimization, BCS searches for the sparse solution from a Bayesian probability perspective [121]. The algorithms proposed in [117]-[119] were constructed based on *a-priori sparsity* information. That information ensures the unknowns, such as the equivalent currents [117] or the contrast function [118], are sparse enough with respect to single-resolution pixels for a successful reconstruction. However, those methods cannot accurately recover the non-sparse unknowns for non-sparse scatterers that include multiple single-resolution connected pixels such as in microwave biomedical imaging scenarios. Based on the experimental results included in

[117]-[119], the performance of BCS-based algorithms degrades significantly if the sparsity of the investigated domain decrease. Recently, an alternative method to deal with the non-sparse scenario was proposed [122]. That method is based on the total variation (TV), which considers the discrete gradient of large size scatterers [123]-[125]. The method is accurate in reconstructing the contrast-field profile of large non-sparse objects that are composed of multiple connected single-resolution pixels. However, in many microwave biomedical applications, such as head imaging, the variation in the dielectric properties of different tissues are not significant and thus the imaged domain has a relatively "smooth" contrast-field profile, where the discrete gradient values at the edges of the objects are very small even compared with the zero values at the non-edges areas. Furthermore, many biomedical imaging domains, such as the human head, are complex with many tissues and thus many edges that can degrade the sparsity of the TV transform causing a reduction in the accuracy of the reconstructed profile.

In Chapter 4, an imaging scheme using the wavelet transform and block sparse Bayesian learning (BSBL) [126]-[127] combined with Born iterative method (BIM) is proposed. The wavelet transform is adopted because of the relative "smooth" representation of the contrast-field profile of the targeted imaging domain, the human head. The non-significant changes on the values of the contrast profile result in a sparse representation on the wavelet domain. The reason for the utilization of BSBL is that unlike BCS-based methods [117]-[119], BSBL adopts the correlation between each unknown elements in the sparse domain and this merit significantly improves the accuracy of the sparse recovery. The proposed imaging scheme needs only a small number of antennas (receivers) unlike most of the inverse problem solvers (such as BIM) which requires a large number of antennas to mitigate the ill-posedness of the problem. To that end, the transformation from the non-sparse domain to sparse domain with respect to the normalized dielectric profile is implemented using Haar wavelet, which is suitable for microwave biomedical imaging application. The unknown sparse domain is then divided into several blocks and hyper-parameters are imposed on these blocks to enable using the Bayesian inference theory. The expectation-maximization (EM) method is used to solve these hyper-parameters and then the unknown blocks can be analytically solved. The inverse Haar wavelet transform is then implemented on the solved blocks to reconstruct the original dielectric profile.

2. The diagnosis and therapy of brain stroke is a world-wide problem. Brain stroke is the leading cause of disabilities in the world. The quick and exact detection by means of head imaging

within four hours of the incident is the governing factor of proper, fast treatment to ensure the best possible recovery of the patient. Current imaging systems, such as MRI or CT scan, can diagnose stroke but the size and cost of the system limit their applications especially in rural areas and outside the hospital environment. During the past few years, microwave imaging systems have exhibited their potential as a low-cost and portable approach in bio-medical applications, especially in stroke detection [36], [40]. Several imaging algorithms for microwave stroke detection have also been presented [49]-[50], [145]-[147]. These algorithms can be generally divided into three types: tomography-based algorithms [49]-[50], radar-based algorithm [145] and compressive sensing based algorithms [146]-[147]. Although the algorithms in [49]-[50], [145]-[147] achieved satisfying results with regard to localizing the position of the stroke, one important and critical aspect, that is stroke classification, has not been addressed in these imaging algorithms. Stroke classification cannot be done by physicians based on the symptoms as they are the same for the two types of stroke. It is to be noted that even after stroke detection, medication cannot be given to stroke affected patients unless the stroke is classified. The reason behind this comes from the fact that the medication needed for Ischaemic stroke has exactly the opposite effect to that needed for Haemorrhagic stroke. In the algorithms described in [49]-[50], [145]-[147], intra-cerebral haemorrhagic stroke (a break of the blood vessel causing bleeding in the brain, known as ICH) was the only focus. However, ICH is not the most common case among patients suffering from stroke. In fact, almost 85% of strokes are ischaemic (a blood clot blocking the blood vessel, known as IS).

In [43], a microwave-based stroke classification system was built based on the reflection coefficients of the antennas and singular value decomposition (SVD)-based classifier. The system utilized a helmet-shaped patch antenna array to measure the reflected signals (reflection coefficients of each of the antennas) from the brain. The measured signals were then used to construct (train) the SVD-based classifier. In that study, 45 patients with detected stroke (either ICH or IS stroke) were tested using the system. Despite the promising results, there were some drawbacks of the system. Firstly, the system cannot localize the position of the stroke (no images were generated from the system) and secondly, while 90% of ICH patients were correctly differentiated by the system, only 65% of IS patients were correctly classified. Therefore, it is important to develop an algorithm which can fulfil two main aims: (1) localize and (2) classify the stroke with satisfactory sensitivity and specificity. Tomography-based imaging algorithms [49]-[50] have the potential to meet the first required aim, i.e. localization. Based on [148]-[149], the dielectric properties (permittivity and

conductivity) of ischaemic affected brain tissues are around 10%-15% lower than the healthy tissue while the dielectric properties of ICH stroke are higher than the main healthy brain tissue [108], and only lower than those of cerebral spinal fluid. Since the tomography-based imaging algorithm is capable of calculating the dielectric properties in the imaging domain, it is possible to image and classify the stroke. After finding the dielectric properties, the type of the stroke can be differentiated using a sample trained classifier. To that end, a support vector machine (SVM) [150] can be used to fulfil the classification requirements. SVMs originated from statistical learning theory [151] and have found numerous applications, such as face recognition, speech identification, handwritten digits recognition, text categorization and DNA analysis [152]-[156]. Besides these traditional applications, SVMs have also been recently developed for biomedical imaging applications [157]. Therefore, it is possible to both localize and classify stroke with requisite accuracy by combining a tomography-based algorithm with an SVM classifier.

In Chapter 6, a framework for microwave-based stroke localization and classification is proposed. It is based on microwave tomography technique, k-means clustering, and support vector machine. The general framework includes three steps: (1) Tomography to calculate the dielectric property profile of the brain, (2) k-mean clustering to categorize the calculated properties, and (3) SVM classifier to carry out the classification (decide the type of the stroke). The details of the framework are introduced in the following sections.

Chapter 3: Compressive Sensing in Radar-based Imaging Techniques

3.1 Theory of Compressive Sensing

Compressive sensing (CS) technique is used to reconstruct the original signal (full-sampled signal) from using under-sampled signal [87]-[89]. It is essentially an alternative method to obtain the signal. Based on the CS theory, the original signal can be reconstructed by using fewer signal samples which is obtained from a random measurement matrix. For example, the original signal s with N samples can be reconstructed by using a random measurement matrix to randomly select M samples in which $M \ll N$ [90]. One of the major requirement of CS reconstruction is that the signal has to be sparse; thus, non-sparse signal used in CS reconstruction may lead to distorted results. The meaning of sparsity is that the non-zero elements in the signal is small compared with the entire length of the signal. The sparse representation of a set of signal can be achieved by properly selecting the basis of the signal. A time domain signal $g(t)$ can be expressed as a linear combination of N orthonormal basis vectors:

$$g(t) = \sum_{j=1}^{N} x_j \psi_i(t) \tag{3.1}$$

When the number of nonzero values in x is $K \ll N$, then the time domain signal $g(t)$ is K sparse. The entire process of CS reconstruction can be summarized below [90]:

1. A set of randomly selected M samples are obtained from the original signal g with the size of $N \times 1$ by using a random measurement matrix ϕ with the size of $M \times N$:
$$y = \phi g \tag{3.2}$$

2. Based on the requirement of CS reconstruction, the original signal g has to be sparse aim to be properly recovered from CS algorithm. For non-sparse signal g, a transformation need to be implemented on it to transfer the non-sparse signal into its sparse domain. This transformation is implemented by using an orthogonal matrix ψ with the size of $N \times N$:
$$g = \psi s \tag{3.3}$$

3. Combining (3.2) and (3.3), a linear under-determined system can be obtained as:
$$y = \phi \psi s = As \tag{3.4}$$

The linear under-determined system (3.4) may have numerous solutions thus numerical optimization algorithms need to be used to achieve the sparest solution. The entire process of CS reconstruction is shown in Figure 3.1.

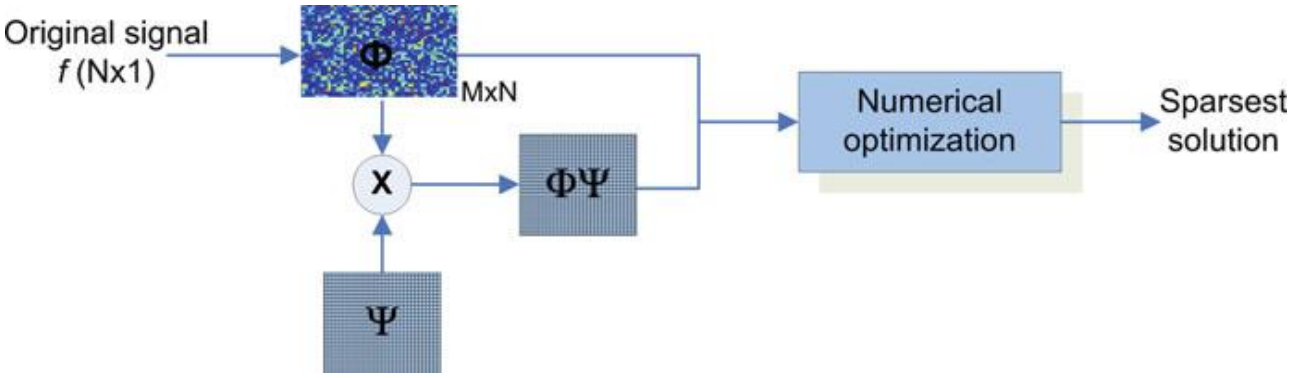

Fig 3. 1: The entire process of compressive sensing reconstruction [90].

The random measurement matrix ϕ and the transformation matrix ψ need to satisfy two criteria in order to successfully recover the under-sampled signal; the incoherence principle [91]-[92] and restricted isometry property (RIP) [93]. The incoherence between the measurement matrix ϕ and transformation matrix ψ implies the probability of successfully recovering the original signal from the under-sampled signal [90] and the RIP implies the robustness of the reconstruction when the noises are imposed on the signal [94]-[95]. If the measurement matrix ϕ and the transformation matrix ψ are completely coherent, the original signal can only be recovered using full-sampled coefficients. Conversely, if the rows of matrix ϕ cannot be used to express a sparse representation of the columns of matrix ψ, t these two matrix are incoherent [90]. The coherence of the two matrix ϕ and ψ can be calculated as [90]:

$$\mu(\phi,\psi) = \sqrt{N} \max_{k\geq 1, j\leq N} \left|\langle \phi_k, \psi_j \rangle\right| \tag{3.5}$$

where N is the length of the signal, ϕ_k is the kth row of matrix ϕ and ψ_j is the jth column of matrix ψ. The value of μ satisfies the relation shown below:

$$1 \leq \mu \leq \sqrt{N} \tag{3.6}$$

The coherence value μ can be used to define the minimum number of measurements which is required to obtain the maximum probability of successful reconstruction since the number of measurements M and the coherence value μ satisfy the following relation:

$$M \geq C \cdot K \cdot \mu(\phi,\psi) \cdot logN \tag{3.7}$$

where K is the sparsity of the signal in its corresponding sparse domain and C is a constant. From (3.7), we can induce that when lower value of μ is achieved, then smaller number of measurements need to be used for reconstructing the original signal. The isometry constant δ_K is defined as the smallest number which satisfy the following relation [90]:

$$(1-\delta_K)\|s\|_{l_2}^2 \leq \|As\|_{l_2}^2 \leq (1+\delta_K)\|s\|_{l_2}^2 \tag{3.8}$$

where s is the sparse representation of the original signal g, K is the sparsity of s, $A = \phi\psi$, and $\|\cdot\|_{l_2}$ is the second-order norm operator. The RIP implies that the subset of columns of matrix A is almost orthogonal. The sensing matrix A will satisfy the RIP with high probability if the following relation is hold for A [90]:

$$M \geq C \cdot K \cdot log\left(\frac{N}{K}\right) \tag{3.9}$$

The linear under-determined system in (3.4) can be solved by searching the sparsest solution of s with respect to the l_1 norm which is expressed as:

$$min\|s\|_{l_1}, \qquad s.b.j: y = As \tag{3.10}$$

When the noise factor is imposed on the signal, the under-determined system (3.4) is re-wrote as:

$$y = \phi\psi s + e = As + e \tag{3.11}$$

where e is the noise and the energy e is restricted as $\|e\|_{l_2} = \epsilon$. The optimization problem corresponds to (3.11) can now be expressed as:

$$min\|s\|_{l_1}, \qquad s.b.j: \|y - As\|_{l_2} \leq \epsilon \tag{3.12}$$

Both the optimization problems in (3.10) and (3.12) are convex optimization thus they can be solved by using linear programming (LP) methods.

CS technique in radar-based imaging systems has been investigated by several research groups. In [96]-[101], CS technique is applied in high resolution synthetic aperture radar (SAR) or inverse synthetic aperture radar (ISAR) systems. CS technique has also been used in three-dimensional (3D) microwave imaging [102]-[103] and ground penetrating radars (GPR) [104]-[105]. Although CS technique has been used in several radar-imaging applications, the utilization on radar-based bio-medical applications is seldom investigated. In the following sections, two CS-based algorithms will be proposed for radar-based head imaging system. The proposed algorithms aim to solve the first two

problems elaborated in Chapter 1 which are reducing the number of antennas used in the array and decreasing the number of stepped frequencies used in the transceiver system.

3.2 Compressive Sensing to Reduce the Number of Antennas

3.2.1 Theory

In traditional radar-based microwave imaging systems, step frequency continues waveform (SFCW) is chosen as the transmitted signal and based on the definition of SFCW, it can be expressed as:

$$S_T(t) = \sum_{n=0}^{N-1} rect\left(\frac{t - nT_r}{T_p}\right) e^{j2\pi(f_0 + n\Delta f)t} \tag{3.13}$$

where $rect()$ is the rectangular function, N, T_r, T_p, f_0 and Δf are the number of sub-pulses, pulse repetition interval, pulse width, initial frequency and frequency step size, respectively. For head imaging application, the desirable frequency range is proved to be 1-2 GHz. The target area is selected as a horizontal cross section of the entire brain. Assuming the target area contains *I* scatters with reflection coefficient $\delta_i \triangleq \delta(x_i, y_i)$ and the distance from current used antenna to the ith scatter is R_i, thus the corresponding time delay is $\tau_i = 2R_i/c$ (c is the wave speed of propagation in free space). Consequently, the received signal (echo) is:

$$S_R(t) = \sum_{i=1}^{I} \delta_i \sum_{n=0}^{N-1} rect\left(\frac{t - nT_r - \tau_i}{T_p}\right) e^{j2\pi[(f_0 + n\Delta f)(t - \tau_i)]} \tag{3.14}$$

The reflection coefficient δ for stroke and other tissues can be calculated using formulas in [106]:

$$\delta = \frac{Z_L - Z_o}{Z_L + Z_o} \tag{3.15}$$

Z_L and Z_o are the wave impedance of brain tissues and air which can be calculated using formulas shown below:

$$Z = \sqrt{\frac{j\omega\mu}{\sigma + j\omega\varepsilon}} \tag{3.16}$$

where μ is the magnetic permeability, ε is the electric permittivity and σ is the electrical conductivity of the tissue the wave is travelling through. The value of these dielectric properties of human tissues can be achieved in [39]. In order to use CS theory in SFCW radar imaging problem, a linear system

has to be constructed through row or column stacking. Based on the method described in [99], suppose the reflection coefficient for the ith cell of the imaging area is δ_i, then the reflection coefficient vector for the entire imaging area is:

$$\boldsymbol{\vartheta} = [\delta_1;\ \cdots;\ \delta_i;\ \cdots;\ \delta_I] \tag{3.17}$$

where I is the total number of cells inside the imaging area and δ_i can be calculated using (3.15). Assume the total number of antennas used in the array before performing CS is M=16 and the received signal from the mth antenna is a $N \times 1$ vector $\boldsymbol{w}^{(m)}$, where N is the total number of step transmitted frequencies. The received signal $\boldsymbol{w}^{(m)}$ can be modelled as:

$$\boldsymbol{w}^{(m)} = \boldsymbol{\Psi}^{(m)}\boldsymbol{\vartheta} \tag{3.18}$$

where $\boldsymbol{\Psi}^{(m)}$ is an $N \times 1$ sparse dictionary matrix which can be expressed as:

$$\boldsymbol{\Psi}^{(m)} = \begin{bmatrix} \boldsymbol{\Psi}_{11} & \cdots & \boldsymbol{\Psi}_{1I} \\ \vdots & \ddots & \vdots \\ \boldsymbol{\Psi}_{N1} & \cdots & \boldsymbol{\Psi}_{NI} \end{bmatrix} \tag{3.19}$$

where $\boldsymbol{\Psi}_{ni}$ is calculated as:

$$\boldsymbol{\Psi}_{ni}(\boldsymbol{t}_{step}) = rect\left(\frac{\boldsymbol{t}_{step} - nT_r - \tau_i}{T_p}\right) e^{j2\pi[(f_0 + n\Delta f)(\boldsymbol{t}_{step} - \tau_i)]} \tag{3.20}$$

In (3.20), $\boldsymbol{t}_{step}$ is the time vector for one signal step frequency pulse. To use CS to recover the image, two dimensional reconstruction process is implemented on the received signal. Firstly, the measurement antennas are randomly selected from the entire M antennas, which means that the measurement aspect angle is randomly selected. Secondly, the transmitted step frequencies are also selected randomly which means that not all the step frequencies are used over the whole frequency band. Assume the number of selected antenna is P ($P \leq M$) and the number of selected frequencies is K ($K \leq N$). The process of the random selection of frequency can be implemented by using a $K \times N$ measurement matrix $\boldsymbol{\Phi}^{(p)}$ for the pth angle of antenna and it can be modelled as a permutation matrix. Therefore, the received signal from the pth antenna by using randomly selected frequencies is:

$$\boldsymbol{y}^{(p)} = \boldsymbol{\Phi}^{(p)}\boldsymbol{w}^{(m)} = \boldsymbol{\Phi}^{(p)}\boldsymbol{\Psi}^{(m)}\boldsymbol{\vartheta} \tag{3.21}$$

where $\boldsymbol{y}^{(p)}$ is a $K \times 1$ vector and $\boldsymbol{\Phi}^{(p)}$ is a $K \times N$ permutation matrix.

Let

$$\boldsymbol{y} = \left[\boldsymbol{y}^{(1)};\ \boldsymbol{y}^{(2)};\ \cdots;\ \boldsymbol{y}^{(p)};\ \cdots;\ \boldsymbol{y}^{(P)}\right] \tag{3.22}$$

$$\boldsymbol{\Psi} = \left[\boldsymbol{\Psi}^{(1)};\ \boldsymbol{\Psi}^{(2)};\ \cdots;\ \boldsymbol{\Psi}^{(p)};\ \cdots;\ \boldsymbol{\Psi}^{(P)}\right] \tag{3.23}$$

$$\boldsymbol{\Phi} = diag\left\{\boldsymbol{\Phi}^{(1)};\ \boldsymbol{\Phi}^{(2)};\ \cdots;\ \boldsymbol{\Phi}^{(p)};\ \cdots;\ \boldsymbol{\Phi}^{(P)}\right\} \tag{3.24}$$

then the compressive sensing model for head imaging is

$$\boldsymbol{y} = \boldsymbol{\Phi}\boldsymbol{\Psi}\boldsymbol{\vartheta} \tag{3.25}$$

Considering the sparsity of the target reflection coefficient $\boldsymbol{\vartheta}$ and CS theory, $\boldsymbol{\vartheta}$ can be recovered via solving a nonlinear convex optimization problem:

$$\begin{aligned} &\widehat{\boldsymbol{\vartheta}} = argmin\|\boldsymbol{\vartheta}\|_1 \\ s.b.j \quad &\|\boldsymbol{y} - \boldsymbol{\Phi}\boldsymbol{\Psi}\boldsymbol{\vartheta}\|_2 \le \epsilon \end{aligned} \tag{3.26}$$

where ϵ is the amount of noise in the measured data. There are numerous algorithms to solve this convex optimization problem and a fast and accurate first-order algorithm named NESTA [107] is applied here.

The CS algorithm elaborated above is based on the assumption that that target area is sparse enough, which means the reflection coefficient of the stroke is much higher than the other tissues surround it. However, this assumption is not appropriate in the realistic scenario. For the real situation, the difference of reflection coefficient between stroke and surrounded tissues might be small. Consider a more reasonable scenario that the reflection coefficients of the tissues around the stroke are the same but with small difference from the stroke. Under this assumption, the CS algorithm proposed above is not suitable since the target area is far from sparse. However, through implementing an extra transformation, the CS algorithm is still able to be utilized in this situation. A transformation similar with total variation transform is applied as:

$$T_{i,j} = (\delta_{i,j} - j\delta_{i,j+1}) + (j\delta_{i,j} - \delta_{i+1,j}) \tag{3.27}$$

where $\delta_{i,j}$ is the reflection coefficient at (i,j)th cell. Figure 3.2 indicate a configuration of the imaging cells aim to illustrate (3.27).

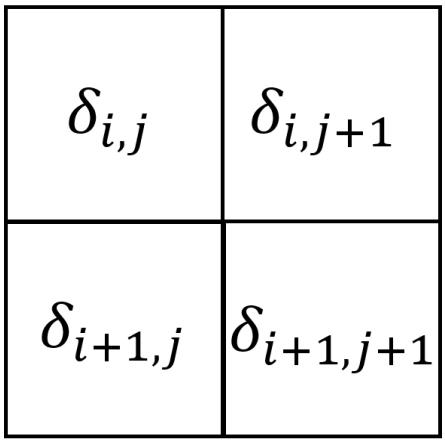

Fig 3. 2: Configuration of the imaging cells

Based on (3.27), the convex optimization problem in (3.26) can be modified as an analysis-based problem:

$$\begin{aligned} & \widehat{\boldsymbol{\vartheta}} = argmin\|\boldsymbol{T}\boldsymbol{\vartheta}\|_1 \\ s.b.j \quad & \|\boldsymbol{y} - \boldsymbol{\Phi}\boldsymbol{\Psi}\boldsymbol{\vartheta}\|_2 \leq \epsilon \end{aligned} \tag{3.28}$$

where $\boldsymbol{T}$ is the transformation matrix which implements the linear transform expressed in (3.27). The same optimization algorithm (NESTA) is still used to solve this problem. Figure 3.3 illustrates the block diagram contains the entire process of the CS reconstruction using the $\boldsymbol{T}$ transformation. It can be seen from Figure 3.3 that the entire process of CS reconstruction can be divided into four steps for the low-contrast scenario:

1. Collect the received signals from the transceiver system. The received signals are from the N antennas (full-sampled spatial data).
2. The signals received from a certain number of antennas (say M antennas and $M \ll N$) are randomly selected from the original received signals (the signals received from N antennas). This random selection process is implemented by using a random permutation matrix $\boldsymbol{\Phi}$.
3. A dictionary matrix $\boldsymbol{T}\boldsymbol{\Psi}$ is constructed aim to transfer the non-sparse imaging domain into a sparse domain. The entries in the matrix $\boldsymbol{T}$ and $\boldsymbol{\Psi}$ are determined using (3.20) and (3.27).
4. An under-determined system is built for CS reconstruction. The unknown reflection coefficients for the imaging area are achieved by solving a l_1 norm-based convex optimization problem which is expressed in (3.28). A numerical method named NESTA is used to solve the problem in (3.28).

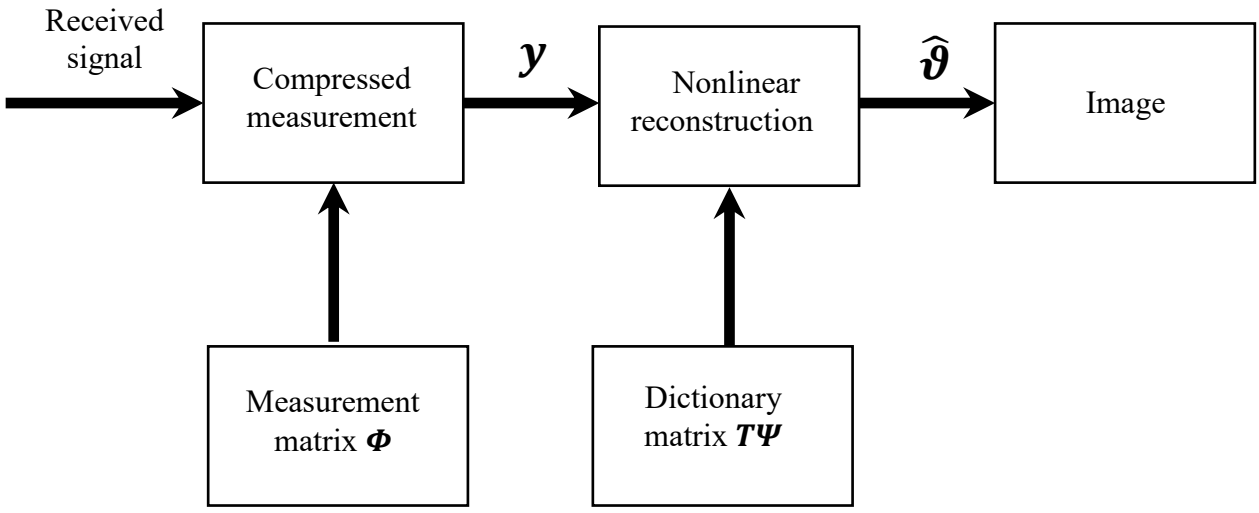

Fig 3. 3: The block diagram of the entire CS reconstruction process

3.2.2 Simulation Results and Discussions

As an initial test of the CS approach, a homogeneous head model with realistic shape and size as the human head is constructed (with dimensions x=160 mm and y=130 mm). The configuration of the antenna array around the head is shown in Figure 3.4. The range of the frequency band is chosen from 1-2 GHz which is proven to be suitable for head imaging application [108]. Initially, the number of stepped frequencies is taken as N=50 and the number of antennas is M=16 with interval angel of 22.5°. One stroke is assumed in the head model with a size of $5mm \times 5mm$, conductivity $\sigma = 1.8$ and relative permittivity $\varepsilon_r = 60$ i.e. haemorrhagic stroke. Based on this dielectric property, the reflection coefficient of the stroke is calculated using (3.15)-(3.16) as 0.2 and the reflection coefficient surround the stroke is assumed to be 0. A full number of antennas are used firstly and the confocal imaging algorithm is used for the imaging. After producing the image using 16 antennas, the number of antennas is reduced to 4 (only 4 antennas are randomly selected from the full 16 antennas) and the confocal algorithm is used again without implementing the CS technique. Then, CS-based imaging algorithm as proposed above is carried out and the results after using CS imaging algorithm are compared with the results using traditional confocal imaging algorithm as shown in Figure 3.5.

It can be seen from Fig 3.5 (b) that by using 16 antennas and performing confocal algorithm for the imaging, the position of the target can be detected but with some noise emerged from the used confocal processing (mainly from the sidelobes of the match filter). When the number of antennas is reduced to 4, the position of the target cannot be determined if the traditional confocal imaging algorithm is used (Fig 3.5 (c)). However, after using CS-based imaging algorithm with 4 antennas, the position of the target is successfully detected with very clear image (Fig 3.5 (d)). The noise in the

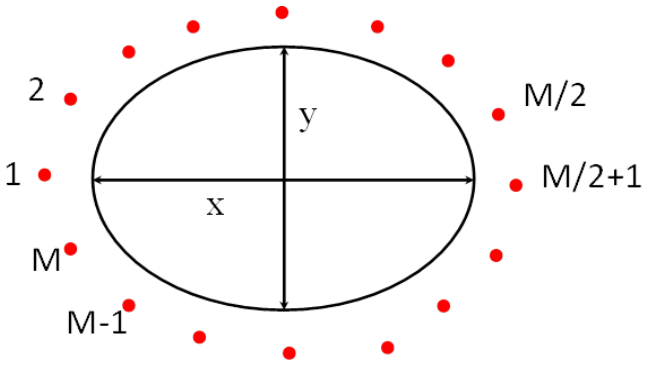

Fig 3. 4: Antenna array setup. The elliptical area represents the head model and the discrete red points denote M antenna array elements.

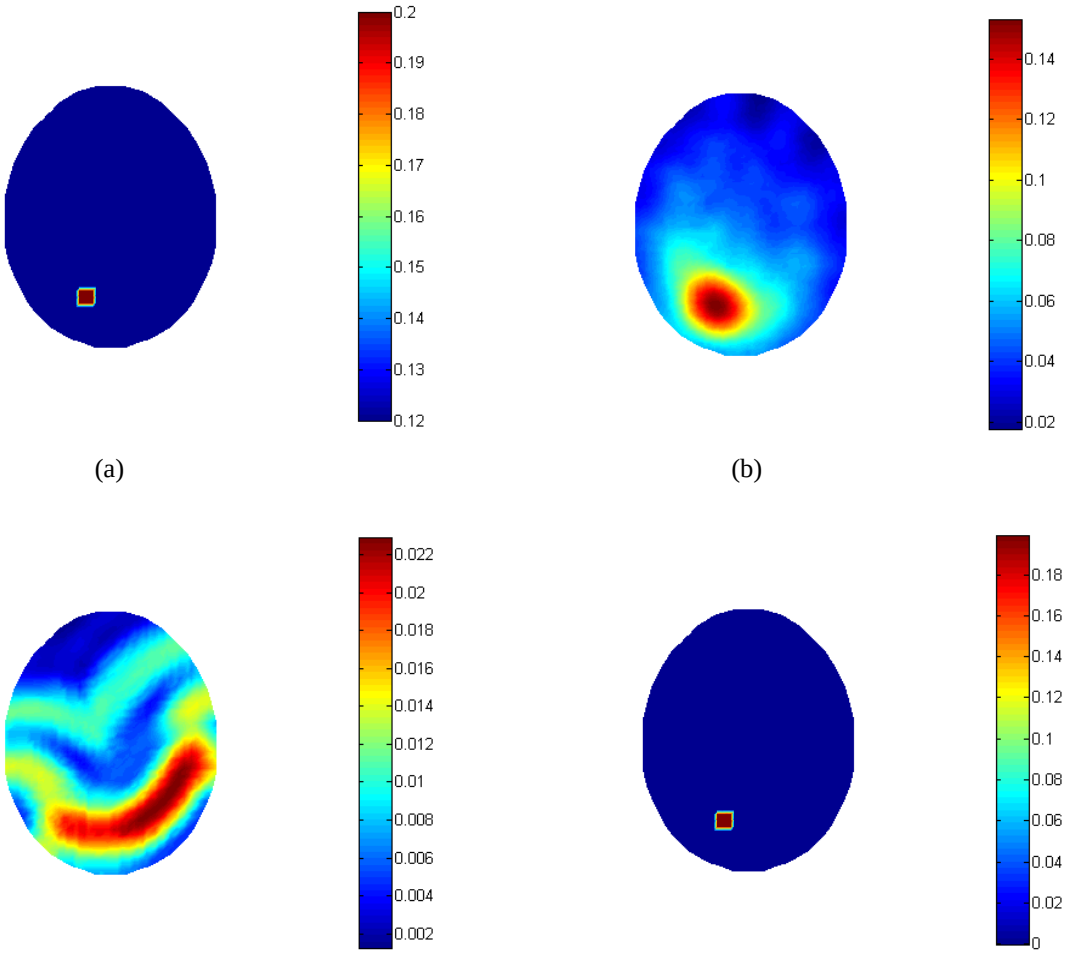

(a) (b)

(c) (d)

Fig 3. 5: Head imaging results with high contrast of target area. (a) The used head model with a bleeding stroke indicated by a bright square; (b) Image from using 16 antennas and confocal imaging algorithm; (c) Image from using 4 antennas and confocal algorithm; (d) Image from using 4 antennas and CS-based imaging algorithm.

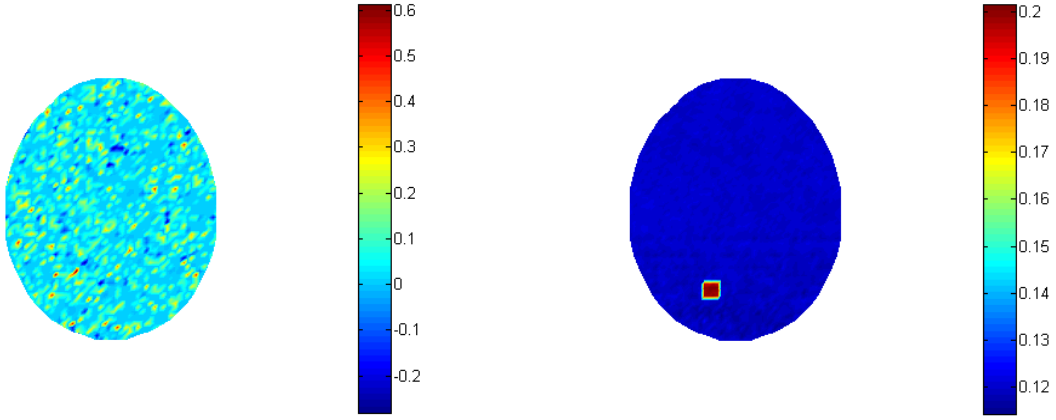

(a) (b)

Fig 3. 6: CS-based imaging result with low contrast of target area. (a) Image from using original CS algorithm; (b) Image from using improved CS algorithm (with approximated TV transformation)

image is eliminated in this case because of the well sparsity of the target area. However, in realistic scenario, the target area is commonly not sparse enough. Being lack of the well sparsity, the original CS-based imaging algorithm is not suitable and an extra transformation has to be implemented to overcome the problem of non-sparsity. In the next step, the CS-based imaging algorithm is tested in low contrast target area which is more close to the realistic situation by using reflection coefficient of the stroke as 0.2 and an average reflection coefficient of other tissues surround the stroke as 0.12. The result by using original CS algorithm on this scenario is shown in Figure 3.6 (a). It can be seen from Fig 3.6 (a) that the image recovered from original CS algorithm is corrupted and there is no information can be extracted from the image. This is mainly because the lack of sparsity of the target area. The non-sparsity of the target area can be alleviated by using an approximated total variant (TV) transform as defined in (3.27). The result from using improved CS algorithm (after adding approximated TV transform in the convex optimization) is shown in Figure 3.6 (b). Compared with the result obtained from using original CS algorithm, it can be seen from Figure 3.6 (b) that the location of the target can be recovered accurately by using improved CS algorithm after implementing the approximated TV transformation.

3.3 Compressive Sensing to Reduce the Number of Stepped Frequencies

Beside using large number of antennas in the array, to achieve reasonable images that enable a successful detection, microwave systems designed for head imaging use wide frequency bands extending from 1 GHz up to 4 GHz [36]. Thus, the antenna arrays utilized in those frequency domain

systems collect huge data at many frequency steps within the used band. For example, the system explained in [36] uses 401 frequency steps to achieve acceptable imaging results. However, the large number of frequency steps also increases the time needed for data acquisition and scanning. Moreover, to make microwave imaging systems portable, recent designs replace the conventional vector network analyser with a CMOS based stepped frequency continuous-wave transceiver, which requires a long calibration procedure for all the frequency steps [16]. On the other hand, it is well known that a patient with brain injury is an emergency case and the procedure for diagnosis and medication should be finished within several hours from the onset of the symptoms [36]. Therefore, it is vital for such an application to use a minimum number of frequency steps without degrading the quality of the image.

In the following section, the CS theory is implemented to recover the time domain correlation (TDC) signals from limited number of frequency steps by utilizing the sparsity of those signals. The final image is generated from those recovered TDC signals using the well-known confocal algorithm. To validate the proposed approach, it is tested using three different CS techniques on measurements done using a recently developed head imaging system [36]. The presented results indicate that the suggested technique can produce satisfactory images based on two quality metrics using less than half the number of frequency steps needed in the non-CS traditional confocal imaging approach.

3.3.1 Theory

Figure 3.7 shows the general configuration of a microwave imaging system using antenna array of P elements. In the conventional stepped frequency microwave imaging approach, each of the antenna elements in the array is used to transmit continuous signals at N frequency steps from f_1 to f_N. The same transmitting antenna (monostatic) or all the antennas of the array (multistatic) collect the reflected/scattered signals. Figure 3.8 shows the time domain signals received by 16 antennas from the recently developed microwave head imaging system [36]. The antennas used in the array is exponentially corrugated tapered slot antenna which can be operated across the band from 1 to 4 GHz. The optimized distance between the adjacent antennas is 6 cm which is aiming to achieve better than 20 dB mutual coupling between two antennas. The incident pulse with the band from 1 GHz to 4 GHz was generated by using R&S ZVA24 VNZ and totally 401 stepped frequency points were generated to synthetize the wideband pulse. To transmit the signals to the antenna array, two single-pole eight-throw (SP8T) microwave coaxial switches were used in the system. The first switcher was used to control the signals transmitted to the 1-8 antennas in the array and the second switcher was used to

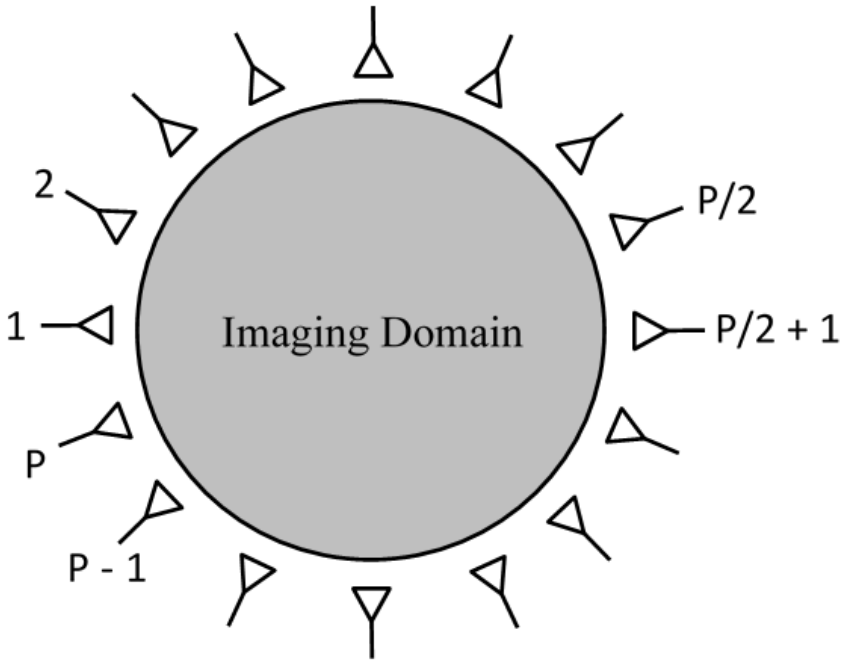

Fig 3. 7: A general domain of microwave imaging system using antenna array of P antenna elements.

control the signals transmitted to the 9-16 antennas in the array. A realistic head phantom was used to obtain the measured scattered data. The head phantom includes gray matter, white matter, cerebral spinal fluid (CSF), and skull. To model a brain stroke, an elliptic object with volume of $1.4 \times 0.7 \times 0.5\ cm^3$ and electrical properties of blood was embedded inside the phantom. The materials used to fabricate the head phantom are gelatin, corn flour, water, sodium azide, agar, and propylene. To achieve close approximation to the real electrical properties of the brain tissues, the values reported in [38]-[39] were used to guide the mixture procedure of the aforementioned materials. Figure 3.9 and 3.10 show the system platform and used realistic head phantom to obtain the measurement data shown in Figure 3.8. It can be seen from Figure 3.8 that the time domain correlated signals received by the 16 antennas all exhibited sparse characteristic (the high energy of the time domain signals are all focused in a certain period of time, which is from 0.5 ns to 1.5 ns). This sparse characteristic is

result from the truth that only one stroke will be emerged in the brain, thus the strong reflection only happened within a small district, which is the district contained the stroke. The sparse characteristic supplies the possibility that the time domain correlated signals can be reconstructed using less number of frequency points if a transformation from the frequency domain data to time domain data can be found.

Assume the frequency domain data (reflection coefficients) using monostatic approach is expressed as:

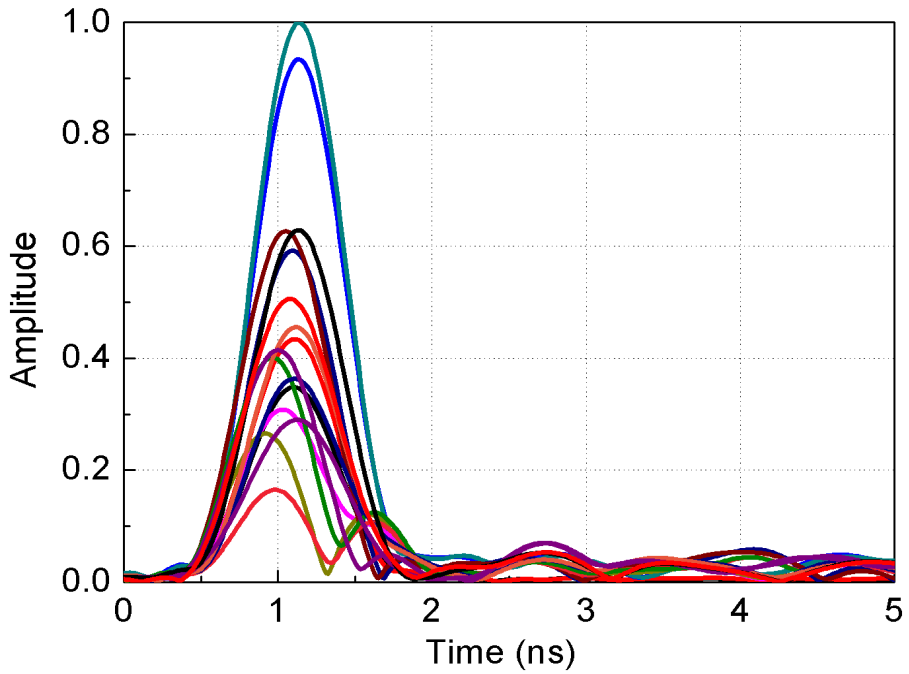

Fig 3. 8: Examples of time domain correlation signals received at each of the 16 antennas from 401 frequency steps using the head imaging system in [36].

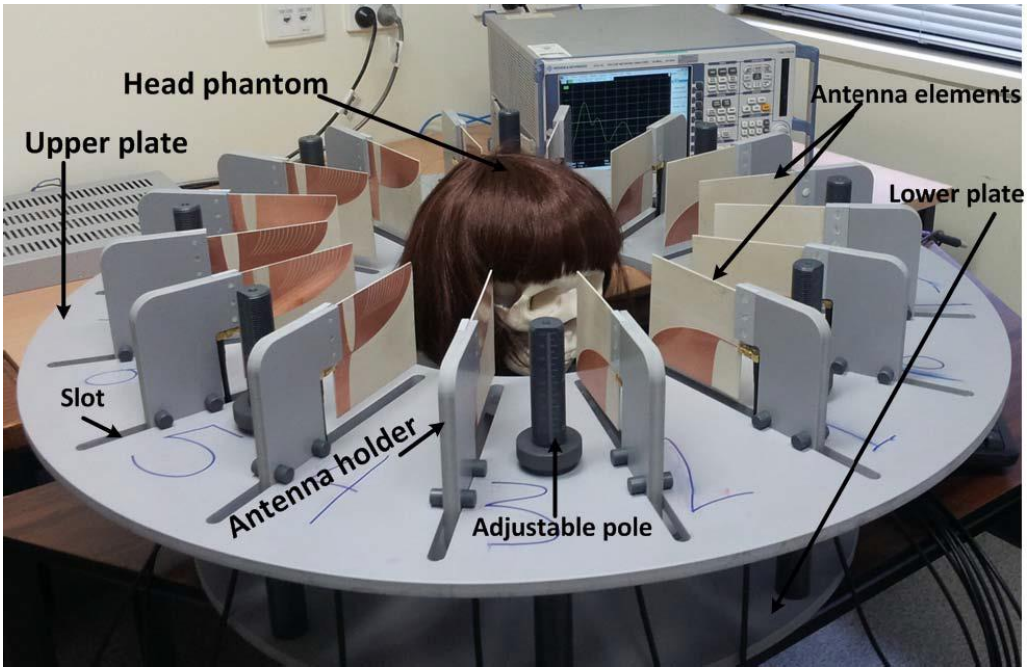

Fig 3. 9: System platform used to obtain the measured data [36].

$$\boldsymbol{S} = \begin{bmatrix} S^1(f_1) & \cdots & S^P(f_1) \\ \vdots & \ddots & \vdots \\ S^1(f_N) & \cdots & S^P(f_N) \end{bmatrix} \tag{3.29}$$

where $S^p(f_n)$ is the reflection coefficient for the pth antenna at the nth frequency step. The inverse Fourier transform of $\boldsymbol{S}$ is the time domain correlation matrix $\boldsymbol{\mathcal{T}}$ which can be expressed as:

$$\boldsymbol{\mathcal{T}} = \boldsymbol{\mathcal{F}}^{-1}\boldsymbol{S} = \begin{bmatrix} \mathcal{t}^1(0) & \cdots & \mathcal{t}^P(0) \\ \vdots & \ddots & \vdots \\ \mathcal{t}^1\left(\frac{N-1}{\Delta f N}\right) & \cdots & \mathcal{t}^P\left(\frac{N-1}{\Delta f N}\right) \end{bmatrix} \tag{3.30}$$

where $\mathcal{t}^P\left(\frac{n-1}{\Delta f N}\right)$ is the time domain correlation coefficient for the pth antenna at $\frac{n-1}{\Delta f N}$th time step. $\boldsymbol{\mathcal{F}}$ is the Fourier transform matrix which can be represented as:

$$\boldsymbol{\mathcal{F}} = \begin{bmatrix} 1 & 1 & 1 & & 1 \\ 1 & W_N^1 & W_N^2 & \cdots & W_N^{N-1} \\ 1 & W_N^2 & W_N^4 & & W_N^{N-2} \\ & \vdots & & \ddots & \vdots \\ 1 & W_N^{N-1} & W_N^{N-2} & \cdots & W_N^1 \end{bmatrix} \tag{3.31}$$

where W_N^n can be expressed as:

$$W_N^n = \exp\left(-\frac{j2\pi n}{N}\right) \tag{3.32}$$

and $\boldsymbol{\mathcal{F}} \in \mathbb{C}^{N\times N}$. The time domain correlation coefficients represent the time delays between the incident and reflected signals. The head imaging scenario has usually a sparse characteristic with up to two strong scatterers (skin interface and any brain stroke). Thus, the time domain correlation coefficients exhibit a sparse characteristic which means that correlation coefficients with significant values only occupy a certain period of time. This property indicates that through using compressive sensing techniques to recover the time domain correlation signal using under-sampled frequency domain data.

The target is to generate the same quality images using much smaller number of frequency steps M ($M \ll N$) than the steps needed in the previously explained traditional approach. The under-sampled frequency domain data can be represented in this case as:

$$\boldsymbol{S}^{cs} = \begin{bmatrix} S^1(f_1') & \cdots & S^P(f_1') \\ \vdots & \ddots & \vdots \\ S^1(f_M') & \cdots & S^P(f_M') \end{bmatrix} \tag{3.33}$$

where $f_1' \geq f_1$ and $f_M' \leq f_N$. This under-sampling process can be implemented using a random permutation measurement matrix $\boldsymbol{\phi}$;

$$\boldsymbol{S}^{cs} = \boldsymbol{\phi}\boldsymbol{S} \tag{3.34}$$

If this under-sampled data is directly used to generate an image, it will be distorted by the level of under-sampling of the frequency domain signals. Nevertheless, if the original time domain data for

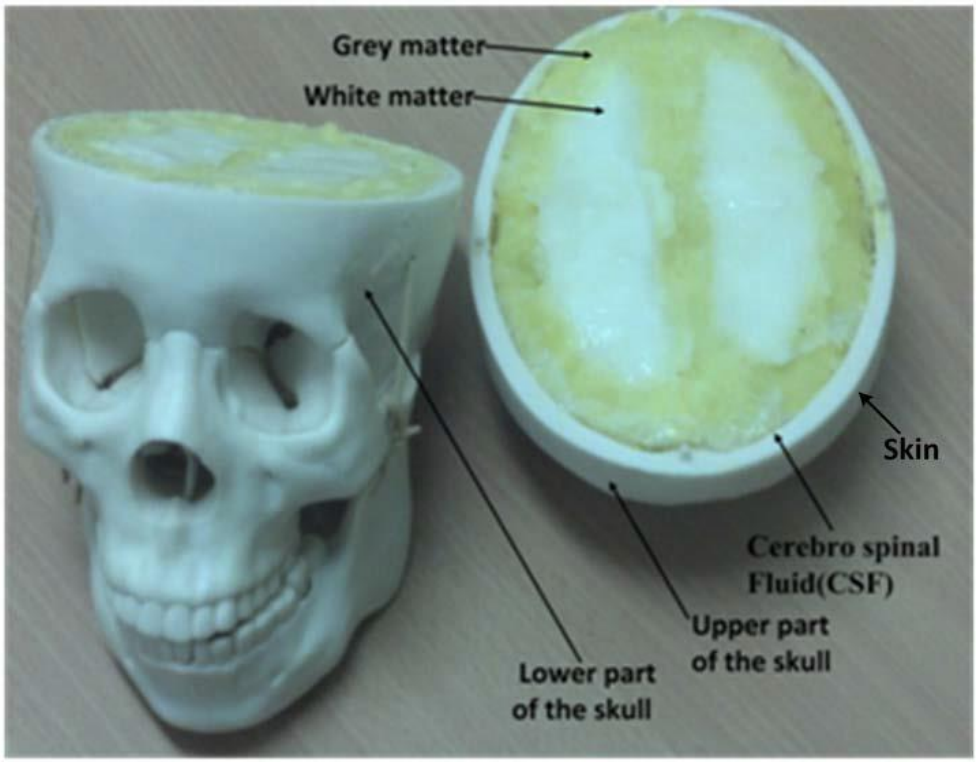

Fig 3. 10: The fabricated realistic head phantom used to obtain the measurement data [36]

each of the antennas is sparse enough, it can be reconstructed accurately from solving a constraint l_1 norm convex optimization problem:

$$min\left\|\boldsymbol{\mathcal{T}}_{:p}^{cs}\right\|_1, subject\ to\ \left\|\boldsymbol{S}_{:p}^{cs} - \boldsymbol{\phi}\boldsymbol{\mathcal{F}}\boldsymbol{\mathcal{T}}_{:p}^{cs}\right\|_{l_2} \leq \epsilon \tag{3.35}$$

where $\boldsymbol{\mathcal{T}}_{:p}^{cs}$ and $\boldsymbol{S}_{:p}^{cs}$ is the *p*th column of $\boldsymbol{\mathcal{T}}^{cs}$ and $\boldsymbol{S}^{cs}$, respectively, $\boldsymbol{\mathcal{T}}_{:p}^{cs}$ represents the recovered time domain correlation signal for the *p*th antenna using the under-sampled frequency steps, and ϵ is the tolerated error for the convex optimization problem. This l_1 norm convex optimization problem can be solved using several algorithms. In this paper, the three accurate and fast algorithms NESTA [107], SPGL$_1$ [109], and CoSaMP [110] are used and compared to evaluate the proposed approach.

3.3.2 Imaging Results and Discussions

The correlation coefficients of the original and recovered TDC signals are used to quantitatively evaluate the performance of the reconstruction for all the TDC signals of the 16 antennas. A value of correlation coefficient close to 1 indicates a high similarity between with the original signal, whereas a value close to 0 indicates dissimilarity. The correlation coefficients are calculated based on 100 trails of the CS reconstruction and an average correlation coefficient (ACC) is taken for the

evaluation. The number of the frequency steps M in the reconstruction is chosen as 300, 200 and 100. It is notable that since the TDC signals are zero for the 1st and 9th antennas due to the skin interface effect removal process [37], the TDC correlation coefficients for these two antennas are ignored here. The results depicted in Figure 3.11 show that when $M = 300$, the values of ACC are close to 1 for the three CS techniques indicating a high similarity between the original and reconstructed TDC signals. However, when $M = 100$, the ACC values are around 0.3 indicating distorted TDC signals. It also can be seen from Figure 3.11 that the signals reconstruction using $SPGL_1$ are generally better than reconstructed signals using the other two methods. Figure 3.11 also shows that CoSaMP has the worst performance due to its need for pre-defined signal sparsity, which is usually antenna-dependent (the TDC signal from different antennas possess different sparsity) and thus difficult to define. In this assessment, the sparsity of the signal is defined as 20% of the TDC signal length for all the antennas' signals when implementing CoSaMP method.

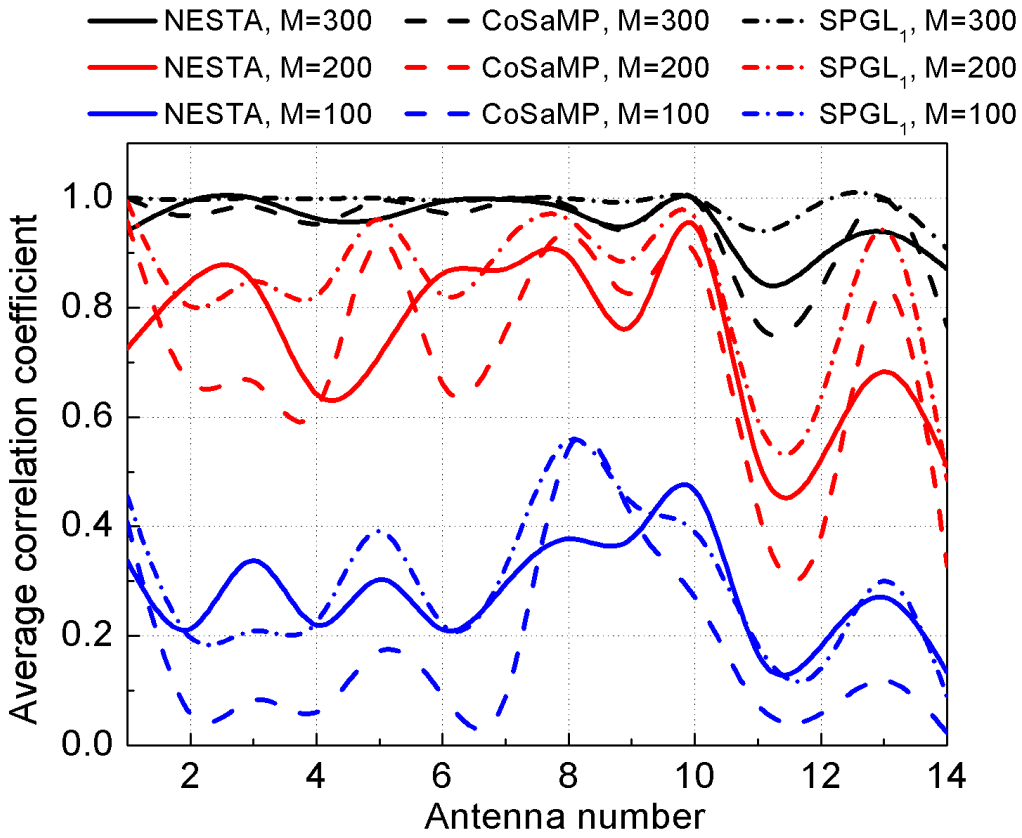

Fig 3. 11: Comparison between the average correlation coefficients (ACC) of the original and recovered TDC signals for different antennas using three different $\boldsymbol{l_1}$ norm optimization solvers.

To further verify the quality of images after using the explained CS technique to recover TDC signals at different frequency steps, the radar-based imaging algorithm [37] is utilized. To that end, the recovered TDC signals are used to produce an image of the head after applying that confocal-based

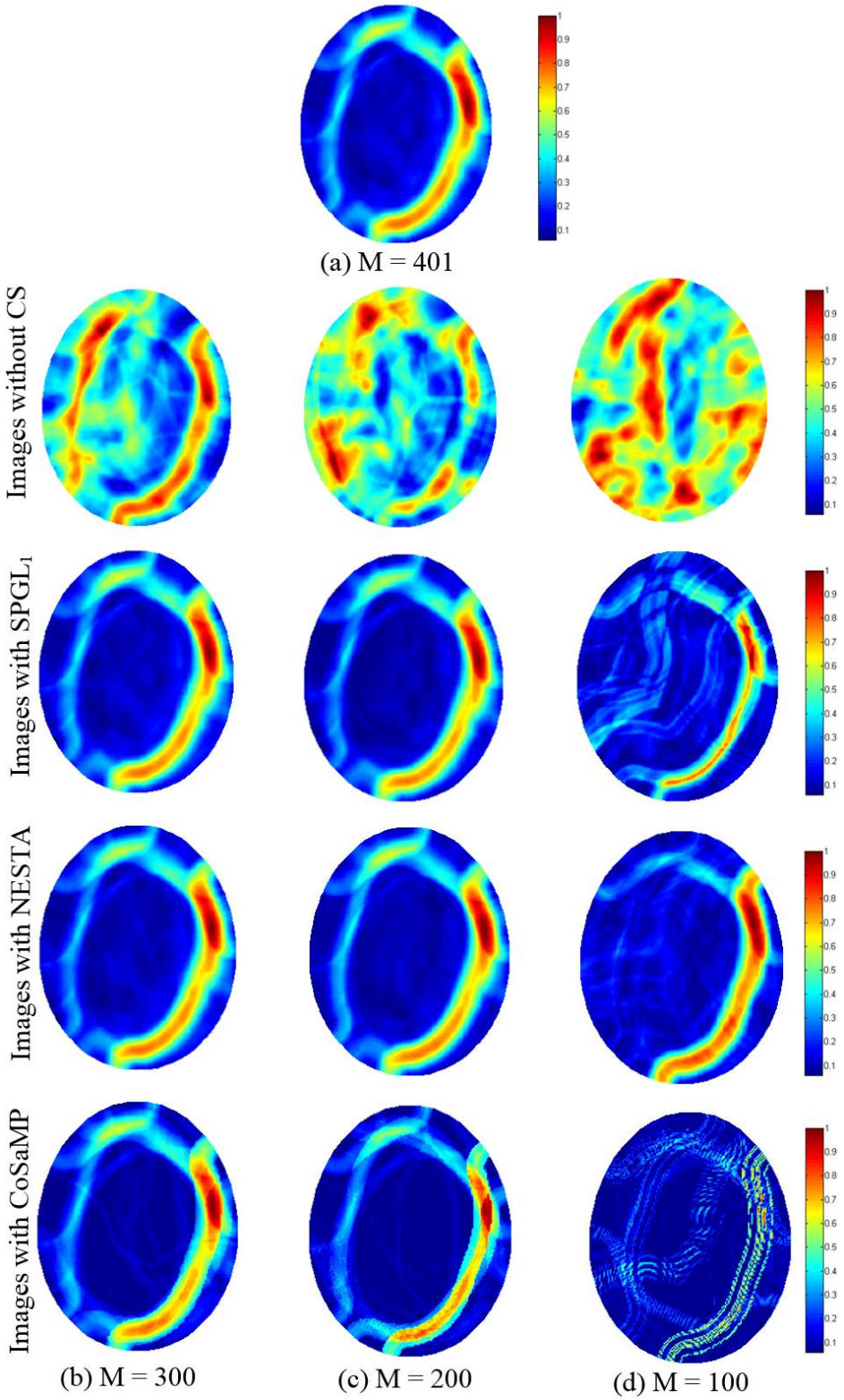

Fig 3. 12: Constructed head images from using (a) full number (M=401) of available frequency steps in the traditional method, and (b), (c), and (d) under-sampled frequency steps (M=300, M=200, and M=100, respectively) using traditional and three CS methods.

algorithm. Figure 3.12 shows the produced images with and without CS for different numbers of frequency steps that are randomly selected within the band 1-4 GHz. It can be seen from Fig 3.12 that the position of the brain stroke can be accurately located when using CS methods ($SPGL_1$, NESTA

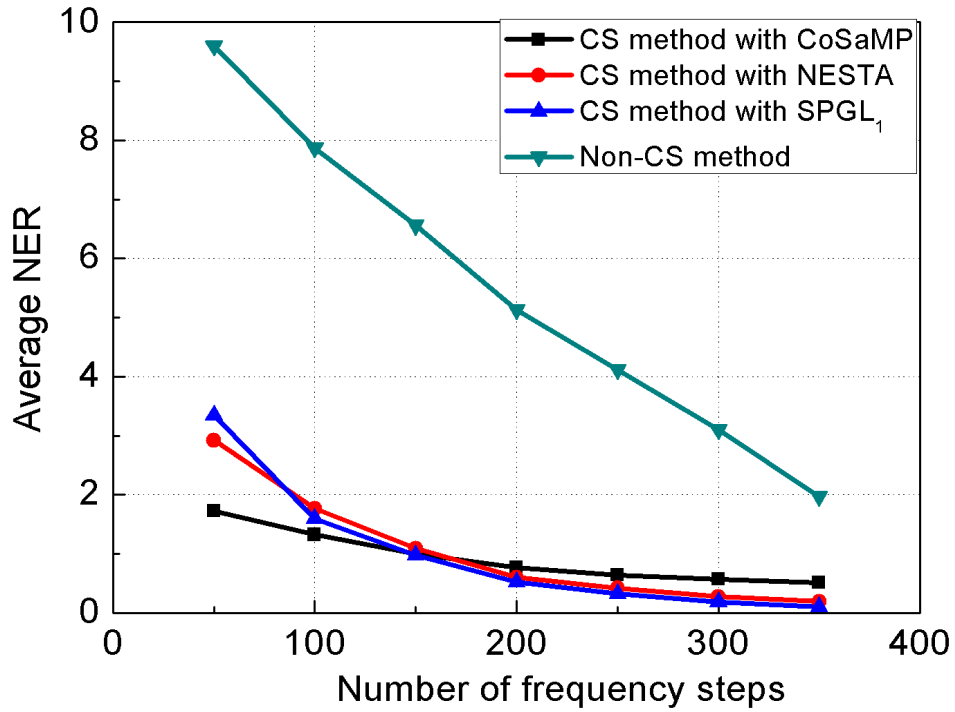

Fig 3. 13: Average NER using traditional and CS methods under different number of frequency steps

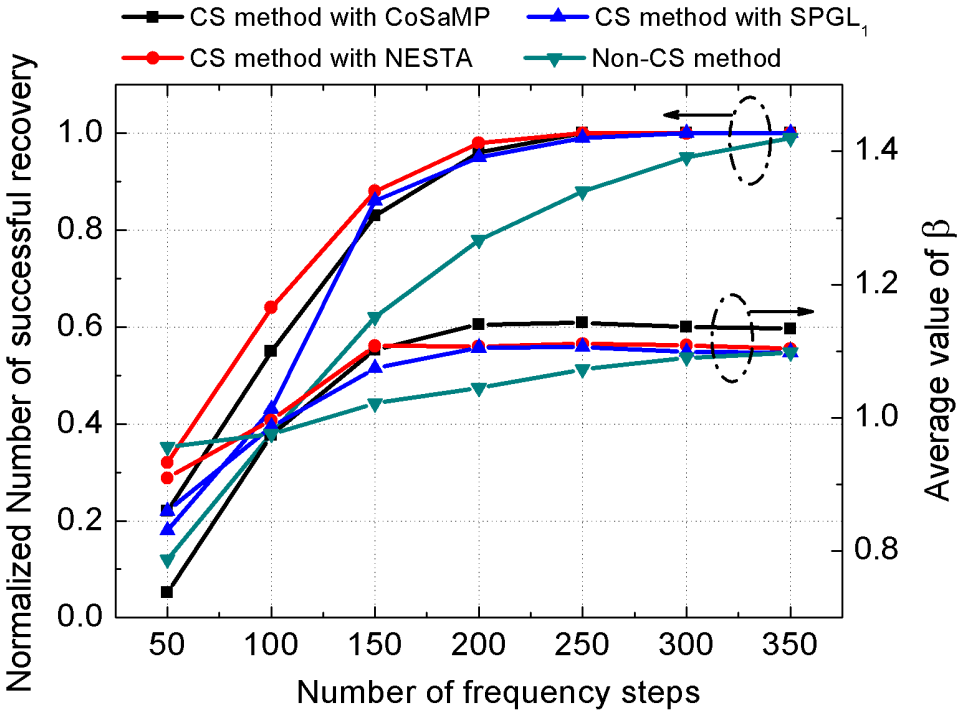

Fig 3. 14: Number of successful reconstructions and values of quality metric $\boldsymbol{\beta}$ using non-CS and CS methods for different number of frequency steps.

and CoSaMP) when the number of frequency steps is less than half of the original steps. It is also notable that when M=100 (quarter of the original frequency steps), the CS methods using $SPGL_1$ and NESTA can still recover the image accurately, whereas CoSaMP results in a low quality image. On the other hand, the reconstructed images from TDC signals without using CS are highly distorted when using small number of frequency steps.

Besides assessing the recovered images using CS and non-CS methods, it is also important to investigate the lowest number of frequency steps needed for an acceptable image reconstruction. To that end, two metrics are defined for quantitatively find the quality of the images and decide the lowest value of M for satisfactory images. The reconstruction normalized error rate (NER), which is the difference between the intensity of all pixels of the imaged domain using the under-sampled steps and the original full steps intensity:

$$NER = \sqrt{\frac{1}{K}\sum_{k=1}^{K}\left|\frac{I_G(h_k) - I(h_k)}{I_G(h_k)}\right|^2}, \forall h_k \in \mathcal{H} \tag{3.36}$$

where K is the number of pixels within the entire head area $\mathcal{H}$, $I(h_k)$ is the recovered image intensity for the kth pixel and $I_G(h_k)$ is the image intensity of the original image using full-sampled frequency steps (M=401). The second metric used to evaluate quality of the reconstruction images is β, which is defined as:

$$\beta = \frac{max[I(h_k)]}{max[I(h'_k)]} \quad \begin{matrix} \forall h_k \in \mathcal{S} \\ \forall h'_k \in \mathcal{H} \text{ and } h'_k \notin \mathcal{S} \end{matrix} \tag{3.37}$$

where $\mathcal{S}$ is the set of pixels within the real injury area. β can be used to assess the contrast of the maximum intensity for the images. $\beta < 1$ means the position of the brain stroke is not located correctly and $\beta > 1$ means the position of the brain stroke is recovered successfully.

The aforementioned metrics are calculated from 100 trails using non-CS and CS methods under different values of frequency steps (M) and the average value of NER and normalized successful image reconstruction ($\beta > 1$) are calculated. The results for NER are shown in Figure 3.13, which indicates that the CS-methods can successfully reconstruct the images with much lower value of NER than the images recovered using non-CS method for different number of frequency steps. It is notable that when M=150, all of the three CS methods achieve almost the same acceptable value of NER, while the performance concerning NER starts to deteriorate with different performances of the three CS methods when using M smaller than 150.

The normalized number of successful reconstructions ($\beta > 1$) and the average value of β is shown in Figure 3.14, which confirms that the number of successful reconstructions using CS methods is higher than the traditional method. It is notable that the number of successful reconstructions dramatically decrease when the number of frequency steps becomes less than 150 for all the three used CS methods. For the average value of β, the results also clearly indicate that when the number

of frequency steps is more than 150, the average value of β is maintained at more than 1, which implies successful recovery; however, when the number of frequency steps is less than 150, the average value of β is smaller than 1 indicating an incorrect localization of the brain stroke. These results correspond well to the average NER evaluation. Thus, using CS methods with 150 frequency samples always results in stable performance in the investigated system.

3.4 Discussions and Conclusions

Two compressive sensing based methods have been presented to solve two main problems in current microwave brain imaging algorithms. The first method aims to reduce the number of antennas used in the antenna array. To achieve this target, compressive sensing (CS) technique was used with the traditional confocal imaging algorithm. The reason of using CS technique is based on the fact that the reflection coefficients of the imaging area is sparse (only one stroke could develop in the brain thus the strong reflection can only happen within a certain area). A CS model combined with confocal algorithm was built and the reflection coefficients of the imaging area were reconstructed by solving a l_1 norm convex optimization problem. The proposed method was tested by using a simple high contrast head model (sparse model) with a bleeding stroke inside. The results indicate that when only 4 antennas were used to transmit and receive the signals, the generated image is largely distorted by using traditional confocal imaging algorithm, however, when the proposed CS-based method was applied, the position of the stroke can be clearly detected. To make the proposed method more realistic (in low-contrast imaging domain), an approximated total variant (TV) transform was proposed to transfer the non-sparse imaging area (low-contrast imaging area) to a sparse domain. This TV transform was integrated into the l_1 norm convex optimization problem and the proposed method was further assessed using a low-contrast head model. The results indicated that when 4 antennas and the original CS method were used in the reconstruction, the generated image will be corrupted and few information can be extracted from the reconstructed image. However, when the improved CS method was used, the position of the bleeding stroke can be successfully recovered by using four antennas. Using small number of antennas in the antenna array can reduce the mutual coupling between the adjacent antennas, and it also reduce the size of the entire system.

The second method aims to reduce the number of stepped frequencies used in the transceiver system. CS-based method was used to solve this problem and the reason of using CS technique is based on the fact that the time domain correlation (TDC) signals captured in frequency domain are sparse. Using data from experiments done on artificial head phantoms, it has been shown that CS methods have successfully detected brain strokes using less than half of the frequency steps needed in the

conventional non-CS imaging technique. A further investigation was implemented to obtain the minimum number of stepped frequencies which can be used to successfully recover the images. Based on two defined metrics (reconstruction normalized error rate (NER) and β which is used to measure the successful rate of the CS algorithm), it was found that when 150 frequency points were used in the reconstruction, all the CS-based methods can achieve satisfactory results, whereas when the number of frequency points were lower than 150, the recovered image quality will be largely degraded. Using small number of frequency steps in microwave imaging enables reducing data acquisition time and complexity of the system, which are especially important in the recent efforts to build portable, real-time imaging systems using compact stepped frequency transceiver.

Chapter 4: Compressive Sensing with Tomography -based Imaging Techniques

4.1 Compressive Sensing on Non-Sparse Imaging Domain

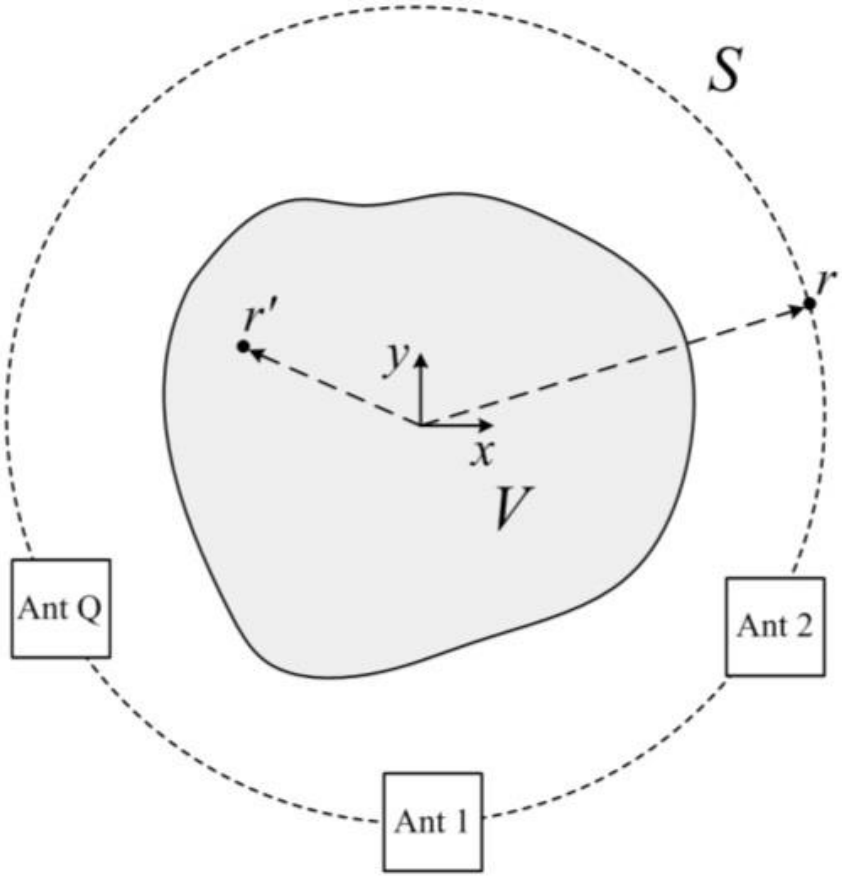

Fig 4. 1: Diagram of a general imaging problem

To explain the proposed technique, let us assume the general imaging configuration shown in Figure 4.1. There are Q uniformly spaced antennas that are positioned at the measurement contour S. The scattering domain V is illuminated at a certain frequency by a transverse-magnetic wave where $E_{inc}^{q}(x,y) = E_{inc}^{q}(x,y)\tilde{\mathbf{z}}$ $(q = 1, \dots, Q)$, with a time-dependent factor of $\exp(-j2\pi ft)$. The domain V is discretised into N square cells ($V_{n=1,\dots,N}$) with certain dielectric properties.

Therefore, it is convenient to define the normalized dielectric profile (NDP) of the problem as:

$$\mathcal{X}(x,y) = \left[\varepsilon_r(x,y) + \frac{\sigma(x,y)}{j\omega}\right] \Big/ \widetilde{\varepsilon_s} \tag{4.1}$$

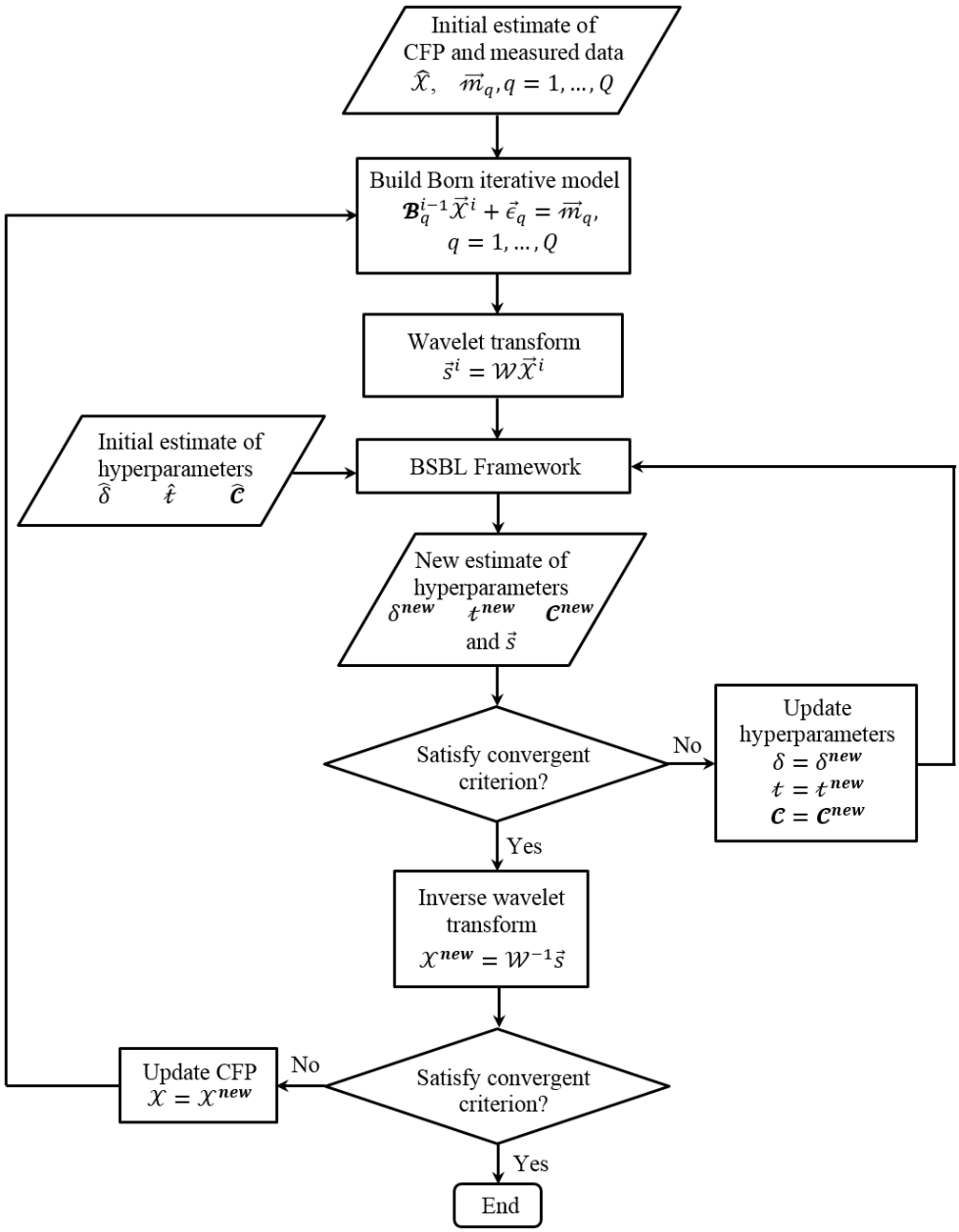

Fig 4. 2: Block diagram of the proposed imaging scheme

where $\tilde{\varepsilon_s}$ is effective dielectric constant of the surrounding material which is defined as $\tilde{\varepsilon_s} = \varepsilon_s + j\sigma_s/\omega$. Based on the explained configuration, the proposed imaging scheme is depicted by the flowchart of Figure 4.2. A preliminary guess of the unknown $\mathcal{X}$, which is assumed here simply as $\vec{\mathcal{X}} = [1, \ldots, 1]$, and the measured scattered signal $\vec{m}_q$ $(q = 1, \ldots, Q)$ are used as initial input parameters for the algorithm. The Born iterative model is then built as illustrated in the following section. Three initial hyper-parameters [127] are needed to start the BSBL algorithm. A reasonable estimation for these three parameters is also explained in the following section. To this end, the BSBL framework along with the wavelet transform is used to find the new values for those three parameters and the new NDP in the wavelet domain. The BSBL solver is terminated when a certain convergent

criterion is satisfied. The details of the BSBL framework will be shown in the following section. An inverse wavelet transform is then applied to convert the new estimated of NDP to the original domain. The new estimated $\mathcal{X}^{new}$ is judged in the convergent criterion and used to replace the previous estimate if the convergent condition is not satisfied, and the whole process is thus repeated again. The details of the algorithm are explained hereafter.

4.1.1 Born Iterative Method Framework

Born iterative method (BIM) [75] is the fundamental framework of the proposed technique. The inverse scattering problem under the scenario shown in Figure 4.1 can be formulated as [74]:

$$E_{tot}^{q}(r) = E_{inc}^{q}(r) - \frac{jk_s^2}{4}\iint_V [\mathcal{X}(r') - 1]E_{tot}^{q}(r')H_0^{(2)}(k_s\rho)dr', r \in S;\ r' \in V; q = 1, \dots, Q \qquad (4.2)$$

where $E_{tot}^{q}(r)$ is the total electric field due to the qth known incident wave, $E_{inc}^{q}(r)$ is the incident electric field of the qth incident source, $\rho = \|r' - r\|$ and k_s can be expressed as:

$$k_s = \sqrt{\omega^2\mu_o\varepsilon_o\varepsilon_s - \frac{j\omega\mu_o\sigma_s}{\varepsilon_o}} \qquad (4.3)$$

ε_o and μ_o are permittivity and permeability of free space. $H_0^{(2)}(k_s\rho)$ is the zero order Hankel function. Equation (4.2) can be re-written in an operator form as [128]:

$$E_{tot}^{q}(r) = E_{inc}^{q}(r) + A_i\left(\mathcal{X}E_{tot}^{q}\right) = (I - A_i\mathcal{D})^{-1}E_{inc}^{q}(r), r \in S; q = 1, \dots, Q \qquad (4.4)$$

where A_i is the integral operator, I is the identity operator and $\mathcal{D}$ is the diagonal operator. Based on the value of $\|A_i\mathcal{D}\|$, the equation (4.4) can be represented in Born series [128]-[129]. When $\|A_i\mathcal{D}\| \ll 1$, the Born series representation becomes Born approximation which means $E_{tot}^{q}(r)$ can be directly approximated as $E_{inc}^{q}(r)$. However, in the realistic situation, $\|A_i\mathcal{D}\|$ is not strictly satisfy Born approximation condition ($\|A_i\mathcal{D}\| \ll 1$), thus solving the above inverse scattering problem (4.2) based on this approximation is not accurate.

Born iterative method (BIM) and distorted Born iterative method (DBIM) are two alternative methods which can be used to solve (4.2). The differences of these two methods are, the kernel of the integral (zero order Hankel function) in BIM remains the same for each of the iterations, whereas in DBIM the kernel is upgraded for each of the iterations. The BIM is adopted here since compared with DBIM,

BIM is more robust to noise and consume much less computation time [74]. Since the scattered electric field satisfies the relation $E_{scat}^{q}(r) = E_{tot}^{q}(r) - E_{inc}^{q}$, thus based on BIM and (4.2), $E_{scat}^{q}(r)$ can be expressed as:

$$\tilde{E}_{scat,q}(r) = -\frac{jk_s^2}{4}\iint_V \left[\mathcal{X}^i(r') - 1\right] E_{tot,q}^{i-1}(r') H_0^{(2)}(k_s\rho)dr', r \in S;\ r' \in V; q = 1, \dots, Q \tag{4.5}$$

where $\tilde{E}_{scat,q}(r)$ denotes the measured electric field at the qth antenna, i is the iteration index, $E_{tot,q}^{i-1}(r')$ is the total electric field calculated in the last iteration step and $\mathcal{X}^i(r')$ is the unknown NDP in the current iteration. Based on (4.5) and assume $\epsilon_q(r_m)$ ($r_m \in S, m = 1, \dots, M$) is additive Gaussian noise with zero mean and unknown variance for the mth measurement of the scattered electric field under the qth incident wave, then rearranging (4.5) in a matrix form, an ill-posed equation can be achieved as:

$$\boldsymbol{\mathcal{B}}_q^{i-1}\vec{\mathcal{X}}^i + \vec{\epsilon}_q = \vec{m}_q \tag{4.6}$$

where $\vec{m}_q = \left[\tilde{E}_q(r_1), \dots, \tilde{E}_q(r_M)\right]^T$, $\vec{\epsilon}_q = \left[\epsilon_q(r_1), \dots \epsilon_q(r_M)\right]^T$, $\vec{\mathcal{X}}^i = \left[\mathcal{X}^i(r_1), \dots, \mathcal{X}^i(r_N)\right]$; $r_n \in V, n = 1, \dots, N$, ($M$ is the number of antenna points and N is the number of cells) and $\boldsymbol{\mathcal{B}}_q^{i-1}$ is the matrix calculated in the last iteration under the qth incident wave. The elements in $\boldsymbol{\mathcal{B}}_q^{i-1}$ are:

$$b_{mn} = \frac{-jk_s^2}{4}\iint_{V_n} E_{tot,q}^{i-1}(r_n')H_0^{(2)}(k_s\rho)dr' \tag{4.7}$$

where $\rho = \|r_n' - r_m\|$. The surface integral in (4.7) can be numerically calculated by using Richmond's technique proposed in [77]. To somehow alleviate the ill-posedness in (4.6), one method is to increase the number of measurement antennas M and apply some regularization scheme to minimize the spurious solutions. In [50], 32 antennas are used for the measurement and Tikhonov's regularization scheme [78] is used in the final least square optimization. However, the method in [50] request huge computation time for the convergence (~250 min) and this is not acceptable in realistic application. Therefore, a probabilistic method based on block sparse Bayesian learning by using less number of antennas ($M = 6$) is proposed and illustrated in the following sections.

4.1.2 Wavelet Transform

The ill-posed equation (4.6) can be solved using compressive-sensing Bayesian-based probabilistic methods [117]-[119] which require a sparse $\vec{\mathcal{X}}$ for a convergent solution. However, the sparsity of $\vec{\mathcal{X}}$ is not possessed in many realistic situations, such as in biomedical imaging. Thus, it is necessary to transform the non-sparse $\vec{\mathcal{X}}$ into a sparse domain where the Bayesian-based probabilistic method can be applied. The wavelet transform is a suitable candidate for the sparse transformation due to the relative smooth characteristic of the normalized dielectric profile (NDP) with weak scatter ($\mathcal{X}(x,y)$ has close values in the cells of the target area). The discrete signal $f[n]$ can be approximated as [130]:

$$f[n] = \frac{1}{\sqrt{M}} \sum_{k} W_{\phi}[j_0, k]\, \phi_{j_0,k}[n] + \frac{1}{\sqrt{M}} \sum_{j=j_0}^{\infty} \sum_{k} W_{\psi}[j,k] \psi_{j,k}[n] \tag{4.8}$$

where $\phi_{j_0,k}[n]$ is discrete scaling function defined as:

$$\phi(t) = \begin{cases} 1 & 0 \le t \le 1 \\ 0 & otherwise \end{cases} \tag{4.9}$$

and $\psi_{j,k}[n]$ is discrete wavelet function defined as:

$$\psi(t) = \begin{cases} 1 & 0 \le t < \frac{1}{2} \\ -1 & \frac{1}{2} \le t < 1 \\ 0 & otherwise \end{cases} \tag{4.10}$$

Since the scaling functions and wavelet functions are orthogonal to each other, thus the wavelet coefficients can be calculated as [130]:

$$W_{\phi}[j_0, k] = \frac{1}{\sqrt{M}} \sum_{n} f[n] \phi_{j_0,k}[n] \tag{4.11}$$

$$W_{\psi}[j,k] = \frac{1}{\sqrt{M}} \sum_{n} f[n] \psi_{j,k}[n]\,, j \ge j_0 \tag{4.12}$$

In (4.11), $W_{\phi}[j_0, k]$ is the approximation coefficient and in (4.10), $W_{\psi}[j,k]$ is the detailed coefficient. To verify that the wavelet transformation can transform the low-contrast NDP into a sparse wavelet domain, a simple model with low-contrast NDP is firstly built to test the transformation and it is

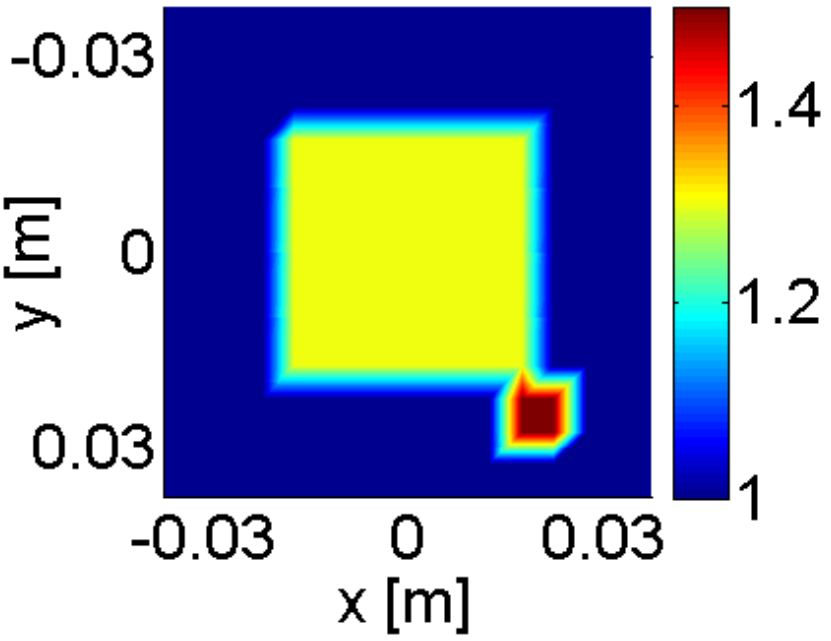

Fig 4. 3: The non-sparse model used to test the wavelet transformation

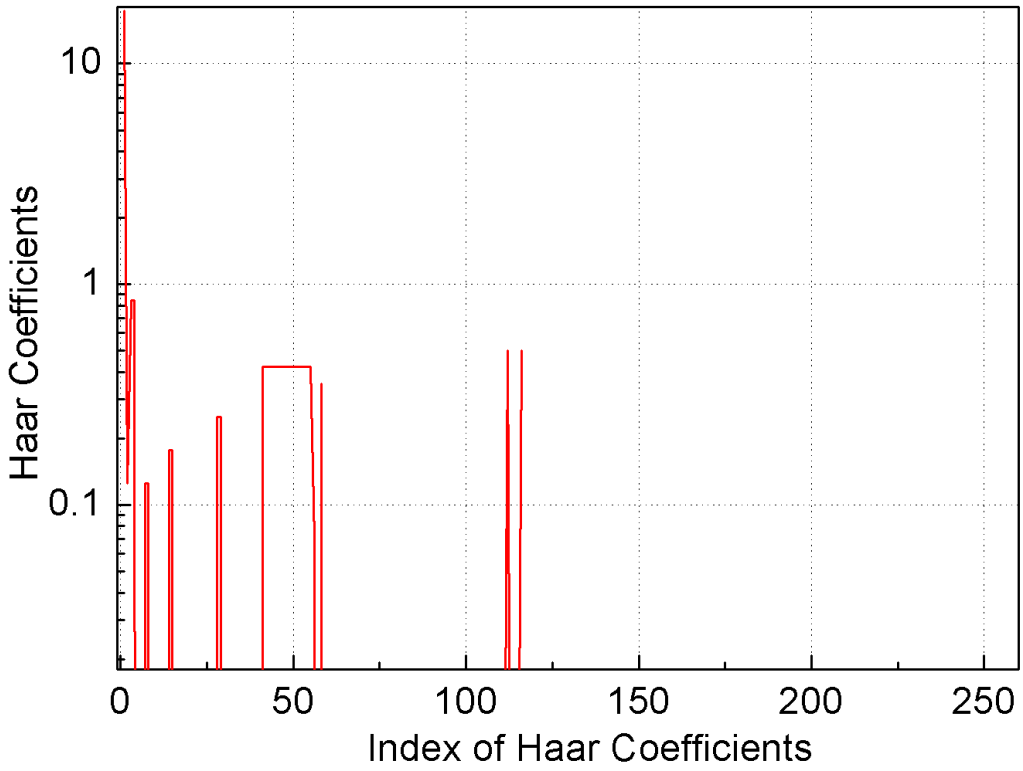

Fig 4. 4: The Haar wavelet coefficients (one-dimensional representation) for the non-sparse model used to assess the proposed imaging shceme

shown in Figure 4.3. The non-sparse model has the dimensions of 80 $mm \times 80\ mm$ ($0.4\lambda_o \times 0.4\lambda_o$), where λ_o is the wavelength in free space at the central frequency ($f = 1.5\ GHz$). The investigation

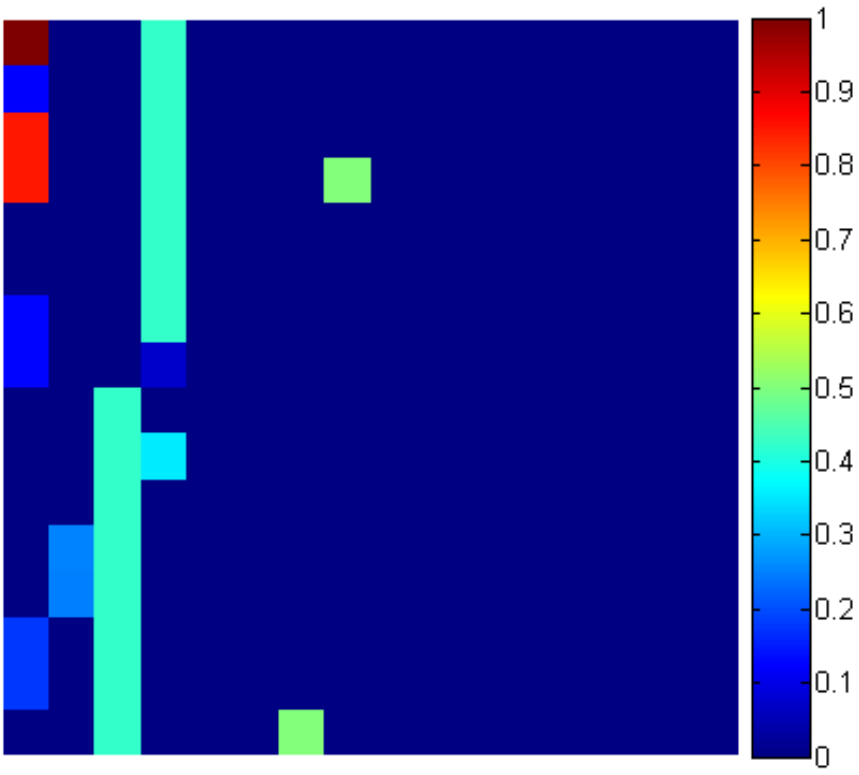

Fig 4. 5: The Haar wavelet coefficients (two-dimensional representation) for the non-sparse model used to assess the proposed imaging scheme.

domain is discretized with $N = 16 \times 16$ grids; the size of each grid is $5\ mm \times 5\ mm$. A square with size of $40\ mm \times 40\ mm$ and contrast of 1.3 is included at the central of the investigation domain. This square can be regarded as the background in a realistic imaging application. Another square with size of $10\ mm \times 10\ mm$ and contrast of 1.5 is positioned at the right corner of the former one. This small square can be considered as the target to be detected. It is worth mentioning that the contrast between the target and the background is only 1.15:1, which is a very low value indicating a challenging imaging problem.

The non-sparse model shown in Figure 4.3 is represented using Haar wavelet basis. The one-dimensional representation of Haar wavelet coefficients obtained through transforming the NDP of the non-sparse model in the wavelet domain is shown in Figure 4.4 and the two-dimensional representation is shown in Figure 4.5. It is indicated from Figure 4.4 and 4.5 that the number of non-zero Haar wavelet coefficients is 29. Since the length of the entire Haar basis is 256 in this case, the sparsity of the model after the Haar wavelet transformation is $(256 - 29)/256 = 89\%$. This sparsity value implies the potential for the original NDP to be reconstructed using the proposed algorithm.

To further prove that wavelet transformation can transform the non-sparse NDP of human brain into a sparse domain, a realistic head model acquired from MRI scans [79] is used to test the transformation. The head model consists of $128 \times 128 \times 128$ cubical elements; each has the

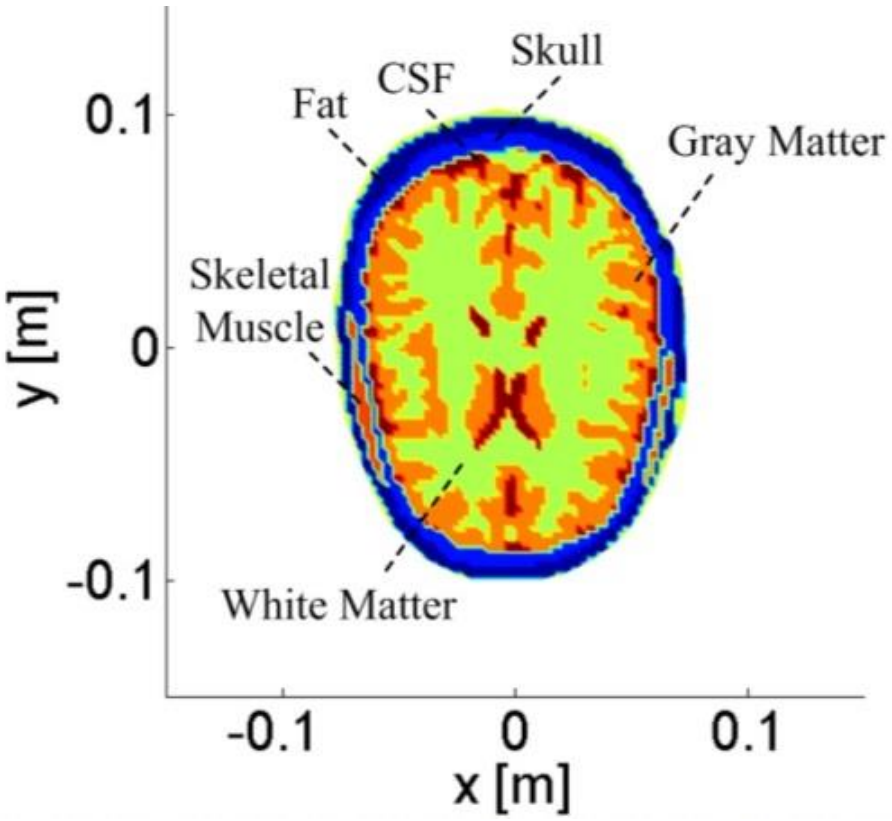

Fig 4. 6: The realistic head model used to test the wavelet transformation

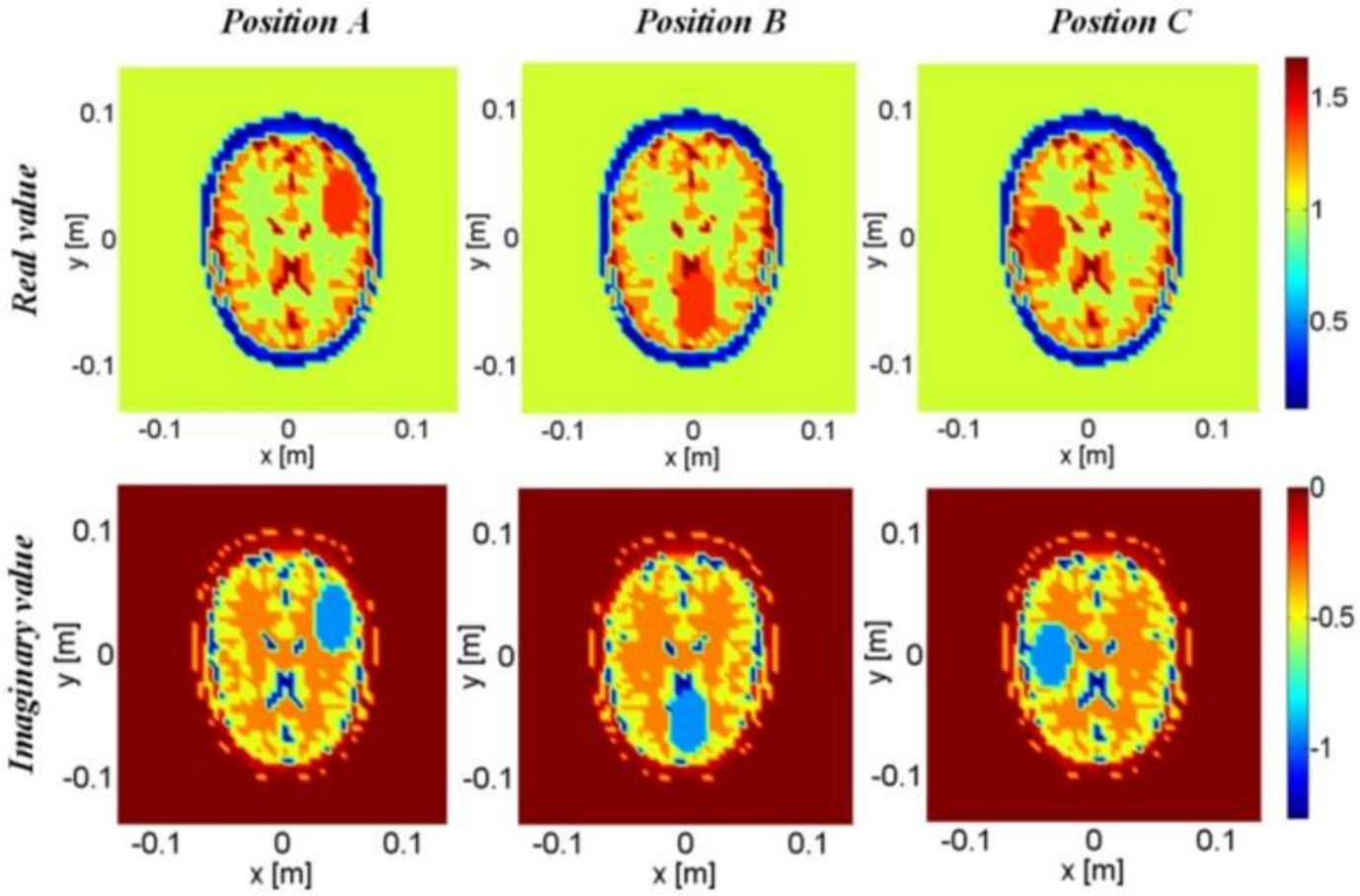

Fig 4. 7: Normalized dielectric profile (NDP) of the realistic head phantom with a hemorrhagic stroke located at different positions.

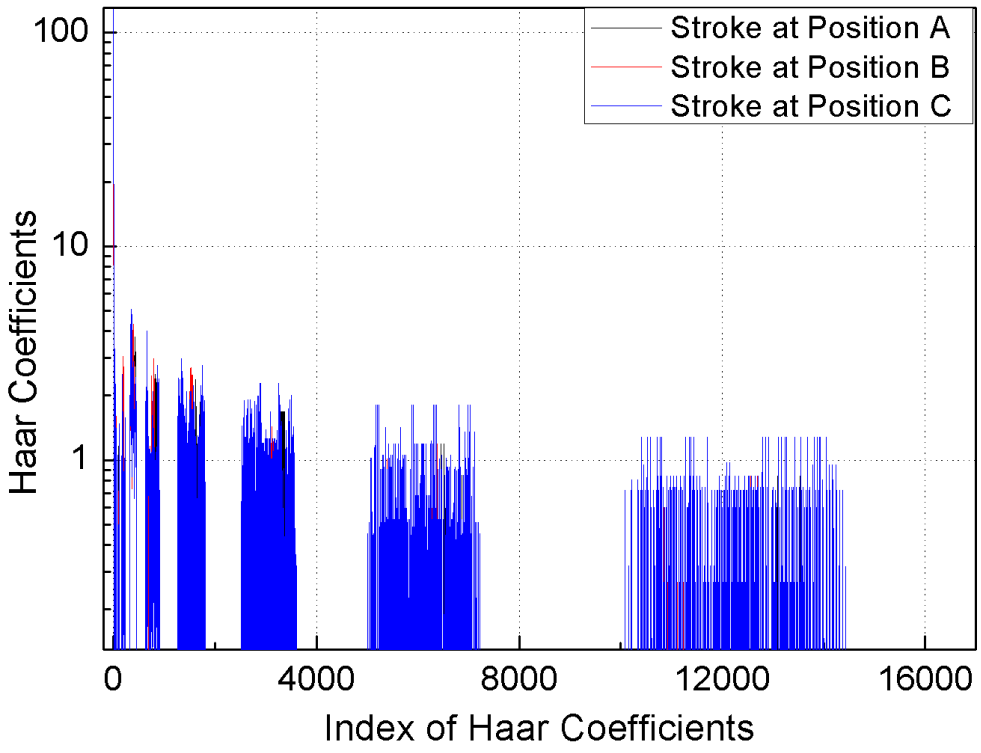

Fig 4. 8: The Haar wavelet coefficients (one-dimensional representation) for the head model with a hemorrhagic stroke placed at three different positions.

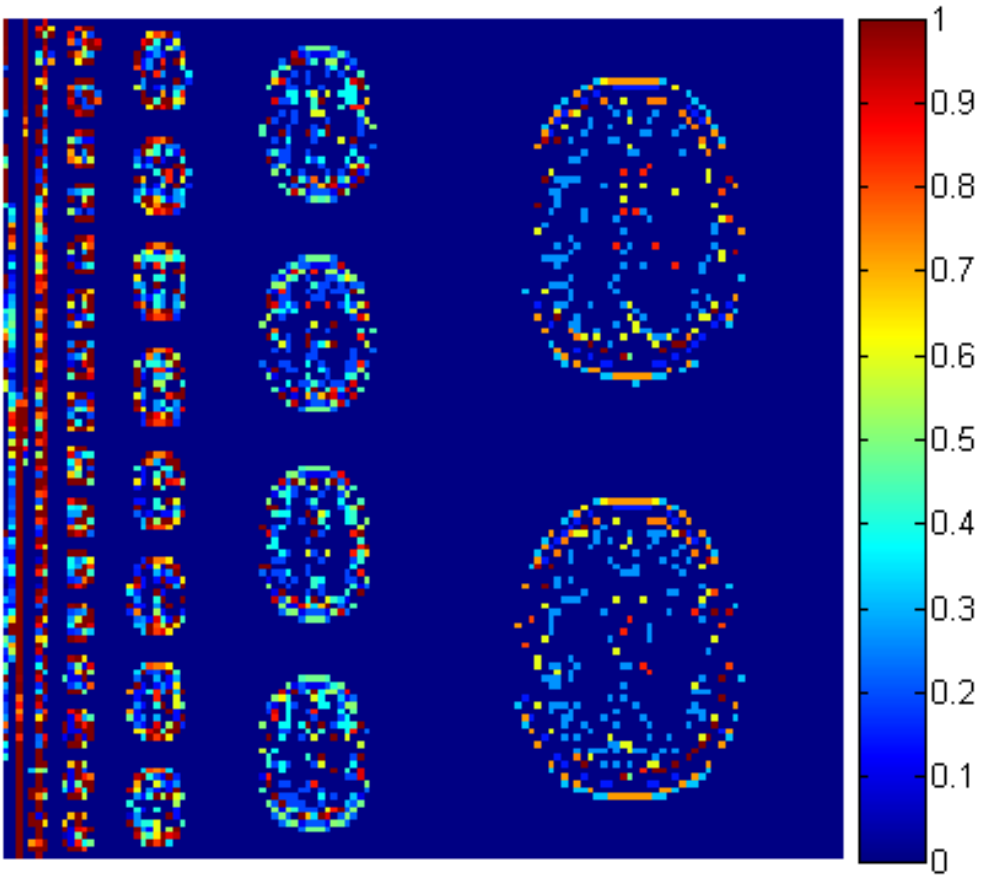

Fig 4. 9: The Haar wavelet coefficients (two-dimensional representation) for the head model with a hemorrhagic stroke placed at three different positions.

dimensions (mm) of 1.1 × 1.1 × 1.4. A transverse slice of the model at around 30 mm from the top of the head is shown in Figure 4.6. The seven main head tissues are included in the model; skin, skull, skeletal muscle, fat, blood, dura, cerebral spinal fluid (CSF), gray and white matter. These tissues were assumed to have the realistic dielectric properties as a function of frequency [80]. Figure 4.7 shows the NDP of the use head model. An elliptical hemorrhagic stroke was placed at different positions (A: x=2 cm, y=1.5 cm, B: x=0 cm, y=2.5 cm, C: x= 1.5 cm, y=0 cm) with a major axis of 5.5 cm and minor axis of 1.6 cm. The selected size of the stroke is chosen based on the available data from MRI and CT scans. The wavelet transformation is implemented on the head models A, B and C, respectively. The one-dimensional wavelet coefficients for the three head models are shown in Figure 4.8 (in log scale) and the two-dimensional representations are shown in Figure 4.9. It can be seen from Figure 4.8 and 4.9 that the transformed NDP of the head model exhibits a sparse characteristic with respect to the Haar wavelet coefficients. The numbers of the non-zero Haar coefficients for the head model with stroke placed at positions A, B and C are 2613, 2615 and 2572, respectively. Knowing that the length of the Haar basis is 16384 in these three cases, the Haar basis sparsity of these three cases can be found as 84.05%, 84.03% and 84.3%, respectively. These sparsity values imply the potential for the original NDP of the head model with stroke to be successfully reconstructed using the proposed scheme.

4.1.3 Block-Sparse Bayesian Learning

The ill-posed equation (4.6) can be solved using a probabilistic method based on block sparse Bayesian learning (BSBL) [126]-[127] that needs a small number of antennas and short convergent time. To use BSBL method, a sparse representation of $\vec{\chi}$ is required for achieving a convergent solution. However, the sparsity of $\vec{\chi}$ is not possessed in many realistic situations, such as in biomedical imaging. Thus, it is necessary to transform the non-sparse $\vec{\chi}$ into a sparse domain where the Bayesian-based probabilistic method can be applied. The wavelet transformation which was introduced in the last section is a suitable candidate for the sparse transformation due to the relative smooth characteristic of the normalized dielectric profile (NDP) with weak scatter ($\vec{\chi}(x, y)$ has close values in the cells of the target area). The validity of using wavelet transformation to transform the non-sparse NDP of human head into a sparse wavelet domain has been proved in the last section. Through using Haar-based wavelet transformation, the equation (4.6) can be re-written as:

$$\boldsymbol{\mathcal{B}}_q^{i-1}\boldsymbol{\mathcal{W}}^{-1}\vec{s}^{\,i} + \vec{\epsilon}_q = \vec{m}_q \tag{4.13}$$

where $\boldsymbol{\mathcal{W}}^{-1}$ is the inverse wavelet transform matrix and $\vec{s}$ is the sparse representation of $\vec{\mathcal{X}}$ in the wavelet domain. Equation (4.13) can be re-written as:

$$\boldsymbol{\phi}_q^{i-1}\vec{s}^{\,i} + \vec{\epsilon}_q = \vec{m}_q \tag{4.14}$$

where $\boldsymbol{\phi}_q^{i-1} = \boldsymbol{\mathcal{B}}_q^{i-1}\boldsymbol{\mathcal{W}}^{-1}$. In (4.14), $\vec{m} \in \mathcal{R}^{M\times 1}$ is the known measurement vector, $\boldsymbol{\phi} \in \mathcal{R}^{M\times N}$ ($M \ll N$) is the dictionary matrix and $\vec{s} \in \mathcal{R}^{N\times 1}$ is the sparse vector to be recovered.

The block/group structure [131]-[132] can be utilized to solve the ill-posed model given by (4.14). To that end, $\vec{s}$ can be considered as consisting of K blocks:

$$\vec{s} = [\vec{s}_1^{\,T}, \dots, \vec{s}_k^{\,T}, \dots, \vec{s}_K^{\,T}]^T \tag{4.15}$$

If we assume the length of each block l, then the kth block of $\vec{s}$ is represented as:

$$\vec{s}_k^{\,T} = \left[s_{(k-1)\times l+1}, \dots, s_{k\times l}\right] \tag{4.16}$$

The block structure of $\vec{s}$ has a sparse characteristic which means only p ($p \ll K$) blocks are nonzero but at unknown positions. Based on (4.15) and [126]-[127], each block $\vec{s}_k \in \mathcal{R}^{l\times 1}$ is assumed to have a multivariate Gaussian distribution as:

$$p(\vec{s}_k;\, t_k, \boldsymbol{\mathcal{C}}_k) = \frac{1}{\sqrt{(2\pi)^l|\boldsymbol{\Sigma_k}|}}\exp\left(-\frac{1}{2}\vec{s}_k^{\,T}\boldsymbol{\Sigma}_k^{-1}\vec{s}_k\right) \tag{4.17}$$

where $|\boldsymbol{\Sigma_k}|$ is the determinant of $\boldsymbol{\Sigma_k}$ and $\boldsymbol{\Sigma}_k = t_k\boldsymbol{\mathcal{C}}_k$. t_k is a nonnegative parameter which can be used to control the sparsity of $\vec{s}_k$. $\boldsymbol{\mathcal{C}}_k \in \mathcal{R}^{l\times l}$ is a positive-definite matrix which exhibits the correlation of the kth block. Because the diagonal elements in $\boldsymbol{\Sigma_k}$ represent the variant of each member in $\vec{s}_k$, $\vec{s}_k$ becomes zero when $t_k = 0$ (notice that the mean of $\vec{s}_k$ is zero based on (4.17)). Assuming that the noise vector $\vec{\epsilon}$ satisfies the Gaussian distribution with $p(\vec{\epsilon}|\delta)\sim\mathcal{N}(0, \delta I)$ where δ is a positive scalar, the posterior of $\vec{s}$ is given by [133]:

$$p\left(\vec{s}\middle|\vec{m}, \delta, \{t_k, \boldsymbol{\mathcal{C}}_k\}_{k=1,\dots,K}\right) = \frac{1}{\sqrt{(2\pi)^N|\boldsymbol{\Sigma_x}|}} \times \exp\left(-\frac{1}{2}\left(\vec{s}-\vec{\mu}_x\right)^T\boldsymbol{\Sigma_x}^{-1}\left(\vec{s}-\vec{\mu}_x\right)\right) \tag{4.18}$$

$$\vec{\mu}_x = \frac{1}{\delta}\boldsymbol{\Sigma_x}\boldsymbol{\phi}^{\boldsymbol{T}}\vec{m} \tag{4.19}$$

$$\boldsymbol{\Sigma_x} = \left(\boldsymbol{\Sigma}_o{}^{-1} + \frac{1}{\delta}\boldsymbol{\phi}^{\boldsymbol{T}}\boldsymbol{\phi}\right)^{-1} \tag{4.20}$$

where

$$\boldsymbol{\Sigma}_o = diag\{t_1\boldsymbol{\mathcal{C}}_1, \dots, t_K\boldsymbol{\mathcal{C}}_K\} \tag{4.21}$$

Therefore, after the hyper-parameters δ and $\{t_k, \boldsymbol{\mathcal{C}}_k\}_{k=1,\dots,K}$ are determined, the sparse vector $\vec{s}$ (the sparse representation of $\vec{X}$) can be decided as the mean of the posterior, which means $\vec{s} = \vec{\mu}_x$. In [134], it is indicated that over fitting emerges if different covariance matrices $\boldsymbol{\mathcal{C}}_k$ are assigned to different blocks $\vec{s}_k$. To avoid this situation, only one positive definite matrix $\boldsymbol{\mathcal{C}}$ is used to model each of the blocks $\vec{s}_k$.

Equation (4.20) indicates that:

$$\boldsymbol{\Sigma}_x = \left(\boldsymbol{\Sigma}_o{}^{-1} + \frac{1}{\delta}\boldsymbol{\phi}^T\boldsymbol{I}\boldsymbol{\phi}\right)^{-1} \tag{4.22}$$

Using the matrix identity:

$$(A + CBC^T)^{-1} = A^{-1} - A^{-1}C(B^{-1} + C^TA^{-1}C)^{-1}CA^{-1} \tag{4.23}$$

(4.22) can be rearranged as:

$$\boldsymbol{\Sigma}_x = \boldsymbol{\Sigma}_o - \boldsymbol{\Sigma}_o\boldsymbol{\phi}^T(\delta\boldsymbol{I} + \boldsymbol{\phi}\boldsymbol{\Sigma}_o\boldsymbol{\phi}^T)^{-1}\boldsymbol{\phi}\boldsymbol{\Sigma}_o \tag{4.24}$$

Substituting (4.24) in the expression of $\vec{\mu}_x$, one can achieve

$$\vec{\mu}_x = \left(\boldsymbol{\Sigma}_o\boldsymbol{\phi}^T - \boldsymbol{\Sigma}_o\boldsymbol{\phi}^T\left(\delta\boldsymbol{I} + \boldsymbol{\phi}\boldsymbol{\Sigma}_o\boldsymbol{\phi}^T\right)^{-1}\boldsymbol{\phi}\boldsymbol{\Sigma}_o\boldsymbol{\phi}^T\right)\vec{m} \tag{4.25}$$

Using the matrix identity:

$$(I + AB)^{-1}A = A(I + BA)^{-1} \tag{4.26}$$

$$(I + AB)^{-1} = I - A(I + BA)^{-1}B \tag{4.27}$$

(4.25) can be re-written as:

$$\vec{\mu}_x = \boldsymbol{\Sigma}_o\boldsymbol{\phi}^T(\boldsymbol{I} - \boldsymbol{\phi}\boldsymbol{\Sigma}_o\boldsymbol{\phi}^T(\delta\boldsymbol{I} + \boldsymbol{\phi}\boldsymbol{\Sigma}_o\boldsymbol{\phi}^T)^{-1})\vec{m} = \boldsymbol{\Sigma}_o\boldsymbol{\phi}^T(\delta\boldsymbol{I} + \boldsymbol{\phi}\boldsymbol{\Sigma}_o\boldsymbol{\phi}^T)^{-1}\vec{m} \tag{4.28}$$

$$\vec{\mu}_x \to \vec{s} \tag{4.29}$$

Assuming the hyper-parameters as $H = \{t_1, \dots, t_K, \boldsymbol{\mathcal{C}}, \delta\}$, the expectation maximization method (EM) [126]-[127] seeks to maximize the $\mathcal{O}$ function which treats $\vec{s}$ as hidden variables as shown below:

$$\mathcal{O}(H|H^{old}) = E_{\vec{s}|\vec{m};H^{old}}[\log L(\vec{m}, \vec{s};\ H)] = E_{\vec{s}|\vec{m};H^{old}}[\log p(\vec{m}|\vec{s};\delta)]$$

$$+E_{\vec{s}|\vec{m};H^{old}}[\log p(\vec{s};\ t_1, \dots, t_K, \boldsymbol{\mathcal{C}})] \tag{4.30}$$

where H^{old} is the value of the hyper-parameters from the last iteration. Aiming to estimate $\boldsymbol{t}$=$[t_1, \dots, t_K]$ and $\boldsymbol{\mathcal{C}}$ which can maximize (4.30) by using the derivative of $\mathcal{O}(H|H^{old})$, the first term in (4.30) can be ignored since it is not related to $\boldsymbol{t}$ and $\boldsymbol{\mathcal{C}}$. Recall that

$$p(\vec{s};\ t_1, \dots, t_K, \boldsymbol{\mathcal{C}}) = \frac{1}{\sqrt{(2\pi)^{Kl}|\boldsymbol{\Sigma}_o|}} exp\left(-\frac{1}{2}\vec{s}^T\boldsymbol{\Sigma}_o^{-1}\vec{s}\right) \tag{4.31}$$

where $\boldsymbol{\Sigma}_o = \boldsymbol{\mathcal{T}} \otimes \boldsymbol{\mathcal{C}}$ and $\boldsymbol{\mathcal{T}} = diag(t_1, \dots, t_K)$. $\boldsymbol{A}\otimes\boldsymbol{B}$ represents the Kronecker product of the two matrices $\boldsymbol{A}$ and $\boldsymbol{B}$. Take the logarithm of (4.31) one can obtain

$$\log p(\vec{s};\ \boldsymbol{t}, \boldsymbol{\mathcal{C}}) \propto -\frac{1}{2}\log(|\boldsymbol{\mathcal{T}}|^l|\boldsymbol{\mathcal{C}}|^K) - \frac{1}{2}\vec{s}^T(\boldsymbol{\mathcal{T}}^{-1}\otimes\boldsymbol{\mathcal{C}}^{-1})\vec{s} \tag{4.32}$$

The notation of $\propto$ indicates that the terms which do not contribute to the next optimization process of the parameters are dropped. The derivation of (4.32) used some identities of linear algebra as shown below:

$$(\boldsymbol{A}\otimes\boldsymbol{B})^{-1} = \boldsymbol{A}^{-1}\otimes\boldsymbol{B}^{-1} \tag{4.33}$$

$$det(\boldsymbol{A}\otimes\boldsymbol{B}) = \det(\boldsymbol{A})^{rank(\boldsymbol{B})}det(\boldsymbol{B})^{rank(\boldsymbol{A})} \tag{4.34}$$

Substituting (4.32) into (4.30),

$$\mathcal{O}(\boldsymbol{t}, \boldsymbol{\mathcal{C}}) \propto -\frac{l}{2}\log(|\boldsymbol{\mathcal{T}}|) - \frac{K}{2}\log(|\boldsymbol{\mathcal{C}}|) - \frac{1}{2}Tr\left[(\boldsymbol{\mathcal{T}}^{-1}\otimes\boldsymbol{\mathcal{C}}^{-1})\left(\boldsymbol{\Sigma}_x + \vec{\mu}_x\vec{\mu}_x{}^T\right)\right] \tag{4.35}$$

where $\boldsymbol{\Sigma}_x$ and $\vec{\mu}_x$ are the covariance matrix and mean value of $\vec{s}$, respectively. They are calculated from (4.19)-(4.20) using the old value of H (the value from the last iteration). Notice that in (4.35), $p(\vec{s}|\vec{m}; H^{old})$ is dropped since tis value only depends on the old value of H; thus it is not related to the next optimization of H. To estimate the values of $\boldsymbol{t}$ which can maximize (4.32), the derivative of (4.35) with regard to $\boldsymbol{t}$ is

$$\frac{\partial \mathcal{O}}{\partial t_k} = -\frac{l}{2t_k} + \frac{1}{2{t_k}^2} Tr[\boldsymbol{\mathcal{C}}^{-1}(\boldsymbol{\Sigma}_x^k + \vec{\mu}_x^k(\vec{\mu}_x^k)^T)] \tag{4.36}$$

By setting (4.36) equal to zero, the estimation of t_k can be achieved as

$$t_k = \frac{1}{l} Tr[\boldsymbol{\mathcal{C}}^{-1}(\boldsymbol{\Sigma}_x^k + \vec{\mu}_x^k(\vec{\mu}_x^k)^T)] \tag{4.37}$$

where $\vec{\mu}_x^k \in \mathcal{R}^{l\times 1}$ is the kth block in $\vec{\mu}_x$ and $\boldsymbol{\Sigma}_x^k \in \mathcal{R}^{l\times l}$ is the kth principle diagonal block in $\boldsymbol{\Sigma}_x$.

To estimate $\boldsymbol{\mathcal{C}}$, the derivative of (4.35) in regard to $\boldsymbol{\mathcal{C}}$ can be expressed as

$$\frac{\partial \mathcal{O}}{\partial \boldsymbol{\mathcal{C}}} = -\frac{K}{2}\boldsymbol{\mathcal{C}}^{-1} + \frac{1}{2}\sum_{k=1}^{K}\frac{1}{t_k}\boldsymbol{\mathcal{C}}^{-1}(\boldsymbol{\Sigma}_x^k + \vec{\mu}_x^k(\vec{\mu}_x^k)^T)\boldsymbol{\mathcal{C}}^{-1} \tag{4.38}$$

The derivation of (4.38) uses the following identities:

$$\frac{\partial ln|det(\boldsymbol{X})|}{\partial \boldsymbol{X}} = (\boldsymbol{X}^{-1})^T \tag{4.39}$$

$$\frac{\partial Tr(\boldsymbol{A}\boldsymbol{X}^{-1}\boldsymbol{B})}{\partial \boldsymbol{X}} = -(\boldsymbol{X}^{-1}\boldsymbol{B}\boldsymbol{A}\boldsymbol{X}^{-1})^T \tag{4.40}$$

Since $\boldsymbol{\mathcal{C}}$ and $\boldsymbol{\Sigma}_x^k$ in (4.38) are symmetric matrices, the transpose is dropped. By setting (4.38) equal to zero, the estimate of $\boldsymbol{\mathcal{C}}$ can be achieved as

$$\boldsymbol{\mathcal{C}} = \frac{1}{K}\sum_{k=1}^{K}\frac{\boldsymbol{\Sigma}_x^k + \vec{\mu}_x^k(\vec{\mu}_x^k)^T}{t_k} \tag{4.41}$$

δ can be estimated using a similar method and in this case the second term in (4.30) is ignored since it is not related to δ.

Recall that $p(\vec{m}|\vec{s};\delta) \sim \mathcal{N}_{\vec{m}|\vec{s}}(\boldsymbol{\phi}\vec{\boldsymbol{s}}, \delta\boldsymbol{I})$, which can be expressed as

$$p(\vec{m}|\vec{s};\delta) = \frac{1}{\sqrt{(2\pi)^M|\delta\boldsymbol{I}|}} e^{\left(-\frac{1}{2}(\vec{m}-\boldsymbol{\phi}\vec{\boldsymbol{s}})^T(\delta\boldsymbol{I})^{-1}(\vec{m}-\boldsymbol{\phi}\vec{\boldsymbol{s}})\right)} \tag{4.42}$$

Thus, the $\mathcal{O}$ function with regard to δ can be expressed as

$$\mathcal{O}(\delta) = E_{\vec{s}|\vec{m};H^{old}}[\log p(\vec{m}|\vec{s};\delta)] \propto -\frac{M}{2}log(\delta) - \frac{1}{2\delta}E_{\vec{s}|\vec{m};H^{old}}[\|\vec{m} - \boldsymbol{\phi}\vec{\boldsymbol{s}}\|_2^2]$$

$$= -\frac{M}{2}log(\delta) - \frac{1}{2\delta}[\|\vec{m} - \boldsymbol{\phi}\vec{\mu}_x\|_2^2 + Tr(\boldsymbol{\Sigma_x}\boldsymbol{\phi}^{\boldsymbol{T}}\boldsymbol{\phi})]$$
$$= -\frac{M}{2}log(\delta) - \frac{1}{2\delta}[\|\vec{m} - \boldsymbol{\phi}\vec{\mu}_x\|_2^2 + \delta^{old}Tr\left(\boldsymbol{\Sigma_x}(\boldsymbol{\Sigma_x^{-1}} - \boldsymbol{\Sigma_o^{-1}})\right)$$
$$= -\frac{M}{2}log(\delta) - \frac{1}{2\delta}[\|\vec{m} - \boldsymbol{\phi}\vec{\mu}_x\|_2^2 + \delta^{old}[N - Tr(\boldsymbol{\Sigma_x}\boldsymbol{\Sigma_o^{-1}})] \quad (4.43)$$

By setting (4.43) equal to zero, the estimation of δ can be achieved as

$$\delta = \frac{\|\vec{m} - \boldsymbol{\phi}\vec{\mu}_x\|_2^2 + \delta^{old}[N - Tr(\boldsymbol{\Sigma_x}\boldsymbol{\Sigma_o^{-1}})]}{M} \quad (4.44)$$

where δ^{old} is the value of δ from the last iteration. Rearranging (4.19)-(4.20) and using some matrix identities, the profile $\vec{\mathcal{X}}$ can be calculated from

$$\vec{\mathcal{X}} = \boldsymbol{\mathcal{W}}^{-1}\boldsymbol{\Sigma}_o\boldsymbol{\phi}^{\boldsymbol{T}}(\delta\boldsymbol{I} + \boldsymbol{\phi}\boldsymbol{\Sigma}_o\boldsymbol{\phi}^{\boldsymbol{T}})^{-1}\vec{m} \quad (4.45)$$

The parameters δ and $\boldsymbol{\Sigma}_o$ can be calculated using (4.37), (4.41) and (4.44). Thus, an iterative algorithm, which iterates between (4.19)-(4.20) and (4.44) is needed until a certain convergent criterion is satisfied. To the end, a reasonable initial guess for the hyper-parameters has to be determined.

As a summary, the procedure of the proposed imaging scheme includes the following steps

1) Obtain the measurement data $\vec{m}_q$ for each observation view ($q = 1, \dots, Q$) and initialize the NDP using the initial estimation $\vec{\mathcal{X}} = [1, \dots, 1]$.

2) Calculate the elements in $\boldsymbol{\mathcal{B}}_q^{i-1}$ by using $\vec{\mathcal{X}}$ and build the Born iterative model.

3) Transfer the original NDP $\vec{\mathcal{X}}$ into a sparse domain $\vec{s}$ by using the wavelet transform. Initialize the hyper-parameters δ and $\{t_k, \boldsymbol{\mathcal{C}}_k\}_{k=1,\dots,K}$ and build the BSBL framework. According to [126]-[127], reasonable initial values for these parameters are $\hat{\delta} = 1 \times 10^{-3}, \hat{t}_k = 1$, and $\hat{\boldsymbol{\mathcal{C}}}$=identity matrix.

4) Use BSBL framework based on expectation-maximization to obtain the new estimated hyper-parameters and $\vec{s}$ (the sparse representation of $\vec{\mathcal{X}}$ in the wavelet domain).

5) If the convergent criterion for the hyper-parameters is satisfied, go to step 6. If it is not satisfied, update the values of the hyper-parameters and go to step 4.

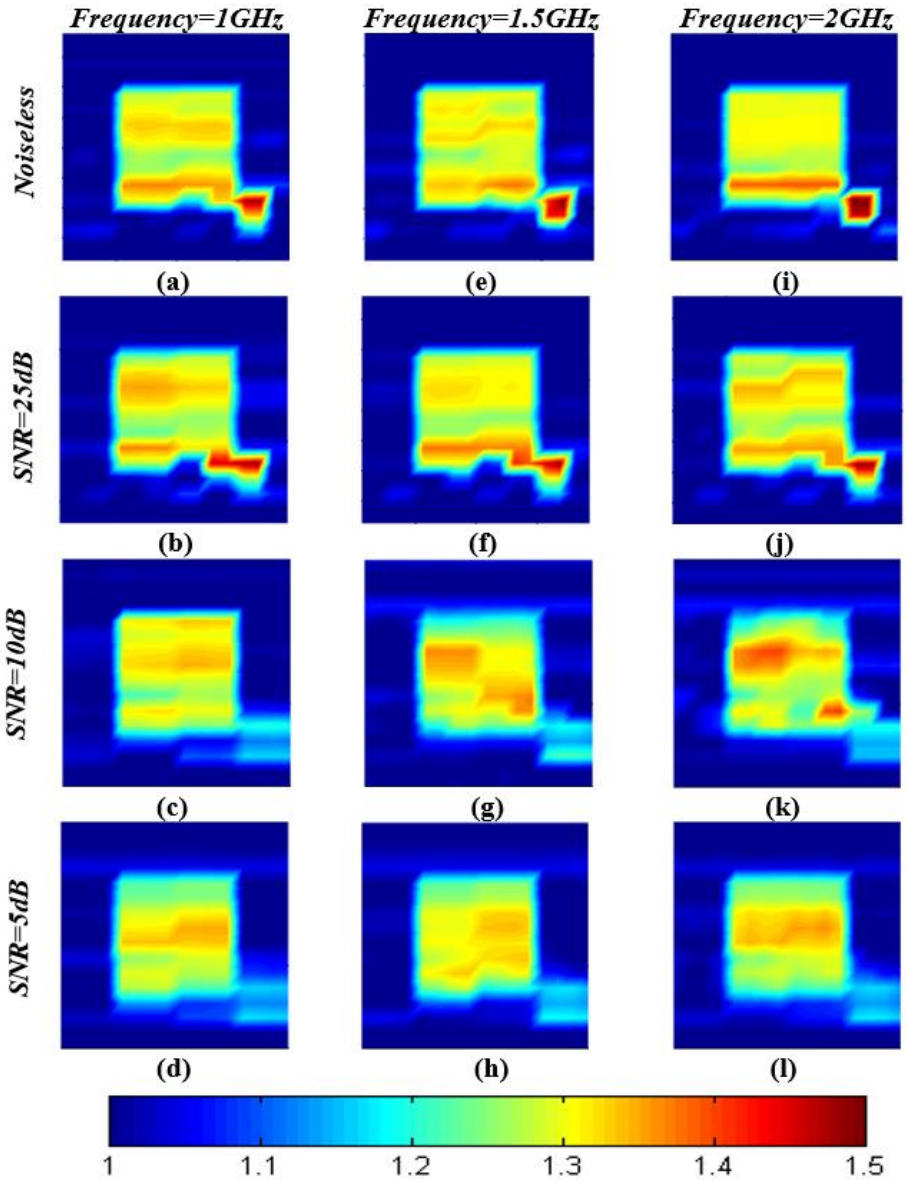

Fig 4. 10: Reconstructed normalized dielectric profile (NDP) using proposed technique at (a)-(d) 1 GHz, (e)-(h) 1.5 GHz, and (i)-(l) 2 GHz with different SNR levels.

6) Use the inverse wavelet transform to transfer the sparse representation of $\overrightarrow{\mathcal{X}}$ back to the original domain then calculate the new profile ($\vec{\mathcal{X}}^{new}$).

7) If the convergent criterion for the profile is satisfied, return $\vec{\mathcal{X}}^{new}$ and end the entire procedure. If it is not satisfied, update $\vec{\mathcal{X}}$ with $\vec{\mathcal{X}}^{new}$ and go to step 2.

4.2 Evaluation on Simple Non-Sparse Model

The proposed algorithm is firstly assessed using a simple non-sparse model as shown in Figure 4.3. The details of this model have been elaborated in the above section. Six (Q=6) uniformly distributed antennas are placed around the investigation domain of Figure 4.3. One antenna is responsible for illuminating the investigation domain, whereas the other five antennas collect the scattered fields.

The model is reconstructed using the proposed imaging scheme under three different frequencies (1 GHz, 1.5 GHz and 2 GHz) and different signal-to-noise (SNR) defined as [81]

$$SNR = 10\log\frac{\|\vec{m}\|^2}{2QM\sigma^2} \tag{4.46}$$

The reconstructed normalized dielectric profiles (NDP) under different incident frequencies and SNR levels are shown in Figure 4.10. It indicates that the NDP of the non-sparse model can be accurately reconstructed using the proposed method for reasonable values of signal-to-noise ratio (SNR), i.e. around 25 dB. For lower values of SNR, the accuracy of reconstructed NDP starts to deteriorate, but the target is still detectable till SNR of around 10 dB. As expected, the resolution of the reconstructed images improves at higher frequencies.

To quantify the performance of the imaging algorithm, the reconstruction normalized error rate (*NER*) is used:

$$NER = \sqrt{\frac{1}{N}\sum_{n=1}^{N}\left|\frac{\mathcal{X}_G(x_n,y_n)-\vec{\mathcal{X}}(x_n,y_n)}{\mathcal{X}_G(x_n,y_n)}\right|^2} \tag{4.47}$$

where $\mathcal{X}_G(x_n,y_n)$ is the NDP of the ground truth, i.e. the real profile. The accuracy of the recovery (*NER*) is calculated using (4.47) and the results are shown in Figure 4.11. It can be seen from Figure 4.11 that the proposed scheme can achieve satisfactory result with the value of NER smaller than 2×10^{-4}. The algorithm can achieve better result when higher frequency is used (the value of NER is better than 1×10^{-4} when 2 GHz incident wave is used). Recall from Figure 4.2 that two iterative processes are involved in the proposed imaging scheme; the internal iteration to estimate the hyper-parameters using expectation-maximization (EM) method and the external iteration to decide if the estimated NDP achieves certain convergent criterion. Therefore, it is important to investigate the convergence performance of the internal and external iterative process. The $\mathcal{O}$ function defined by (4.30) is used to evaluate the convergence rate of the internal iteration, whereas the NER of the estimated NDP is used to evaluate the convergence of the external iterative process. The values of $\mathcal{O}$ and NER at each iteration are shown in Figure 4.12 and 4.13, respectively. The two figures indicate that the $\mathcal{O}$ function and NER converge after 30 and 7 iterations, respectively, at the investigated incident frequencies for both noiseless case and signal to noise ratio (SNR) of 25 dB. Those results indicate that the proposed imaging scheme can achieve a satisfactory convergence rate at both the internal and external iterative processes. To compare the performance of the proposed method with

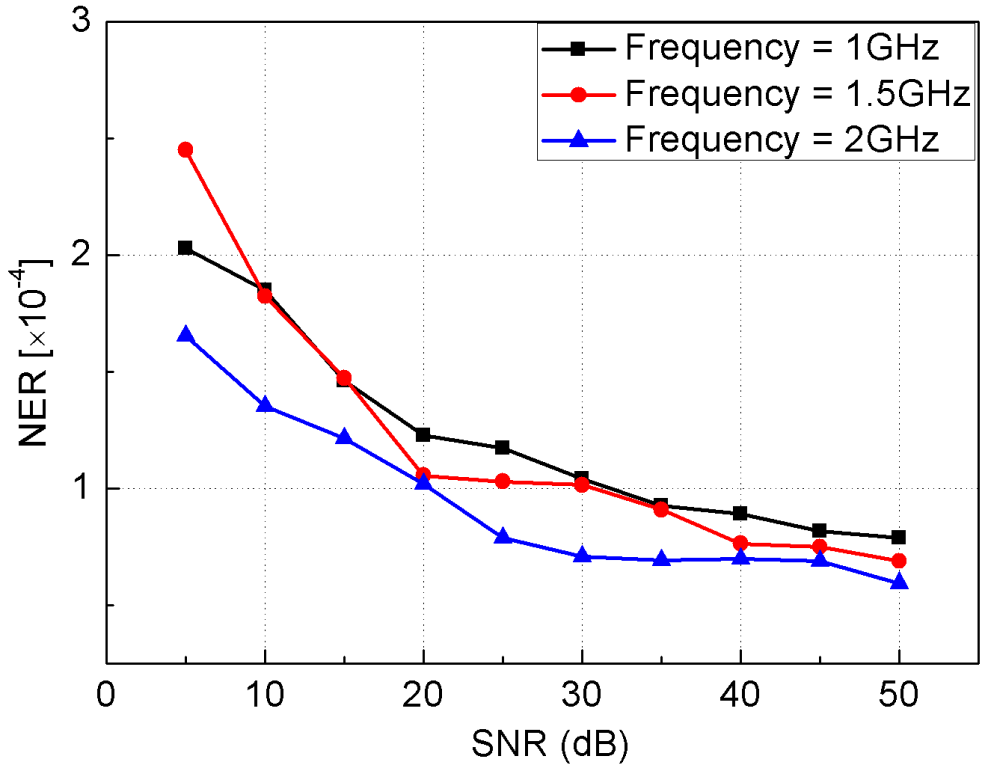

Fig 4. 11: NER performance of the proposed technique versus SNR at different frequencies.

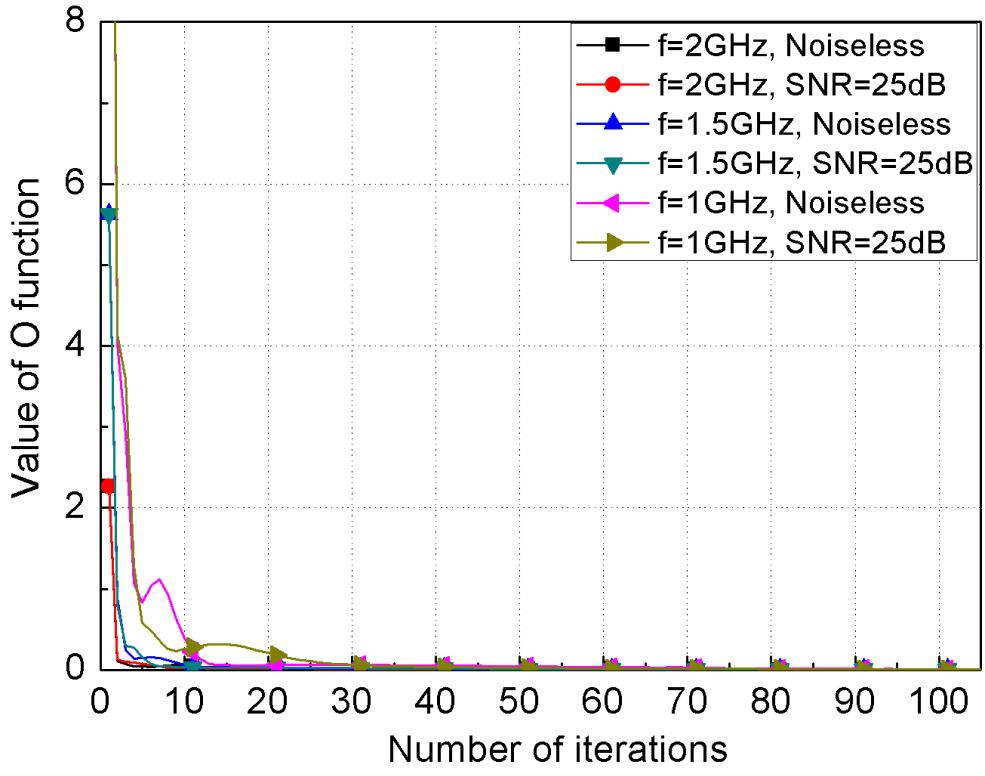

Fig 4. 12: The convergence rate of the expectation-maximization (EM) method used in the internal iteration at different incident frequencies and noise levels.

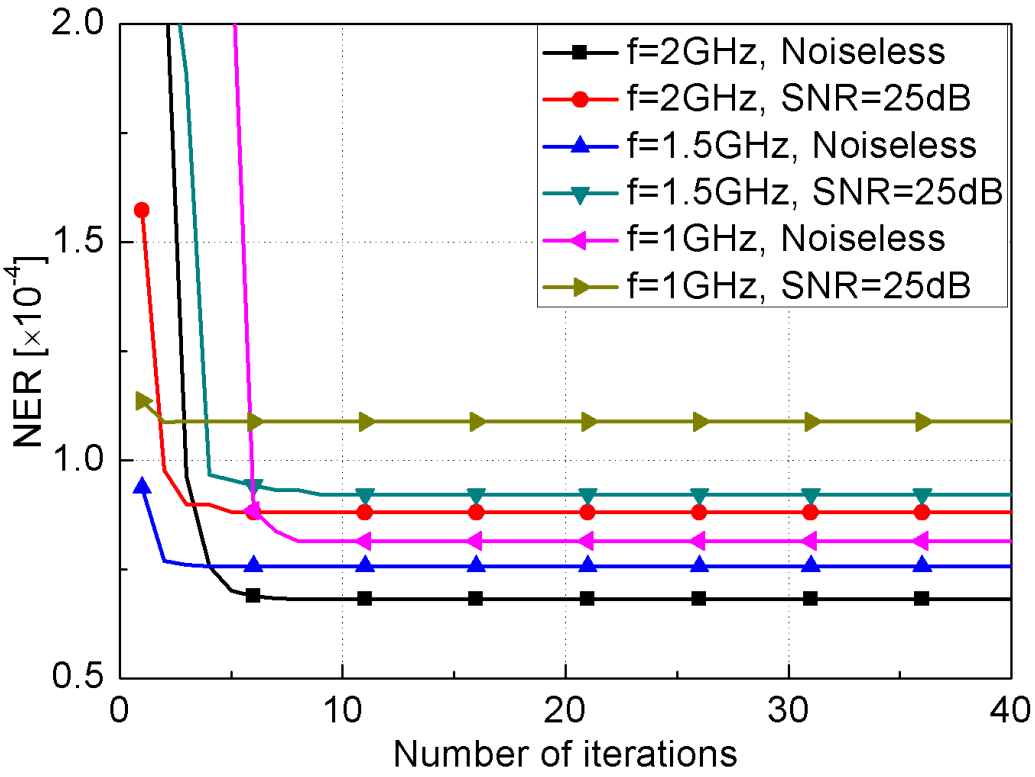

Fig 4. 13: The convergence rate for NER of the estimated NDP in the external iteration at different incident frequencies and noise levels.

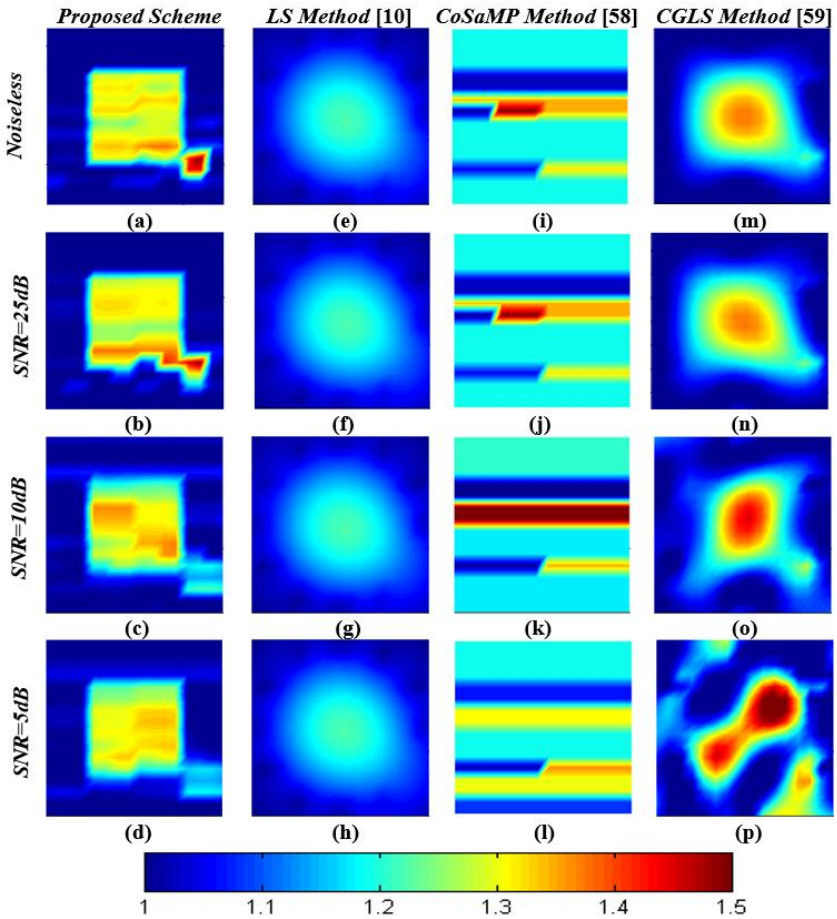

Fig 4. 14: Reconstructed NDP at 1.5 GHz using (a)-(d) proposed, (e)-(h) BIM-LS [50], (i)-(l) CoSaMP [110], and [m]-[p] CGLS methods [135].

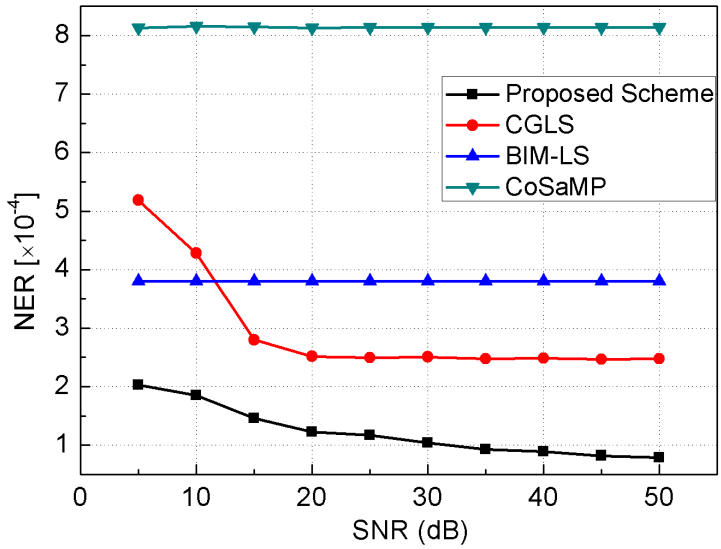

(a)

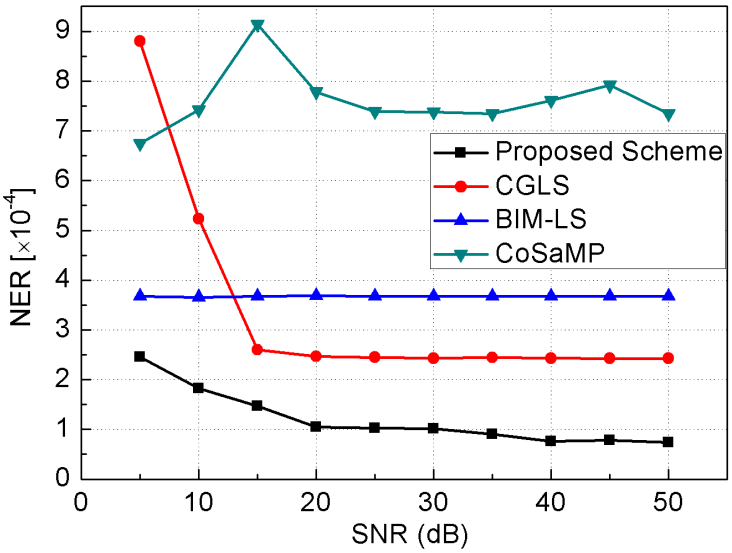

(b)

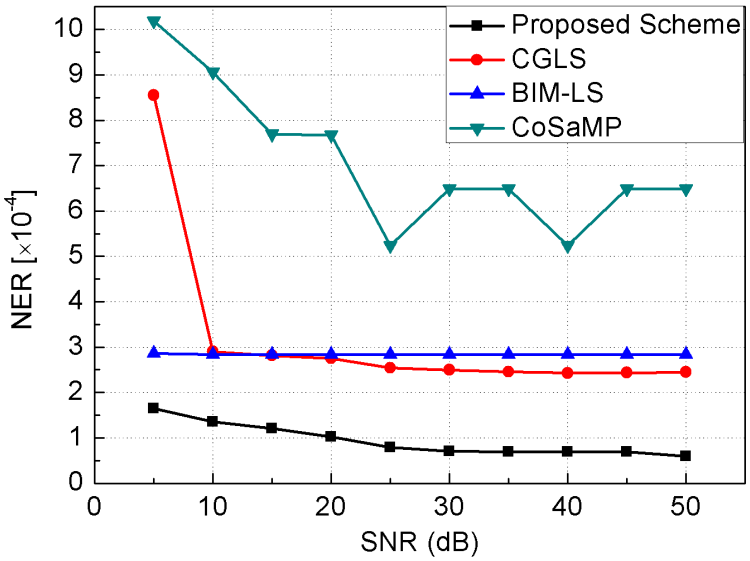

(c)

Fig 4. 15: Performance of different imaging techniques at (a) 1 GHz, (b) 1.5 GHz, and (c) 2 GHz.

other methods, the non-sparse model of Figure 4.3 is reconstructed using three published methods (BIM-LS, CoSaMP, and CGLS) [50], [110], [135] as shown in Figure 4.14. For the Born iterative formulation solved using least square (LS) method, the NDP cannot be recovered accurately because only a small number of antennas (6 in this case) are used in the recovery and thus it suffers from the ill-posedness of the inverse problem. If the CS based method (CoSaMP) is applied on solving (4.13), the non-sparse profile cannot be recovered as that method needs the sparsity of the profile to be initially pre-defined. The common way to pre-define the sparsity of the profile is to take the value of the sparsity as large as possible but less than or equal to 1/3 of the measurement number [136]. Since one of our main targets is to use small number of antenna, i.e. only six antennas, in the proposed model for head imaging, the number of measurements is 36; thus, the maximum sparsity can be pre-defined as 12. Since this value is smaller than the true sparsity of the model, the recovered image using CoSaMP is significantly distorted.

Table 4. 1: Computation time of different methods

Frequency [GHz]	Method	Δt [s]		
		Noiseless	SNR=25 dB	SNR=5 dB
1	This work	14.3	10.2	10.6
	CoSaMP	25	25.8	25.8
	BIM-LS	10.1	10.1	10.3
	CGLS	9.9	9.5	10.3
1.5	This work	11	10.7	11.3
	CoSaMP	28.4	27.1	27.5
	BIM-LS	11.2	10.6	10.3
	CGLS	11.8	11.5	11.5
2	This work	10.6	10.4	10.3
	CoSaMP	25.7	25.1	26.2
	BIM-LS	10.7	11.4	10.6
	CGLS	13.6	13.6	13.4

The conjugate gradient least square (CGLS) method can generate better results compare with BIM-LS and CoSaMP methods. However, it still suffers from the ill-posedness of the inverse problem due to the small number of used antennas (receivers). Additionally, it can be seen from Fig. 4.14 that when the SNR becomes low, such as less than 10 dB, the reconstructed NDP using CGLS method deteriorates significantly compared with BIM-LS and the proposed method.

Figure 4.15 illustrates the NER performance of different methods versus SNR at different frequencies. It can be concluded from Figure 4.15 that the proposed method can achieve much better performance than the other three methods at any environment, i.e. any SNR. The computation time is also a vital issue for NDP recovery problem since in realistic applications, such as in head stroke detection, the time to get imaging results is critical in that emergent scenario. Table 4.1 indicates the computation time required for each of the tested methods. It is clear from Table 4.1 that the computational time of the proposed method is comparable to those of BIM-LS and CGLS. Taking the accuracy of reconstruction and computation time into account, it is possible to conclude from Figure 4.15 and Table 4.1 that the proposed method is more efficient than the other three methods in a realistic imaging environment.

4.3 Evaluation on Numerical Head Phantom

To further assess the proposed imaging scheme, it is tested on microwave-based head imaging using a realistic head model which was elaborated in Figure 4.6, section 4.2.2. Six uniformly distributed antennas were used to irradiate the head model at suitable frequencies and capture the scattered signals. The proposed imaging technique was then used to detect the position of the haemorrhagic stroke in the head model. Figure 4.16-4.18 shows the reconstructed dielectric profiles using the proposed imaging technique. The obtained results indicate that the technique can successfully detect the position of the assumed strokes when the SNR is around 25 dB, which is a realistic value for this imaging environment.

The convergent rate is another vital issue in microwave head imaging algorithms since it influences the computation time, which is a critical factor in head imaging due to the need for a fast detection and medication of any brain injury. Figure 4.19 shows NER as a function of the iteration time under different noise levels. It can be seen that the proposed algorithm quickly converges after only 10 iterations with a total time of around 100 s. The performance of the proposed method was also numerically assessed and the results are shown in Figure 4.20 for different SNRs. It can be seen that the presented method has almost similar performances when using different frequencies if the SNR is more than 25 dB. However, the use of lower frequencies achieves better performance at the noisy environment (SNR less than 10 dB). This result can be explained by the fact that the attenuation due to signal penetration inside the head is much higher at the high frequencies. Thus, the scattered signals

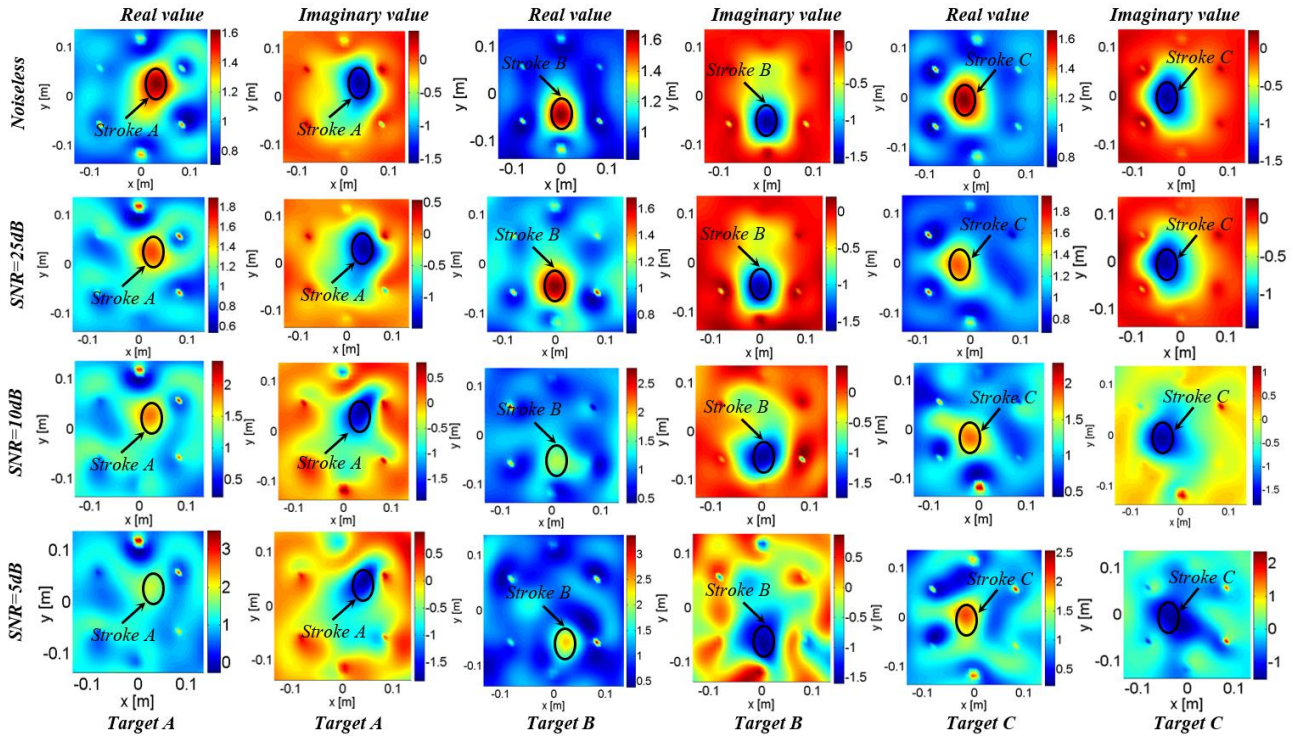

Fig 4. 16: The reconstructed dielectric profiles of a realistic head phantom with a haemorrhagic stroke located at different positions using the proposed imaging technique. The performance is evaluated under different SNR levels and the incident frequency f=0.6 GHz.

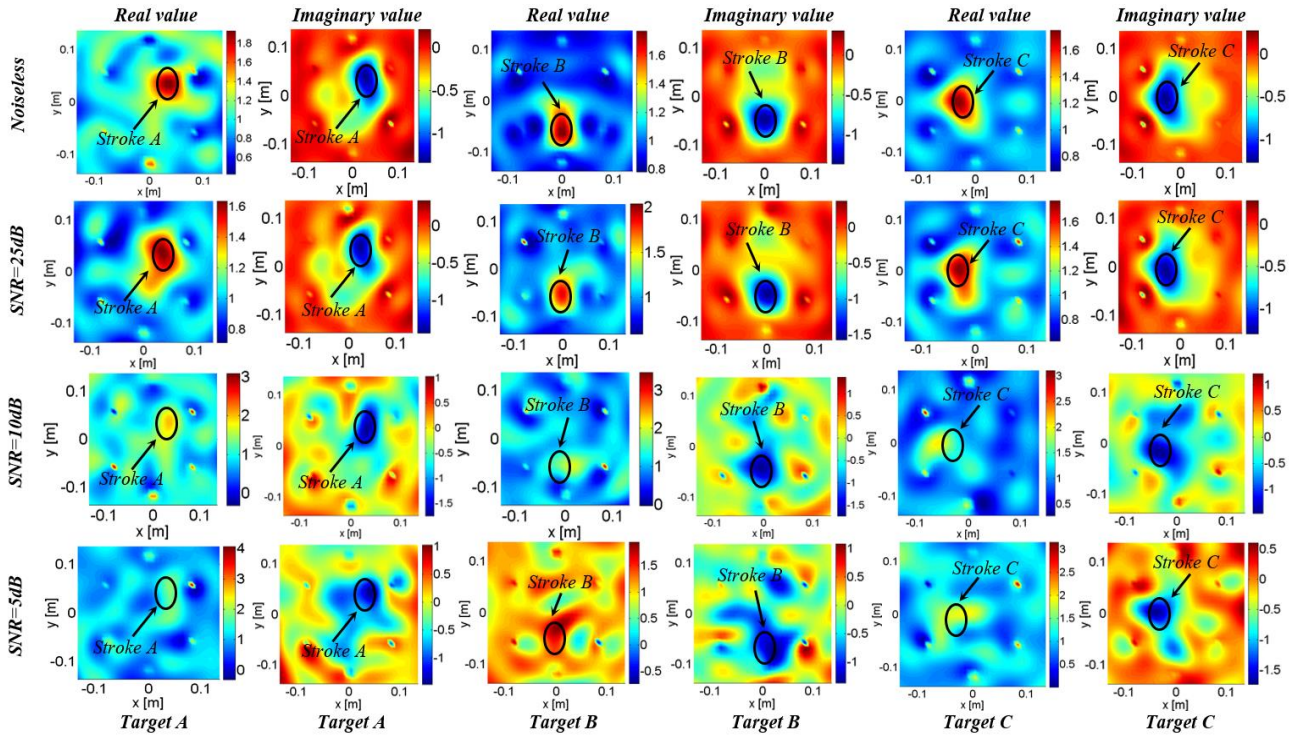

Fig 4. 17: The reconstructed dielectric profiles of a realistic head phantom with a haemorrhagic stroke located at different positions using the proposed imaging technique. The performance is evaluated under different SNR levels and the incident frequency f=0.8 GHz.

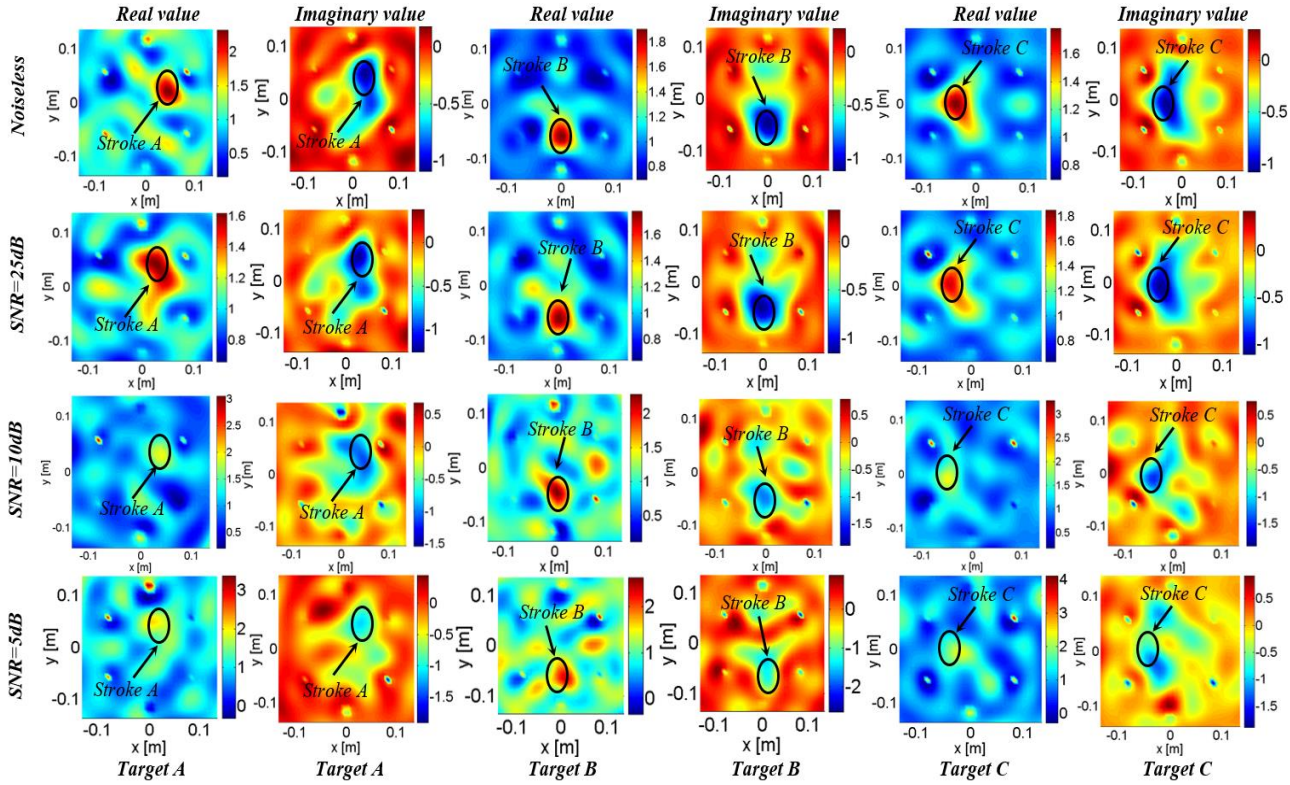

Fig 4. 18: The reconstructed dielectric profiles of a realistic head phantom with a haemorrhagic stroke located at different position using the proposed imaging technique. The performance is evaluated under different SNR levels and the incident frequency f=1 GHz.

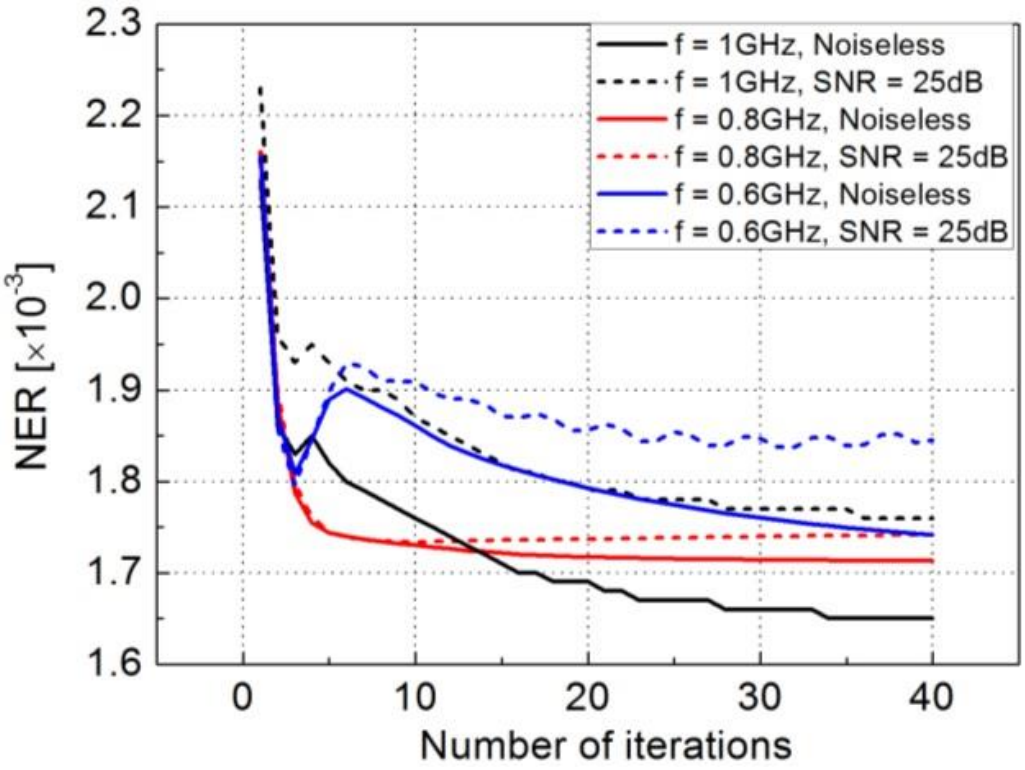

Fig 4. 19: NER as the function of iteration time under different noise levels.

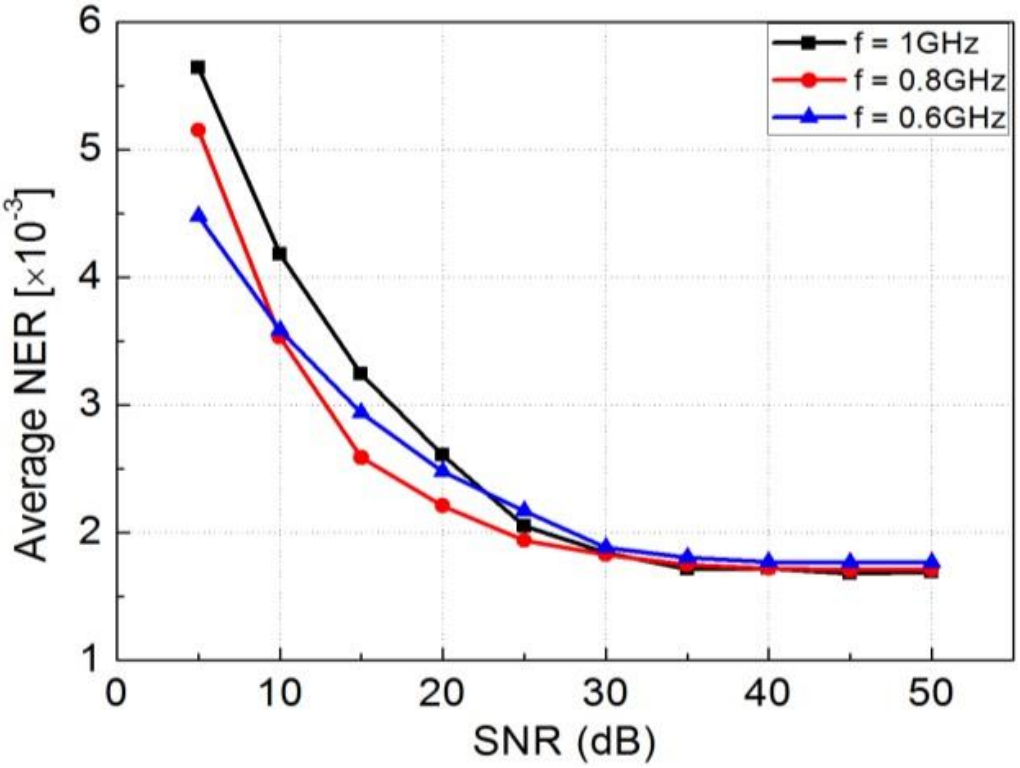

Fig 4. 20: NER of the proposed techniques when used in head imaging with different SNR

from different tissues inside the head that are needed in the profile reconstruction are much lower. Under the noisy environment, those signals can be fully embedded in the noise.

4.4 Discussions and Conclusions

In this chapter, an innovative imaging scheme based on block sparse Bayesian learning (BSBL) and wavelet transform has been proposed. The proposed method aims to solve the problem of the inability to use large number of antennas when microwave tomography method is used to reconstruct electrical properties of a limited-volume imaged object. Since the contrast-field profile of the imaged object is not sparse in many applications, such as head imaging, the wavelet transform was applied to convert the non-sparse profile into a sparse domain (the wavelet domain). The contrast-field profile of the object was then recovered using BSBL along with the Born iterative method. The proposed imaging scheme has been successfully evaluated using a non-sparse model. Compared with other techniques, the proposed one can reconstruct the profile of the non-sparse domain using small number of antennas (only 17% number of antennas are used when compared with other traditional methods) with a fast convergent time. To further assess the proposed techniques on a real-life problem, it was used to reconstruct the dielectric profile of a numerical head model, which includes all the main head tissues with their realistic dielectric properties. The presented results have indicated the capability of

the technique to reconstruct the dielectric profile of the head successfully and to accurately detect a haemorrhagic stroke placed at different positions.

Chapter 5: Optimization Techniques for Radar-based Imaging

5.1 Optimization-based Confocal Algorithm in Microwave Head Imaging

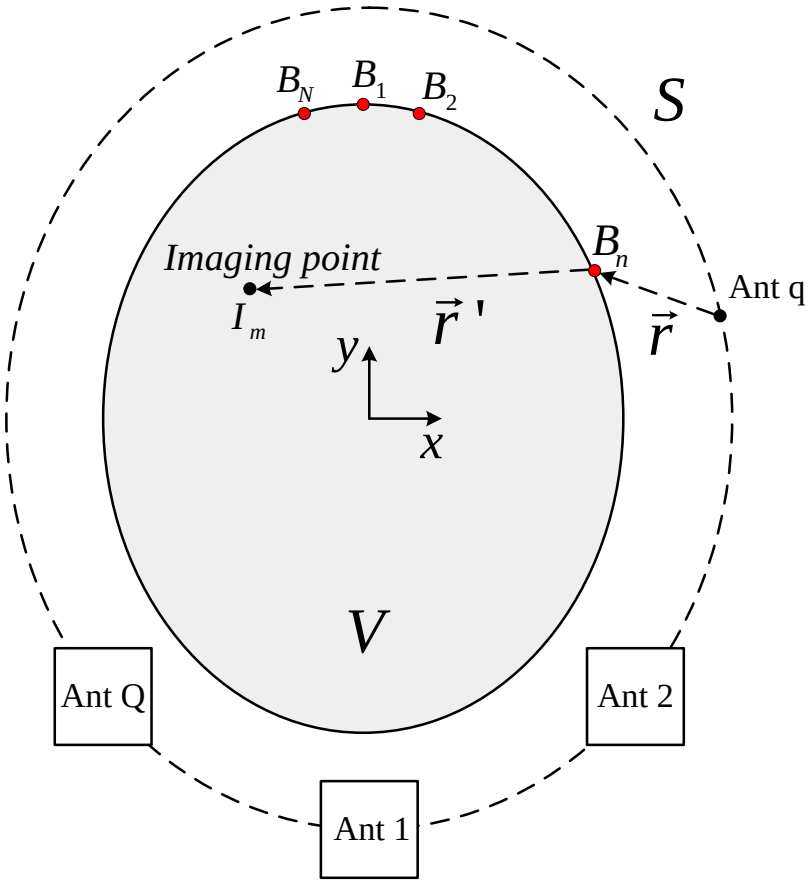

Fig 5. 1: The imaging domain

Assume the imaging domain of Figure 5.2. An antenna array of Q elements uniformly surrounds the imaging domain along the contour S. The positions of the antennas are denoted as

$$\boldsymbol{A} = \left[\boldsymbol{a_1}, \ldots \boldsymbol{a_q}, \ldots, \boldsymbol{a_Q}\right]^T \tag{5.1}$$

where $\boldsymbol{a_q} = \left[x_q^{\boldsymbol{a}}, y_q^a\right]^T$ is the coordinate of the qth antenna. The imaging area is represented by V and the imaging points within V are denoted as

$$\boldsymbol{I} = [\boldsymbol{i_1}, \ldots \boldsymbol{i_m}, \ldots, \boldsymbol{i_M}]^T \tag{5.2}$$

where $\boldsymbol{i_m} = \left[x_{\boldsymbol{m}}^{\boldsymbol{i}}, y_m^i\right]^T$ is the coordinate of the mth imaging point. The boundary of the imaged object is divided into N entry points which are represented as

$$\boldsymbol{B} = [\boldsymbol{b_1}, \dots, \boldsymbol{b_n}, \dots, \boldsymbol{b_N}]^T \tag{5.3}$$

where $\boldsymbol{b_n} = \left[x_{\boldsymbol{n}}^{\boldsymbol{b}}, y_n^b\right]^T$ is the coordinate of the nth entry point. Each of the entry points is assigned the dielectric constants expressed by the vector

$$\boldsymbol{\varepsilon} = [\varepsilon_1, \varepsilon_2, \dots, \varepsilon_N] \tag{5.4}$$

The number of the entry points should be more than the number of antenna elements. Much larger number of entry points gives better imaging results but needs longer time to converge.

Assume using a mono-static approach with the operating frequency range from f_1 to f_K, which is sampled as the vector $\boldsymbol{F} = [f_1, \dots, f_k, \dots, f_K]^T$. Thus, the reflection coefficients measured at the Q antennas are the data needed for imaging and detection and can be expressed as:

$$\boldsymbol{S} = \begin{bmatrix} S(\boldsymbol{a_1}, f_1) & \cdots & S(\boldsymbol{a_Q}, f_1) \\ \vdots & \ddots & \vdots \\ S(\boldsymbol{a_1}, f_K) & \cdots & S(\boldsymbol{a_Q}, f_K) \end{bmatrix} \tag{5.5}$$

where $S(\boldsymbol{a_q}, f_k)$ is the reflection coefficient for the qth antenna at the kth frequency point and $\boldsymbol{S} \in \mathbb{C}^{K\times Q}$ is a complex matrix. The inverse Fourier transform is then implemented to transfer the frequency domain data $\boldsymbol{S}$ to the time domain

$$\boldsymbol{\mathcal{T}} = \boldsymbol{\mathcal{F}}^{-1}\boldsymbol{S} = \begin{bmatrix} t(\boldsymbol{a_1}, 0) & \cdots & t(\boldsymbol{a_Q}, 0) \\ \vdots & \ddots & \vdots \\ t\left(\boldsymbol{a_1}, \dfrac{K-1}{\Delta f K}\right) & \cdots & t\left(\boldsymbol{a_Q}, \dfrac{K-1}{\Delta f K}\right) \end{bmatrix} \tag{5.6}$$

where $\boldsymbol{\mathcal{T}} \in \mathbb{C}^{K\times Q}$ is the matrix with time domain data and $t\left(\boldsymbol{a_q}, \frac{k-1}{\Delta f K}\right)$ is the time domain data for the qth antenna at the time $\frac{k-1}{\Delta f K}$. $\boldsymbol{\mathcal{F}}$ is the Fourier transform matrix which can be represented as

$$\boldsymbol{\mathcal{F}} = \begin{bmatrix} 1 & 1 & 1 & & 1 \\ 1 & W_K^1 & W_K^2 & \dots & W_K^{K-1} \\ 1 & W_K^2 & W_K^4 & & W_K^{K-2} \\ & \vdots & & \ddots & \vdots \\ 1 & W_K^{K-1} & W_K^{K-2} & \cdots & W_K^1 \end{bmatrix} \tag{5.7}$$

where $W_K^k = \exp(-j2\pi k/K)$ and $\boldsymbol{\mathcal{F}} \in \mathbb{C}^{K\times K}$.

In head imaging, the small backreflected signals from tissues, including any stroke, inside the head can be dominated by strong reflection (clutter) from the skin-free space interface. To avoid that scenario, the clutter is removed by subtracting the time domain data of two adjacent antennas. The reason for adopting this approach is the similarity in the clutter received by any pair of neighbouring antennas. This process can be represented as:

$$\begin{cases} t\left(\boldsymbol{a_q}, \dfrac{k-1}{\Delta f K}\right) = t\left(\boldsymbol{a_q}, \dfrac{k-1}{\Delta f K}\right) - t\left(\boldsymbol{a_{q-1}}, \dfrac{k-1}{\Delta f K}\right), q \neq 1 \\ t\left(\boldsymbol{a_q}, \dfrac{k-1}{\Delta f K}\right) = t\left(\boldsymbol{a_Q}, \dfrac{k-1}{\Delta f K}\right) - t\left(\boldsymbol{a_q}, \dfrac{k-1}{\Delta f K}\right), q = 1 \end{cases} \tag{5.8}$$

The propagation time of the signal from any antenna to a certain point $I_m \in V$ within the imaged domain is calculated using the dielectric constant ε_n assigned to the entry points of that signal. Thus, the propagation time from the qth antenna to the mth point inside the head, $\tau_q(\boldsymbol{i_m})$, is

$$\tau_q(\boldsymbol{i_m}) = min_{\boldsymbol{b_n} \in \boldsymbol{B}} \left\{ \frac{\left\| \boldsymbol{a_q} - \boldsymbol{b_n} \right\|}{c} + \frac{\| \boldsymbol{b_n} - \boldsymbol{i_m} \| \sqrt{\varepsilon_n}}{c} \right\} \tag{5.9}$$

It is notable that in traditional confocal algorithms, $\sqrt{\varepsilon_n}$ is replaced by a certain effective dielectric constant $\sqrt{\varepsilon_{eff}}$ irrespective of the antenna's position, entry point of the signal, and its reflection point.

In the proposed imaging algorithm, the propagation time from the qth antenna to the mth imaging point is a function of the dielectric constant assigned to each entry point $\boldsymbol{b_n}$ and thus it can be further denoted as $\tau_q(\boldsymbol{i_m}, \boldsymbol{\varepsilon})$. After $\tau_q(\boldsymbol{i_m}, \boldsymbol{\varepsilon})$ is calculated, the image intensity of I_m is calculated as:

$$\mathcal{Z}(\boldsymbol{i_m}, \boldsymbol{\varepsilon}) = \sum_{q=1}^{Q} \left| t\left(\boldsymbol{a_q}, 2\tau_q(\boldsymbol{i_m}, \boldsymbol{\varepsilon})\right) \right| \tag{5.10}$$

It is apparent from (5.5)-(5.10) that the image intensity I_m and thus quality of the generated image depends on the dielectric constant vector $\boldsymbol{\varepsilon}$. In head imaging, if there is a stroke, the image intensity should be focused at the position of the stroke assuming that the strong clutter due to the skin-free space interface is removed in the pre-processing step. That focusing can always converge to the position of the stroke if the dielectric constant vector $\boldsymbol{\varepsilon}$ is chosen appropriately. This concept indicates that a better image quality can be achieved through optimizing $\boldsymbol{\varepsilon}$. To optimize $\boldsymbol{\varepsilon}$, an optimization objective has to be defined firstly. To that end, an image intensity related metric $\mathcal{O}$ is defined as the

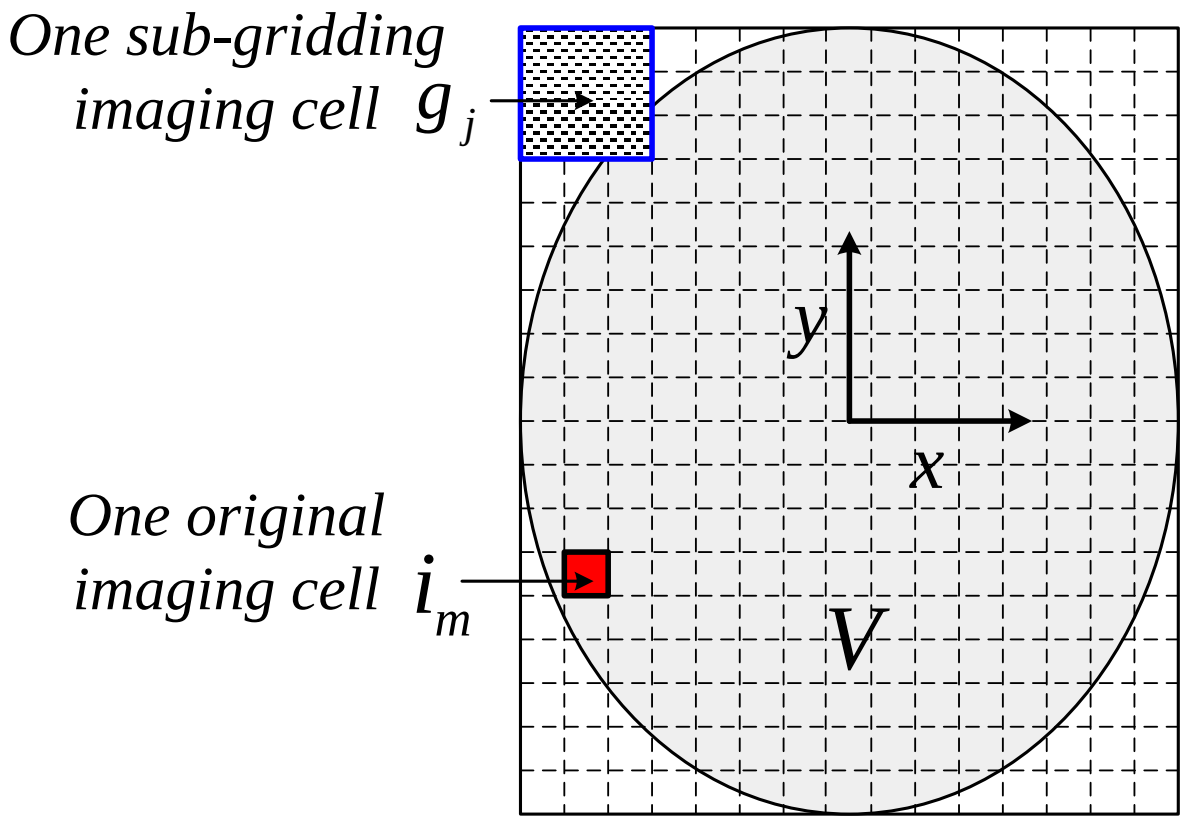

Fig 5. 2: Expansion and sub-gridding of the imaged area $\boldsymbol{V}$

optimization objective. To calculate $\mathcal{O}$, the imaging area V is firstly expanded to form a rectangular area and then sub-gridded as shown in Figure 5.3.

Sub-gridding is used to enable to optimization objective to find the optimum value of $\boldsymbol{\varepsilon}$ that focuses the image at a certain region not a cell. The normal size of one imaging cell $\boldsymbol{i_m}$ is too small ($1 \times 1mm^2$). Thus, if the algorithm is based on the intensity at one cell, it might converge at one imaging cell resulting in a focused imaging area that is too small and might be even considered as noise source. The small size of the imaging cell also increases the possibility of divergent solution. It is notable that the sub-gridded imaging cell is only used for the optimization process to achieve the optimum $\boldsymbol{\varepsilon}$ but the final image will still use the original imaging cell (size of $1 \times 1mm^2$). For early stage detection, the size of the stroke can be considered around $2 \times 2cm^2$. Thus, the size of each sub-gridding cell $\boldsymbol{g_j}$ is assumed as $2 \times 2cm^2$, which means each sub-gridded cell includes 400 original imaging cells. For simplicity, the utilized sub-gridding expands the imaging area to a general rectangular shape.

It can be seen from Figure 5.3 that the imaging cells are divided into two parts; cells inside and outside the imaged domain V. The intensity in cells outside V is set to 0. Therefore, the image intensity for the entire imaging area is calculated as

$$\begin{cases} \mathcal{Z}(\boldsymbol{i_m}, \boldsymbol{\varepsilon}) = \sum_{q=1}^{Q} \left| t\left(\boldsymbol{a_q}, 2\tau_q(\boldsymbol{i_m}, \boldsymbol{\varepsilon})\right) \right|, & \boldsymbol{i_m} \in V \\ \mathcal{Z}(\boldsymbol{i_m}, \boldsymbol{\varepsilon}) = 0, & \boldsymbol{i_m} \notin V \end{cases} \tag{5.11}$$

Assume the original imaging cells $\boldsymbol{i_m}$ within one sub-gridding cell $\boldsymbol{g_j}$ is denoted as the set Ω_j, then the image intensity for $\boldsymbol{g_j}$ is calculated as

$$\mathcal{Z}_{\boldsymbol{g_j}}^{sub}(\boldsymbol{i_m}, \boldsymbol{\varepsilon}) = \frac{\sum_{\boldsymbol{i_m}} \mathcal{Z}(\boldsymbol{i_m}, \boldsymbol{\varepsilon})}{\sum_{\boldsymbol{i_m}} \chi_V(\boldsymbol{i_m})}, \boldsymbol{i_m} \in \Omega_j \tag{5.12}$$

where $\chi_V(\cdot)$ is the indicator function for the set V. It can be seen from (5.12) that the image intensity $\boldsymbol{g_j}$ is the average intensity of one sub-gridded cell after excluding the original imaging cells outside the imaging domain V. This exclusion aims to avoid effect of boundary head cells. The imaging intensity for all the sub-gridded cells is calculated using (5.12) and denoted as the vector

$$\boldsymbol{G} = \left[\mathcal{Z}_{\boldsymbol{g_1}}^{sub}, \dots, \mathcal{Z}_{\boldsymbol{g_j}}^{sub}, \dots, \mathcal{Z}_{\boldsymbol{g_J}}^{sub}\right] \tag{5.13}$$

where J is the number of sub-gridding.

The objective of the optimization is defined using the metric $\mathcal{O}$, which is calculated as

$$\mathcal{O}(\boldsymbol{\varepsilon}) = \frac{\max(\boldsymbol{G})}{\|\boldsymbol{G}\|_{\boldsymbol{1}} - \max(\boldsymbol{G})} \tag{5.14}$$

Thus, the optimum estimate of the dielectric constant vector $\boldsymbol{\varepsilon}^{opt}$ can be achieved through maximizing $\mathcal{O}$

$$\boldsymbol{\varepsilon}^{opt} = \underset{\boldsymbol{\varepsilon}}{\operatorname{argmax}}\{\mathcal{O}(\boldsymbol{\varepsilon})\} \tag{5.15}$$

The process of searching the optimum $\boldsymbol{\varepsilon}^{opt}$ to maximize $\mathcal{O}(\boldsymbol{\varepsilon})$ is implemented using particle swarm optimization (PSO) and the details of PSO method will be explained in the following section. The proposed algorithm is depicted by the flowchart shown in Figure 5.4 and summarized for head imaging by following steps:

1) Collect the frequency domain data $\boldsymbol{S}$ (the reflection coefficients) from the antenna array.
2) Transfer the frequency domain $\boldsymbol{S}$ to time domain data $\boldsymbol{\mathcal{T}}$ using (5.5)-(5.7) then remove the skin reflections using (5.8) to obtain τ.
3) Initialize the dielectric constant vector $\boldsymbol{\varepsilon}$.

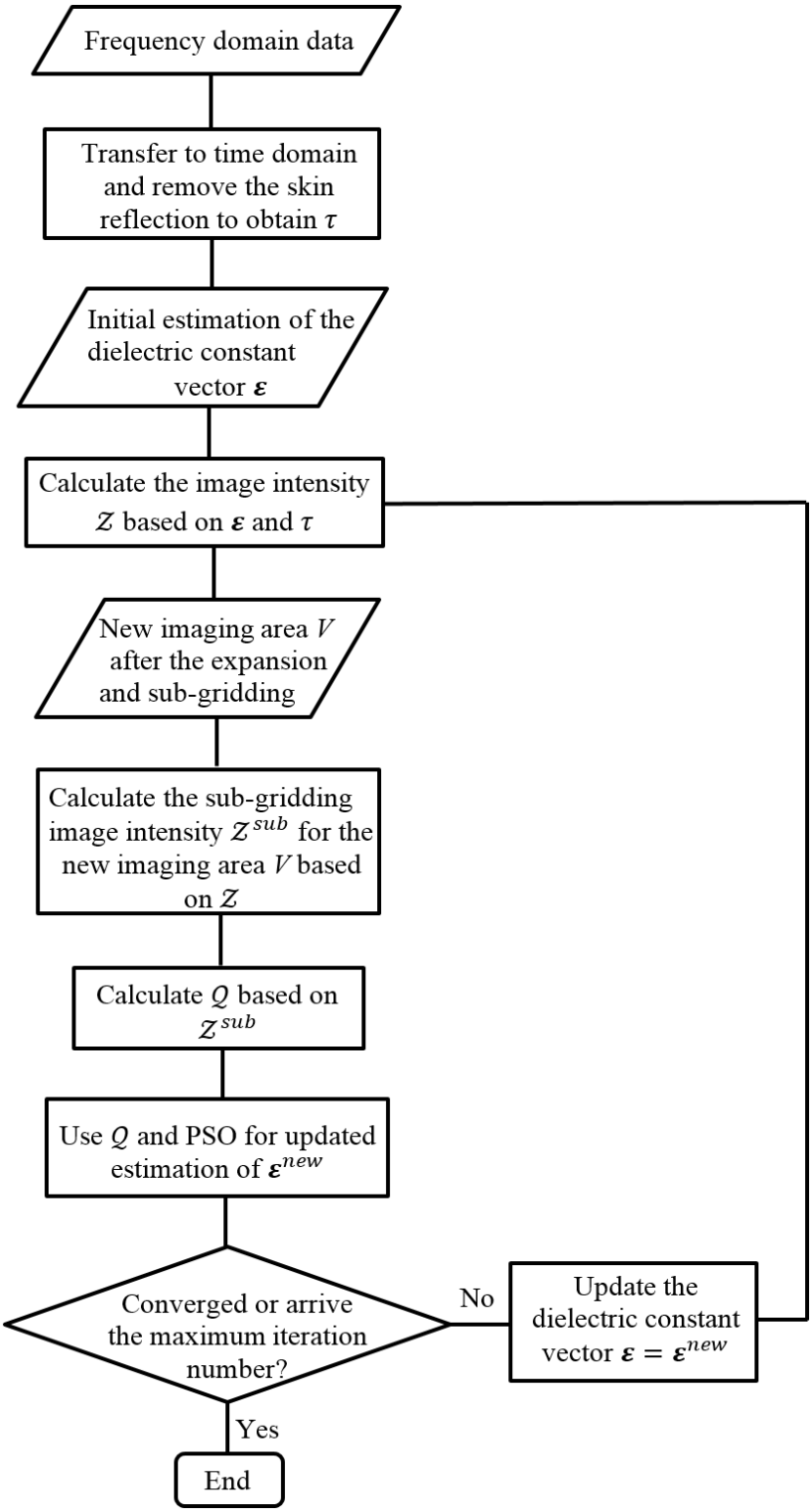

Fig 5. 3: Flowchart of the proposed algorithm

4) Calculate the image intensity $\mathcal{Z}$ for each of the imaging cells using $\boldsymbol{\varepsilon}$ and (5.9)-(5.10).
5) Expand and sub-grid the original imaging area as the new area V and calculate the image intensity $\mathcal{Z}^{sub}$ for each of the sub-gridded cells in V using (5.11)-(5.12).

6) Calculate the metric $\mathcal{O}$ using (5.14) then use PSO to find $\boldsymbol{\varepsilon}^{new}$ as the new estimation for $\boldsymbol{\varepsilon}$ to maximize $\mathcal{O}$.
7) Continue the optimization by updating $\boldsymbol{\varepsilon}$ and going to step (4) until $\mathcal{O}$ is converged (the increase in $\mathcal{O}$ between two consecutive iterations is smaller than 1×10^{-5}), which is the usual case if there is a stroke, or the entire procedure arrives the maximum iteration time, which is the usual case when there is no stroke.

5.2 Particle Swarm Optimization

Particle swarm optimization (PSO) is based on a stochastic process [142]. Different from evolutionary algorithms, PSO does not resample the populations in the mutation procedure but "Tweaked" the populations based on the newly discovered space. PSO method is inspired by the behaviour of swarms, in which the candidate solutions are not referred as a population of individuals but as a swarm of particles [142]. A particle is composed with two parts:

1. The location of a particle in the searching space which is defined as $\vec{x} = (x_1, x_2, \dots)$.
2. The velocity of a particle which is defined as $\vec{v} = (v_1, v_2, \dots)$. Assume at times $t-1$ and t, the locations of a particle is $\vec{x}^{t-1}$ and $\vec{x}^{t}$, respectively, then the velocity of the particle at time t is calculated as $\vec{v} = \vec{x}^{t} - \vec{x}^{t-1}$.

Each particle is initialized with a random location and a random velocity vector. Three factors are defined in the optimization process [142]:

1. The best location $\vec{x}^{*}$ that the particle $\vec{x}$ has found so far.
2. The best location $\vec{x}^{+}$ that any of the informants of the particle $\vec{x}$ have found so far. The informants of the particle $\vec{x}$ consist of a small set of particles which are randomly selected during each iteration. The particle $\vec{x}$ belongs to its own informants.
3. The best location $\vec{x}^{!}$ that all the particles have found so far.

During each iteration, the following operations are implemented [142]:

1. Calculate the quality of each particle and update the best locations if the current ones are better than the previous ones.
2. Each particle $\vec{x}$ is updated by its velocity vector $\vec{v}$. The velocity vector is calculated by adding in a vector towards $\vec{x}^{+}$ ($\vec{v}^{+}$), a vector towards $\vec{x}^{!}$ ($\vec{v}^{!}$), and a vector towards $\vec{x}^{*}$ ($\vec{v}^{*}$). This summation is affected by a random noise.
3. Each particle is moved based on its velocity vector.

The pseudocode of the PSO method is shown below [142]:

Particle Swarm Optimization (PSO)

Initialization:

Swarmsize ← the number of particles

α ← proportion of the velocity $\vec{v}$ to be reserved

β ← proportion of the velocity $\vec{v}^*$ to be reserved

γ ← proportion of the velocity $\vec{v}^+$ to be reserved

δ ← proportion of the velocity $\vec{v}^!$ To be reserved

ε ← the size of a jump for a particle

$P \leftarrow \{\}$

$\overrightarrow{Best} \leftarrow \{\}$

for *swarmsize times* ***do***

$P \leftarrow P \cup \{$new particle $\vec{x}$ with random velocity $\vec{v}\}$

repeat

for each particle $\vec{x} \in P$ with velocity $\vec{v}$ ***do***

AssessFitness($\vec{x}$)

if $\overrightarrow{Best} = \{\}$ or Fitness($\vec{x}$)>Fitness($\overrightarrow{Best}$) ***then***

$\overrightarrow{Best} \leftarrow \vec{x}$

for each particle $\vec{x} \in P$ with velocity $\vec{v}$ ***do***

$\vec{x}^* \leftarrow$ previous best location of the particle $\vec{x}$

$\vec{x}^+ \leftarrow$ previous best location from the informants of the particle $\vec{x}$

$\vec{x}^! \leftarrow$ previous best location from any of the particles

for each dimension i ***do***

$b \leftarrow$ random number between 0 and β

$c \leftarrow$ random number between 0 and γ

$d \leftarrow$ random number between 0 and δ

$v_i \leftarrow \alpha v_i + b(x_i^* - x_i) + c(x_i^+ - x_i) + d(x_i^! - x_i)$

for each particle $\vec{x} \in P$ with velocity $\vec{v}$ ***do***

$\vec{x} \leftarrow \vec{x} + \varepsilon\vec{v}$

until $\overrightarrow{Best}$ is the most optimum solution or it achieves the maximum iteration time

return $\overrightarrow{Best}$

The five parameters α, β, γ, δ, and ε are explained as follows [142]:

- α: the proportion of the original velocity to be reserved.
- β: the proportion of the personal best to be reserved. If β is large, the particle prefer to move towards its own best position rather than the global best position.
- γ: the proportion of the informants' best to be reserved. The influence of γ is between α and β. If the number of informants is large, the informants' best is more close to the global best, and small number of informants make the informants' best close the local best.
- δ: the proportion of the global best to be reserved. If δ is large, the particles prefer to move towards the best position where they have already discovered. Since this parameter might make the optimization procedure highly exploitative, it is usually set to 0.
- ε: how fast the particle moves. If ε is big, the particles make a big step towards the better district. A big value of ε allows the optimization process converge faster, however, it also increase the possibility that global optimum might be missed. This value is usually set to 1.

5.3 Evaluation in Full-Wave Simulation Environment

The proposed optimization-based imaging algorithm is firstly evaluated using the electromagnetic simulator (CST Microwave Studio). An accurate realistic head phantom [139] surrounded by an antenna array of 16 elements is used. The utilized antennas have three dimensional structure that is fed using a coplanar waveguide [143]. The antennas have an operating band from 0.8 to 2.2 GHz with stable unidirectional radiation patterns of about 9 dB front-to-back ratio. The distance between the antenna array and the boundary of the head is 1 cm. During the simulations, three different scenarios are taken into account (Figure 5.5); unhealthy brain with shallow and deep strokes, and healthy brain. For the unhealthy cases, a haemorrhagic (bleeding) stroke is assumed with size of $2 \times 2cm^2$.

To verify the robustness of the proposed algorithm for different initial values of $\boldsymbol{\varepsilon}$, the initial effective values $\boldsymbol{\varepsilon_1^{init}} = 30 \times I, \boldsymbol{\varepsilon_2^{init}} = 40 \times I,$ and $\boldsymbol{\varepsilon_3^{init}} = 50 \times I$ ($I \in \mathbb{R}^{N\times 1}$ is the identity vector) are used and the value range of $\boldsymbol{\varepsilon}$ during optimization is set from 25 to 65 (a reasonable range due to the high dielectric constants for the main head tissues as depicted in Figure 5.1). The size of one imaging cell is $1 \times 1mm^2$ and the size of one sub-grid is $2 \times 2\ cm^2$. The number of the entry points is taken as 100 (larger than the number of antennas) and the maximum iteration time is set at 50 (larger value gives further assurance of optimization but needs longer time). The obtained results are shown in Figures 5.6, 5.7, and 5.8 for shallow stroke, deep stroke, and healthy head, respectively. It can be seen from Figure 5.6 and 5.7 that the images obtained using the proposed algorithm always converge to

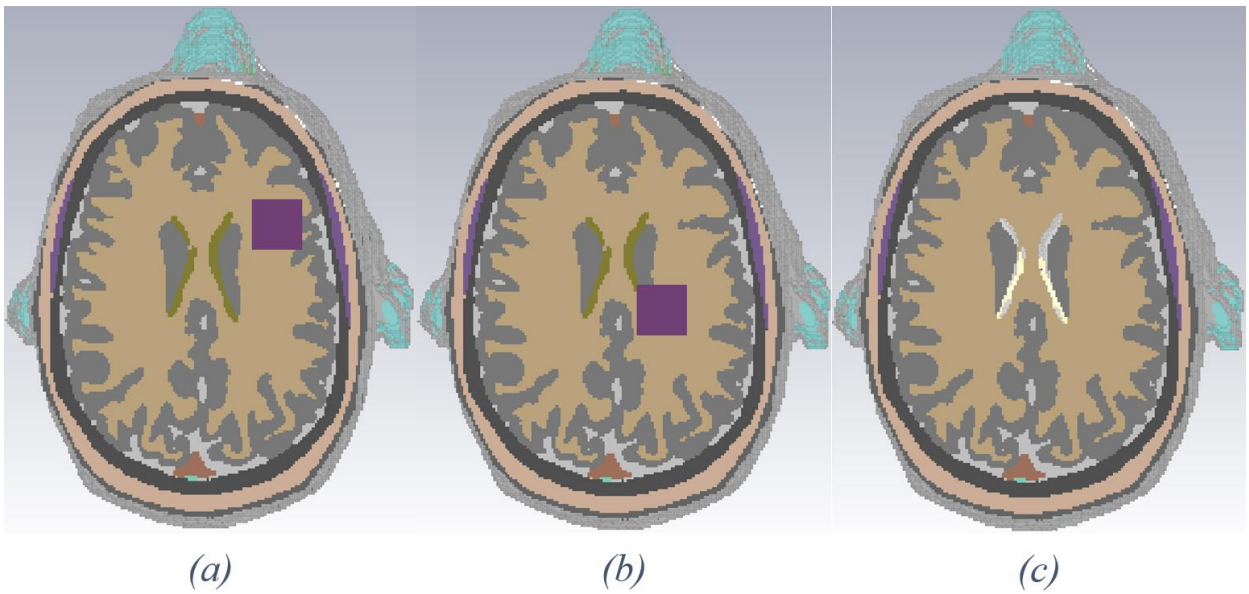

Fig 5. 4: Two-dimensional section of the numerical head model used in simulations. (a) Shallow, (b) deep stroke, and (c) healthy brain.

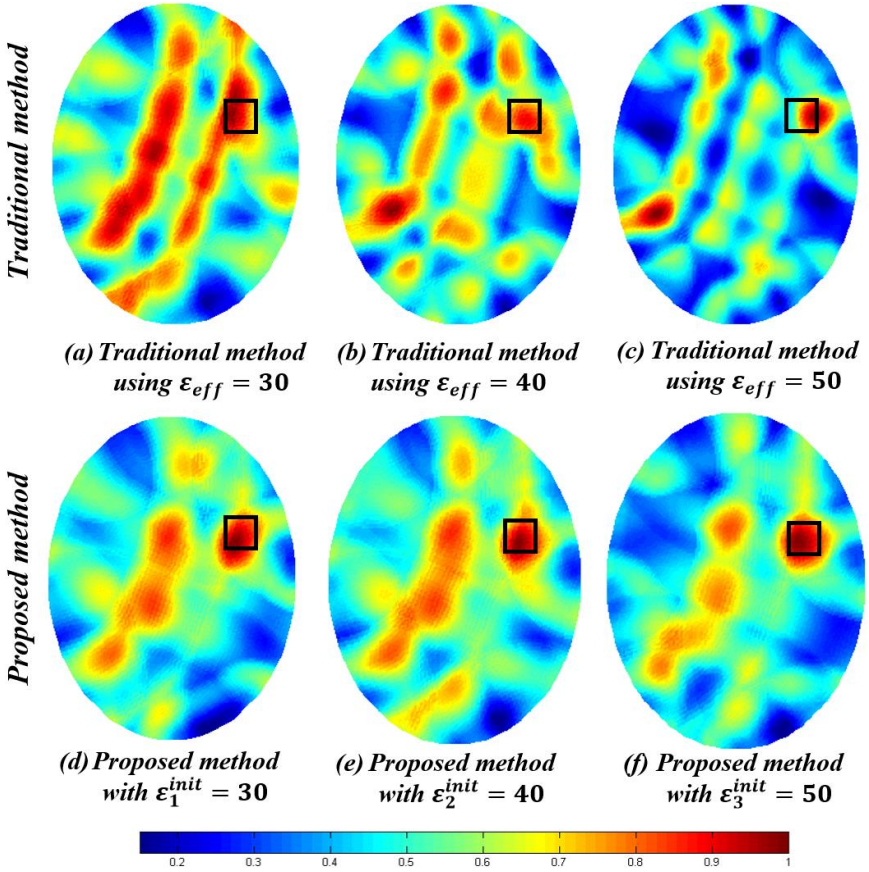

Fig 5. 5: Simulation results using the traditional and proposed methods for head with shallow stroke indicated by the black square.

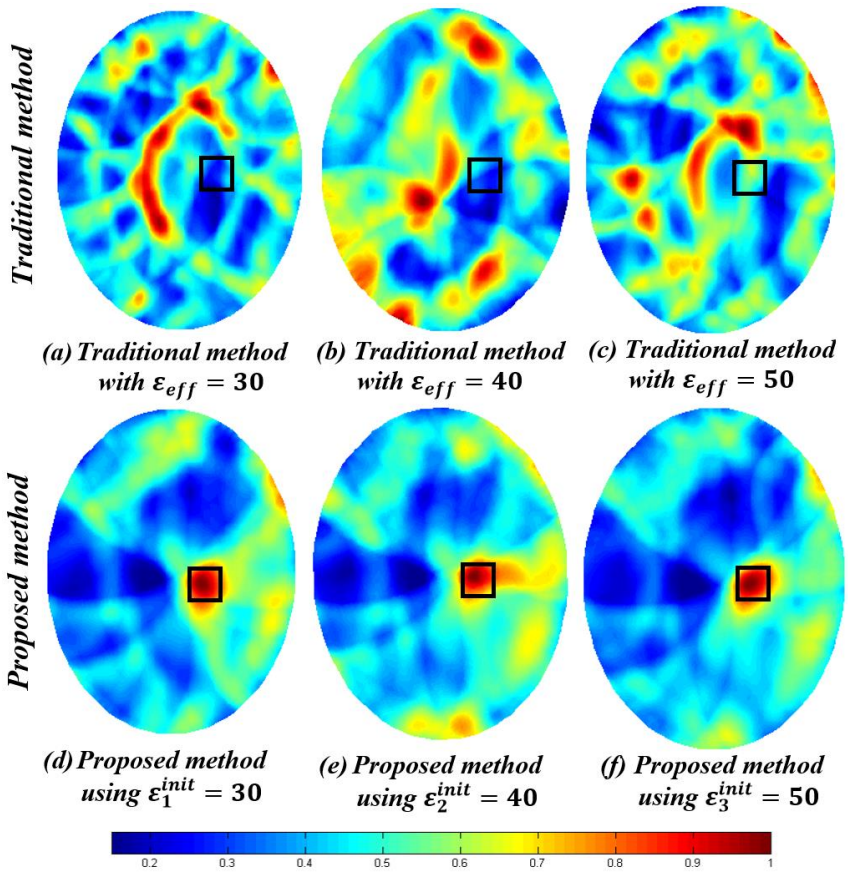

Fig 5. 6: Simulation results using traditional and proposed method for head with deep stroke

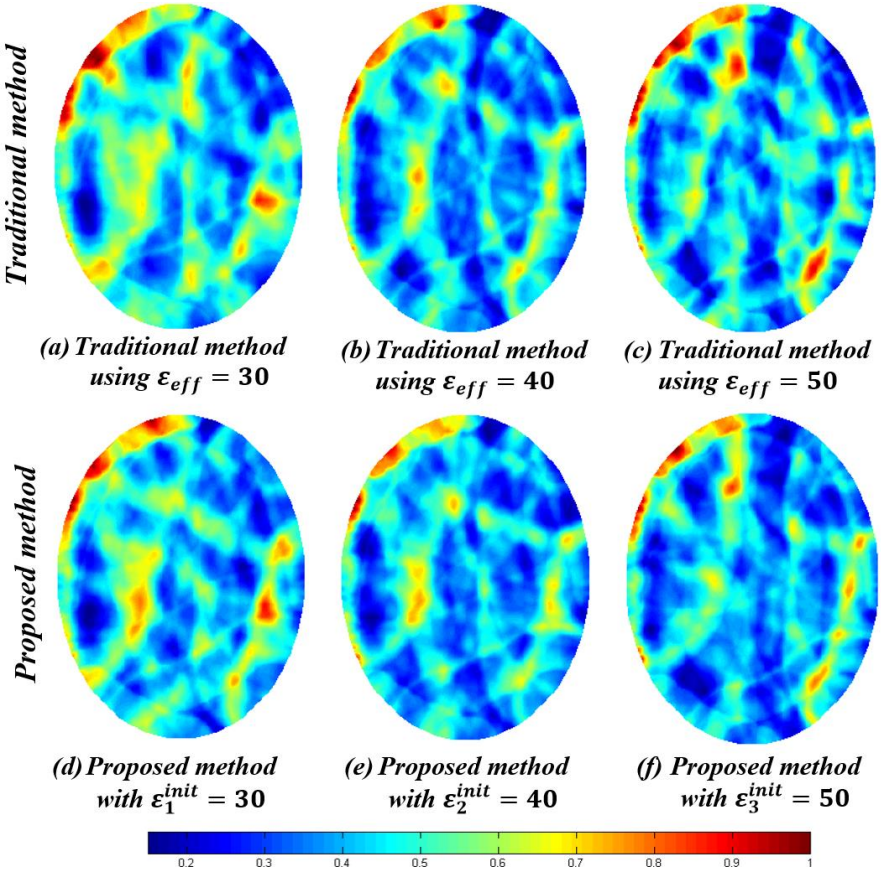

Fig 5. 7: Simulation results using traditional and proposed methods for healthy head.

the correct focused one irrespective of the assumed initial dielectric constants. If the head is healthy, the proposed algorithm does not create a false positive target as depicted in Figure 5.8. For the images obtained using the traditional method, they are highly affected by the assumed effective dielectric constant. The detected location of the stroke and quality of the images are dependent on the assumed dielectric constant.

The convergence index is important for optimization-based algorithms as it defines the required time to produce accurate image and this is critical especially in head imaging. Assume the convergence index is defined as μ which is the increase in the quality metric $\mathcal{O}$ between two iteration times expressed as $\mu = \mathcal{O}^{i+1} - \mathcal{O}^{i}$. Figure 5.9 shows variation of the convergence index with number of iterations for the three investigated cases. Based on the random characteristic of PSO, the required iteration number for convergence is case dependent. However, it can be seen from Figure 5.9 that for all these cases, the algorithm converges after 50 iterations regardless of the choice of the initial estimation of $\boldsymbol{\varepsilon}^{init}$. It is interesting to see from the results in Figure 5.9 that using an initial value of dielectric constant close to 30 guarantee convergence after only 22 iterations knowing that the required time for each of the iteration using a general purpose PC is around 8 seconds. For other initial values, the algorithm also converges in less than 22 iterations except for the case of a shallow target, which requires around 50 iterations. The reason behind that is the huge effect of strong skin interface reflections that are close in the time domain to shallow target reflection. The use of our pre-processing approach enables reducing the effect of those strong skin interface reflections, but cannot of course remove them completely.

To evaluate the quality of the images generated using the traditional and proposed method, two metrics are used. The metric γ is used to compare ratio of the average intensity of the stroke area $\mathcal{L}$ to the rest of the head area $\mathcal{H}$.

$$\gamma = \frac{\overline{\mathcal{Z}(I_{\boldsymbol{m}})}}{\overline{\mathcal{Z}(I'_{\boldsymbol{m}})}} \qquad \begin{matrix} \forall I_m \in \mathcal{L} \\ \forall I'_m \in \mathcal{H} \;\&\; I'_m \notin \mathcal{L} \end{matrix} \tag{5.16}$$

Another metric σ is used to evaluate the distance between the real center of the stroke area and the detected position.

$$\begin{matrix} \sigma = \|\boldsymbol{i}^*_m - \mathcal{C}\| \\ \boldsymbol{i}^*_m = argmax\{\mathcal{Z}(\boldsymbol{i}_m)\} \quad \forall \boldsymbol{i}_m \in \mathcal{H} \end{matrix} \tag{5.17}$$

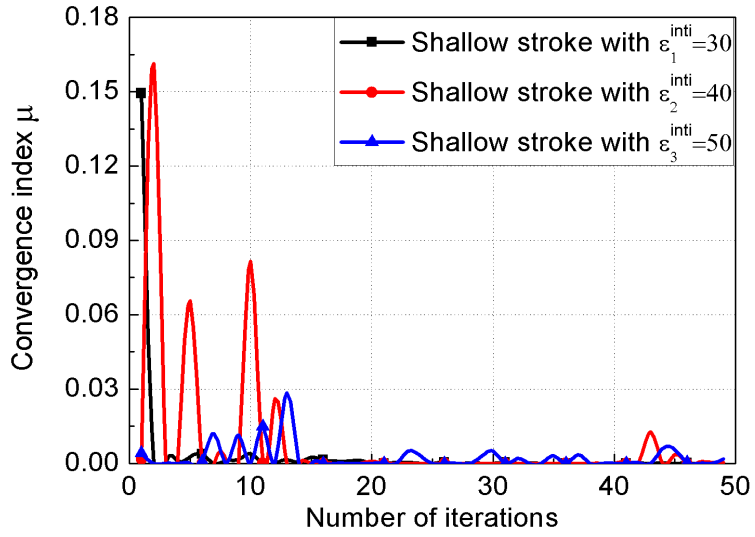

(a)

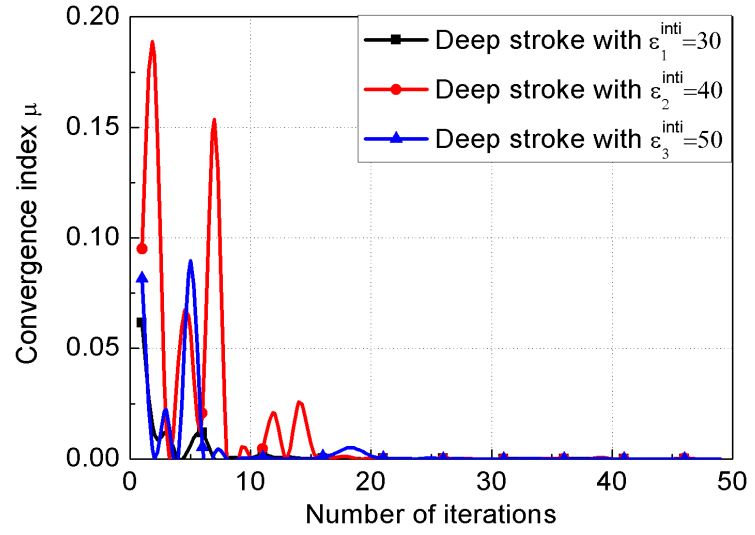

(b)

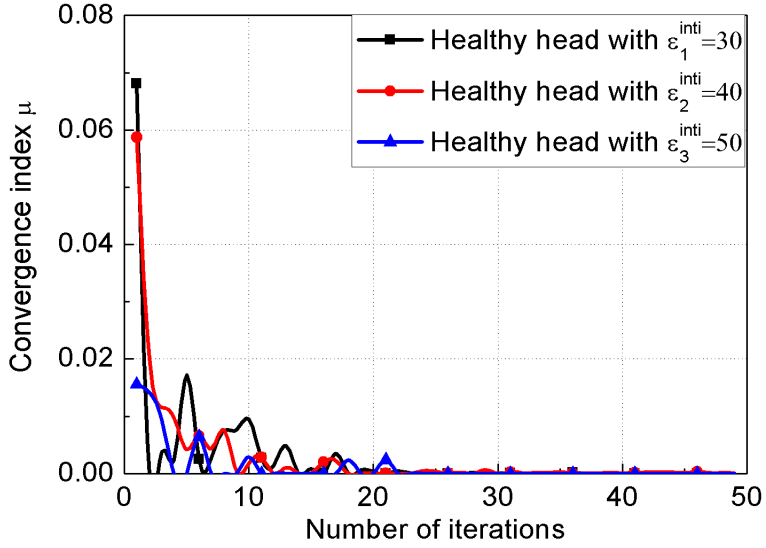

(c)

Fig 5. 8: Variation of the convergence index $\boldsymbol{\mu}$ with number of iterations for (a) shallow stroke, (b) deep stroke, and (c) healthy head

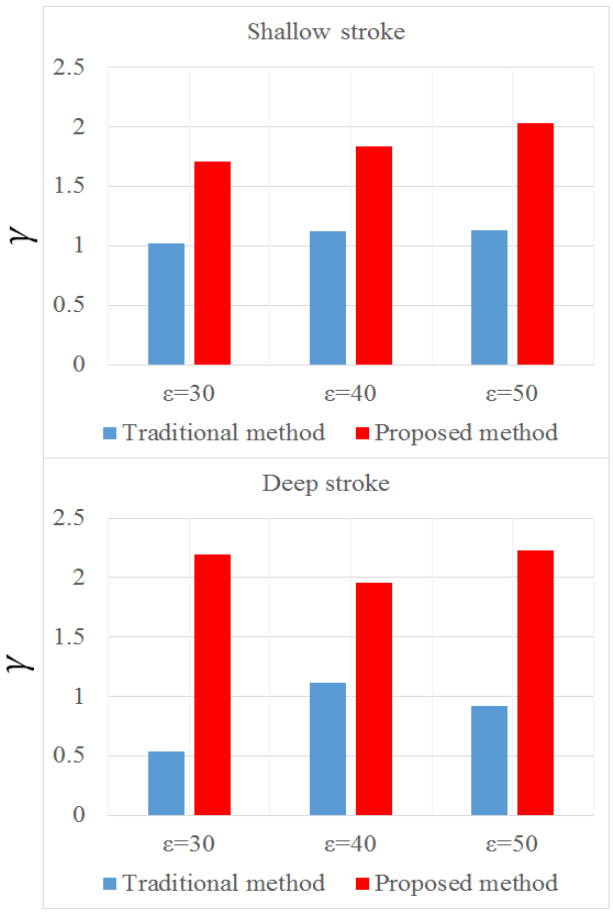
Shallow stroke
2.5
2
1.5
1
0.5
0
γ
ε=30
ε=40
ε=50
Traditional method
Proposed method
Deep stroke
2.5
2
1.5
1
0.5
0
γ
ε=30
ε=40
ε=50
Traditional method
Proposed method

(a)

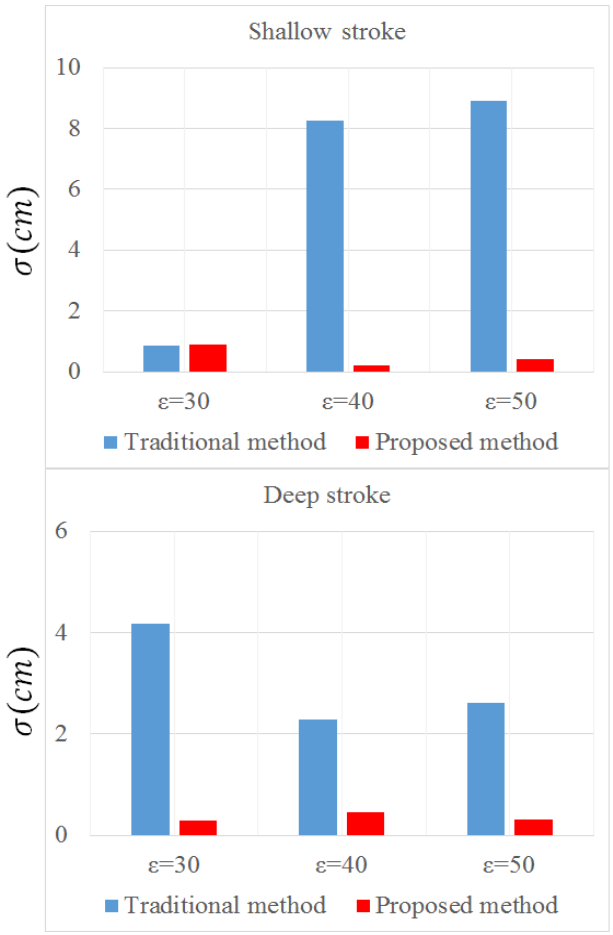
Shallow stroke
10
8
6
4
2
0
σ(cm)
ε=30
ε=40
ε=50
Traditional method
Proposed method
Deep stroke
6
4
2
0
σ(cm)
ε=30
ε=40
ε=50
Traditional method
Proposed method

(b)

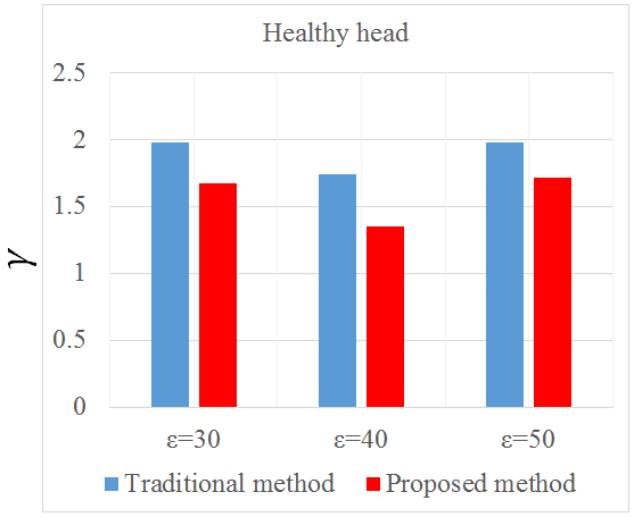

(c)

Fig 5. 9: The value of (a) $\boldsymbol{\gamma}$ and (b) σ from using the traditional and proposed method on two cases (shallow and deep stroke) and different initial values of dielectric constants, and (c) $\boldsymbol{\gamma}$ for a healthy case.

where $\mathcal{C}$ is the position of the real stroke center. It can be seen from (5.16)-(5.17) that an ideal image quality requires γ to be high positive number and σ to be close to 0.

Figure 5.10 shows the value of the metrics for the images produced using the traditional and proposed methods for the three cases (shallow stroke, deep stroke and healthy head) with different initial estimations of the dielectric constant. It can be seen from Figure 5.10 (a) that the value of metric γ in the proposed method is almost twice its value when using the traditional method. The results also indicate that the choice of the initial estimation of $\boldsymbol{\varepsilon}$ does not affect the performance of the proposed method. Figure 5.10 (b) shows that the proposed method can localize the stroke accurately with σ less than 1 cm for the two cases, while the traditional method predicts an incorrect stroke position for the two cases. The traditional method is very sensitive to the initial value of the dielectric constant as depicted in Figure 5.10, whereas the proposed method is not sensitive in any way to that value and this is of great importance when imaging human subjects. To inspect effect of using the proposed approach on a healthy case, the metric γ is calculated from the obtained images of that case and the result is presented in Figure 5.10 (c). It is clear that the proposed method reduces the probability of false positive alarm as γ is reduced compared with using the traditional method.

5.4 Evaluation on Realistic Measurement Data

To further verify the proposed algorithm, two sets of experiments are conducted using the imaging systems shown in Figure 5.11, [40], [141]. The utilized system of Figure 5.11 (a) uses the portable microwave transceiver Agilent (N7081A) to send and receive microwave signals with a maximum dynamic range of 80 dB. An adjustable platform is used to collect the scattered signals from the imaging object. One antenna, which uses a combination of slotted dipole element and a folded parasitic structure to cover the band 1.1-3.4 GHz, is used in the system. The system depicted in Figure 5.11 (b) uses R&S ZVA24 vector network analyser for signal generation and data acquisition. It uses a single three-dimensional antenna that covers the band from 1.2 to 2.75 GHz. To emulate data from using 32 antennas, several sets of measurements with the mechanical rotation of the platform carrying the head phantoms under test is performed when doing the experiments. The experiments are conducted on two realistic head phantoms, which includes the main tissues of the head, such as skin, fat, muscular, skull, Dura, cerebrospinal fluid, gray matter, white matter, cerebellum, and spinal cord [40], [144]. The two phantoms are built using MRI-derived models. A mixture of materials, such as water, corn flour, gelatin, agar, sodium azide, and propylene glycol, are used to assemble different tissues of the head. The dielectric properties of those artificial tissues are verified using the dielectric probe HP85070 to make sure of their match to the real tissues. To emulate a haemorrhagic stroke in the experiments, a small volume of blood-imitating chemical material with the size of $2 \times 2 \times 1cm^3$ and $1.5 \times 1.5 \times 0.5cm^3$ is positioned inside the head phantoms of the systems depicted in Figure 5.11 (a) and (b), respectively.

The obtained images from using the proposed and traditional algorithms to process the collected data from the experiments on the two systems are shown in Figures 5.12 and 5.13. It can be seen from those images that the position of the stroke can be approximately localized using the traditional method but with low focused images. However, the targets in the images generated using the proposed method can be accurately detected and localized from the highly focused images. The results also indicate that the proposed method always converges regardless of the initial choice of the assumed dielectric constant. Figure 5.14 shows the convergence rate of the proposed method in the two experiments. It can be seen from Figure 5.14 that the proposed algorithm converges in less than 50 iterations (actually around 20 iterations) regardless of the initial choice of the dielectric constant $\boldsymbol{\varepsilon}$.

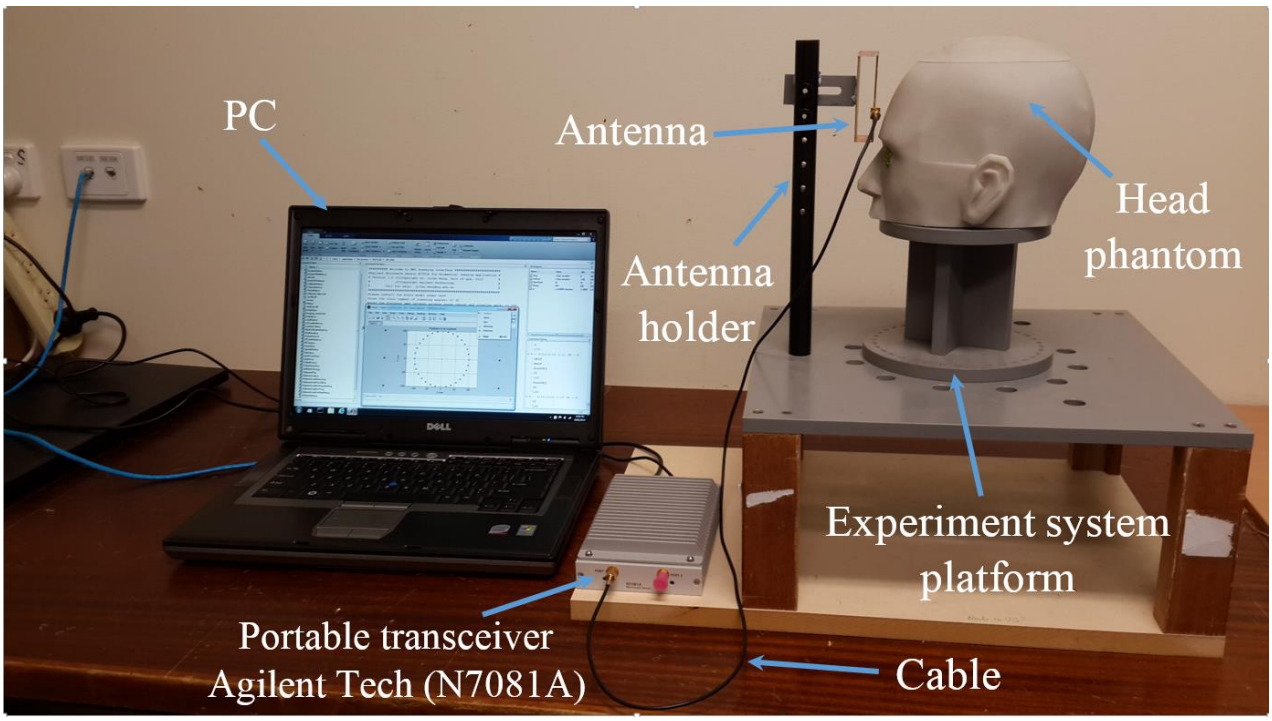

(a)

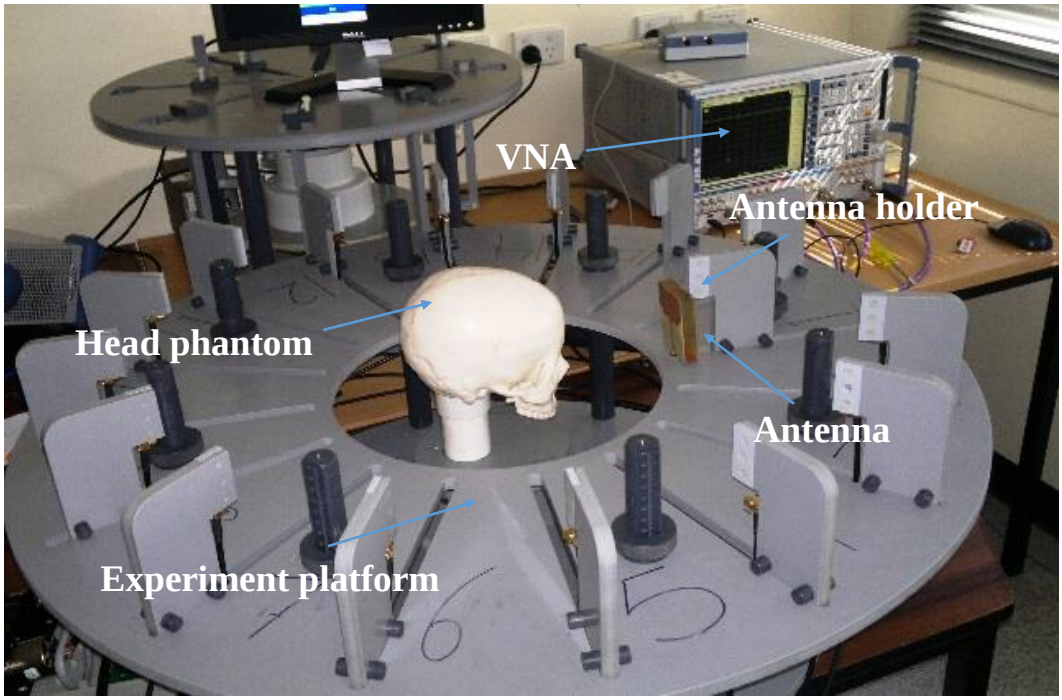

(b)

Fig 5. 10: The experimental system used to test the proposed algorithm. (a) System described in [40], and (b) system described in [141].

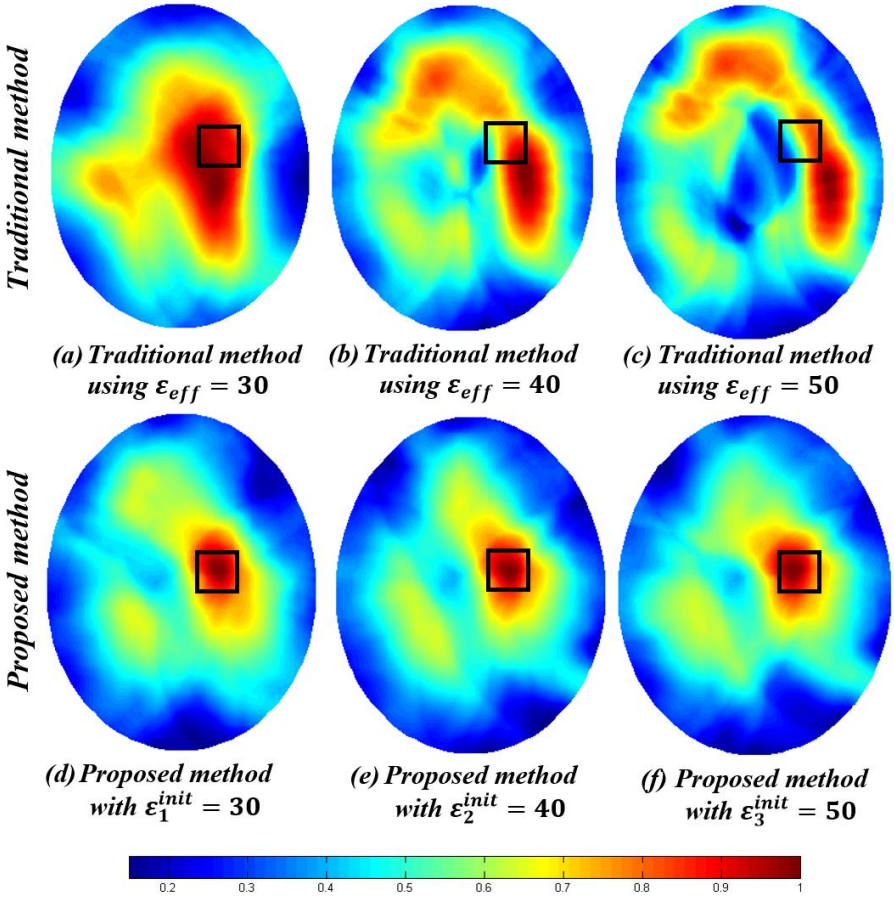

Fig 5. 11: Experimental results using the system in [141].

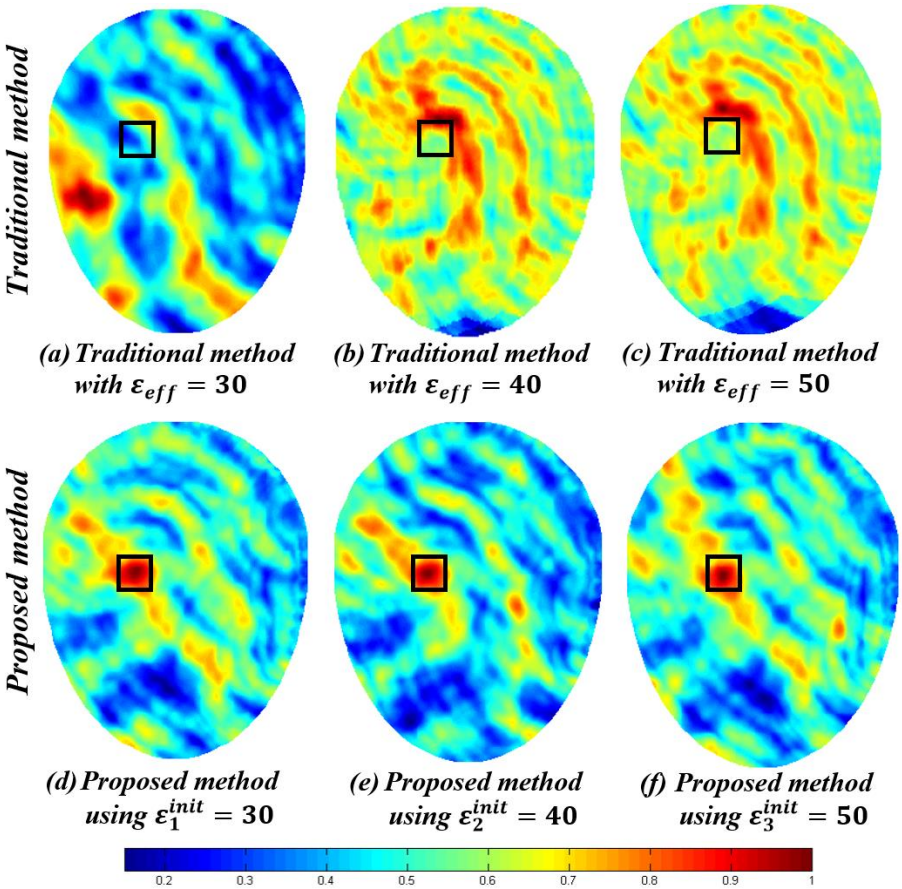

Fig 5. 12: Experimental results using the system in [40].

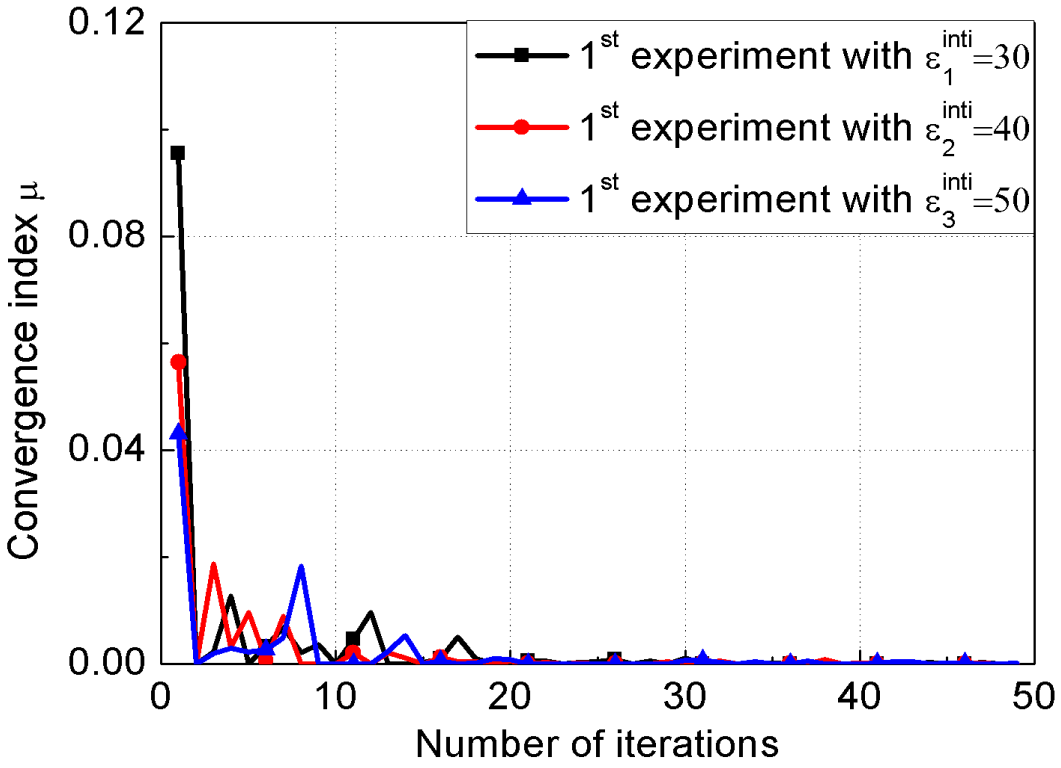

(a)

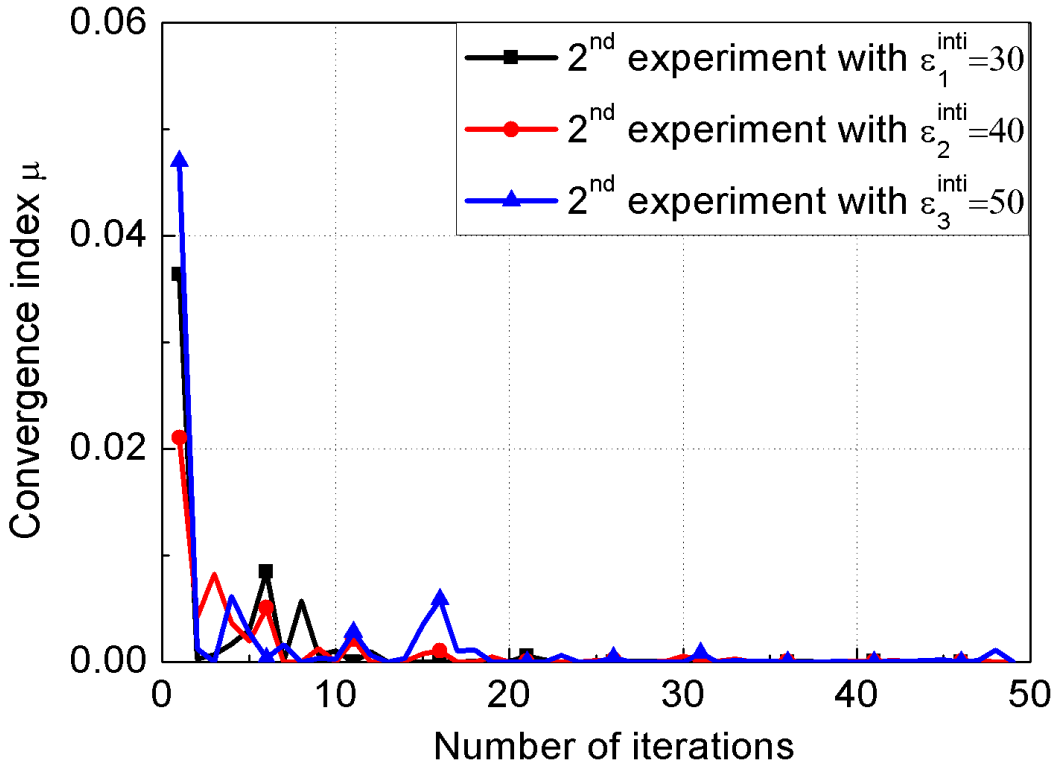

(b)

Fig 5. 13: The convergence index $\boldsymbol{\mu}$ with iteration time for (a) 1st experiment and (b) 2nd experiment.

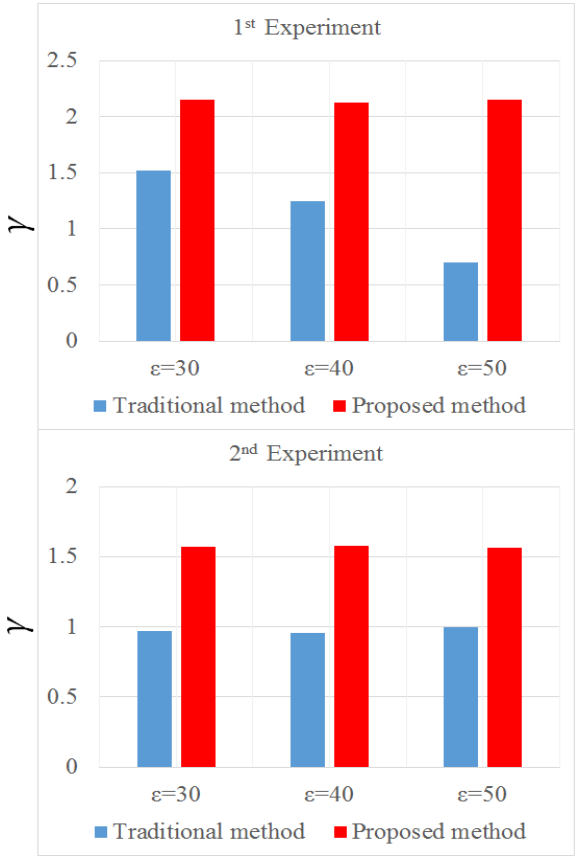

(a)

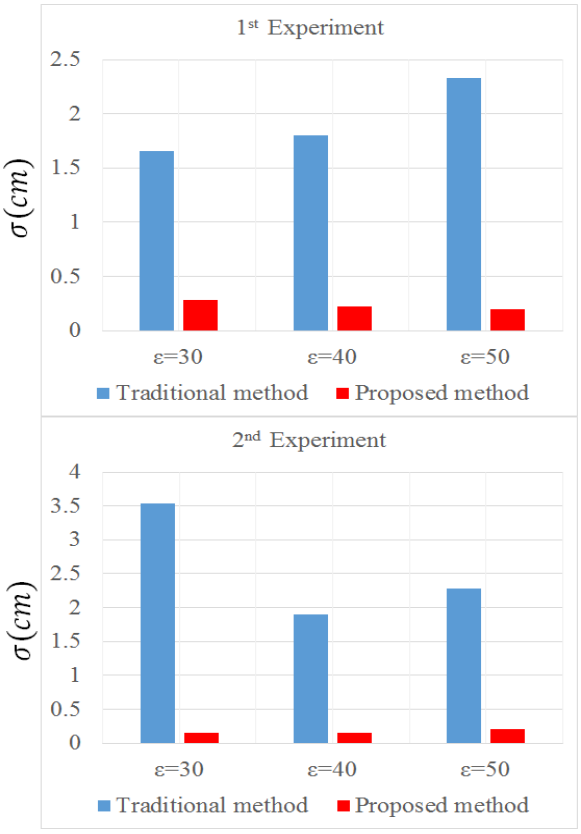

(b)

Fig 5. 14: Quality metrics (a) $\boldsymbol{\gamma}$ and (b) σ of images produced using the traditional and proposed method in two experiments.

To quantify the obtained images in Figure 5.12 and 5.13, the two metrics γ and σ are calculated and shown in Figure 5.15. The value of metric γ is significantly improved when using the proposed method compared with the traditional method irrespective of the initial value of $\boldsymbol{\varepsilon}$. Figure 5.15 (b) shows that the proposed method can localize the stroke accurately with σ less than 0.5 cm in the two experiments, while the traditional method leads to an inaccurate localization of the stroke with more than 1.5 cm error. The value of σ is also stable at a very low value (ideally zero) irrespective of the initial value of the dielectric constant when using the proposed algorithm. The experimental results validate the simulations in that the proposed algorithm is not sensitive to the initial values in constrast to the traditional method.

5.5 Discussions and Conclusions

An optimization-based confocal algorithm for medical imaging has been presented in this chapter. The proposed algorithm optimizes position-dependent dielectric constants based on a certain objective equation to obtain a highly focused image that accurately maps scatterers within the imaged object. This is in clear contrast to the traditional confocal algorithm, which uses one pre-assumed effective dielectric constant and is thus highly dependent on that assumed value. The proposed method has been tested successfully in head imaging for stroke detection using simulations and experiments. The simulations are based on accurate numerical head model, whereas the experiments are implemented using realistic artificial head phantoms. Compared with the results using traditional method, the proposed algorithm significantly improves the quality of the images for both healthy and unhealthy cases with correct detection and localization of the targets (brain stroke) and reduced probability pf positive false alarms. The sensitivity and specificity of the proposed algorithm will be investigated during the preclinical tests of the imaging system, which is aimed to be part of ambulance equipment for onsite stroke diagnosis.

Chapter 6: Brain Stroke Classification in Microwave Imaging

6.1 Classification Using Machine Learning Techniques

6.1.1 K-Means Clustering

To construct an SVM classifier, the dielectric properties of the brain with suspicious stroke need to be firstly estimated. This is implemented using the Born iterative method (BIM) which was introduced in section 4.2.1, chapter 4. Assume the normalized dielectric profile (NDP) $\mathcal{X}(x, y)$ is defined as (4.1), then $\mathcal{X}(x, y)$ can be reconstructed by solving the ill-posed inverse problem (4.6). The recovered NDP from BIM is usually inaccurate due to the ill-posed nature of the inverse problem. Therefore, it is difficult to classify the type of the stroke based on the BIM generated NDP. Figure 6.1 and 6.2 indicate the BIM-generated NDP (the frequency used is 0.85 GHz, which is proved to be an appropriate frequency for microwave head imaging tomography [50]) using two MRI scanned phantom [79], [158] (Phantom A, which is an MRI-derived and constructed with $256\times 256 \times 128$ cubical elements with dimensions of $1.1\ mm \times 1.1\ mm \times 1.4\ mm$ [79] and Phantom B, which is also MRI-derived and constructed with 256×256 elements and the size of each element is $2mm$ [158]) with two inserted types of stroke (ICH and IS stroke).

It can be seen from Figure 6.1-6.2 that the position and type of the stroke are difficult to be localized and classified merely from the real and imaginary part of the calculated NDP $\mathcal{X}(x, y)$ especially for phantom A. One way to emphasize the position of the stroke is by taking the amplitude of NDP (termed as $\mathcal{C}_{\mathcal{X}}$):

$$\mathcal{C}_{\mathcal{X}} = \sqrt{\mathcal{R}e^2(\mathcal{X}) + \mathcal{I}m^2(\mathcal{X})} \tag{6.1}$$

where $\mathcal{R}e(\mathcal{X})$ is the real part of $\mathcal{X}$ and $\mathcal{I}m(\mathcal{X})$ is the imaginary part of $\mathcal{X}$. Figure 6.3 shows the calculated $\mathcal{C}_{\mathcal{X}}$ for the reconstructed NDP for the images in Fig. 6.1 and 6.2. It can be seen from Figure 6.3 that the position of the stroke (both for ICH and IS in phantoms A and B) can be localized from the $\mathcal{C}_{\mathcal{X}}$ profile. However, the strokes are still difficult to classify based on the profile since the reconstructed values of the other tissues might be very close to that of the stroke (the calculated value for ICH stroke is close the gray matter and CSF) due to the error from the BIM. Therefore, it is desirable to reduce the influence of the other tissues when the $\mathcal{C}_{\mathcal{X}}$ profile is used as the input for a

classifier. Hence, the k-means clustering method is used to cluster the $\mathcal{C}_\chi$ profile into three clusters that enable the differentiation of the various tissue types.

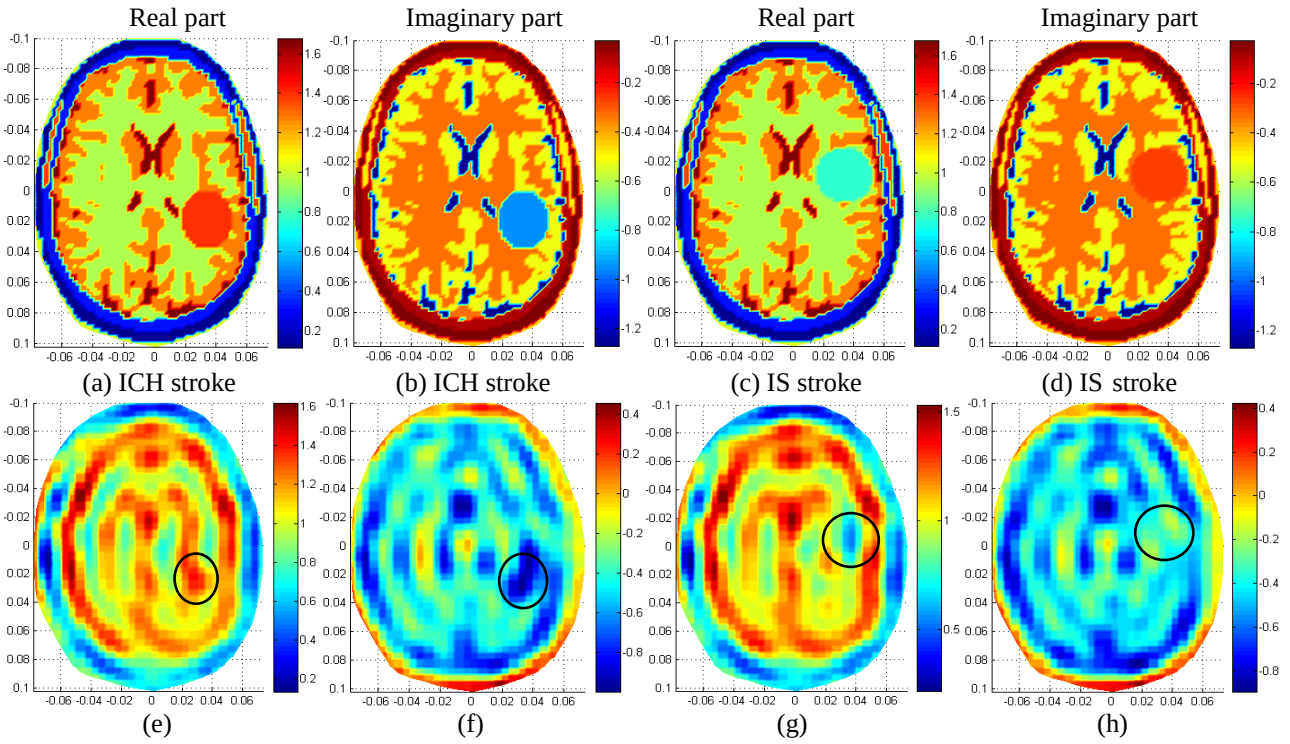

Fig 6. 1: (a)-(b) The phantom A with ICH stroke and (c)-(d) phantom A with IS stroke, (e)-(h) the calculated NDP using BIM corresponding to each of the cases shown in (a)-(d).

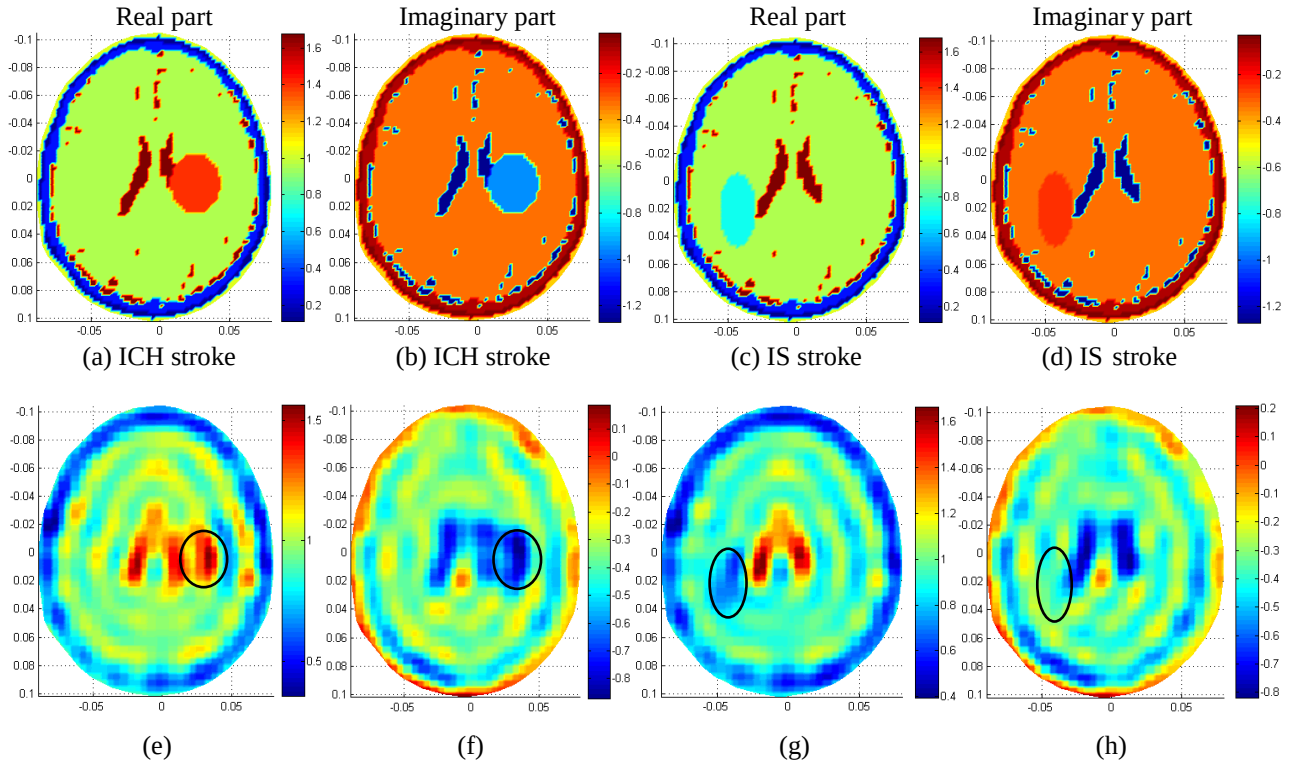

Fig 6. 2: (a)-(b) The phantom B with ICH stroke and (c)-(d) the phantom B with IS stroke, (e)-(h) the calculated NDP using BIM corresponding to each of the cases shown in (a)-(d).

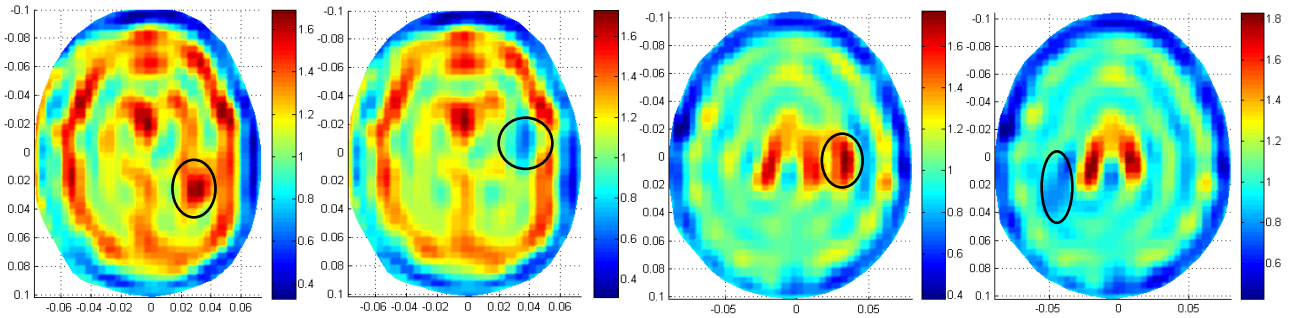

(a) (b) (c) (d)

Fig 6. 3: The calculated $\mathcal{C}_x$ for (a) phantom A with ICH; (b) phantom A with IS; (c) phantom B with ICH and (d) phantom B with IS.

K-means clustering divides *N* data points in *I* dimensional space into *K* clusters. Each of the clusters is featured by its mean value $\mu^{(k)}$. One of the simplest algorithms used to solve this problem is Lloyd's algorithm [159]. With this algorithm, the distance between two data points is defined as:

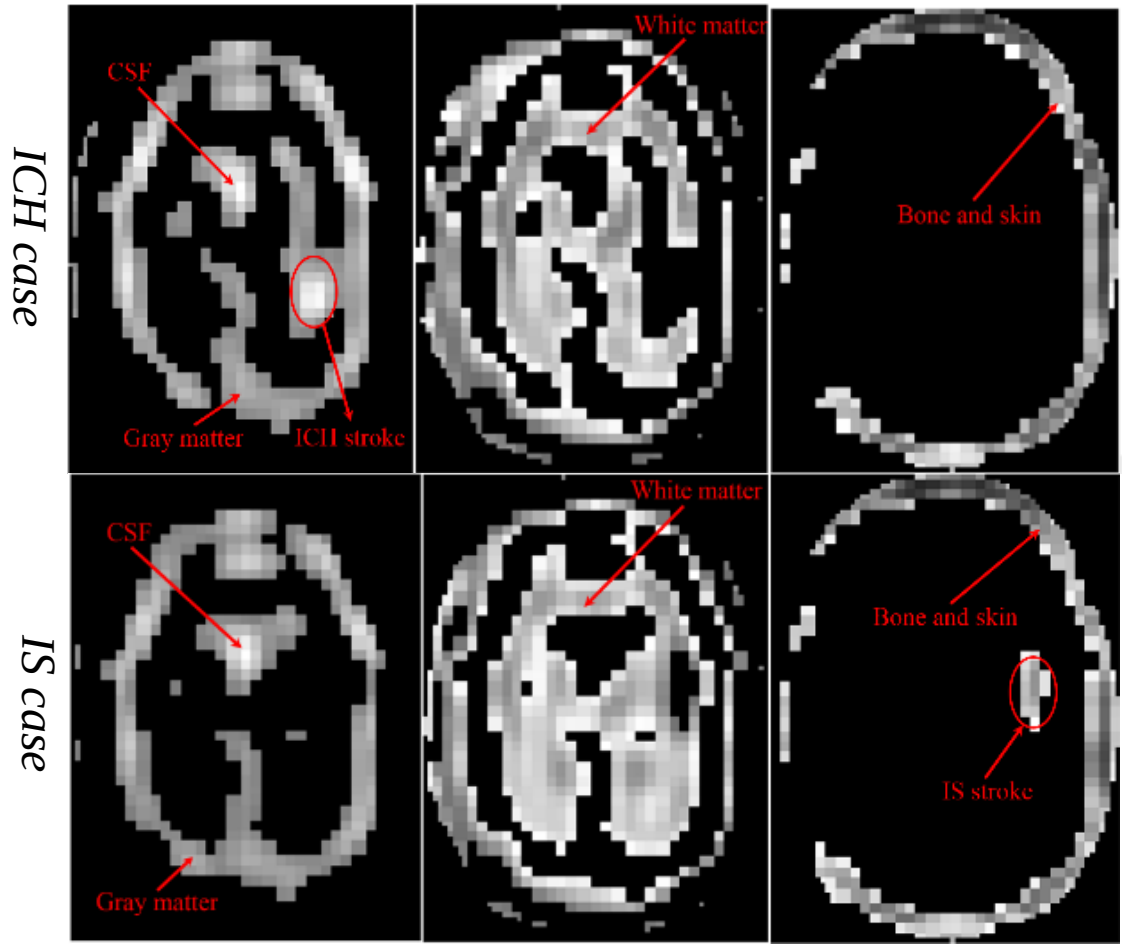

(a) The 1st cluster (b) The 2nd cluster (c) The 3rd cluster

Fig 6. 4: The clustered $\mathcal{C}_x$ profile for phantom A using k-means method when two types of stroke (ICH and IS) are placed inside the brain.

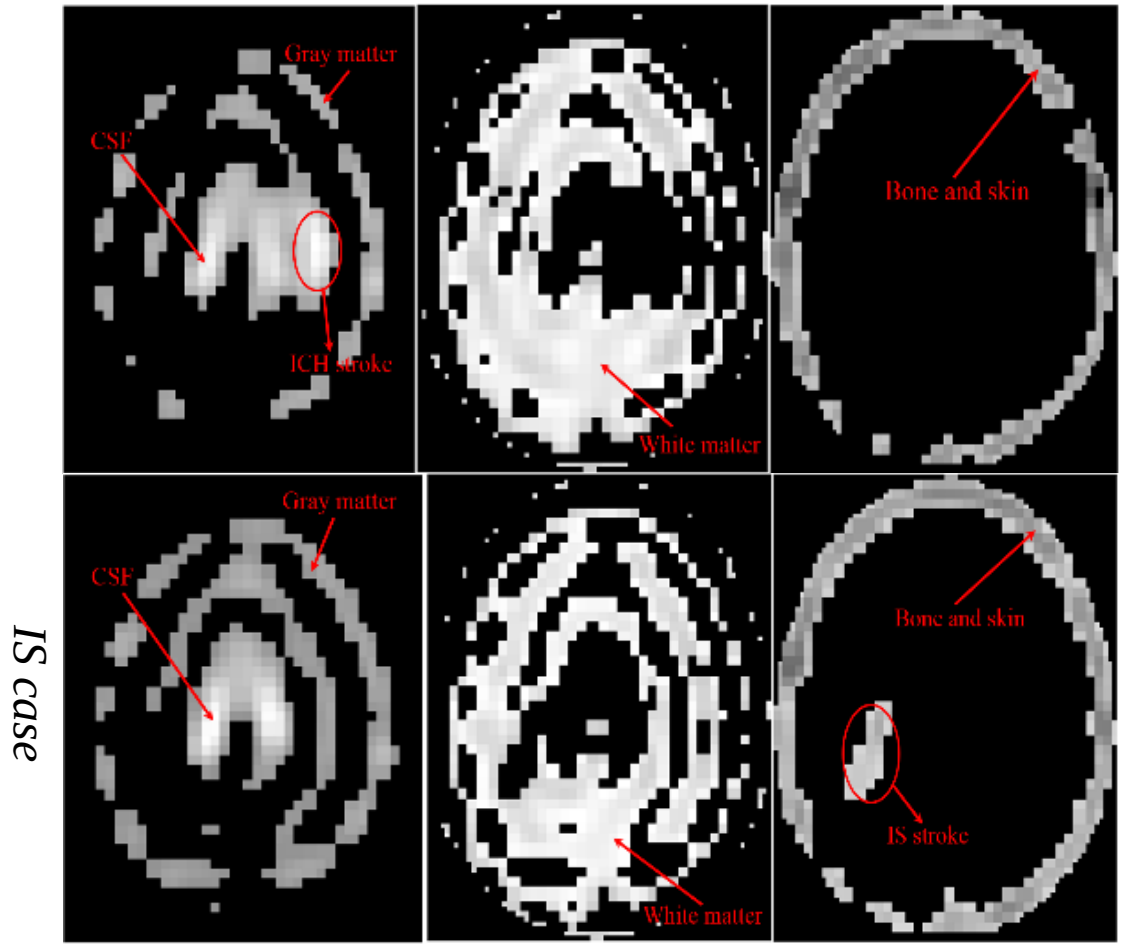

(a) The 1st cluster (b) The 2nd cluster (c) The 3rd cluster

Fig 6. 5: The clustered $\boldsymbol{c_x}$ profile for phantom B using k-means method when two types of strokes (ICH and IS) are placed inside the brain.

$$d(x,y) = \frac{1}{2}\sum_{i}^{I}(x_i - y_i)^2 \tag{6.2}$$

Lloyd's algorithm indicates that the optimal placement of a cluster center is at the centroid (the mean value of each cluster, $\mu^{(k)}$) of the associated cluster. Let us assume $\mathcal{U}$ a set of centers with each center $\mu^{(k)} \in \mathcal{U}$, and define $\mathcal{T}_k$ as the neighbourhood points of $\mu^{(k)}$ (the set of data points with nearest distance to $\mu^{(k)}$). At each stage of Lloyd's algorithm, every center point $\mu^{(k)}$ is moved to the centroid of $\mathcal{T}_k$ (the mean value of $\mathcal{T}_k$) and updated by recalculating the distance from each point to its nearest center. These two steps are repeated until a convergence condition is satisfied [160]. This procedure is written as:

Initialization: Set K centers $\mu^{(k)}$with random values.
Assignment step:

$$\mathcal{T}_k = \left\{x_n: \left\|x_n - \mu^{(k)}\right\|^2 \leq \left\|x_n - \mu^{(j)}\right\|^2 \ \forall j, 1 \leq j \leq K\right\}$$

Update step: $\mu^{(k)} = \frac{1}{|\mathcal{T}_k|}\sum_{x_i \in \mathcal{T}_k} x_i$

Repeat assignment and update steps until converged

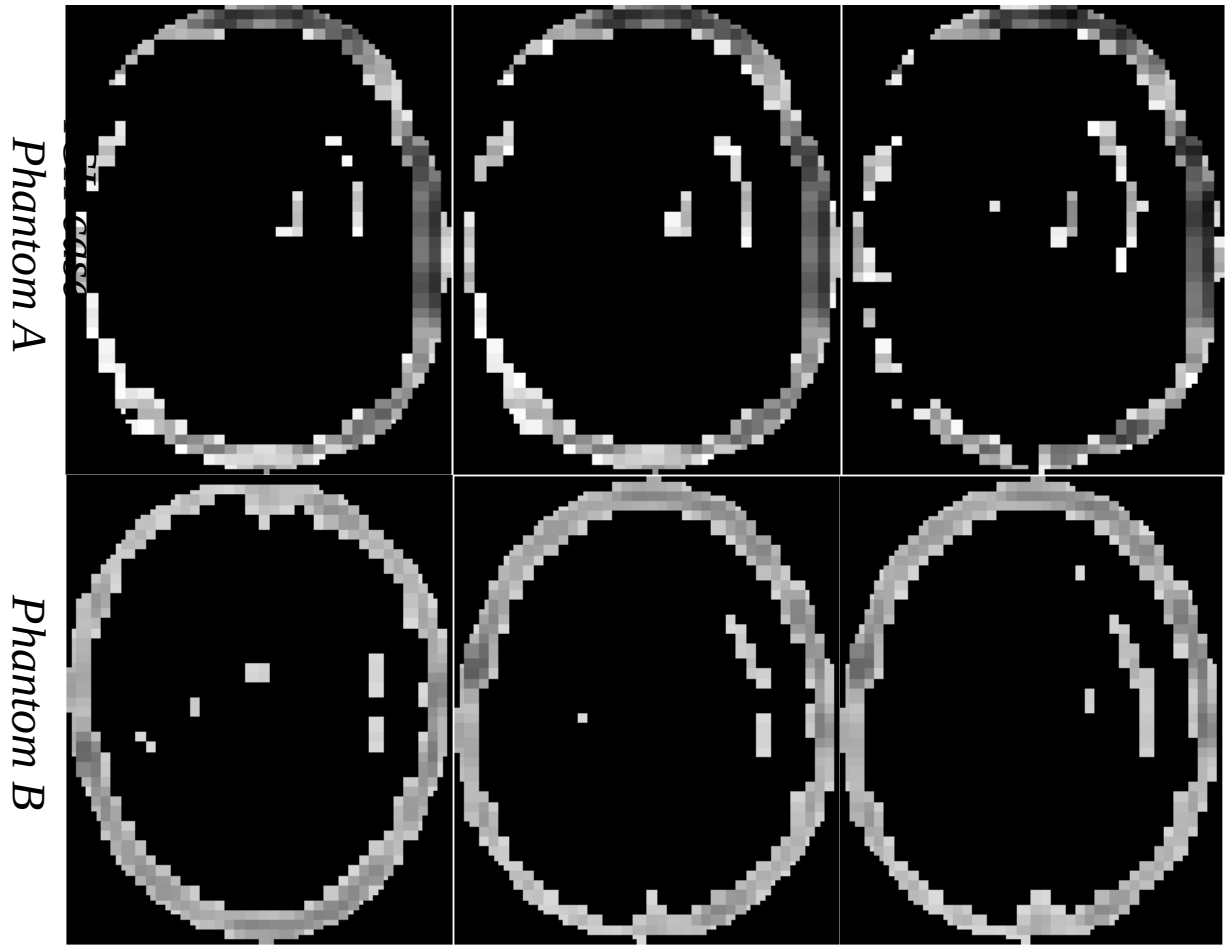

(a) SNR=40 dB (b) SNR=25 dB (c) SNR=10 dB

Fig 6. 6: The third clusters of the ICH cases for phantom A and B indicate that the inner part of the head boundary is not a null space.

The calculated $\mathcal{C}_\chi$ profile shown in Figure 6.3 is clustere using the described k-means method and the results are shown in Figure 6.4-6.5. It can be seen from Figure 6.4-6.5 that the $\mathcal{C}_\chi$ profile can be clustered into three categories. The first contains the gray matter and CSF, the second contains the white matter, while the third contains the bone and skin of the brain (the boundary of the head). Due to the different characteristics of the dielectric properties for ICH and IS strokes, they are clustered into different categories. Figure 6.4 and 6.5 indicate that the ICH stroke is clustered with the gray matter and CSF (the first category) due to their almost identical dielectric properties, whereas the IS stroke is clustered with the bone and skin of the brain (the boundary) also due to their close dielectric properties. Therefore, it is possible to implement the classification task based on the clustered

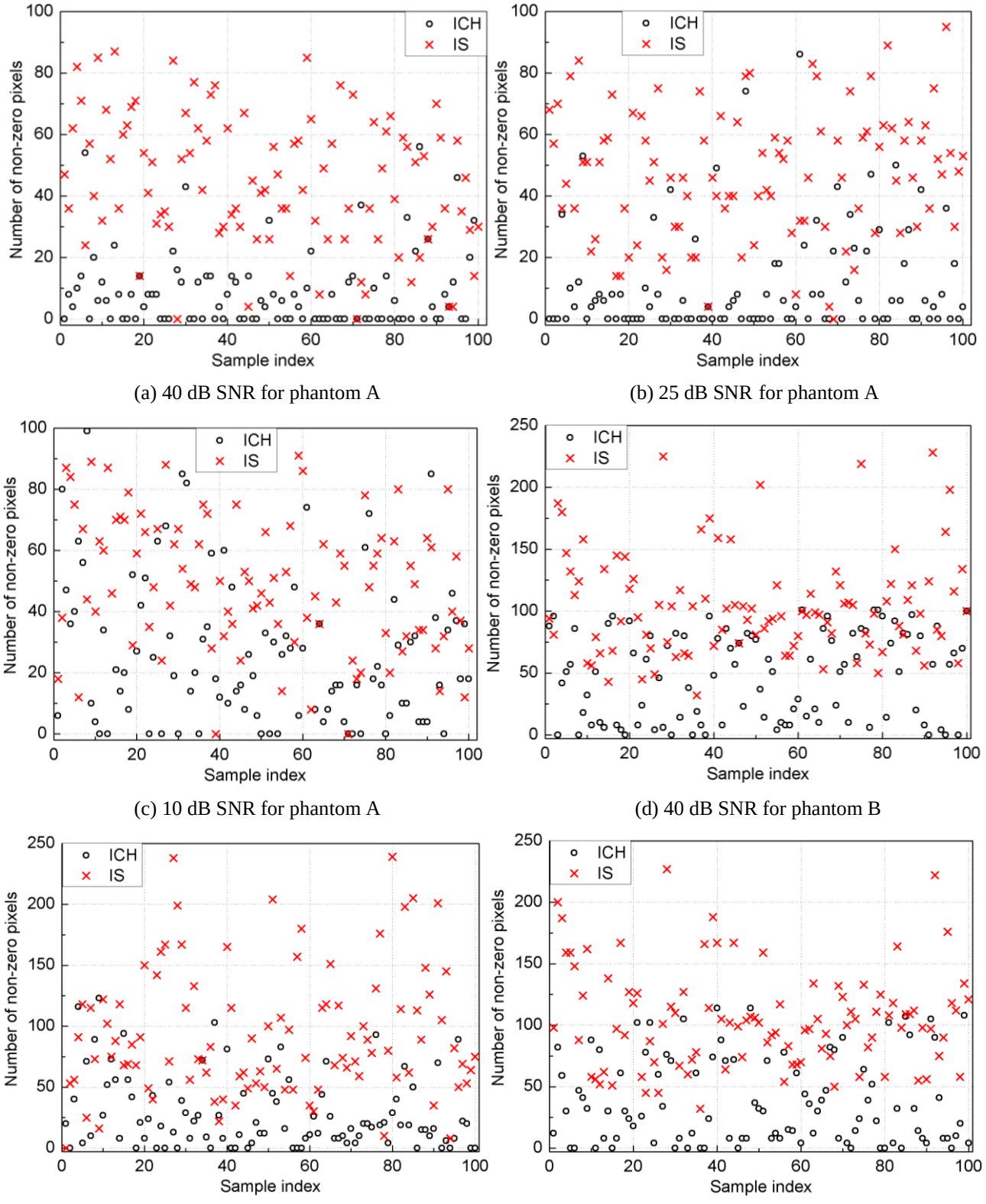

(a) 40 dB SNR for phantom A

(b) 25 dB SNR for phantom A

(c) 10 dB SNR for phantom A

(d) 40 dB SNR for phantom B

(e) 25 dB SNR for phantom B

(f) 10 dB SNR for phantom B

Fig 6. 7: The number of non-zero pixels within the inner part of the third cluster for both ICH and IS cases when the SNRs are 40, 25, and 10 dB for (a)-(c) phantom A and (d)-(f) phantom B.

categories since the ICH and IS strokes are clustered into different categories. In the proposed method, the third cluster (the cluster containing the bone and skin) is used to implement the classification. The reason of taking the third cluster for the classification task is because it also defined the boundary of

the brain. The ICH and IS cases have the most significant difference when the inner part of the third cluster (the area inside the brain boundary) is individually taken. For the ICH case, the inner part of the third cluster is a null space (the number of non-zero pixels with respect to the intensity is zero). However, it is not always guaranteed that the inner part of the third cluster is a null space for the ICH case due to the deviation and error from the BIM process and *k*-means clustering. Figure 6.6 indicates that, in some cases, the inner part of the third cluster for the ICH case is not a null space. It can be seen from Figure 6.6 that under different SNR levels, the inner part of the head boundary in the third cluster contains some connected pixels which may possibly be IS cases. This situation is worse in the noisy environment (SNR$\leq$10 dB).

To further illustrate the uncertainty of using the inner part of the head boundary in the third cluster to implement the classification, a sample database is constructed under three SNR levels (SNR=40, 25, and 10 dB). In total, 200 samples are created at each SNR level (100 samples for ICH case and 100 samples for IS case) and the sample database is constructed for both phantom A and B. The detailed information for constructing this database was described in the following section. Figure 6.7 shows the number of non-zero pixels within the inner part of the third cluster for both IS and ICH cases from all the three SNR levels. It can be seen from Figure 6.7 that even when the SNR level is 40 dB (low noise environment), the number of non-zero pixels within the inner part of the third cluster may still be significant for some samples (the number of non-zero pixels is greater than 30 for some samples from phantom A and greater than 50 for some samples from phantom B). This undesirable situation becomes worse when the SNR level is 10 dB (noisy environment). Based on this reasoning, the SVM classifier is used to minimize this adverse effect and build a linear model for a decision curve needed for classification.

6.1.2 Support Vector Machine

Assuming that the subject under test had been diagnosed with stroke, the focus of the proposed method is on the stroke localization and classification. Thus, the stroke classification can be treated as a two-class pattern classification problem. Let $\boldsymbol{x} \in \mathbb{C}^N$ denote the image of the third cluster after vectorization, and let the scalar y represents the class labels ($y = +1$ denotes the ICH case and $y = -1$ denotes the IS case). Additionally, assume $\{(\boldsymbol{x}_i, y_i), i = 1, \dots, l\}$ is a set of training samples. The problem is now how to construct a decision function which can correctly classify an input pattern by using the training samples. In stroke classification scenario, the training samples are usually not linearly separable in the original data space. Hence, to separate the data but still use a linear classifier

model, the original data is mapped into a higher dimensional space, this is implemented using a mapping function $\phi(\cdot)$. To that end, a linear function with the following form is selected

$$f(\boldsymbol{x}) = \boldsymbol{w}^T \phi(\boldsymbol{x}) + b \tag{6.3}$$

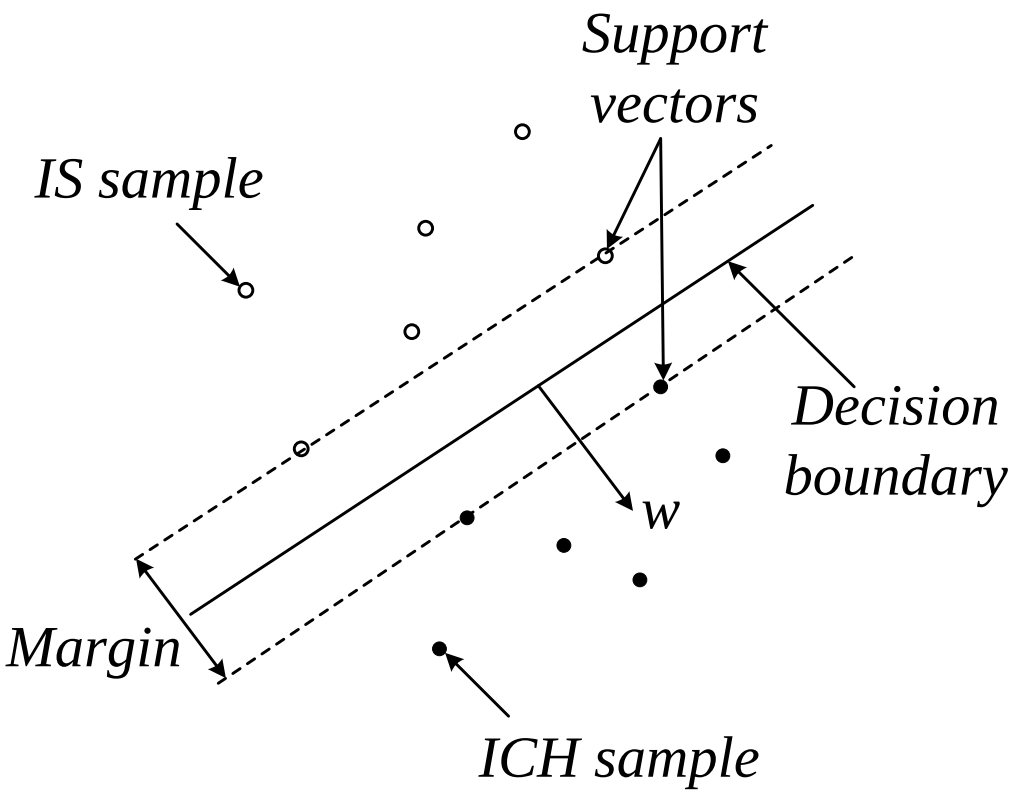

Fig 6. 8: SVM classifier: the decision boundary $\boldsymbol{f(x) = w^T x + b}$ (the thick line) which is defined by a normal vector of the hyperplane and an offset. The margin is the minimal distance of any training points in the two classes (blank circle represents the IS case and solid circle represents the ICH case) to the hyperplane. The support vectors are the training samples lying on the boundary hyperplanes of the two classes.

such that $f(\boldsymbol{x_i}) \geq 0$ for $y_i = 1$ and $f(\boldsymbol{x_i}) \leq 0$ for $y_i = -1$. $\phi(\boldsymbol{x})$ is a nonlinear function which maps the input feature vector into a higher dimensional space. Assume the training samples are separated by several hyperplanes in the space $\mathcal{F}$. The SVM classifier seeks the hyperplane that maximizes the separating margin between the two classes (as shown in Figure 6.8). For non-separable data, this hyperplane can be found by solving the following convex optimization problem [161]-[162]:

$$\min_{\boldsymbol{w},b,\xi} \left\{ \frac{1}{2} \|\boldsymbol{w}\|^2 \right\} + C \sum_{i=1}^{l} \xi_i$$

$$s.b.j: \begin{cases} y_i[\boldsymbol{w}^T\phi(x_i)+b] \geq 1-\xi_i \\ \xi_i \geq 0 \end{cases}, i=1,\dots,l \tag{6.4}$$

where $\xi_i, i=1,\dots,l$ are slack-variables, which are introduced to relax the hard margin constraint [150], [163] and avoid overfitting [161] (the hard margin constraint is $y_i[\boldsymbol{w}^T\phi(x_i)+b] \geq 1$ which is suitable for separable data), $C>0$ is a regularization constant. A larger value of C implies a higher penalty to the errors. The convex optimization problem (6.4) was solved using its corresponding primal Lagrangian and an algorithm named successive minimal optimization [164]-[165] from a library for support vector machine [166]. Using Lagrange multipliers $\alpha_i, \gamma_i \geq 0, i=1,\dots,l$ for each of constraints in (6.4) (α_i is the Lagrange multiplier for constraint $y_i[\boldsymbol{w}^T\phi(\boldsymbol{x})+b] \geq 1-\xi_i$ and γ_i is the Lagrange multiplier for $\xi_i \geq 0$), the corresponding primal Lagrange is:

$$L_P = \frac{1}{2}\|\boldsymbol{w}\|^2 + C\sum_{i=1}^{l}\xi_i - \sum_{i=1}^{l}\gamma_i\xi_i - \sum_{i=1}^{l}\alpha_i\{y_i[\boldsymbol{w}^T\phi(x_i)+b]-1+\xi_i\} \tag{6.5}$$

By applying Karush-Kuhn-Tucker (KKT) conditions on the primal problem (6.5), the following constraints can be achieved:

$$\frac{\partial L_P}{\partial \boldsymbol{w}} = \boldsymbol{w} - \sum_{i=1}^{l}\alpha_i y_i\phi(x_i) = 0 \tag{6.6}$$

$$\frac{\partial L_P}{\partial b} = -\sum_{i=1}^{l}\alpha_i y_i = 0 \tag{6.7}$$

$$\frac{\partial L_P}{\partial \xi_i} = C-\alpha_i-\gamma_i = 0 \tag{6.8}$$

$$y_i[\boldsymbol{w}^T\phi(x_i)+b]-1+\xi_i \geq 0 \tag{6.9}$$

$$\alpha_i \geq 0, \gamma_i \geq 0, \xi_i \geq 0 \tag{6.10}$$

$$\alpha_i\{y_i[\boldsymbol{w}^T\phi(x_i)+b]-1+\xi_i\} = 0 \tag{6.11}$$

$$\gamma_i\xi_i = 0 \tag{6.12}$$

The constraint (6.8) implies that $\alpha_i \leq C$ due to the condition $C>0$ and (6.10). Substituting (6.6)-(6.7) into (6.5), the dual problem can be achieved:

$$\max_{\alpha} \sum_{i=1}^{l} \alpha_i - \frac{1}{2} \sum_{i=1}^{l} \sum_{j=1}^{l} \alpha_i \alpha_j y_i y_j \mathcal{K}(x_i, x_j)$$
$$s.b.j: \begin{cases} 0 \leq \alpha_i \leq C, & i = 1, \dots, l \\ \sum_{i=1}^{l} \alpha_i y_i = 0 \end{cases} \quad (6.13)$$

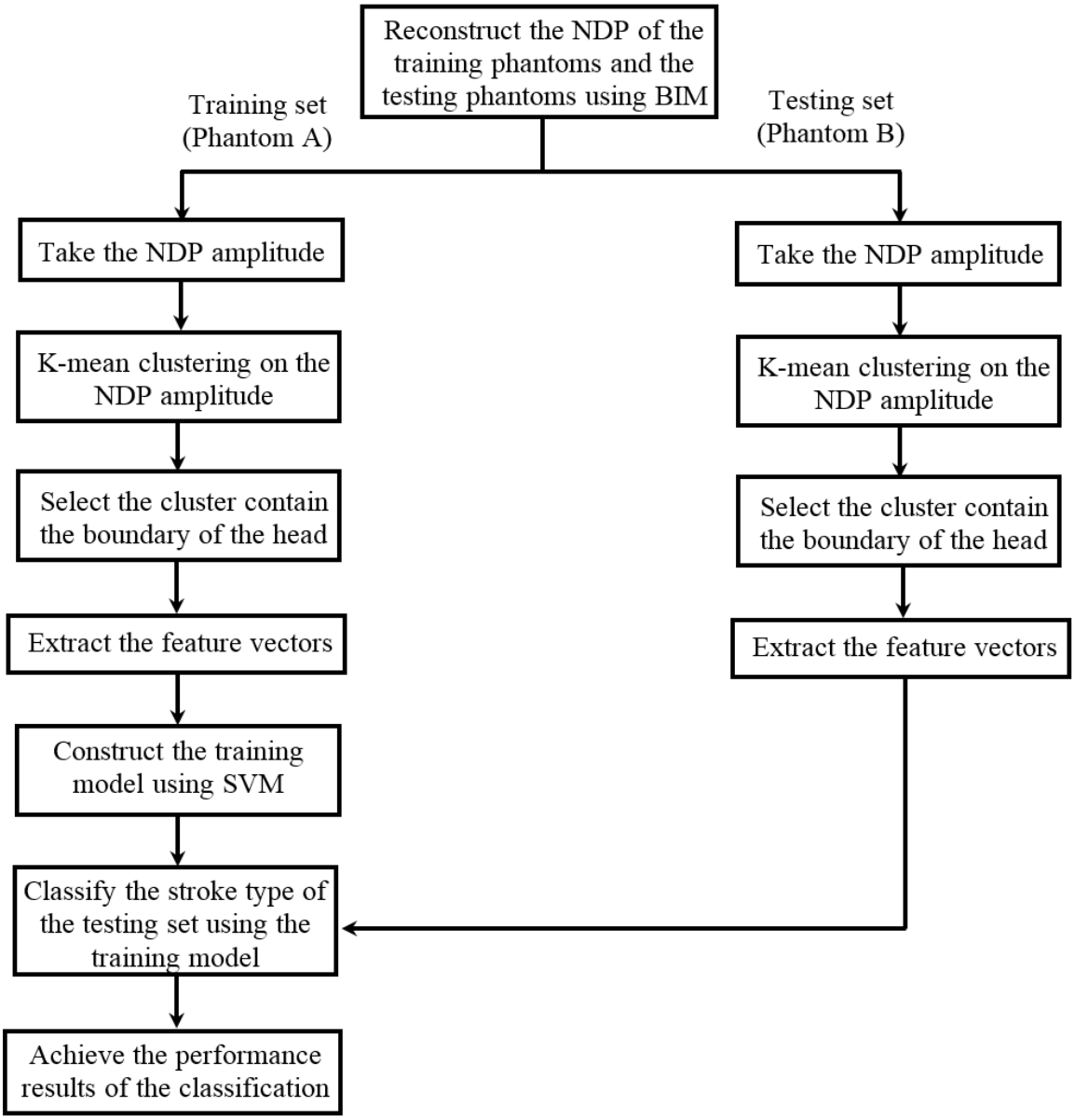

Fig 6. 9: Flowchart of the proposed algorithm framework

This convex optimization problem (6.13) can be numerically solved using quadratic programming. After solving (6.13), the SVM classifier model can be determined using the KKT conditions from (6.6)-(6.12). It is notable that three conditions can be deduced from the KKT conditions (6.6)-(6.12)

1. $$\alpha_i = 0 \rightarrow y_i[\boldsymbol{w}^T\phi(x_i) + b] \geq 1 \; and \; \xi_i = 0 \tag{6.14}$$
2. $$\alpha_i = C \rightarrow y_i[\boldsymbol{w}^T\phi(x_i) + b] \leq 1 \; and \; \xi_i \geq 0 \tag{6.15}$$
3. $$0 < \alpha_i < C \rightarrow y_i[\boldsymbol{w}^T\phi(x_i) + b] = 1 \; and \; \xi_i = 0 \tag{6.16}$$

For the training set in which the data can be well classified, (6.14) indicates that the SVM solution is sparse (most of the training points are outside the margin area) and (6.16) implies that the SVM classifier is actually decided by the support vectors (the training points lying on the boundary of the margin). Therefore, denote $s_i, \alpha_i^*, i = 1, \dots, l_s$ as the support vectors and the corresponding coefficients, the SVM decision function can be expressed as:

$$f(\boldsymbol{x}) = \sum_{i}^{l_s} \alpha_i^* \, y_i \mathcal{K}(s_i, \boldsymbol{x}) + b \tag{6.17}$$

where α_i^* satisfy $0 < \alpha_i^* < C$ is the Lagrange multiplier, $\mathcal{K}(\cdot)$ is the kernel function defined as:

$$\mathcal{K}(x, y) = \phi^T(x)\phi(y) \tag{6.18}$$

The Gaussian RBF function which satisfies the Mercer condition [167] is selected as the kernel function in this paper:

$$\mathcal{K}(x, y) = e^{\left(-\frac{\|x-y\|^2}{2\sigma^2}\right)} \tag{6.19}$$

The entire procedure of constructing and testing the SVM classifier is shown in a flowchart of Figure 6.9 and summarized in the following steps:

1) Reconstruct the NDP of the training phantoms (phantom A) and test phantoms (phantom B) using BIM.
2) Transfer the reconstructed NDP to $\mathcal{C}_\mathcal{X}$ profile using (6.1).
3) Implement k-means clustering on the $\mathcal{C}_\mathcal{X}$ profile to construct three different clusters.
4) Select the cluster containing the bone of the brain and select the inner parts of this cluster that are inside the boundary of the head (the boundary is defined by the bone of the brain).
5) Vectorize the image of the cluster containing the head boundary as the feature vectors.
6) For training set, use the feature vectors to construct the SVM classifier. For testing set, use the feature vectors to evaluate the SVM classifier.

6.2 Classifier Training Procedure

To use support vector machine (SVM), the training database and testing database need to be constructed. In the proposed framework, these two datasets are constructed under three different SNR levels (SNR=40 dB, 25 dB, and 10 dB). For each SNR level, 100 images for ICH case and 100 images for IS case are generated. Two sets of 600 Born iterative method (BIM) generated images are used for the training and testing databases respectively. The dataset structure is indicated in Figure 6.10.

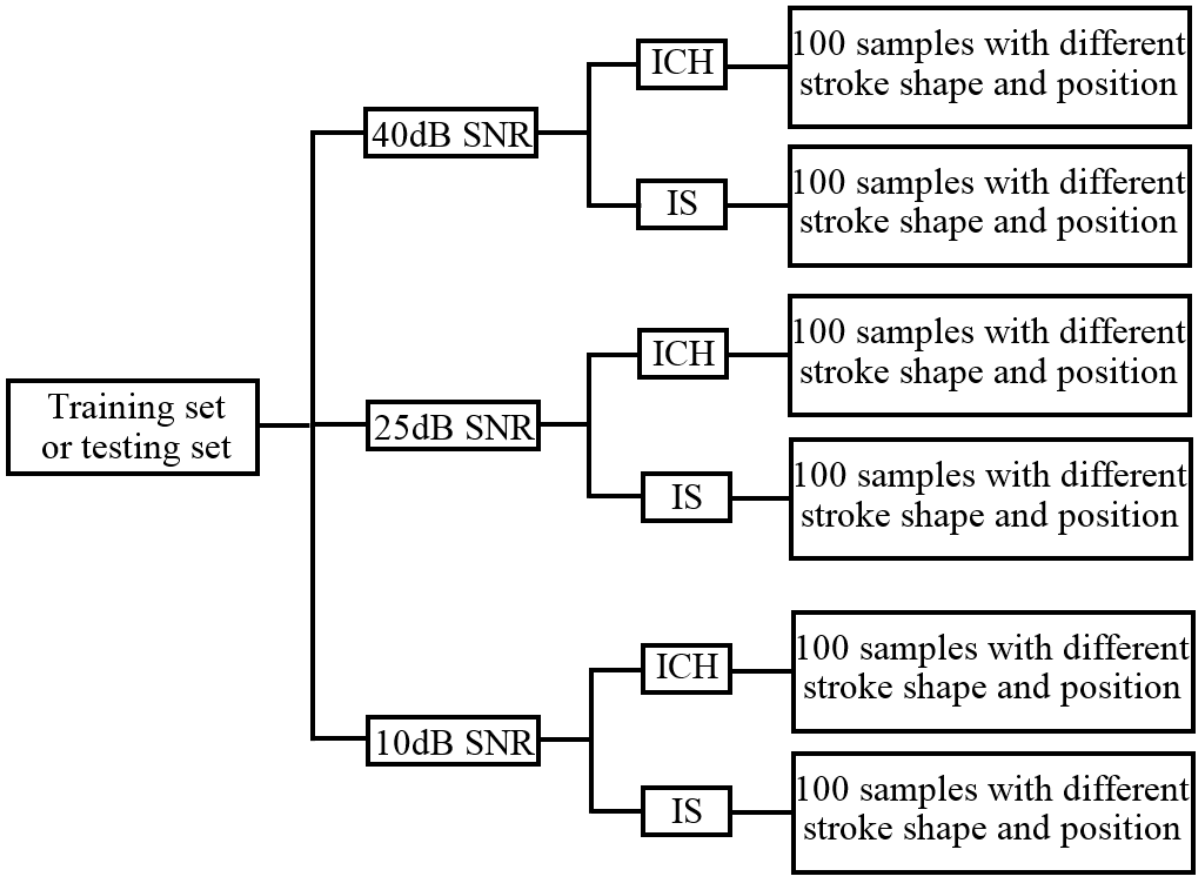

Fig 6. 10: Database structure used in the SVM training and testing

Among all of the images, the positions and shapes of the stroke are different. The shape of the stroke is elliptical with the major and minor axis following the Gaussian distribution (maximum of the major axis=19 mm, minimum of the minor axis=11 mm) and position of the stroke is randomly selected inside the brain. To avoid biasing results, two head phantoms (phantom A [79] for constructing the training dataset and phantom B [158] for constructing the testing dataset) are used in the classification process as shown in Figure 6.9. A transverse slice of the phantom at approximate 50 mm from the crown of the head is extracted from the 3D phantom. The phantom contains the major tissues inside the human brain (skin, skull, skeletal muscle, fat, blood, dura, CSF, gray and white matter). A transceiver slice at about 60 mm from the crown of the head of phantom B that includes the main

brain tissues (skin, skull, muscle, fat, blood, CSF, gray and white matter) is extracted. The data volume was rescaled and interpolated to produce cubical voxels with the size of 2 mm [158].

After the training dataset is constructed, the SVM decision function (6.17) is found by solving the convex problem (6.4). However, before implementing any quadratic programing algorithm to solve (6.4), two parameters need to be determined: the regularization constant C and the parameter σ in the Gaussian RBF kernel function. These two parameters are determined using v-fold cross-validation [161]. In v-fold cross-validation, the training set is firstly divided into v subsets with equal size. For each pair of parameters (C, σ), the SVM classifier is trained v times. For each time of training, one of the subset is chosen as the validation set and the remaining $v - 1$ subsets are used to train the SVM model. Therefore, a total of v classification accuracy values are recorded and the average value is taken as the cross-validation accuracy for this SVM model. Among all the evaluated pairs of (C, σ) values (C and σ are selected as exponentially growing sequences), the one with the best cross-validation accuracy is finally used in the SVM model.

6.3 Classification Results

The performance of the constructed SVM classifier is quantitatively evaluated under four scenarios. The first situation only considers the samples from SNR=40 dB dataset. Following the procedure mentioned in section 6.2-6.3, 200 feature vectors are extracted for each of the training and testing

Table 6. 1: Support vector machine (SVM) classification accuracy under four scenarios

	40 dB dataset	25 dB dataset	10 dB dataset	Combined dataset
Accurate number	187/200	171/200	162/200	528/600
Accuracy rate	92%	85.5%	81%	88%

sets. Among 200 feature vectors, 100 of them are from ICH cases and another 100 samples are from IS cases as shown in Figure 6.10. The second and third scenarios used the same procedure, but the samples are taken from SNR=25 dB and 10 dB dataset. The last scenario combines the SNR=40 dB, 25 dB and 10 dB dataset together to form 600 feature vectors for the training and testing sets (300 samples for each of the stroke type). The classification accuracy achieved by using the trained SVM classifier on the testing set under these four scenarios are listed in Table 6.1 (the threshold for achieving Table 6.1 is set as 0). It can be seen from Table 6.1 that for the low-noise environment (40

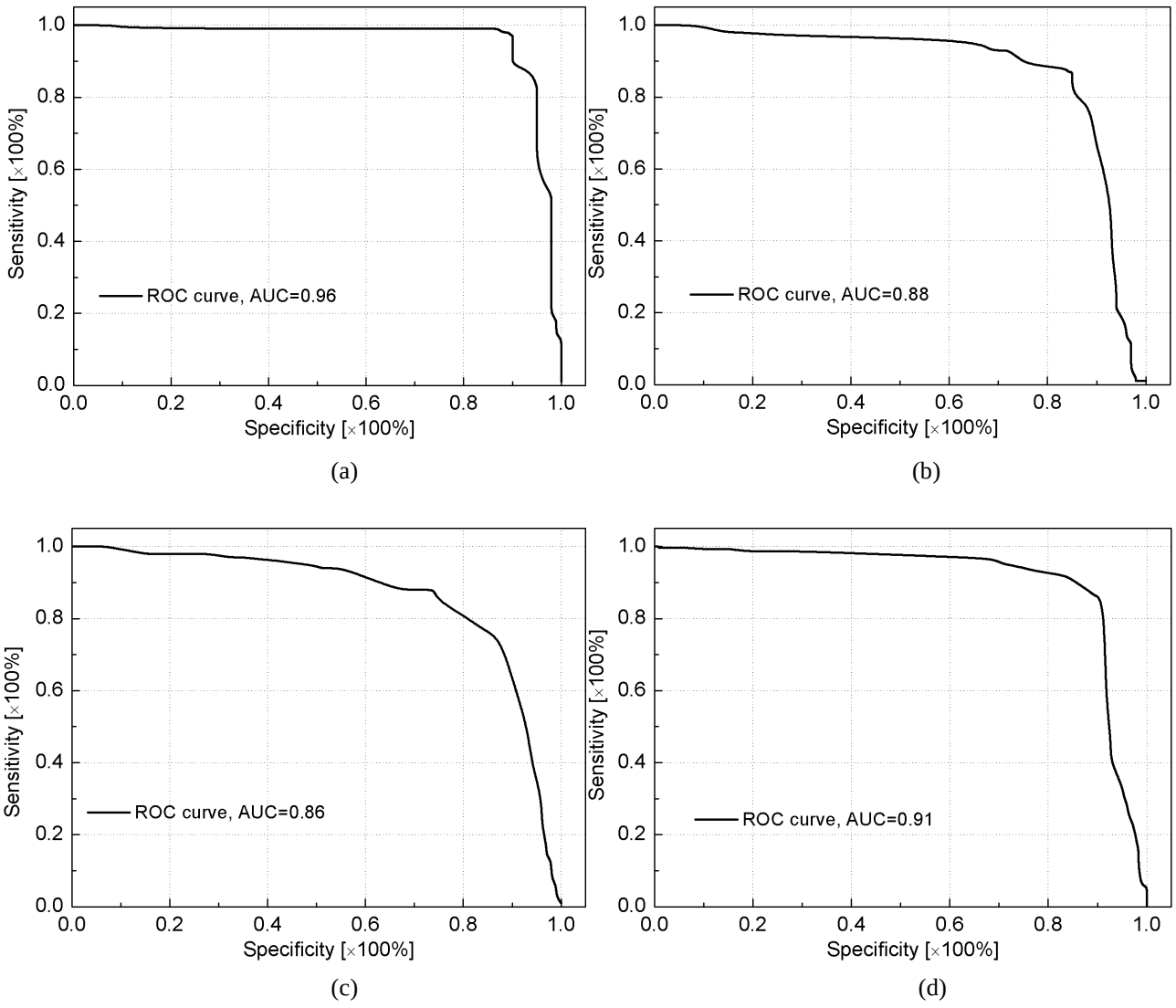

Fig 6. 11: The ROC curves for (a) SNR=40 dB, (b) SNR=25 dB, (c) SNR=10 dB, (d) all the three SNR cases combined. The AUC value is indicated in the legend of each graph

dB case), a 93.5% (187/200) classification accuracy can be achieved and for the noisy environment (10 dB case), the classification accuracy can be maintained above 81% (162/200). When the three SNR level cases (40 dB, 25 dB and 10 dB) are combined together, 88% (528/600) classification accuracy can be achieved using the proposed framework. The receiver operator characteristic (ROC) curve which indicates both the sensitivity and specificity of the classifier [168] is created and parameterized by a decision threshold. The area under the ROC curve (AUC) [169] is a metric that measures the classifier's quality, which is the probability of correctly ranking an ICH case with a higher score than an IS case. The case AUC=1 is the situation where the classifier can perfectly separate the two classes, while AUC=0.5 indicates that the classifier randomly assigns the labels to the classes. The ROC curves from all the four scenarios mentioned above are shown in Figure 6.11. It can be seen that in the low-noise environment (SNR=40 dB), the AUC of the classifier is 0.96, and when the SNR level is low (noisy environment), the classifier can still achieve desirable AUC of 0.86.

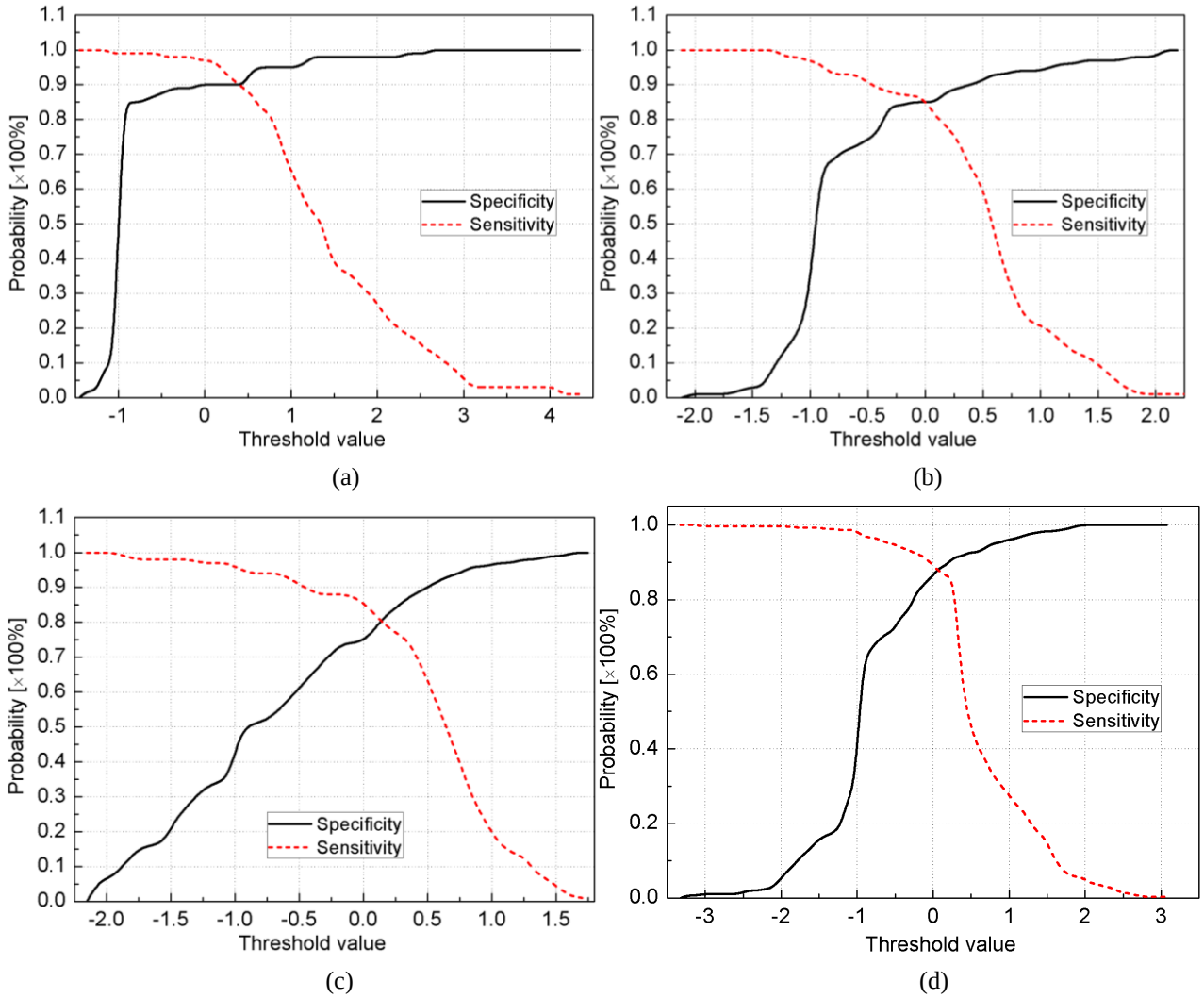

Fig 6. 12: Variation of the sensitivity and specificity with the threshold values in SVM for (a) SNR=40 dB, (b) SNR=25 dB, (c) SNR=10 dB, (d) all the three SNR cases combined.

When all the three SNR levels are taken into account, the classifier can achieve an AUC of 0.91. It is notable that when all the three SNR levels are considered, 91% sensitivity to detect IS stroke can be achieved when approximately 87% (i.e., specificity) of the ICH strokes are safely classified.

Figure 6.12 illustrates how different threshold values in SVM influence the sensitivity and specificity of the four investigated scenarios. It can be seen in Figure 6.12 that for all the four different scenarios, identical sensitivity and specificity can be achieved, when the threshold value in SVM is set at zero. Therefore, to achieve balanced classification results with regard to the sensitivity and specificity, a threshold equal to zero is taken in the SVM model and also used to tabulate the results shown in Table 6.1.

6.4 Discussions and Conclusions

A framework for stroke localization and classification has been presented in this chapter. It is based on microwave tomography, k-means clustering and a support vector machine method. The normalized dielectric profile (NDP) of the brain with suspicious stroke was firstly calculated using Born iterative method (BIM) and the amplitude of the calculated NDP was used to facilitate the k-means clustering. The clusters containing the brain bone (the boundary of the head) were selected as the feature vectors to train and test the SVM classifier. A database generated from two phantoms (one to train the SVM model and another to test the model) under three different noise levels for the two stroke types was built to construct the SVM classifier. The ROC curves was used to evaluate the performance of the constructed SVM classifier. The obtained results indicate that the proposed framework can successfully localize the stroke and achieve 91% sensitivity and 87% specificity.

Chapter 7: Conclusions and Future Work

7.1 Conclusions

During the past few years, microwave imaging has been drawing increasing interests especially on bio-medical applications due to its huge potential to be developed as a portable and low-cost diagnostic instrument. Among numerous bio-medical applications, brain stroke detection is one of the promising and valuable application for microwave imaging system. A complete microwave brain imaging system includes hardware (antennas, microwave transceivers, and switching network) and software (signal processing and imaging algorithms). The processing and imaging techniques, which are the topic of this thesis, use the collected microwave signals via the antenna array to generate the final microwave image of the brain. Numerous microwave imaging techniques applied on bio-medical applications have been researched during the past few years. Those proposed techniques exhibited the great potential of microwave systems on medical diagnosis, however, several serious drawbacks still exist in those algorithms and need to be solved. In this thesis, four novel microwave imaging techniques which were explicitly elaborated in Chapter 3, 4, 5, and 6 were proposed to solve the challenges of microwave head imaging systems. The proposed algorithms increase the efficiency and accuracy of the system, and resolved the main defects in the current imaging algorithms.

In Chapter 3, two methods based on compressive sensing (CS) were applied on radar-based imaging technique. The proposed methods aim to solve two problems existed in current microwave imaging algorithms:

1. Reduce the number of antennas used in the array system.
2. Reduce the number of stepped frequencies used in the transceiver system.

The theoretical explanations of the proposed methods were illustrated and the algorithms were verified through using simple numerical head model and realistic microwave imaging system. Based on the imaging results, it can be concluded that by using the proposed algorithms, the number of antennas and stepped frequencies can be largely reduced while the quality of the images can be retained completely. Through implementing a quantitative analysis, it was found that the minimum number of stepped frequencies can be used to recover high quality image is 150 cover the band from 1 to 4 GHz (the original number of stepped frequencies used in the system is 401). This result can be utilized to design efficient portable microwave transceiver system.

In Chapter 4, a compressive sensing (CS) based algorithm was proposed for decreasing the number of antennas used in microwave tomography technique. The core concept in the proposed algorithm was to use wavelet transform to map the non-sparse imaging domain into a sparse wavelet space. After implementing the wavelet transform, a CS-based algorithm named block sparse Bayesian learning (BSBL) was used to recover the electrical properties of the imaging domain. The sparsity of the dielectric profile in the wavelet domain was investigated in this chapter and the theoretical analysis was also illustrated. The proposed algorithm was firstly evaluated on a simple non-sparse model and the recovered results with respect to the dielectric profile were compared with other traditional methods. The comparison results indicated that when less number of antennas were used to transmit and receive the signals, the images generated by using traditional methods were largely distorted whereas the proposed method can recover the images perfectly. To further verify the superior performance of the proposed algorithm, a numerical head phantom was used to test the algorithm. The results indicated that both the position and electrical properties (permittivity and conductivity) of the brain stroke can be recovered by using the proposed method when only four antennas were used in the system whereas the traditional microwave tomography methods use more than 30 antennas.

In Chapter 5, an optimization-based confocal imaging algorithm was proposed to solve the third problem in current radar-based imaging algorithms, which is the estimation of the effective dielectric constant. In the traditional radar-based imaging algorithms, an effective dielectric constant of the imaging area has to be pre-defined. However, the value of effective dielectric constant is difficult to be estimated since little information with regard to the imaging area can be extracted before the images are generated. Inaccurate estimation of effective dielectric constant leads to distorted images. In the proposed algorithm, a set of effective dielectric constants depends on the signal's entry points was firstly defined rather than using a single value in the traditional methods. This set of effective dielectric constants was optimized based on a metric which was used to measure the quality of the image. The purpose of the optimization was to seek the optimum values of the effective dielectric constants which can be used to achieve the best images. The proposed algorithm was assessed by using simulations in CST and two realistic microwave head imaging systems. The results indicated that when the traditional method was used to generate the head image, the image quality was largely varied with the estimated dielectric constant. A small deviation on the estimated dielectric constant lead to large distortion in the final image generated using the traditional approach. However, the proposed algorithm is insensitive to the initial choice of the set of dielectric constants. When different sets of dielectric constants were used to initialize the optimization process, a focused and accurate

image can always be generated by using the proposed algorithm. This performance was verified in both simulation and realistic measurement environment.

In Chapter 6, a machine learning based framework was proposed to solve another important problem in current microwave head imaging systems, which is the classification of the brain stroke (classify the brain stroke between haemorrhagic and ischaemic stroke). The Born iterative method (BIM) was used to reconstruct the electrical properties of the brain. The K-means clustering method and support vector machine (SVM) technique were further used to construct the classifier. Aim to build the classifier and evaluate the performance of the proposed algorithm, a database was constructed by using two different numerical head phantoms. The first phantom was used to build the classifier and the second phantom was used to test the performance of the classifier. The receiver operator characteristic (ROC) curve was used to measure the accuracy of the classification. The results indicated that under the ideal environment (low-noise environment), 92% accuracy rate can be achieved by using the proposed algorithm. When noisy environment was imposed on the evaluation, 81% accuracy rate can still be achieved. When all the three noise levels (low-noise, medium-noise, and high noise) were considered together, 91% sensitivity to detect ischaemic stroke can be achieved when approximately 87% (i.e. specificity) of the haemorrhagic strokes were safely classified. These results exhibited the potential to use microwave system to accurately classify the types of brain stroke.

7.2 Future Work

In this thesis, four novel algorithms were proposed to solve the four main problems in current microwave imaging algorithms. Although the results are promising, several remaining issues can still be addressed in the future research plan:

1. All of the four algorithms proposed in this thesis are two-dimensional imaging algorithms. This drawback affects the practical values of the proposed algorithms. In clinical brain stroke application, both the xy-coordinate and the z-coordinate are required to localize the position of the stroke. Therefore, it is important to extent the proposed algorithms to three-dimensional.
2. In Chapter 4 and 6, the proposed algorithms were tested using numerical head phantom from MRI scan. The reason of not having experimental verification is that the tomography-based microwave head imaging system is still under development thus the experiment data is not available at this stage. It is clear that using numerical head phantom to test the proposed algorithms is different from testing the algorithms in clinical trials. Therefore, it is important

to build tomography-based head imaging system which can be applied in clinical trials. However, the construction of microwave head imaging system based on tomography technique faces a number of major challenges such as the coupling between the antennas and the objects under imaging and the calibration of the received data. These technical issues are critical for tomography-based system and need to be solved in the future.

3. In Chapter 3, 4, and 5, the proposed algorithms were successfully applied on haemorrhagic stroke detection. However, the feasibility on ischaemic stroke detection has not been investigated. Due to the fact the more than 85% of the brain stroke are ischaemic, it is vital to evaluate the performance of the proposed algorithms when ischaemic stroke is placed in the brain.
4. In Chapter 5 and 6, single frequency tomography method was used to recover the electrical properties of the imaging area. However, during recent years, multi-frequency tomography method is attracting more attentions due to its potential to generate higher resolution images. Since detailed electrical properties profile is required for inspection and final decision by specialists in the hospital, the single frequency tomography method used in Chapter 5 and 6 can be replaced by novel multi-frequency method in order to achieve more detailed electrical properties of the brain.
5. The brain stroke classification algorithm proposed in Chapter 6 was only evaluated under the simulation environment. With the aim to test the proposed algorithm into clinical trials, realistic head phantoms with two types of strokes (haemorrhagic and ischaemic) at different locations will be used to assess the algorithm. The final goal is to collect the measurement data from brain stroke patients who suffers from haemorrhagic or ischaemic stroke and use the proposed algorithm to classify the types of the stroke.

References

[1] National Stroke Foundation. Clinical Guidelines for Stroke Management., Melbourne Australia. Sep. 2010. ISSBN0-978-0-9805933-3-4.

[2] A. Thrift, H. Dewey, R. Macdonell, J. McNeil, and G. Donnan, "Incidence of the major stroke subtypes: initial findings from the North East Melbourne stroke incidence study (NEMESIS). *Stroke*., vol. 32, pp. 1732-1738, 2001.

[3] G. Donnan, M. Fisher, M. Macleod, and S. Davis, "Stroke," *The Lancet*., vol. 373, no. 9674, pp. 1612-1623, May. 2008.

[4] M. Mullins, P. Schaefer, A. Sorensen, E. Halpern, H. Ay, J. He, W. Koroshetz, and R. Gonzalez, "CT and conventional and diffusion-weighted MR imaging in acute stroke: study in 691 patients at presentation to the emergency department," *Radiology*., vol. 224, pp. 353-360, 2002.

[5] C. Kidwell, J. Chalela, J. Saver, et al, "Comparison of MRI and CT for detection of acute intracerebral haemorrhage," *JAMA*., vol. 292, pp. 1823-1830, 2004.

[6] A. Alexandrov, C. Molina, J. Grotta, et al, "Ultrasound-enhanced systemic thrombolysis for acute ischemic stroke," *N Engl J Med*., vol. 351, pp. 2170-2178, 2004.

[7] C. Johnson and A. Guy, "Nonionizing electromagnetic wave effects in biological materials and systems," *Proc. IEEE*., vol. 60, pp. 692-718, 1972.

[8] J. Lin and M. Clarke, "Microwave imaging of cerebral edema," *Proc. IEEE*., vol. 70, no. 5, May. 1982.

[9] S. Hagness, A. Taflove, and J. Bridges, "Two-dimensional FDTD analysis of a pulsed microwave confocal system for breast cancer detection: fixed-focus and antenna-array sensors," *IEEE Trans. Biomed. Eng*., vol. 45, no. 12, pp. 1470-1479, Dec. 1998.

[10] J. Bridges, "Noninvasive system for breast cancer detection," U.S. Patent 5704355, Jan. 6, 1998.

[11] J. Bourqui, M. Okoniewski, and E. Fear, "Balanced antipodal Vivaldi antenna with dielectric director for near-field microwave imaging," *IEEE Trans. Antennas Propag*., vol. 58, no. 7, pp. 2318-2326, Jul. 2010.

[12] X. Yun, E. Fear, and R. Johnston, "Compact antenna for radar-based breast cancer detection," *IEEE Trans. Antennas Propag*., vol. 53, no. 8, pp. 2374-2380, Aug. 2005.

[13] H. Bahramiabarghouei, E. Porter, A. Santorelli, B. Gosselin, M. Popovic, and L. Rusch, "Flexible 16 antenna array for microwave breast cancer detection," *IEEE Trans. Biomed. Eng*., vol. 62, no. 10, pp. 2516-2525, Oct. 2015.

[14] S. Aguilar, M. Joumayly, M. Burfeindt, N. Behdad, and S. Hagness, "Multiband miniaturized patch antennas for a compact, shielded microwave breast imaging array," *IEEE Trans. Antennas Propag*., vol. 62, no. 3, pp. 1221-1231, Mar. 2014.

[15] R. Amineh, M. Ravan, A. Trehan, and N. Nikolova, "Near-field microwave imaging based on aperture raster scanning with TEM horn antennas," *IEEE Trans. Antennas Propag*., vol. 59, no. 3, pp. 928-940, Mar. 2011.

[16] M. Bassi, M. Caruso, M. Khan, A. Bevilacqua, A. Capobianco, and A. Neviani, "An integrate microwave imaging radar with planar antennas for breast cancer detection," *IEEE Trans. Microw. Theory Tech*., vol. 61, no. 5, pp. 2108-2118, May. 2013.

[17] M. Bassi, A. Bevilacqua, A. Gerosa, and A. Neviani, "Integrated SFCW transceiver for UWB breast cancer imaging: architectures and circuit constraints," *IEEE Trans. Circuits Syst. I, Reg. Papers*., vol. 59, no. 6, pp. 1228-1241, Jun. 2012.

[18] C. Top and N. Gencer, "Harmonic motion microwave Doppler imaging: a simulation study using a simple breast model," *IEEE Trans. Med. Imag*., vol. 33, no. 2, pp. 290-300, Feb. 2014.

[19] Y. Xie, B. Guo, L. Xu, J. Li, and P. Stoica, "Multistatic adaptive microwave imaging for early breast cancer detection," *IEEE Trans. Biomed. Eng*., vol. 53, no. 8, pp. 1647-1657, Aug. 2006.

[20] X. Li, S. Davis, S. Hagness, D. Weide, and B. Veen, "Microwave imaging via space-time beamforming: experimental investigation of tumor detection in multilayer breast phantoms," *IEEE Trans. Microw. Theory Tech*., vol. 52, no. 8, pp. 1856-1865, Aug. 2004.

[21] E. Fear, J. Sill, and M. Stuchly, "Experimental feasibility study of confocal microwave imaging for breast tumor detection," *IEEE Trans. Microw. Theory Tech*., vol. 51, no. 3, pp. 887-892, Mar. 2003.

[22] M. Elahi, A. Shahzad, M. Glavin, E. Jones, and M. Halloran, "Hybrid artefact removal for confocal microwave breast imaging," *IEEE Antennas Wireless Propag. Lett*., vol. 13, pp. 149-152, 2014.

[23] D. Winters, J. Shea, E. Madsen, G. Frank, B. Veen, and S. Hagness, "Estimating the breast surface using UWB microwave monostatic backscatter measurements," *IEEE Trans. Biomed. Eng*., vol. 55, no. 1, pp. 247-256, Jan. 2008.

[24] M. Halloran, E. Jones, and M. Glavin, "Quasi-multistatic MIST beamforming for the early detection of breast cancer," *IEEE Trans. Biomed. Eng*., vol. 57, no. 4, pp. 830-840, Apr. 2010.

[25] W. Zhi and F. Chin, "Entropy-based time window for artefact removal in UWB imaging of breast cancer detection," *IEEE Signal Process. Lett*., vol. 13, no. 10, pp. 585-588, Oct. 2006.

[26] E. Bond, X. Li, S. Hagness, and B. Veen, "Microwave imaging via space-time beamforming for early detection of breast cancer," *IEEE Trans. Antennas Propag*., vol. 51, no. 8, pp. 1690-1705, Aug. 2003.

[27] E. Fear, X. Li, S. Hagness, and M. Stuchly, "Confocal microwave imaging for breast cancer detection: localization of tumors in three dimensions," *IEEE Trans. Biomed. Eng*., vol. 49, no. 8, pp. 812-822, Aug. 2002.

[28] H. Lim, N. Nhung, E. Li, and N. Thang, "Confocal microwave imaging for breast cancer detection: delay-multiply-and-sum image reconstruction algorithm," *IEEE Trans. Biomed. Eng*., vol. 55, no. 6, pp. 1697-1704, Jun. 2008.

[29] X. Li and S. Hagness, "A confocal microwave imaging algorithm for breast cancer detection," *IEEE Microw. Wireless Compon. Lett*., vol. 11, no. 3, pp. 130-132, Mar. 2001.

[30] D. Ireland and M. Bialkowski, "Feasibility study on microwave stroke detection using a realistic phantom and the FDTD method," in *Proceedings of Asia-Pacific Microwave Conference*, pp. 1360-1363, 2010.

[31] H. Mesri, M. Najafabadi, and T. McKelvey, "A multidimensional signal processing approach for classification of microwave measurements with application to stroke type diagnosis," in *IEEE 33th Annual Int. Conf. EMBS*, pp. Boston, U.S, pp. 6465-6469, 2011.

[32] S. Mustafa, A. Abbosh, B. Henin, and D. Ireland, "Brain stroke detection using continuous wavelets transform matching filters," in *Int. Biomed. Eng. Conf*, Cairo, Egypt, pp. 194-197, 2012.

[33] B. Mohammed, A. Abbosh, and D. Ireland, "Stroke detection based on variations in reflection coefficients of wideband antennas," in *IEEE Proceedings of International Symposium on Antennas and Propagation*, Chicago, U. S, pp. 1-2, 2012.

[34] B. Mohammed, A. Abbosh, and D. Ireland, "Directive wideband antenna for microwave imaging system for brain stroke detection," in *Proceedings of Asia-Pacific Microwave Conference*, Kaohsiung, Taiwan, pp. 640-642, 2012.

[35] A. Mobashsher, B. Mohammed, S. Mustafa, and A. Abbosh, "Ultra wideband antenna for portable brain stroke diagnostic system," in *IEEE MTT-S, IMWS-BIO*, Singapore, pp. 1-3, 2013.

[36] B. Mohammed, A. Abbosh, S. Mustafa, and D. Ireland, "Microwave system for head imaging," *IEEE Trans. Instrum. Meas*., vol. 63, no. 1, pp. 117-123, Jan. 2014.

[37] S. Mustafa, B. Mohammed, and A. Abbosh, "Novel preprocessing techniques for accurate microwave imaging of human brain," *IEEE Antennas Wireless Propag. Lett*., vol. 12, pp. 460-463, 2013.

[38] S. Gabriel, R. Lau, and C. Gabriel, "The dielectric properties of biological tissues: III. Parametric models for the dielectric spectrum of tissues," *Phys. Med. Biol*., vol. 41, no. 11, pp. 2271-2293, 1996.

[39] C. Gabriel and S. Gabriel. Complication of the Dielectric Properties of Body Tissues at RF and Microwave Frequencies [Online] Available: http://www.emfdosimetry.org/dielectric/Title/Title.html, 1996

[40] A. Mobashsher, A. Abbosh, and Y. Wang, "Microwave system to detect traumatic brain injuries using compact unidirectional antenna and wideband transceiver with verification on realistic head phantom," *IEEE Trans. Microw. Theory Tech*., vol. 62, no. 9, pp. 1826-1836, Sep. 2014.

[41] S. Semenov, B. Seiser, E. Stoegmann, and E. Auff, "Electromagnetic tomography for brain imaging: from virtual to human brain," *in IEEE Conf. Antennas Meas & Appl*, pp. 1-4, 2014.

[42] S. Semenov, R. Planas, M. Hopfer, A. Hamidipour, A. Vasilenko, E. Stoegmann, and E. Auff, "Electromagnetic tomography for brain imaging: initial assessment for stroke detection," in *IEEE Conf. BioCAS, Atlanta*, GA, USA, pp. 1-4, 2015.

[43] M. Persson, A. Fhager, H. Trefna, Y. Yu, T. McKelvey, G. Pegenius, J. Karlsson, and M. Elam, "Microwave-based stroke diagnosis making global pre-hospital thrombolytic treatment possible," *IEEE Trans. Biomed. Eng*., vol. 61, no. 11, pp. 2806-2817, Nov. 2014.

[44] M. Hashemi and M. Shenawee, "A comparative study of different tomography methods for breast cancer application," in *IEEE Region 5 Technical Conference*, Fayetteville, U.S, pp. 21-24, 2007.

[45] M. Guardiola, S. Capdevila, J. Romeu, and L. Jofre, "3-D microwave magnitude combined tomography for breast cancer detection using realistic breast models," *IEEE Antennas Wireless Propag. Lett*., vol. 11, pp. 1622-1625, 2012.

[46] A. Bulyshev, S. Semenov, A. Souvorov, R. Svenson, A. Nazarov, Y. Sizov, and G. Tatsis, "Computational modeling of three-dimensional microwave tomography of breast cancer," *IEEE Trans. Biomed. Eng*., vol. 48, no. 9, pp. 1053-1056, Sep. 2001.

[47] F. Gao, B. Veen, and S. Hagness, "Sensitivity of the distorted Born iterative method to the initial guess in microwave breast imaging," *IEEE Trans. Antennas Propag*., vol. 63, no. 8, pp. 3540-3547, Aug. 2015.

[48] T. Gurbuz, B. Aslanyurek, A. Yapar, H. Sahinturk, and I. Akduman, "A nonlinear microwave breast cancer imaging approach through realistic body-breast modeling," *IEEE Trans. Antennas Propag*., vol. 62, no. 5, pp. 2596-2605, May. 2014.

[49] M. Jalilvand, C. Wu, J. Schmid, and T. Zwick, "Quantitative imaging of numerically realistic human head model using microwave tomography," *Electron. Lett*., vol. 50, no. 4, pp. 255-256, Feb. 2014.

[50] D. Ireland, K. Bialkowski, and A. Abbosh, "Microwave imaging for brain stroke detection using Born iterative method," *IET Microw. Antennas Propag*., vol. 7, no. 11, pp. 909-915, May. 2013.

[51] C. Gilmore, P. Mojabi, A. Zakaria, M. Ostadrahimi, C. Kaye, S. Noghanian, L. Shafai, S. Pistorius, and J. LoVetri, "A wideband microwave tomography system with a novel frequency selection procedure," *IEEE Trans. Biomed. Eng*., vol. 57, no. 4, pp. 894-904, Apr. 2010.

[52] J. Marimuthu, K. Bialkowski, and A. Abbosh, "Software-defined radar for medical imaging," *IEEE Trans. Microw. Theory Tech*., vol. 64, no. 2, pp. 643-652, Feb. 2016.

[53] J. Marimuthu, K. Bialkowski, and A. Abbosh, "Stepped frequency continuous wave software defined radar for medical imaging," in *Proc. IEEE Antennas Propag. Soc. Int. Symp*., Memphis, TN, USA, pp. 1909-1910, 2014.

[54] J. Marimuthu, K. Bialkowski, and A. Abbosh, "Reconfigurable software defined radar for medical imaging," in *Proc. 1st Australian Microw. Symp.*, Melbourne, Vic., Australia, pp. 15-16, 2014.
[55] K. Bialkowski, J. Marimuthu, and A. Abbosh, "Biomedical imaging system using software defined radio," in *IEEE Antennas Propag. Soc. Symp.*, Vancouver, BC, Canada, pp. 542-543, 2015.
[56] X. Zeng, A. Fhager, Z. He, M. Persson, P. Linner, and H. Zirath, "Development of a time domain microwave system for medical diagnostics," *IEEE Trans. Instrum. Meas.*, vol. 63, no. 12, pp. 2931-2939, Dec. 2014.
[57] P. Meaney, M. Fanning, D. Li, S. Poplack, and K. Paulsen, "A clinical prototype for active microwave imaging of the breast," *IEEE Trans. Microw. Theory Tech.*, vol. 48, no. 11, pp. 1841-1853, Nov. 2000.
[58] M. Klemm, I. Craddock, J. Leendertz, A. Preece, and R. Benjamin, "Radar-based breast cancer detection using a hemispherical antenna array-experimental results," *IEEE Trans. Antennas. Propag.*, vol. 57, no. 6, pp. 1692-1704, Jun. 2009.
[59] E. Fear and M. Stuchly, "Microwave detection of breast cancer," *IEEE Trans. Microw. Theory Tech.*, vol. 48, no. 11, pp. 1854-1863, Nov. 2000.
[60] S. Haykin, *Adaptive Filter Theory*, 3rd ed. Upper Saddle River, NJ: Prentice-Hall, 1996.
[61] T. Cover and J. Thomas, *Elements of Information Theory*. New York: Wiley, 1991.
[62] R. Baraniuk, P. Flandrin, A. Janssen, and O. Michel, "Measuring time-frequency information content using the Rényi entropies," *IEEE Trans. Inf. Theory.*, vol. 47, no. 4, pp. 1391-1409, May. 2001.
[63] W. Williams, M. Brown, and A. Hero, "Uncertainty, information and time-frequency distributions," *SPIE-Adv. Signal Process. Alg.*, vol. 1556, pp. 144-156, 1991.
[64] S. Aviyente and W. Williams, "Entropy based detection on the time-frequency plane," in *Proc. IEEE Int. Conf. Acoustics, Speech, Signal Processing*, vol. 6, pp. VI-441-444, 2003.
[65] R. Coifman and M. Wickerhauser, "Entropy-based algorithms for best basis selection," *IEEE Trans. Inf. Theory.*, vol. 38, no. 2, pp. 713-718, Mar. 1992.
[66] B. Veen and K. Buckley, "Beamforming: a versatile approach to spatial filtering," *IEEE ASSP Magazine.*, vol. 5, pp. 4-24, Apr. 1988.
[67] S. Haykin, *Adaptive Filter Theory*, 3rd ed. Upper Saddle River, NJ: Prentice-Hall, 1996.
[68] H. Cox, R. Zeskind, and M. Owen, "Robust adaptive beamforming," *IEEE Trans. Acoust., Speech, Signal Processing.*, vol. ASSP-35, pp. 1365-1376, Oct. 1987.
[69] D. Ireland and M. Bialkowski, "Microwave head imaging for stroke detection," *Prog. Electromag. Res.*, vol. 21, pp. 163-175, 2011.
[70] M. Bialkowski and Y. Wang, "UWB cylindrical microwave imaging system employing virtual array antenna concept for background effect removal," *Microwave Opt Tech Lett.*, vol. 53, no. 5, pp. 1100-1104, May. 2011.
[71] M. Bialkowski, "Ultra wideband microwave system with novel image reconstruction strategies for breast cancer detection," *EuMC2010: 40th European Microwave Conf*, Paris, France, pp. 537-540, 2010.
[72] M. Bialkowski, Y. Wang, A. Bakar, and W. Khor, "Novel image reconstruction algorithm for a UWB cylindrical microwave imaging system," *IMS2010 Digest*, Anaheim, USA, pp. 1-4, 2010.
[73] Y. Wang and A. Abbosh, "Three-dimensional microwave breast imaging using least electrical path method," in *Proceedings of Asia-Pacific Microwave Conference*, Seoul, Korea, pp. 1021-1023, 2013.
[74] W. Chew, *Waves and Fields in Inhomogeneous Media*. Piscataway, NJ, USA: IEEE Press, 1995.
[75] Y. Wang and W. Chew, "An iterative solution of two-dimensional electromagnetic inverse scattering problem," *Int. J. Imaging Syst. Technol.*, vol. 1, no. 1, pp. 100-108, 1989.

[76] W. Chew and Y. Wang, "Reconstruction of two-dimensional permittivity distribution using the distorted Born iterative method," *IEEE Trans. Med. Imaging*., vol. 9, no. 2, pp. 218-225, Jun. 1990.
[77] J. Richmond, "Scattering by a dielectric cylinder of arbitrary cross shape," *IEEE Trans. Antennas Propag*., vol. 13, no. 3, pp. 334-341, May. 1965.
[78] A. Tikhonov and V. Arsenin, *Solution of Ill-Posed Problem. Washington*, DC, USA: Winston & Sons Press, 1977.
[79] I. Zubal, C. Harrell, E. Smith, Z. Rattner, G. Gindi, and P. Hoffer, "Computerized three-dimensional segmented human anatomy," *Med. Phys*., vol. 21, no. 2, pp. 299-302, 1994.
[80] D. Andreuccetti, R. Fossi, and C. Petrucci, "Dielectric properties of body tissues in the frequency range 10 Hz-100 GHz," Available: http://www.niremf.ifac.cnr.it/tissprop/
[81] I. Rekanos, S. Panas, and T. Tsiboukis, "Microwave imaging using the finite element method and a sensitivity analysis approach," *IEEE Trans. Med. Imag*., vol. 18, no. 11, pp. 1108-1114, Nov. 1999.
[82] R. Harrington, *Field Computation by Moment Methods*. Malabar, FL: Krieger. 1983.
[83] University of Wisconsin Cross-Disciplinary Electromagnetic Laboratory (UWCEM) Numerical Breast Phantom Repository [Online]. Available: http://uwcem.ece.wisc.edu.
[84] E. Zastrow, S. Davis, M. Lazebnik, F. Kelcz, B. Veen, and S. Hagness, "Development of anatomically realistic numerical breast phantoms with accurate dielectric properties for modeling microwave interactions with the human breast," *IEEE Trans. Biomed. Eng*., vol. 55, pp. 2792-2800, Dec. 2008.
[85] M. Lazebnik, L. McCartney, D. Popovic, C. Watkins, M. Lindstrom, J. Harter, S. Sewall, A. Magliocco, J. Booske, M. Okoniewski, and S. Hagness, "A large-scale study of the ultrawideband microwave dielectric properties of normal breast tissue obtained from reduction surgeries," *Phys. Med. Biol*., vol. 52, pp. 2637-2656, Apr. 2007.
[86] M. Lazebnik, D. Popovic, L. McCartney, C. Watkins, M. Lindstrom, J. Harter, S. Sewall, T. Ogilvie, A. Magliocco, T. Breslin, W. Temple, D. Mew, J. Booske, M. Okoniewski, and S. Hagness, "A large-scale study of the ultrawideband microwave dielectric properties of normal, benign and malignant breast tissues obtained from cancer surgeries," *Phys. Med. Biol*., vol. 52, pp. 6093-6115, Oct. 2007.
[87] D. Donoho, "Compressed sensing," *IEEE Trans. Inf. Theory*., vol. 52, no. 4, pp. 1289-1306, Apr. 2006.
[88] R. Baraniuk, "Compressive sensing," *IEEE Signal Process. Mag*., vol. 24, no. 4, pp. 118-124, Jul. 2007.
[89] E. Candes and M. Wakin, "An introduction to compressive sampling," *IEEE Signal Process. Mag*., vol. 25, no. 2, pp. 21-30, Mar. 2008.
[90] S. Stankovic, I. Orovic, and E. Sejdic, *Multimedia Signals and Systems*, London, UK: Springer, 2012, pp. 233-253.
[91] D. Donoho and M. Elad, "Optimally sparse representation in general (nonorthogonal) dictionaries via l^1 minimization," *Proc. Natl. Acad. Sci*., vol. 100, no. 5, pp. 2197-2202, 2003.
[92] J. Troop, "Greed is good: algorithmic results for sparse approximation," *IEEE Trans. Inf. Theory*., vol. 50, no. 10, pp. 2231-2242, 2004.
[93] W. Dai and O. Milenkovic, "Subspace pursuit for compressive sensing signal reconstruction," *IEEE Trans. Inf. Theory*., vol. 55, no. 5, pp. 2230-2249, May. 2009.
[94] E. Candes and T. Tao, "Near optimal signal recovery from random projections: universal encoding strategies?" *IEEE Trans. Inf. Theory*., vol. 52, no. 12, pp. 5406-5425, Dec. 2006.
[95] E. Candes, J. Romberg, and T. Tao, "Stable signal recovery from incomplete and inaccurate measurements. *Commun. Pure. Appl. Math*., vol. 59, no. 8, pp. 1207-1223, 2006.
[96] L. Anitori, M. Otten, and P. Hoogeboom, "Compressive sensing for high resolution radar imaging," *Proceeding of Asia-Pacific Microwave Conference*, 2010.

[97] H. Kajbaf, J. Case, Z. Yang, and Y. Zheng, "Compressed sensing for SAR-based wideband three-dimensional microwave imaging system using non-uniform fast Fourier transform," *IET Radar Sonar Navig*., vol. 7, no. 6, pp. 658-670, Mar. 2013.
[98] X. Dong and Y. Zhang, "A novel compressive sensing algorithm for SAR imaging," *IEEE J. Sel. Top. Appl. Earth Observ. Remote Sens*., vol. 7, no. 2, pp. 708-720, Feb. 2014.
[99] J. Liu, S. Xu, X. Gao, and X. Li, "Novel imaging methods of stepped frequency radar based on compressive sensing," *J System Engineering and Electronics*., vol. 23, no. 1, pp. 47-56, Feb. 2012.
[100] L. Zhang, Z. Qiao, M. Xing, Y. Li, and Z. Bao, "High-resolution ISAR imaging with sparse stepped-frequency waveform," *IEEE Trans. Geosci. Remote Sens*., vol. 49, no. 11, pp. 4630-4651, Apr. 2011.
[101] X. Zhang, T. Bai, H. Meng, and J. Chen, "Compressive sensing-based ISAR imaging via the combination of the sparsity and nonlocal total variation," *IEEE Geosci. Remote Sens. Lett*., vol. 11, no. 5, pp. 990-994, May. 2014.
[102] M. Nikolic, G. Tang, and A. Nehorai, "3D electromagnetic imaging using compressive sensing," *IEEE Sensor Array and Multichannel Signal Processing Workshop*, 2010.
[103] J. Shi, X. Zhang, X. Gao, and J. Yang, "Signal processing for microwave array imaging: TDC and sparse recovery," *IEEE Trans. Geosci. Remote Sens*., vol. 50, no. 11, pp. 4584-4598, Nov. 2010.
[104] A. Gurbuz, J. McClellan, and W. Scott, "A compressive sensing data acquisition and imaging method for stepped frequency GPRs," *IEEE Trans. Signal Process*., vol. 57, no. 7, pp. 2640-2650, Jul. 2009.
[105] M. Tuncer and A. Gurbuz, "Ground reflection removal in compressive sensing ground penetrating radar," *IEEE Geosci Remote Sens. Lett*., vol. 9, no. 1, pp. 23-27, Jan. 2012.
[106] D. Pozar, *Microwave Engineering*, 3rd ed. New York: Wiley, 2005.
[107] S. Becker, J. Bobin, and E. Candes, *NESTA: A fast and accurate first-order method for sparse recovery*, California Institute of Technology, April, 2009.
[108] D. Ireland and A. Abbosh, "Modeling human head at microwave frequencies using optimized Debye models and FDTD method," *IEEE Trans. Antenna Prop*., vol. 61, no. 4, pp. 2352-2355, 2013.
[109] E. Van den Berg and M. Friedlander, "Probing the pareto frontier for basis pursuit solutions," *SIAM J. Scientific Computing*., vol. 21, no. 2, pp. 890-912, 2008.
[110] J. Tropp and S. Wright, "Computational methods for sparse solution of linear inverse problems," *Proceeding of IEEE*., vol. 98, no. 6, pp. 948-958, 2010.
[111] H. Harada, D. Wall, T. Takenaka, and M. Tanaka, "Conjugate gradient method applied to inverse scattering problem," *IEEE Trans. Antennas Propag*., vol. 43, pp. 784-792, 1995.
[112] M. Pastorino, "Stochastic optimization methods applied to microwave imaging: A review," *IEEE Trans. Antennas Propag*., vol. 55, no. 3, pp. 538-548, Mar. 2007.
[113] S. Caorsi, A. Massa, and M. Pastorino, "A computational technique based on a real-coded genetic algorithm for microwave imaging purpose," *IEEE Trans. Geosci. Remote Sens*., vol. 38, no. 4, pp. 1697-1708. July. 2000.
[114] P. Rocca, M. Benedetti, M. Donelli, D. Franceschini, and A. Massa, "Evolutionary optimization as applied to inverse problems," *Inv. Prob*., vol. 25, pp. 1-41, 2009.
[115] H. Choi, S. Park, and J. Ra, "Reconstruction of a high-contrast penetrable object in pulsed time domain by using the genetic algorithm," in *Proc. IEEE Int. Geoscience Remote Sensing Symp*., Singapore, Aug. 1997, pp. 136-138.
[116] X. Zhu, Z. Zhao, J. Wang, J. Song, and Q. Liu, "Microwave-induced thermal acoustic tomography for breast tumor based on compressive sensing," *IEEE Trans. Biomed. Eng*., vol. 60, no. 5, pp. 1298-1307, May. 2013.

[117] G. Oliveri, P. Rocca, and A. Massa, "A Bayesian-compressive-sampling-based inversion for imaging sparse scatters," *IEEE Trans. Geosci. Remote Sens*., vol. 49, no. 10, pp. 3993-4006, Oct. 2011.
[118] L. Poli, G. Oliveri, and A. Massa, "Microwave imaging within the first-order Born approximation by means of the contrast-field Bayesian compressive sensing," *IEEE Trans. Antennas Propag*., vol. 60, no. 6, Jun. 2012.
[119] L. Poli, G. Oliveri, F. Viani, and A. Massa, "MT-BCS-based microwave imaging approach through minimum-norm current expansion," *IEEE Trans. Antennas Propag*., vol. 61, no. 9, Sep. 2013.
[120] S. Ji, Y. Xue, and L. Carin, "Bayesian compressive sensing," *IEEE Trans. Signal Process*., vol. 56, no. 6, pp. 2346-2356, Jun. 2008.
[121] J. Bernardo and A. Smith, *Bayesian Theory*, New York: Wiley, 1994.
[122] G. Oliveri, N. Anselmi, and A. Massa, "Compressive sensing imaging of non-sparse 2D scatterers by a total-variation approach within the Born approximation," *IEEE Trans. Antennas Propag*., vol. 62, no. 10, pp. 5157-5170, Oct. 2014.
[123] C. Li, "An Efficient Algorithm for Total Variation Regularization With Applications to the Single Pixel Camera and Compressive Sensing," Master's thesis, Rice Univ., Houston, TX, USA, Sep. 2009.
[124] C. Li, "Compressive Sensing for 3D Data Processing Tasks: Applications, Models, and Algorithms," Pd.D. dissertation, Rice Univ., Houston, TX, USA, Apr. 2011.
[125] C. Li, H. Jiang, P. Wilford, Y. Zhang, and M. Scheutzow, "A new compressive video sensing framework for mobile broadcast," *IEEE Trans. Broadcast*., vol. 59, no. 1, pp. 197-205, Mar. 2013.
[126] Z. Zhang and B. Rao, "Sparse signal recovery with temporally correlated source vectors using sparse Bayesian learning," *IEEE J. Sel. Topics Signal Process*., vol. 5, no. 5, pp. 912-926, 2011.
[127] Z. Zhang and B. Rao, "Extension of SBL algorithms for the recovery of block sparse signals with intra-block correlation," *IEEE Trans. Signal Process*., vol. 61, no. 8, pp. 2009-2015. Apr. 2013.
[128] T. Isernia, L. Crocco, and M. Urso, "New tools and series for forward and inverse scattering problems in lossy media," *IEEE Geosci. Remote Sens*., vol. 1, no. 4, pp. 327-331. Oct. 2004.
[129] O. Bucci, N. Cardace, L. Crocco, and T. Isernia, "Degree of non-linearity and a new solution procedure in scalar 2-D inverse scattering problems," *J. Opt. Soc. Amer. A*., vol. 18, pp. 1832-1845, 2001.
[130] S. Mallat, *A Wavelet Tour of Signal Processing*, 2nd ed. New York: Academic Press, 1998.
[131] R. Baraniuk, V. Cevher, M. Duarte, and C. Hedge, "Model-based compressive sensing," *IEEE Trans. Inf. Theory*., vol. 56, no. 4, pp. 1982-2001, 2010.
[132] Y. Eldar, P. Kuppinger, and H. Bolcskei, "Block-sparse signals: uncertainty relations and efficient recovery," *IEEE Trans. Signal Process*., vol. 58, no. 6, pp. 3042-3054, 2010.
[133] M. Tipping, "Sparse Bayesian learning and the relevance vector machine," *J. Mach. Learn. Res*., vol. 1, pp. 211-244, 2001.
[134] G. Cawley and N. Talbot, "Preventing over-fitting during model selection via Bayesian regularization of the hyper-parameters," *J. Mach. Learn. Res*., vol. 8, pp. 841-861, 2007.
[135] D. Fong and M. Saunders, "CG versus MINRES: An empirical comparison," *SQU Journal for Science*., vol. 17, no. 1, pp. 44-62, 2012.
[136] D. Needell and J. Tropp, "COSAMP: iterative signal recovery from incomplete and inaccurate samples," *Appl. Comput. Harmon. Anal*., vol. 26, pp. 301-321, 2008.
[137] A. Surowiec, S. Stuchly, J. Barr, and A. Swarup, "Dielectric properties of breast carcinoma and the surrounding tissues," *IEEE Trans. Biomed. Eng*., vol. 35, no. 4, pp. 257-263, Apr. 1988.

[138] W. Joines, Y. Dhenxing, and R. Jirtle, "The measured electrical properties of normal and malignant human tissues from 50 to 900MHz," *Med. Phys*., vol. 21, pp. 547-550, Apr. 1994.
[139] S. Mustafa, A. Abbosh, and P. Nguyen, "Modeling human head tissues using fourth-order debye model in convolution-based three-dimensional finite-difference time-domain," *IEEE Trans. Antennas Propag*., vol. 62, no. 3, Mar. 2014.
[140] J. Kennedy and R. Eberhart, "Particle swarm optimization," *IEEE Int. Conf. Neural Networks Procee*., vol. 4, pp. 1942-1948, 1995.
[141] A. Mobashsher, B. Mohammed, S. Mustafa, and A. Abbosh, "Ultra-wideband antenna for portable brain stroke diagnostic system," *IEEE IMWS-Bio Workshop,* Singapore, pp. 1-3, 2013.
[142] S. Luke, "*Essentials of Metaheuristics"*, Lulu, 2009, [Online] Available: http://cs.gmu.edu/~sean/book/metaheuristics/
[143] A. Mobashsher and A. Abbosh, "CPW-fed low-profile directional antenna operating in low microwave band for wideband medical diagnostic system," *Electron. Lett*., vol. 50, no. 4, pp. 246-248, Feb. 2014.
[144] B. Mohammed and A. Abbosh, "Realistic head phantom to test microwave systems for brain imaging," *Micorw. Opt. Tech. Lett*., vol. 56, no. 4, pp. 979-982, 2014.
[145] L. Guo and A. Abbosh, "Optimization-based confocal microwave imaging in medical applications," *IEEE Trans. Antennas Propag*., vol. 63, no. 8, pp. 3531-3539, Aug. 2015.
[146] L. Guo and A. Abbosh, "Microwave imaging of nonsparse domain using Born iterative method with wavelet transform and block sparse Bayesian learning," *IEEE Trans. Antennas Propag*., vol. 63, no. 11, pp. 4877-4888, Nov. 2015.
[147] L. Guo and A. Abbosh, "Microwave stepped frequency head imaging using compressive sensing with limited number of frequency steps," *IEEE Antennas Wireless Prop Lett*., vol. 14, pp. 1133-1136, May. 2015.
[148] D. Holder, "Electrical impedance tomography with cortical or scalp electrodes during global cerebral ischaemia in the anaesthetised rat," *Clin. Phys. Physiol. Meas*., vol. 13, no. 1, pp. 87-98, Oct. 1991.
[149] A. Surowiec, S. Stuchly, and A. Swarup, "Postmortem changes of the dielectric properties of bovine brain tissues at low radiofrequencies," *Bioelectromagnetics*., vol. 7, no. 1, pp. 31-43, 1986.
[150] C. Cortes and V. Vapnik, "Support vector networks," *Machine Learning*., vol. 20, pp. 273-297, 1995.
[151] V. Vapnik, *The Nature of Statistical Theory*, New York: Springer-Verlag, 1995.
[152] E. Osuna, R. Freund, and F. Girosi, "Training support vector machines: Application to face detection," in *Proc. Computer Vision and Pattern Recognition*, Puerto Rico, 1997.
[153] V. Wan and W. Campbell, "Support vector machines for speaker verification and identification," in *Proc. IEEE Workshop Neural Networks for Signal Processing*, Sydney, Australia, 2000.
[154] B. Scholkopf, S. Kah-Kay, C. Burges, F. Girosi, P. Niyogi, T. Poggio, and V. Vapnik, "Comparing support vector machines with Gaussian kernels to radial basis function classifier," *IEEE Trans. Signal Processing*., vol. 45, no. 11, pp. 2758-2765, Nov. 1997.
[155] T. Joachims, "Text categorization with support vector machines: Learning with many relevant features," in *Proc. Europ. Conf. Machine Learning*. Berlin, Germany, 1998.
[156] A. Zien, G. Ratsch, S. Mika, B. Scholkopf, T. Lengauer, and K. Muller, "Engineering support vector machine kernels that recognize translation initiation sites in DNA," *Bioinformatics*., vol. 16, no. 9, pp. 799-807, 2000.
[157] I. EI-Naqa, Y. Yang, M. Wernick, N. Galatsanos, and R. Nishikawa, "A support vector machine approach for detection of microcalcifications," *IEEE Trans. Med. Imag*., vol. 21, no. 12, pp. 1552-1563, Dec. 2002.

[158] P. Dimbylow, "FDTD calculations of the whole-body averaged SAR in an anatomically realistic voxel model of the human body from 1MHz to 1GHZ," *Phys. Med. Biol*., vol. 42, no. 3, pp. 479-490, 1997.
[159] S. Lloyd, "Least squares quantization in PCM," *IEEE Trans. Information Theory*., vol. 28, no. 2, pp. 129-137, Mar. 1982.
[160] T. Kanungo, D. Mount, N. Netanyahu, C. Piatko, R. Silverman, and A. Wu, "An efficient k-means clustering algorithm: analysis and implementation," *IEEE Trans. Pattern Analysis and Machine Intelligence*., vol. 24, no. 7, July. 2002.
[161] K. Muller, S. Mika, G. Ratsch, K. Tsuda, and B. Scholkopf, "An introduction to kernel-based learning algorithms," *IEEE Trans. Neural Networks*., vol. 12, no. 2, Mar. 2001.
[162] C. Burges, "A tutorial on support vector machines for pattern recognition," *Knowledge Discovery and Data Mining*., vol. 2, pp. 121-167, June. 1998.
[163] K. Bennett and O. Mangasarian, "Robust linear programming discrimination of two linearly inseparable sets," *Optimization Methods Software*., vol. 1, no. 1, pp. 23-34, 1992.
[164] R. Fan, P. Chen, and C. Lin, "Working set selection using second order information for training SVM," *J. Mach. Learn. Res*., vol. 6, pp. 1889-1918, 2005.
[165] S. Keerthi, S. Shevade, C. Bhattacharyya, and K. Murthy, "Improvements to Platt's SMO algorithm for SVM classifier design," *Neural Computation*., vol. 13, no. 3, pp. 637-649, Mar. 2001.
[166] C. Chang and C. Lin, "LIBSVM: a library for support vector machines," *ACM Trans. Intelligent Sys. Tech*., vol. 2, pp. 1-27, 2001. Software available: http://www.csie.ntu.edu.tw/~cjlin/libsvm
[167] B. Scholkopf, C. Burges, and A. Smola *Advances in Kernel Methods: Support Vector Learning.* Cambridge, MA: MIT Press, 1999.
[168] M. Zweig and G. Campbell, "Receiver-operating characteristic (ROC) plots: A fundamental tool in clinical medicine," *Clin. Chem*., vol. 39, no. 4, pp. 561-577, Apr. 1993.
[169] A. Bradley, "The use of the area under the roc curve in the evaluation of machine learning algorithms," *Pattern Recognit*., vol. 30, no. 7, pp. 1145-1159, 1997.